

Role of Carbon Nanomaterials as Reinforcing Phase in Improvement of Physico-Chemical Properties of Pozzolana Portland Cement Mortar

A THESIS

*Submitted in fulfillment of the requirement for
the award of the degree
of*

DOCTOR OF PHILOSOPHY

in

CHEMISTRY

by

Kanchna Bhatrola

(Roll No. 19511104)



Under the Supervision of

Dr N C Kothiyal

DEPARTMENT OF CHEMISTRY

**DR B R AMBEDKAR NATIONAL INSTITUTE OF TECHNOLOGY,
JALANDHAR -144011 (PUNJAB), INDIA**

March, 2024

Role of Carbon Nanomaterials as Reinforcing Phase in Improvement of Physico-Chemical Properties of Pozzolana Portland Cement Mortar

A THESIS

*Submitted in fulfillment of the requirement for
the award of the degree
of*

DOCTOR OF PHILOSOPHY

in

CHEMISTRY

by

Kanchna Bhatrola

(Roll No. 19511104)



Under the Supervision of

Dr N C Kothiyal

DEPARTMENT OF CHEMISTRY

**DR B R AMBEDKAR NATIONAL INSTITUTE OF TECHNOLOGY,
JALANDHAR -144011 (PUNJAB), INDIA**

March, 2024



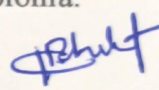
**DR B R AMBEDKAR NATIONAL INSTITUTE OF TECHNOLOGY,
JALANDHAR -144001, PUNJAB (INDIA)
DEPARTMENT OF CHEMISTRY**

CANDIDATE'S DECLARATION

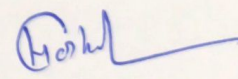
I hereby certify that the work which is being presented in this thesis entitled **"ROLE OF CARBON NANOMATERIALS AS REINFORCING PHASE IN IMPROVEMENT OF PHYSICO-CHEMICAL PROPERTIES OF POZZOLANA PORTLAND CEMENT MORTAR"**, being submitted to the Department of Chemistry, Dr B R Ambedkar National Institute of Technology, Jalandhar (India), in fulfillment of the requirements for the award of the degree of Doctor of Philosophy in an authentic record of my own research work carried out during a period from **July 2019 to November 2023** under the supervision of **Professor (Dr) N C Kothiyal**.

The work embodied in this thesis has not been submitted elsewhere in part or in full, to any other University or Institute for the award of any other degree or diploma.

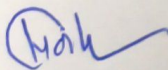
Date: 22/3/2024
Place: NIT, JALANDHAR

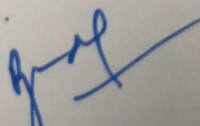

(Kanchna Bhatrola)
Research Scholar
Roll No. 19511104

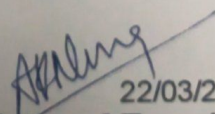
This is to certify that the above statement made by the candidate is correct to the best of my knowledge and the bonafide research work was carried out by her under my supervision and guidance.

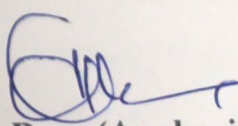

Dr N C Kothiyal
Professor, Department of Chemistry
(Research Supervisor)

The Ph.D. viva-voce Examination of **Kanchna Bhatrola**, Research Scholar, has been held on 22/03/2024.


Supervisor


Head of Department


22/03/2024
External Examiner


Dean (Academic)

ABSTRACT

Cement mortar is a common building material used all over the world and is the foundation of many civil engineering infrastructures. However, it is subject to a number of constraints, some of which include low physico-mechanical strength, quasi brittleness, the cracking phenomena, high permeability, and porous microstructural characteristics. Researchers in the past have used steel fibres, glass fibres, polypropylene fibres, carbon fibres, and other common materials as reinforcing agents in the cement mortar to avoid these problems. But these materials only work to strengthen up to the micro-level, or marco-level, and cracks continue to form at the nano-level in the cement mortar matrix. Nanotechnology has become an interesting way to use nano-sized reinforcements in cement-based materials. Extraordinary mechanical properties can be found in carbon nanomaterials (CNMs), such as one-dimensional functionalized multiwalled carbon nanotubes (FMWCNTs) and two-dimensional graphene oxide (GO). CNMs, with their high surface area, high aspect ratio, and exceptional mechanical potential, add new dimensions at the interface to the cementitious matrix. Despite these benefits, there are several drawbacks to using CNMs in the cementitious matrix. One of these is the difficulty of uniform distribution of CNMs throughout the alkaline cement pore solution.

In light of these observations, it is possible that CNMs can be covalently functionalized and that CNMs can be dispersed by a superplasticizer to improve their dispersion. Another option is to incorporate hybrid CNMs (i.e., FMWCNTs and GO) as nano-reinforcements into the cementitious matrix to take advantage of their synergistic impact. Cement manufacturing seems to be a major contributor to the release of the greenhouse gas carbon dioxide. Using pozzolana portland cement has the potential to reduce cement consumption and consequently cement-related CO₂ emissions. The results of the thesis show that CNMs and hybrid CNMs play a role as reinforcing phases in making pozzolana portland cementitious nanocomposites (CNCMs) stronger. The CNCMs were made with Graphene Oxide (GO), Functionalized Multiwalled Carbon Nanotubes (FMWCNTs), and a hybrid of GO and FMWCNTs. Graphite Powder (GP) was converted into Milled Graphite Powder (MGP) with the help of a planetary ball milling machine (Retsch PM100) ball mill. Using Hummer's

Method, the MGP was subjected to an oxidative treatment in order to produce the GO. Through exposure to nitric acid, the MWCNTs were converted into FMWCNTs. UV-Visible Spectroscopy was utilized to observe the enhanced dispersion of or GO or FMWCNTs. The CNMs were structurally investigated using FE-SEM/EDS, FT-IR, HR-TEM, RAMAN Spectroscopy and PXRD.

For CNMs dosages ranging from 0.0015% to 0.012% (by weight of cement), the impact of CNMs and HCNMs on the compressive and tensile strength of the CNCMs was assessed. Microstructural investigations, crystalline behaviour, and durability (electrical resistivity, capillary water absorption, and acid-sulfate attack) were investigated as additional features of CNCMs. The effects of varying CNMs and HCNMs concentrations and cure times (7, 28, 56, and 90 days), on these characteristics were investigated. After incorporating CNMs/HCNMs, the characteristics of CNCMs were compared to those of Control samples, where no carbon nanomaterial was added. The results demonstrated that HCNMs improved physico-mechanical strength more than CNMs applied alone (i.e., GO or FMWCNTs).

In terms of compressive strength, 0.0015% HCNMs-CNCMs obtained maximum values of 21.32%. However, at 90 days of curing, tensile strength values were discovered to be greatest for 0.0015% HCNMs-CNCMs with respect to control samples, by 35.27%. With the help of microstructural and crystalline studies, it was found that the hydration reactions of CNMs/HCNMs that included CNCMs were better. Electrical resistivity, capillary water absorption, and acid-sulfate attack verify the cementitious matrix improved compactness and finer pore structure.

The current research aimed to improve the physico-mechanical properties of pozzolana portland cementitious nanocomposites by using sterically stabilized CNMs and HCNMs so that safer and sustainable construction materials can be produced with reduced costs and desirable longevity. The results obtained from this study were quite encouraging.

ACKNOWLEDGEMENT

This thesis is the outcome of the research conducted by the author at the Department of Chemistry of Dr B R Ambedkar National Institute of Technology, Jalandhar, India. The successful completion of a thesis project is contingent upon the contributions, encouragement, and substantial support of multiple individuals. In this document, I would like to express my gratitude for the assistance that was extended to me throughout the course of my Ph.D.

Initially, I would like to extend my heartfelt appreciation to my supervisor, Dr N C Kothiyal, who is a Professor in the Department of Chemistry at Dr B R Ambedkar National Institute of Technology, Jalandhar, for granting me the opportunity to participate in this pioneering research investigation. I express my gratitude towards him for exhibiting patience and resilience during the challenging phases of my research period. Along with gratitude to the mentor, due acknowledgement is extended to Dr Kanishk, an Assistant Professor in the Department of Civil Engineering at Dr B R Ambedkar National Institute of Technology, Jalandhar, for offering valuable recommendations during the course of the study and for providing essential laboratory resources in the Department of Civil Engineering to conduct the practical component of this research endeavour.

I also express gratitude towards the Director of Dr B R Ambedkar National Institute of Technology, Jalandhar, for the provision of appropriate infrastructure and the opportunity to successfully complete their Ph.D. degree at the aforementioned institute.

I would like to convey my heartfelt gratitude and deep appreciation to Dr Rajiv Jindal, Associate Professor and Head, Department of Chemistry, Dr B R Ambedkar National Institute of Technology, Jalandhar, for giving me with the chance to work and for providing the required facilities throughout the research work. I also express sincere regards to former HODs, Dr B S Kaith, and Dr Jaspreet Kaur Rajput, for their kind support. At the same time, I also thank all the department faculty members for their kind cooperation and help rendered during the research work.

The prompt advice provided by Dr Sanjay Dhakate, Chief Scientist & Professor (AcSIR), CSIR-National Physical Laboratory, Delhi, is gratefully acknowledged. We gratefully thank his significant contributions to this research.

I am also thankful to Mr. Rajendra Pathak and Ms. Jagmohan Kaur for their cooperative behavior throughout my Ph.D. The timely cooperation of Sh. Khushpal Singh and Sh Satnam Singh, Laboratory Technical Assistant, Department of Civil Engineering, is highly acknowledged.

During the application phase of my research study, the research scholar Mr. Sameer Kumar Maurya, from the Chemistry Department at the Dr B R Ambedkar National Institute of Technology, Jalandhar, and Mr. Chander Prakash research scholar from Industrial Production department at the Dr B R Ambedkar National Institute of Technology, Jalandhar, provided me with invaluable assistance and academic support.

Also, I am indebted to the knowledge shared by my senior, Dr Ramanjit Kaur. Moreover, I express my heartfelt gratitude to my dear friends Ms. Garima and Ms. Keshu for their unwavering support, friendly guidance, and endless inspiration throughout this journey. Additionally, I extend my sincere appreciation to my friends Ms. Deepshikha, Ms. Deepika, Mr. Himanshu, and Mr. Jatinder for their invaluable assistance and constant motivation. Our journey, fondly known as the 'Night Tea' group, began with a cup of tea, and those moments are cherished dearly. I also express thanks to my fellow labmates: Ms. Bharti, Ms. Sakshi, Ms. Vasudha Vaid, and Ms. Sakshi Bawa, for interesting discussions.

I thank almighty God for giving me strength and patience. Finally, I would like to thank my parents, and my siblings Ms. Pooja, Ms. Lata, Mr. Narendra and Mr. Deepak who provided me the strength to keep moving in life in failure or success. I thank my family for holding me high during the lows of life in a way to which no words can explain.

I am also expressing my abounding feelings of gratitude to all those who helped me in this course but have not been listed here.

Kanchna Bhatrola

CONTENTS

CANDIDATE'S DECLARATION	i
ABSTRACT	iii
ACKNOWLEDGEMENT	v
ABBREVIATIONS AND NOTATIONS	xiv
LIST OF TABLES	xvi
LIST OF FIGURES	xviii
Chapter 1	1
INTRODUCTION	1
1.1 GENERAL	1
1.2 LIMITATIONS OF CEMENTITIOUS MATERIALS AND POTENTIAL SOLUTIONS	3
1.3 COMPOSITES AND NANOCOMPOSITES	5
<i>1.3.1 Composite</i>	<i>5</i>
1.3.1.1 Matrix Phase	6
1.3.1.2 Reinforcing Phase	6
1.3.1.3 Interface in Composites	6
<i>1.3.2 Advantages of Composites</i>	<i>7</i>
<i>1.3.3 Nanocomposites</i>	<i>7</i>
<i>1.3.4 Types of Nanocomposites</i>	<i>9</i>
1.3.4.1 Based on Matrix Phase	9
(a) Ceramic Matrix Nanocomposites	9
(b) Polymer Matrix Nanocomposites	9
(c) Metal Matrix Nanocomposites	10
1.3.4.2 Based on Reinforcing Phase	10
(a) Laminated Nanocomposites	10
(b) Particulate Nanocomposites	10
(c) Fibrous Reinforced Nanocomposite	10
1.4 CARBON NANOMATERIALS / HYBRID CARBON NANOMATERIALS BASED CEMENTITIOUS NANOCOMPOSITES	11
<i>1.4.1 Pozzolana Portland Cement</i>	<i>13</i>
1.4.1.1 Composition of Cement	14
1.4.1.2 Hydration Reactions of Cement	15
1.4.1.3 Chemical Admixtures for Cement	20
1 Water-Reducing Admixtures	20
2 Corrosion Inhibitors	20
3 Retarding Admixtures	20
4 Air-Entraining Admixtures	20
5 Superplasticizers	21

6 Shrinkage Reducing Admixtures:	21
1.4.1.4 Supplementary Cementitious Materials (SCMs)	21
1.4.1.4.1 Natural Pozzolans	22
1.4.1.4.2 Artificial pozzolans	23
<i>1.4.2 Nano-Modification of Pozzolana Portland -Fly Ash based Cementitious Matrixes</i>	28
<i>1.4.3 Carbon Nanomaterials/Hybrid Carbon Nanomaterials (CNMs/HCNMs) as Reinforcing Phase</i>	33
1.4.3.1 Carbon Nanotubes (CNTs)	33
(a) Synthesis Methods of CNTs	34
□ Arc-Discharge Method	34
□ Chemical Vapor Deposition (CVD)	34
□ The Laser Ablation Method	35
(b) Properties of CNTs	35
1. Electrical Properties:	35
2. Mechanical Properties:	35
3. Thermal Properties:	36
4. Hydrophobicity	36
1.4.3.2 Graphene Oxide (GO)	36
(A) Synthesis of GO	37
□ Brodie and Staudenmaier Method	37
□ Hummers and Modified Hummer's Method	37
(B) Properties of GO	38
□ Mechanical Properties	38
□ Electrical Properties	39
□ Hygroscopicity	39
<i>1.4.4 Challenges Arising from Carbon Nanomaterial Usage and Potential Remedies</i>	39
<i>1.4.5 HYBRID CARBON NANOMATERIALS (HCNMs)</i>	45
1.5 SIGNIFICANCE OF THE RESEARCH	47
<i>1.5.1 Enhanced Overall Performance</i>	47
<i>1.5.2 Economic Sustainability</i>	48
<i>1.5.3 Environment-friendly Approach</i>	48
1.6 AIM AND OBJECTIVES OF THE RESEARCH	49
<i>1.6.1 Aim of the Research</i>	49
<i>1.6.2 Objectives of the Research</i>	49
1.7 OVERVIEW OF CHAPTERS	50
Chapter 2	53
2.1 HISTORY OF CARBON NANOMATERIALS IN CONSTRUCTION MATERIALS	53

2.2 CARBON NANOMATERIALS BASED CEMENTITIOUS NANOCOMPOSITES (CNCMs)	55
2.2.1 <i>Mechanical Properties of CNCMs</i>	56
2.2.2 <i>Microstructural Properties of CNCMs</i>	65
2.2.3 <i>Crystallization Properties of CNCMs</i>	71
2.2.4 <i>Durability of CNCMs</i>	74
2.2.4.1 <i>Electrical Properties of CNCMs</i>	74
2.2.4.2. Water absorption	76
2.2.4.3. Acid and sulphate attack	77
2.3 CONCLUSIONS DRAWN FROM LITERATURE REVIEW	96
Chapter 3	99
<i>EXPERIMENTAL METHODOLOGY</i>	99
3.1 GENERAL	99
<i>Step I: Material Characterizations</i>	99
<i>Step II: Preparation/ Functionalization of Carbon Nanomaterials (FCNMs)</i>	99
<i>Step III: Dispersion Studies of Carbon Nanomaterials (CNMs) and Hybrid Carbon Nanomaterials (HCNMs)</i>	99
<i>Step IV: Preparation of CNMs/HCNMs based Cementitious Nanocomposites (CNMs/HCNMs-CNCMs)</i>	99
<i>Step V: Determination of the Physico-Mechanical Strength of CNCMs</i>	100
<i>Step VI: Determination of Microstructural and Crystallization Studies of CNCMs</i>	100
<i>Step VII: Determination of Durability Studies of CNCMs</i>	100
3.2 MATERIALS AND METHODOLOGY	100
3.2.1 <i>Materials and Methodology used for Synthesis/Functionalization of Carbon Nanomaterials (CNMs)</i>	102
3.2.1.1 <i>Materials and Methodology for Preparation of Graphene Oxide (GO)</i>	102
(a) Raw Materials	102
(b) Materials and Chemicals	102
(c) Equipment	102
(d) Experimental Methodology for Graphene Oxide (GO) Preparation	103
(e) Characterization of Graphene oxide	103
3.2.1.2 <i>Materials and Methodology for Multiwalled Carbon Nanotubes (MWCNTs)</i>	104
(a) Preparation of Multiwalled Carbon Nanotubes (MWCNTs)	104
(b) Chemicals and Reagents Used	105
(c) Equipment	105
(d) Experimental Methodology for Functionalization of Multiwalled Carbon Nanotubes (FMWCNTs)	105
(e) Characterization of FMWCNTs	106

3.2.2 Steric Stabilization of Carbon Nanomaterials (CNMs) using Superplasticizers (SP) and their Dispersion Studies	106
(a) Raw Materials	106
(b) Chemicals and Reagents Used	106
(c) Equipment	106
(d) Experimental Methodology	107
3.2.3 Materials and Methodology for Fabrication of Control samples and CNMs/HCNMs based CNCMs	107
3.2.3.1 Raw Materials	107
(a) Carbon Nanomaterials and Hybrid Carbon Nanomaterials (CNMs/HCNMs)	107
(b) Binder (Pozzolana Portland Cement)	107
(c) Indian Standard Sand	108
(c) Superplasticizer (SP)	108
(e) Water	109
3.2.3.2 Equipment	109
3.2.3.3 Experimental Methodology for Fabrication of Mortar Samples	109
3.2.4. Materials and Methodology for Determination of Physico-Chemical Behavior of Control samples and CNMs/HCNMs based CNCMs	111
3.2.4.1 Materials and Methodology for Determining Compressive Strength and Tensile Strength of Control Samples and CNMs/HCNMs based CNCMs	112
(a) Raw Materials	112
(b) Equipment	112
(c) Experimental Methodology	113
3.2.4.2 Materials and Methodology for Microstructural Studies of Control Samples and CNMs/HCNMs based CNCMs	114
(a) Raw Materials	114
(b) Equipment	114
(c) Experimental Methodology	114
3.2.4.3 Materials and Methodology for Determining Crystalline Behavior of Control samples and CNMs/HCNMs based CNCMs	115
(a) Raw Materials	115
(b) Equipment	115
(c) Experimental Methodology	115
3.2.4.4 Materials and Methodology for Determining the Electrical Resistivity of Control samples and CNMs/HCNMs based CNCMs	116
(a) Raw Materials	116
(b) Equipment	116
(c) Experimental Methodology	116
Chapter 4	117
<i>RESULTS AND DISCUSSION</i>	<i>117</i>
4.1 GENERAL	117
Section I	118
<i>CHARACTERIZATION AND DISPERSION STUDIES</i>	<i>118</i>
<i>OF CARBON NANOMATERIALS</i>	<i>118</i>

4.2	STRUCTURAL CHARACTERIZATION OF CARBON NANOMATERIALS	118
4.2.1	<i>Structural Characterization of Graphite powder (GP) and Graphene Oxide (GO)</i>	118
4.2.1.1	Results of FE-SEM Analysis of Graphite powder (GP), Milled Graphite powder (MGP) and Graphene Oxide (GO)	118
4.2.1.2	Results of HR-TEM Analysis of MGP and GO	119
4.2.1.3	Results of Raman Spectroscopy Analysis of MGP and GO	120
4.2.1.4	Results of PXRD Analysis of MGP and GO	121
4.2.1.5	Results of FTIR Analysis of MGP and GO	122
4.2.2	<i>Structural Characterization of MWCNTs and FMWCNTs</i>	123
4.2.2.1	Results of FE-SEM Analysis of MWCNTs and FMWCNTs	123
4.2.2.2	Results of HR-TEM Analysis of MWCNTs and FMWCNTs	124
4.2.2.3	Results of PXRD Analysis of MWCNTs and FMWCNTs	125
4.2.2.4	Results of Raman Spectroscopy Analysis of MWCNTs and FMWCNTs	126
4.2.2.5	Results of FTIR Analysis of MWCNTs and FMWCNTs	127
4.3	DISPERSION STUDIES OF CARBON NANOMATERIALS	128
4.3.1	<i>Structural Characterization of Superplasticizers (SP)</i>	128
4.3.1.1	FT-IR Spectroscopy of SP	128
4.3.1.2	DLS analysis of SP Superplasticizer	130
4.3.2	<i>Dispersion Studies of Superplasticizer Stabilized GO, FMWCNTs and HCNMs by UV-Visible Spectroscopy</i>	130
Section II		137
	<i>PHYSICO-MECHANICAL STRENGTH OF CNMs/HCNMs BASED CNCMs</i>	137
4.4	COMPRESSIVE STRENGTH OF CNMs/HCNMs BASED CNCMs	137
4.4.1.	<i>Compressive Strength of GO-CNCMs</i>	137
4.4.2	<i>Compressive Strength of FMWCNTs-CNCMs</i>	140
4.4.3	<i>Compressive Strength of HCNMs-CNCMs</i>	142
4.5	TENSILE STRENGTH OF CNMs/HCNMs BASED CNCMs	146
4.5.1	<i>Tensile Strength of GO-CNCMs</i>	146
4.5.2	<i>Tensile Strength of FMWCNTs-CNCMs</i>	147
4.5.3	<i>Tensile Strength of HCNMs-CNCMs</i>	149
Section III		155
	<i>MICROSTRUCTURAL AND CRYSTALLIZATION BEHAVIOR STUDIES</i>	155
4.6	MICROSTRUCTURAL STUDIES OF CNMs/HCNMs BASED CNCMs	156
4.6.1	<i>Microstructural Studies of Control sample of Mortars</i>	156
4.6.2	<i>Microstructural Studies of GO-CNCMs</i>	158

4.6.2.1 Microstructure Analysis at 7 Days of Curing	158
4.6.2.2 Microstructure Analysis at 28 Days of Curing	159
4.6.2.3 Microstructure Analysis at 56 Days of Curing	160
4.6.2.4 Microstructure Analysis at 90 Days of Curing	161
4.6.3 <i>Microstructural Studies of FMWCNTs-CNCMs</i>	162
4.6.3.1 Microstructure Analysis at 7 Days of Curing	163
4.6.3.2 Microstructure Analysis at 28 Days of Curing	164
4.6.3.3 Microstructure Analysis at 56 Days of Curing	165
4.6.3.4 Microstructure Analysis at 90 Days of Curing	166
4.6.4 <i>Microstructural Studies of HCNMs-CNCMs</i>	167
4.6.4.1 Microstructure Analysis at 7 Days of Curing	167
4.6.4.2 Microstructure Analysis at 28 Days of Curing	168
4.6.4.3 Microstructure Analysis at 56 Days of Curing	169
4.6.4.4 Microstructure Analysis at 90 Days of Curing	170
4.7 CRYSTALLIZATION BEHAVIOR STUDIES OF CNMs/HCNMs BASED CNCMs	171
4.7.1 <i>Crystallization Behavior of GO-CNCMs</i>	174
4.7.1.1 Effect of GO dosage	174
4.7.1.2 Impact of Curing Time	174
4.7.2 <i>Crystallization Behavior of FMWCNTs-CNCMs</i>	175
4.7.2.1 Effect of FMWCNTs dosage	175
4.7.2.2 Effect of Curing Time	176
4.7.3 <i>Crystallization Behavior of HCNMs-CNCMs</i>	177
4.7.3.1 Effect of HCNMs dosage	177
4.7.3.2 Impact of Curing Time	178
4.8 FUNCTIONAL GROUP STUDIES OF CNMs/HCNMs BASED CNCMs	178
4.8.1 <i>FT-IR studies of GO based CNCMs</i>	179
4.8.2 <i>FT-IR studies of FMWCNTs based CNCMs</i>	182
4.8.3 <i>FT-IR studies of HCNMs based CNCMs</i>	185
Section IV	189
<i>DURABILITY STUDIES</i>	189
4.9 ELECTRICAL RESISTIVITY OF CNMs/HCNMs BASED CNCMs	190
4.9.1 <i>Electrical Resistivity of GO-CNCMs</i>	190
4.9.2 <i>Electrical Resistivity of FMWCNTs-CNCMs</i>	192
4.9.3 <i>Electrical Resistivity of HCNMs-CNCMs</i>	194
4.10 CAPILLARY WATER ABSORPTION (WATER ABSORPTION TEST) OF CNMs/HCNMs BASED CNCMs	198
4.10.1 <i>Water Absorption of GO-CNCMs</i>	199
4.10.2 <i>Water Absorption of FMWCNTs-CNCMs</i>	202

4.10.3	<i>Water Absorption of HCNMs-CNCMs</i>	205
4.11	ACID AND SULFATE ATTACK OF CNMs/HCNMs BASED CNCMs	215
4.11.1	<i>Acid and Sulfate Attack on GO-CNCMs</i>	216
4.11.2	<i>Acid and Sulfate Attack of FMWCNTs-CNCMs</i>	218
4.11.3	<i>Acid and Sulfate Attack on HCNMs-CNCMs</i>	220
4.12	A PROPOSED METHOD TO IMPROVE THE WAY GO, FMWCNTs, AND HCNMs BEHAVE MORE EFFECTIVELY	225
4.12.1	<i>Steric stabilization of GO, FMWCNTs, and HCNMs: A proposed mechanism</i>	225
4.12.2	<i>Proposed Mechanism for CNMs/HCNMs Hydration Reaction in CNCMs</i>	227
Chapter 5		229
	<i>CONCLUSIONS AND SCOPE FOR FUTURE RESEARCH</i>	229
5.1	GENERAL	229
5.2	CONCISE CONCLUDING REMARKS	229
5.2.1	<i>Findings from the Synthesis/Functionalization of Carbon Nanomaterials and Dispersion Studies</i>	229
5.2.2	<i>Conclusions derived from the analysis of Compressive Strength</i>	230
5.2.3	<i>Conclusions derived from the analysis of Tensile Strength</i>	231
5.2.4	<i>Conclusions derived from the analysis of Microstructure</i>	231
5.2.5	<i>Conclusions derived from the analysis of Crystallization Behavior</i>	232
5.2.6	<i>Durability Behaviour</i>	233
5.2.6.1	<i>Conclusions derived from the analysis of Electrical Resistivity behaviour</i>	233
5.2.6.2	<i>Studies Conclusions derived from the analysis of Capillary Water Absorption</i>	234
5.2.6.3	<i>Studies Conclusions derived from the analysis compressive strength after acid and sulfate attack</i>	234
5.3	CONCLUDING STATEMENT	235
5.4	SCOPE FOR FUTURE RESEARCH	236
	<i>BIBLIOGRAPHY</i>	237
	<i>RESEARCH PUBLICATIONS</i>	275

ABBREVIATIONS AND NOTATIONS

AFM	Atomic Force Microscopy
Aft	Ettringite
ASTM	American Society for Testing and Materials
BIS	Bureau of Indian Standards
C₂S	Dicalcium Silicate
C₃A	Tricalcium Aluminate
C₃S	Tricalcium Silicate
C₄AF	Tetracalcium Aluminoferrite
CH	Calcium Hydroxide
CNCM(s)	Cementitious Nanocomposite(s)
CNM(s)	Carbon Nanomaterial(s)
CSH	Calcium-Silicate-Hydrate
EDS	Energy Dispersive Spectroscopy
FE-SEM	Field Emission Scanning Electron Microscopy
FT-IR	Fourier Transform Infrared Spectroscopy
GO	Graphene Oxide
GP	Graphite Powder
HCNM(s)	Hybrid Carbon Nanomaterial(s)
IEA	International Energy Agency
MGP	Milled Graphite Powder
MPa	Mega pascal

MWCNT(s)	Multi Walled Carbon Nanotube(s)
PPC	Pozzolana Portland Cement
PXRD	Powdered X-Ray Diffraction
P	Electrical Resistivity
R	Electrical Resistance
SP	Superplasticizer
TEM	Transmission Electron Microscopy
TPa	Tera pascal

LIST OF TABLES

Table No.	Particulars	Page No.
Table 1.1	Physical Properties of Conventional Fibers	4
Table 1.2	Physical Properties of Conventional Nanomaterials	5
Table 1. 3	A General difference between chemical composition of PPC and OPC	13
Table 1. 4	Bogue's Compounds	15
Table 1. 5	Advantages and Disadvantages of Nano-particles in Cementitious Composites	31
Table 1.6	A Summary of Physical & Chemical Dispersion Approach (Kharisov et al., 2014)	40
Table 2.1	A Literature Overview of Mechanical, Microstructural, Crystallization, and Durability Properties of CNMs/HCNMs-CNCMs	79
Table 3.1	Oxide Analysis of Cement	108
Table 3.2	General Specifications of Sand	108
Table 3.3	Mix Designs for CNCMs	111
Table 3.4	Test Procedures, Specimen Details and Curing Time for CNCMs	112
Table 4.1	Elemental Compositions of MGP and GO	119
Table 4.2	Elemental Compositions of MWCNTs and FMWCNTs	124
Table 4.3	Percentage Change in Compressive Strength for GO-CNCMs	139
Table 4.4	Percentage Change in Compressive Strength for FMWCNTs-CNCMs	142
Table 4.5	Percentage Change in Compressive Strength for HCNMs-CNCMs	144
Table 4.6	Average Compressive Strength Values of CNMs/HCNMs based CNCMs	145
Table 4.7	Percentage Change in Tensile Strength for GO-CNCMs	147
Table 4.8	Percentage Change in Tensile Strength for FMWCNTs-CNCMs	149
Table 4.9	Percentage Change in Tensile Strength for HCNMs-CNCMs	151
Table 4.10	Average Tensile Strength Values of CNMs/HCNMs based CNCMs	153
Table 4.11	Electrical Resistivity for GO-CNCMs	192
Table 4.12	Electrical Resistivity for FMWCNTs-CNCMs	194
Table 4.13	Electrical Resistivity for HCNMs-CNCMs	196
Table 4.14	Average Electrical Resistivity Values of CNMs/HCNMs based CNCMs	198

Table 4.15 Water Absorption for GO-CNCMs after 28 Days of curing	201
Table 4.16 Water Absorption for GO-CNCMs after 90 Days of curing	202
Table 4.17 Water Absorption for FMWCNTs-CNCMs after 28 Days of curing	204
Table 4. 18 Water Absorption for FMWCNTs-CNCMs after 90 Days of curing	205
Table 4.19 Water Absorption for HCNMs-CNCMs after 28 Days of curing	208
Table 4.20 Water Absorption for HCNMs-CNCMs after 90 Days of curing	209
Table 4.21 Average Water Absorption Values of CNMs/HCNMs based CNCMs	210
Table 4.22 Percentage Change in Compressive Strength after acid and sulfate cured for GO-CNCMs	218
Table 4.23 Percentage Change in Compressive Strength after acid and sulfate cured for FMWCNTs-CNCMs	220
Table 4.24 Percentage Change in Compressive Strength after acid and sulfate cured for HCNMs-CNCMs	222
Table 4.25 Average Compressive Strength Values of CNMs/HCNMs based CNCMs	223

LIST OF FIGURES

Figure No.	Particulars	Page No.
Figure 1.1	Global Cement Production in the Net Scenario, 2010-2030 Cement, IEA, (International Energy Agency, 2021)	1
Figure 1.2	Worldwide Cement Production 2021 (Cembureau, European Cement Association, 2021)	2
Figure 1.3	Classification of Constituents of Nanocomposites	8
Figure 1.4	Description of Cementitious Nanocomposites Consisting of Carbon Nanomaterials	12
Figure 1.5	Schematic diagram of hydration reaction at initial to 48hrs interval(source (Zhu et al., 2020))	20
Figure 1.6	Some examples of natural pozzolana and artificial pozzolana	22
Figure 1.7	CaO-Al ₂ O ₃ -SiO ₂ Ternary Illustration of Cement and Supplementary Cementitious Materials (Lothenbach et al., 2011)	28
Figure 1.8	The Particle Size versus Specific Surface Area for Different Raw Materials of the Cementitious Matrix (Sanchez & Sobolev, 2010)	30
Figure 1.9	Wrapping of Graphene Sheet into Armchair, Zigzag and Chiral CNTs (Tilmaciu & Morris, 2015)Reproduced with permission)	34
Figure 1.10	Schematic Representation of Hybrid Carbon Nanomaterials (HCNMs)	44
Figure 1.11	Various Orientations of CNTs over Graphene Sheets (Fan et al., 2017)	45
Figure 2.1	A Systematic Overview of the Literature Review	55
Figure 3.1	Details of the Materials and Methods Employed	101
Figure 3.2	FE-SEM Image of Graphite Powder (GP)	102
Figure 3.3	(a) Graphite Powder (GP) (b) Ball-milled Graphite Powder (MGP) (c) Graphene Oxide (GO)	104
Figure 3.4	FE-SEM Image of Multi-Walled Carbon Nanotubes (MWCNTs)	105
Figure 3.5	(a) Set-up for Functionalization of MWCNTs (b) Functionalized MWCNTs (FMWCNTs)	106
Figure 3.6	FE-SEM Images of Cement	108
Figure 3.7	(a)Standard Cubic Mould (70.6 mm × 70.6 mm × 70.6 mm) (b) Vibration Table	110

Figure 3.8(a) Demolded Cubic Specimen after 24 Hours of Molding (b) Curing Tank with Standard Temperature Regulator	110
Figure 3.9 Compression Testing Machine (HC 44.95, Heico)	113
Figure 3.10 Pictorial View of Field Emission-Scanning Electron Microscope (FE- SEM)	114
Figure 3.11 Pictorial View of Powder X-Ray Diffractometer (PXRD)	115
Figure 3.12 Set-up for Electrical Resistivity Measurement of Mortar Samples (a) Top view (b) Side view	116
Figure 4.1 Schematic Representation of Results and Discussion	117
Figure 4.2 FE-SEM Images of (a) Graphite Powder (GP) (b) Milled Graphite Powder (MGP) (c) Graphene Oxide (GO), EDX Patterns of (d) MGP and (e)GO	119
Figure 4.3 HR-TEM Images of (a) MGP (b) GO	120
Figure 4.4 Raman Spectra of MGP and GO	121
Figure 4.5 XRD Patterns of MGP, and GO	122
Figure 4.6 FTIR Analysis of MGP, and GO	123
Figure 4.7 FE-SEM Images of (a) MWCNTs (b) FMWCNTs	124
Figure 4.8 EDX Patterns of (a) MWCNTs (b) FMWCNTs	124
Figure 4.9 HR-TEM Images of (a) MWCNTs (b) FMWCNTs	125
Figure 4.10 PXRD Patterns of MWCNTs, and FMWCNTs	126
Figure 4.11 Raman Spectra of <i>MWCNTs</i> and <i>FMWCNTs</i>	127
Figure 4.12 FTIR Analysis of MWCNTs, and FMWCNTs	128
Figure 4.13 (a) FT-IR Spectra and (b) General Chemical Structure of SP	129
Figure 4.14 Particle Size Distribution of SP	130
Figure 4.15 Plot of Sonication Amplitude versus Absorbance (at 200 nm) for (a) GO and (b) FMWCNTs	132
Figure 4.16 (a) Absorbance Values of HCNMs at Different Ratios and Sonication Amplitudes (b) Dispersion Stability of HCNMs (4:1) at Different Time Periods Post Ultrasonication	134
Figure 4.17 (a) Absorbance Values of HCNMs at Different Ratios (b) Dispersion Stability of HCNMs (4:1) at Different Time Periods Post Ultrasonication in SP	135
Figure 4.18 Absorbance Values of GO, FMWCNTs, and HCNMs (with and without SP) at Different Sonication Amplitudes	136

Figure 4.19 Compressive Strength for Control and GO-CNCMs at Different Dosages and Curing Ages	138
Figure 4.20 Compressive Strength for Control and FMWCNTs-CNCMs at Different Dosages and Curing Ages	141
Figure 4.21 Compressive Strength for Control and HCNMs-CNCMs at Different Dosages and Curing Ages	143
Figure 4.22 Compressive Strength Values (in MPa) for GO, FMWCNTs and HCNMs based CNCMs at 90 Days of Curing	145
Figure 4.23 Tensile Strength for Control and GO-CNCMs at Different Dosages and Curing Ages	147
Figure 4.24 Tensile Strength for Control and FMWCNTs-CNCMs at Different Dosages and Curing Ages	148
Figure 4.25 Tensile Strength for Control and HCNMs-CNCMs at Different Dosages and Curing Ages	151
Figure 4.26 Tensile Strength Values (in MPa) for GO, FMWCNTs and HCNMs based CNCMs at 90 Days of Curing	152
Figure 4.27 FE-SEM Images of Control specimen after (a) 7 days (b) 28 days (c) 56 days and (d) 90 days of Curing	157
Figure 4.28 FE-SEM Images of GO-CNCMs after 7 Days of Curing (a) 0.0015% GO-CNCMs (b) 0.003% GO-CNCMs (c) 0.006% GO-CNCMs (d) 0.012% GO-CNCMs	158
Figure 4.29 FE-SEM Images of GO-CNCMs after 28 Days of Curing (a) 0.0015% GO-CNCMs (b) 0.003% GO-CNCMs (c) 0.006% GO-CNCMs (d) 0.012% GO-CNCMs	160
Figure 4.30 FE-SEM Images of GO-CNCMs after 56 Days of Curing (a) 0.0015% GO-CNCMs (b) 0.003% GO-CNCMs (c) 0.006% GO-CNCMs (d) 0.012% GO-CNCMs	161
Figure 4.31 FE-SEM Images of GO-CNCMs after 90 Days of Curing (a) 0.0015% GO-CNCMs (b) 0.003% GO-CNCMs (c) 0.006% GO-CNCMs (d) 0.012% GO-CNCMs	162
Figure 4.32 FE-SEM Images of FMWCNTs-CNCMs after 7 Days of Curing (a) 0.0015% FMWCNTs-CNCMs (b) 0.003% FMWCNTs-CNCMs (c) 0.006% FMWCNTs-CNCMs (d) 0.012% FMWCNTs-CNCMs	163
Figure 4.33 FE-SEM Images of FMWCNTs-CNCMs after 28 Days of Curing (a) 0.0015% FMWCNTs-CNCMs (b) 0.003% FMWCNTs-CNCMs (c) 0.006% FMWCNTs-CNCMs (d) 0.012% FMWCNTs-CNCMs	164

Figure 4.34 FE-SEM Images of FMWCNTs-CNCMs after 56 Days of Curing (a) 0.0015% FMWCNTs-CNCMs (b) 0.003% FMWCNTs-CNCMs (c) 0.006% FMWCNTs-CNCMs (d) 0.012% FMWCNTs-CNCMs	165
Figure 4.35 FE-SEM Images of FMWCNTs-CNCMs after 90 Days of Curing (a) 0.0015% FMWCNTs-CNCMs (b) 0.003% FMWCNTs-CNCMs (c) 0.006% FMWCNTs-CNCMs (d) 0.012% FMWCNTs-CNCMs	166
Figure 4.36 FE-SEM Images of HCNMs-CNCMs after 7 Days of Curing (a) 0.0015% HCNMs-CNCMs (b) 0.003% HCNMs-CNCMs (c) 0.006% HCNMs-CNCMs (d) 0.012% HCNMs-CNCMs	167
Figure 4.37 FE-SEM Images of HCNMs-CNCMs after 28 Days of Curing (a) 0.0015% HCNMs-CNCMs (b) 0.003% HCNMs-CNCMs (c) 0.006% HCNMs-CNCMs (d) 0.012% HCNMs-CNCMs	168
Figure 4.38 FE-SEM Images of HCNMs-CNCMs after 56 Days of Curing (a) 0.0015% HCNMs-CNCMs (b) 0.003% HCNMs-CNCMs (c) 0.006% HCNMs-CNCMs (d) 0.012% HCNMs-CNCMs	169
Figure 4.39 FE-SEM Images of HCNMs-CNCMs after 90 Days of Curing (a) 0.0015% HCNMs-CNCMs (b) 0.003% HCNMs-CNCMs (c) 0.006% HCNMs-CNCMs (d) 0.012% HCNMs-CNCMs	170
Figure 4.40 PXRD Patterns of GO-CNCMs at 90 Days of Curing	175
Figure 4.41 PXRD Patterns of FMWCNTs-CNCMs at 90 Days of Curing	177
Figure 4.42 PXRD Patterns of HCNMs-CNCMs at 90 Days of Curing	178
Figure 4.43 FT-IR Patterns of GO-CNCMs at (a) 7 Days of Curing, and (b) 90 Days of Curing	182
Figure 4.44 FT-IR Patterns of FMWCNTs-CNCMs at (a) 7 Days of Curing, and (b) 90 Days of Curing	185
Figure 4.45 FT-IR Patterns of HCNMs-CNCMs at (a) 7 Days of Curing, and (b) 90 Days of Curing	188
Figure 4.46 Electrical Resistivity for GO-CNCMs at Different Dosages and Curing Ages	191
Figure 4.47 Electrical Resistivity for FMWCNTs-CNCMs at Different Dosages and Curing Ages	193
Figure 4.48 Electrical Resistivity for HCNMs-CNCMs at Different Dosages and Curing Ages	196
Figure 4.49 Water Absorption for GO-CNCMs after (a) 28 Days of curing, (b) 90 Days of curing	200

Figure 4.50 Water Absorption for FMWCNTs-CNCMs after 28 Days of curing, (b) 90 Days of curing	203
Figure 4.51 Water Absorption for HCNMs-CNCMs after (a)28 Days of curing, (b) 90 Days of curing	207
Figure 4.52 Compressive Strength after 28 and 90 Days of (a)Acid cured GO- CNCMs, (b) Sulfate cured GO-CNCMs	217
Figure 4.53 Compressive Strength after 28 and 90 Days of (a)Acid cured FMWCNTs-CNCMs, (b) Sulfate cured FMWCNTs-CNCMs	219
Figure 4.54 Compressive Strength after 28 and 90 Days of (a)Acid cured HCNMs- CNCMs, (b) Sulfate cured HCNMs-CNCMs	221
Figure 4.55 Depicting the Stabilization of using GO and FMWCNTs by Comb- Shaped SP Molecules	225
Figure 4.56 Diagram Depicting the Stabilization of CNMs and HCNMs Using SP Molecules	226
Figure 4.57 Schematic Diagram Illustrating the Growth of Hydration Products on Active Sites of HCNMs in CNCMs	227
Figure 5.1 Overview of Concluding Remarks	229

1.1 GENERAL

Cement-based composites such as concrete and mortar are prominent and popular construction materials worldwide. It acts as a basis for a range of civil infrastructures, such as roads, highways, bridges, buildings, tunnels, railway tracks, airports, and dams. Cement binds all the entities present in the cement mortar, concrete or reinforced cement concrete (RCC), providing intactness to the whole structural framework.

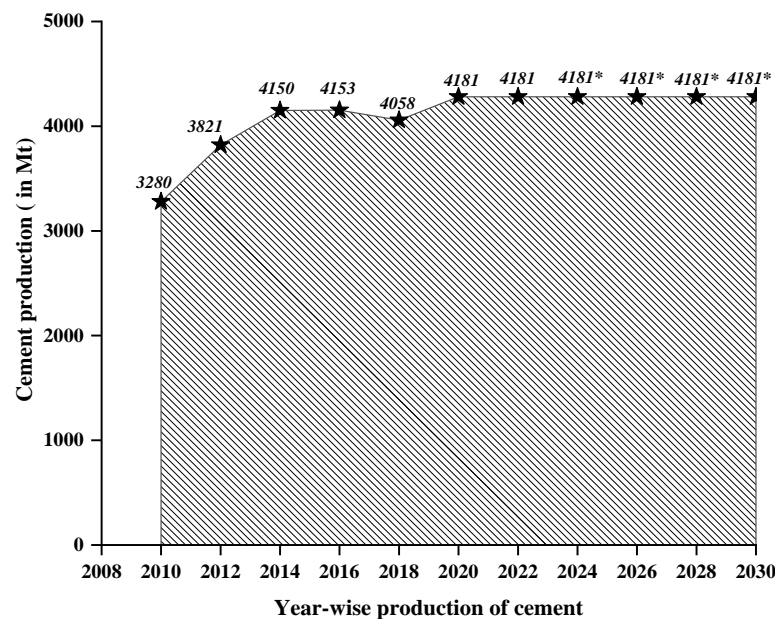


Figure 1.1 Global Cement Production in the Net Scenario, 2010-2030 Cement, IEA, (International Energy Agency, 2021)

Optimizing the usage of cement can assist reduce demand throughout the construction supply chain, hence reducing carbon dioxide (CO₂) emissions from cement manufacturing. Therefore, in the Net Zero Emissions by 2050 scenario, demand in 2030 is 6% lower than in a baseline scenario where no actions are expected to minimize demand (International Energy Agency, 2021). 4181 metric megaton (Mt) of

cement was manufacture globally in the year of 2020, as depicted in Figure 1.1(International Energy Agency, 2021). China is the largest cement producer, accounting for about 57.2% of global production, followed by India at 7.0%, as depicted in Figure 1.2(Report, 2021).

Cement production has many benefits, but its drawbacks have become a global issue. Cement production accounts for about 5-7% of all man-made CO₂ emissions worldwide, with each tonne of cement produced releasing about a tonne of CO₂ into the atmosphere(Damineli et al., 2010; Gupta et al., 2020; Shen et al., 2015)

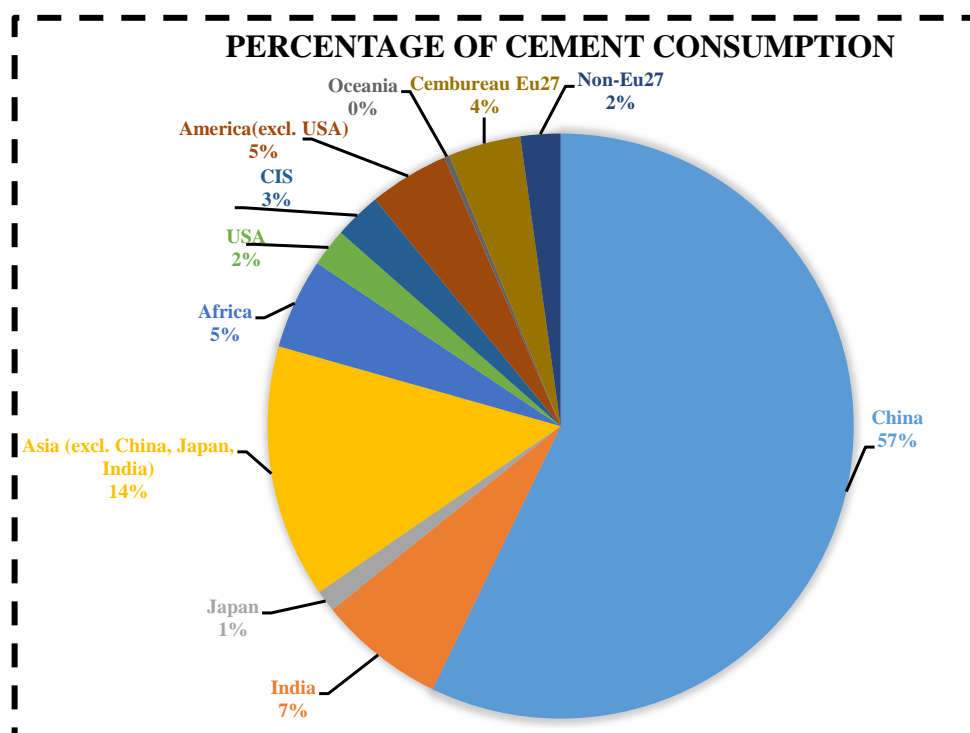


Figure 1.2 Worldwide Cement Production 2021 (Cembureau, European Cement Association, 2021)

Cement and cementitious materials have a number of drawbacks that limit their usefulness, including low physico-mechanical strength, quasi-brittleness, high permeability/porosity, crack initiation, crack propagation, etc.(Chintalapudi & Pannem, 2020; Hu et al., 2019; Shaikh & Supit, 2014; Tayeh et al., 2020; Torabian Isfahani et al., 2016a). Cementitious materials develop cracks, which propagates when exposed to fatigue, aggressive agents, and chemicals. These cracks then propagate from the nanoscale to the micro-scale level as they continue to be under stress. The resulting cracks allow corrosive substances such as salts, acids, and water to penetrate cement-based mortar or concrete, thereby accelerating its degradation(Choinska et al.,

2007; Kobayashi & Kojima, 2017). These issues can be resolved by preventing attack of aggressive agents from penetrating the mortar/bulk concretes through the surface thereby decreasing the initiation and development of cracks in the cement matrices.

1.2 LIMITATIONS OF CEMENTITIOUS MATERIALS AND POTENTIAL SOLUTIONS

Cementitious materials suffer from a wide variety of drawbacks, such as low tensile strength, quasi-brittle behaviour, and inherent flaws like crack generation, crack propagation, high porosity, increased permeability, etc. On being exposed to fatigue, aggressive agents, or chemicals for an extended period, significant deterioration to the concrete/mortars is observed. Due to this, the structural framework loses even more of its mechanical strength and durability, and thus has a much shorter useful life. Over the past few years, researchers have made significant efforts to identify the most effective strategies for reducing these negative outcomes(Akkaya et al., 2007; Lu et al., 2019). As shown in section 1.1 the China is the biggest contributor to global warming, so its CO₂ output is a major focus of climate change mitigation strategies. The production of cement requires an enormous number of resources (both energy and carbon), and this is a major environmental concern. It accounts for 7% of the anthropogenic and 26% of the industrial carbon emission worldwide, making it a major contributor to global anthropogenic CO₂ emissions(Damineli et al., 2010; Pinto et al., 2020; Shen et al., 2015). Researchers have found that using supplementary cementitious materials (SCMs) such as copper slag, fly ash, metakaolin, rice husk, and silica fume ash as cement clinker replacement during cement manufacturing, or as a partial replacement to Portland cement during fabrication of concrete or mortars, can significantly reduce the extensive emissions of CO₂(Aziminezhad et al., 2018; Hossain et al., 2021; Lu et al., 2018; Sotiriadis et al., 2020).

A few properties of cements mortars and concrete, like porosity, permeability, and durability, have been found to improve when SCMs like fly ash are added, but the physico-mechanical properties of the mortar and concrete are negatively affected (Pitroda et al., 2012), because fly ash proceeds pozzolanic reactions at a low rate, the mechanical strength it imparts to mortars at an early age of hydration is less than that of cement-based mortars. Therefore, this issue can be resolved through the production of high-performance cementitious composites that incorporate bars/fibers(Awoyera et

al., 2022). To improve the mechanical performance of concrete and mortar, scientists have experimented with a wide variety of bars and fibres with different sizes, shapes, and geometries, such as polymer fibres, steel bars, steel fibres, glass fibres, polypropylene fibres, carbon fibres, etc(Hassan et al., 2019; Li et al., 2019; Li et al., 2007; Li et al., 2022). These fibres can be introduced into the mixture to increase its ability to resist crack growth during different conditions(Yaghobian & Whittleston, 2022a). They can postpone the beginning of microcracks however they are not able to halt their initiation. The reason is that spacing between fibres is large and microcracks can freely grow in the space between fibres before facing them. Therefore, researchers have conducted studies about nano- fibres in order to limit the initiation of cracking at the nanoscale(Meng & Khayat, 2016; Peyvandi et al., 2013). Although many types of cementitious composites have been proposed and studied for use in actual construction projects around the world, problems with inherent quasi-brittle behaviour and crack generation still exist(Yaghobian & Whittleston, 2022a).

This is due to the fact that the reinforcing ability of conventional reinforcing agents is limited to either macro- or micro-dimensions, and their micro-dimensions prevent them from acting at the nanoscale. This causes nano-scale cracks to form, which in turn weaken the cement-based matrix and make it susceptible to failure under external loads(Wang et al., 2015). High porosity, low mechanical strength, less durability, and a porous microstructure all contribute to the disintegration of the cementitious matrix as it continues to age.

Table 1.1 Physical Properties of Conventional Fibers

<i>Material</i>	<i>Tensile Strength (GPa)</i>	<i>Elastic Modulus (GPa)</i>	<i>Surface Area (m²/g)</i>	<i>Aspect Ratio</i>	<i>References</i>
<i>Steel fiber</i>	1.5	200	0.02	45-80	(Bastos et al., 2016; Yao et al., 2003)
<i>Glass fiber</i>	3.45	72	0.3	600-1500	(Benmokrane et al., 1995; Trens et al., 1996)
<i>Carbon fiber</i>	0.4-5	7-400	0.134	100-1000	(Banthia et al., 1992; Li & Obla, 1994)
<i>Polymeric fiber</i>	0.3-0.9	3-5	0.225	160-1000	(Pelisser et al., 2010; Wang et al., 1990)

In Table 1.1 shows the differences between the physical properties of some recently developed conventional reinforcements used in cement concrete/mortar/RCC. In order to resolve the above challenges; nanomaterials may provide a viable solution to this issue. As a result, studies on nano fibres have been conducted to reduce nano-scale crack initiation. Nanoscale spherical particles (nano-SiO₂, TiO₂, Al₂O₃, Fe₂O₃, etc.), nanotubes and fibres (carbon nanotubes and carbon fibres), and nanoplatelets are the most widely used nanomaterials (nano clays, graphene, and graphite oxide).

Table 1.2. compares the physical characteristics of various nanomaterial reinforcements in cement concrete, cement mortar, and RCC. Graphene oxide (GO) and carbon nanotubes (CNTs) have shown great promise as reinforcing materials in cementitious matrices due to their exceptional properties.

Table 1.2 Physical Properties of Conventional Nanomaterials

Material	<i>Tensile Strength (GPa)</i>	<i>Young's Modulus (TPa)</i>	<i>References</i>
Nano-SiO₂	0.04	0.06	(Ji, 2005)
TiO₂	0.32	0.23	(Sang et al., 2014)
Al₂O₃	0.07	0.22	(Nazari & Riahi, 2011b)
Fe₂O₃	0.22	0.04	(Nazari et al., 2010)
SWCNT	13-53	1.0-5.0	(Krishnan et al., 1998)
MWCNT	16-63;150	0.20-0.95	(Yu et al., 2000)
Graphene Oxide	25	0.38-0.47	(Yang et al., 2012)
Graphene	130	1	(Huh, 2011)

1.3 COMPOSITES AND NANOCOMPOSITES

1.3.1 Composite

A composite material is a multi-phase material comprising two or more chemically or physically discrete phases on the microscopic scale, which are distinctively separated by an interface. A composite usually possesses properties different from the constituent phases. A composite normally has two significant phases/constituents; one is matrix phase another one is Reinforcing phase(Ngo, 2020).

1.3.1.1 Matrix Phase

The constituent phase of the composite, which is often continuous and found to be present in larger quantities in the composite, is called the matrix phase. In other words, it is the matrix phase whose properties are improved in the desired manner after the incorporation of some other specific constituent to obtain a composite. The different types of composites based on the type of matrix phase are Ceramic matrix composite, Polymer matrix composites, Metal matrix composite, and Carbon matrix composites (Kaur & Kothiyal, 2019a; Park & Seo, 2011).

1.3.1.2 Reinforcing Phase

The reinforcing phase generally enhances or reinforces the physico-mechanical properties of the matrix phase and is often stiffer, more durable and harder mechanically than the matrix phase. The effectiveness of reinforcement of the matrix phase highly depends upon the geometry and morphology of the reinforcing phase. The reinforcing phase can be classified into three types: Particulate reinforcements have equal dimensions in all directions and are usually cubic, spherical, or platelet shaped. Fibrous reinforcements have a length larger than cross-sectional dimensions. Here, fiber reinforcements with high aspect ratios are used. In Hybrid reinforcements, either mixed fibers or a mixture of fibers and particulates are used in the matrix. Such composites are designed in order to exploit the different useful properties from various fibers used in the composite structure (Park & Seo, 2011).

1.3.1.3 Interface in Composites

The interface is a boundary between the matrix phase and the reinforcing phase and is vital in defining the final properties of the composite (Hanif, et al., 2018). In a few cases, in order to achieve a desirable bonding between the reinforcement and matrix phase, surface treatment of reinforcing agent is needed. Moreover, the interfacial bond strength needs to be strong enough so that the load can be transferred from the matrix phase to the reinforcement *via* the interface. This condition is indispensable for effectively imparting the stiffness and strength of the reinforcements to the composite. The properties of the composite are highly reliant on the physical and chemical features of the composite interface between matrix and fibers (Matthews & Rawlings, 1999).

1.3.2 Advantages of Composites

The combination or orientation of different constituents provides material (i.e., composite) with superior properties than the constituent phases. Thus, the various features of the materials can be tuned or optimized by fabricating composites with specific constituent phases. Composites present superior physico-chemical and physico-mechanical properties as compared to the matrix phase. The significant advantages, however, are improved strength, high stiffness, and lesser density in comparison to the matrix phase. Additionally, other benefits are enhanced longevity, durability, and chemical/corrosion resistance of the composite (Campbell, 2010; Harris & others, 1999)

1.3.3 Nanocomposites

Nanocomposites are heterogeneous multicomponent materials in which at least one phase domain (called as matrix) is present as a continuous phase, and at least one of the phases (called as nanofiller) should have at least one of the three dimensions in the nanometer range. The major benefit of nanofillers in contrast to conventional micro-sized fillers is (Chen et al., 2007; Szeluga et al., 2015). The concept of nanocomposites is based on the idea of creating a large interface between the matrix phase and nano-sized filler. However, the characteristics of the nanocomposites do not depend only on the interface size but are also determined by other factors such as interactions and the structure. A nanocomposite can be fabricated from two materials with the help of weak interactions such as electrostatic interactions, van der Waals, hydrogen bonding, or covalent bonding between the nanofiller and the matrix phase (Safdari & Al-Haik, 2018). Depending upon the matrix phase and reinforcing phase, nanocomposites can be classified as shown in Figure 1.3.

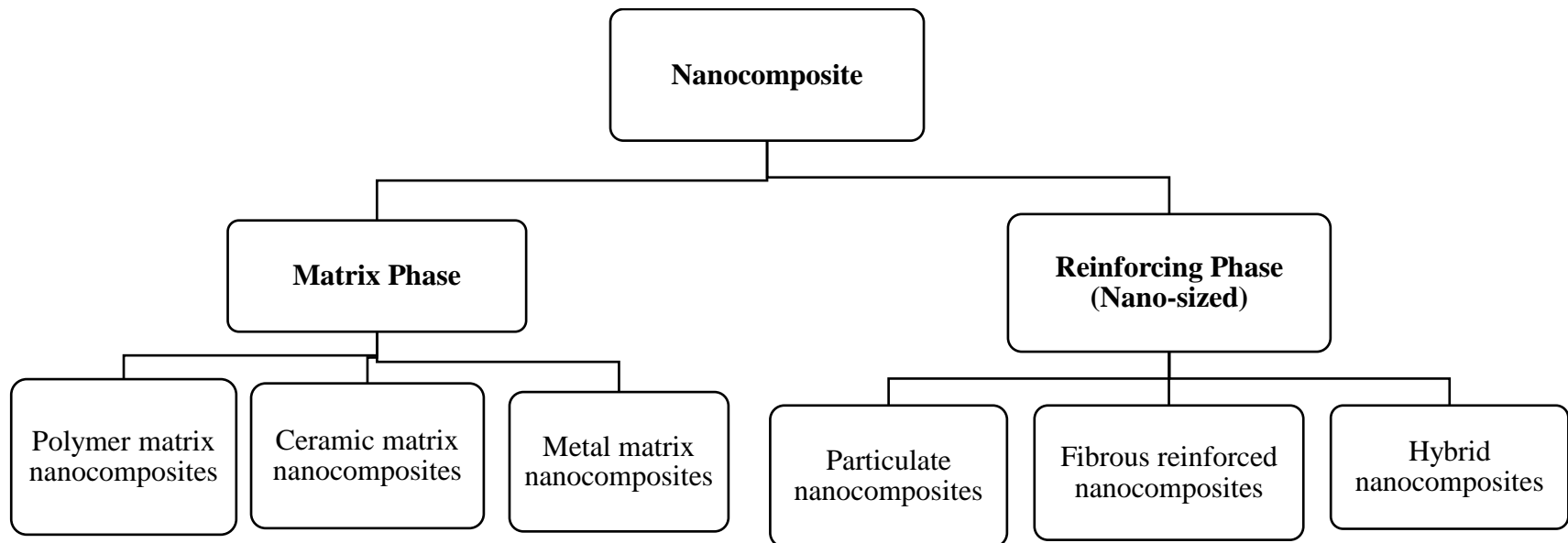


Figure 1.3 Classification of Constituents of Nanocomposites

1.3.4 Types of Nanocomposites

Nanomaterials can be subdivided into various categories based on the various constituents of the matrix phase and reinforcing phase.

1.3.4.1 Based on Matrix Phase

Nanocomposites are categorized according to the matrix phase as follows:

(a) Ceramic Matrix Nanocomposites

In ceramic matrix nanocomposites, the main constituent phase is ceramics such as borides, nitrides, oxides, silicides, etc., which are reinforced with nano-sized fibers, particulates, and platelets dispersed uniformly inside the matrix.

The uniform distribution is achieved to develop the desired properties of inorganic composite materials at the nano-scale. Reinforcing agents such as nano-sized fibers and platelets improve strength, fracture toughness and reduce brittleness by mitigating the generation of the cracks and hence their propagation. The electrical, magnetic, and optical properties are reported to be improved in the ceramic matrix (Kruis et al., 1998; Mera et al., 2015; Ricohermoso et al., 2021; Wu, 2021).

(b) Polymer Matrix Nanocomposites

Polymer matrix nanocomposites include a polymer or copolymer as a principal constituent (i.e., matrix phase), while the reinforcing agent (organic or inorganic nanofiller) is dispersed uniformly in the organic polymer matrix phase. This results in the drastic improvement of properties of the polymer nanocomposite, such as mechanical strength, thermal stability, and barrier properties, etc., as compared to the conventional composites or the pure polymers (Visakh et al., 2016). Various metal (Au, Ag, Fe, and Al etc.), metal oxides (CaCO_3 , TiO_2 , ZnO , Al_2O_3 , etc.), and carbon-based nanomaterials (carbon nanotubes, graphene, graphene oxide, etc.) have been employed to achieve the improved properties of polymer nanocomposites for the applications such as biosensors, medical devices, drug delivery, fire-retardants, packaging materials, adhesives and coatings, etc. (Cui et al., 2018; Ehtesabi, 2020; Gebrekrstos et al., 2022; Jena & Raj, 2007, 2008b, 2008a; Kumar &

Badoni, 2018; Moore & Wei, 2021; Singh Raman & Tiwari, 2014; Xiao et al., 2022).

(c) *Metal Matrix Nanocomposites*

In metal matrix nanocomposites, metal is taken as a matrix phase with reinforcing phases such as metals, organic compounds, or ceramic materials dispersed uniformly inside the matrix. Metal matrix nanocomposites are divided into two types, namely, continuous and non-continuous nanocomposites. The most important emerging metal matrix nanocomposites is carbon nanotubes reinforced metal matrix nanocomposites, where high electrical conductivity and improved tensile strength values are obtained as compared to other carbon nanotubes-based composites. Generally, metals, as well as their alloys, can be used as the matrix phase. For aircraft applications, usually, the matrix phase of magnesium, aluminium, and titanium metals is considered. If high strength enhancements are required, reinforcements of high modulus are used as reinforcing agents(Jena & Raj, 2007, 2008a; Malaki et al., 2019; Sun et al., 2022; Zare et al., 2017; Zare & Shabani, 2016).

1.3.4.2 *Based on Reinforcing Phase*

Depending on the type of reinforcing phase used, nanocomposites can be broadly categorised into three types:

(a) *Laminated Nanocomposites*

In laminated nanocomposites, nanoscale filaments are aligned within matrix phases(He et al., 2022; Seretis et al., 2019).

(b) *Particulate Nanocomposites*

The matrix phase of particulate nanocomposites contains nano-scale spherical particles.

(c) *Fibrous Reinforced Nanocomposite*

In nanocomposites with a fibrous reinforcement, the matrix is reinforced with fibres. In the matrix phase, continuous fibres exhibit high aspect ratios and a particular orientation. Discontinuous fibres, in contrast, have lower aspect ratios and are arranged randomly within the matrix(Huan et al., 2018; Tornabene et al., 2019).

1.4 CARBON NANOMATERIALS / HYBRID CARBON NANOMATERIALS BASED CEMENTITIOUS NANOCOMPOSITES

In the present study, "Carbon Nanomaterials / Hybrid Carbon Nanomaterials-based Cementitious Nanocomposites" refers to the Carbon Nanomaterials (CNMs) and Hybrid Carbon Nanomaterials (HCNMs) incorporated as nano-reinforcing agents into the matrix phases, i.e., Cementitious Nanocomposites (CNCMs). Figure 1.4 provides an overview of the constituents of cementitious nanocomposites. As shown in the diagram, Pozzolana Portland cement (PPC) was used as the matrix phase. On the other hand, the current research used carbon nanomaterials (including multiwalled carbon nanotubes or graphene oxide) and hybrid carbon nanomaterials (like such a mix of multiwalled carbon nanotubes and graphene oxide) as the reinforcing phase.

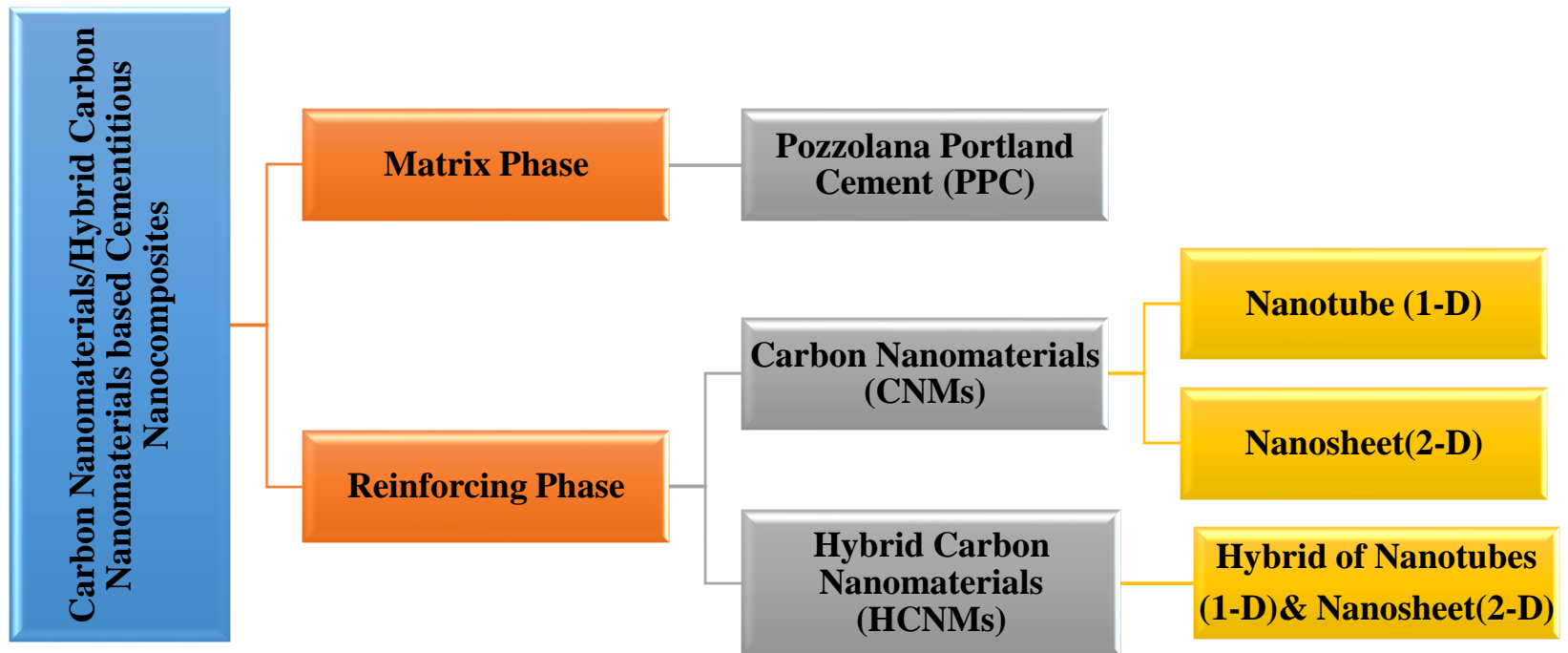


Figure 1.4 Description of Cementitious Nanocomposites Consisting of Carbon Nanomaterials

1.4.1 Pozzolana Portland Cement

Portland Pozzolana Cement (PPC) is a special type of cement produced by adding pozzolanic materials such as fly ash, calcined clay, or silica fumes to Portland cement. This type of cement offers improved physical and chemical properties when compared to Ordinary Portland cement (OPC) and is used in the production of concrete and mortar. PPC is manufactured by combining pozzolanic materials with Portland cement clinker. These pozzolans improve the properties of the cement, making it more resistant to chemical and physical attacks. Pozzolans also increase the hydration rate of cement, resulting in improved workability and strength. In addition, PPC offers better resistance to sulphate attack, alkali-silica reaction, and sea water corrosion (Abrão et al., 2020; Maurya et al., 2023; Pal, 2019).

Table 1.3 A General difference between chemical composition of PPC and OPC

Sr. No.	Chemical composition (Contents)	PPC (%)	OPC (%)
1	CaO	37.6	63.05
2	SiO ₂	34.72	20.13
3	Al ₂ O ₃	11.8	5.32
4	Fe ₂ O ₃	6.99	3.61
5	SO ₃	4.4	2.87
6	K ₂ O	1.29	0.13
7	TiO ₂	1.01	1.63
8	MgO	0.58	2.39
9	Na ₂ O	0.21	0.37
10	MnO	0.15	0.33
11	P ₂ O ₅	0.39	-
12	SiO	0.08	0.23

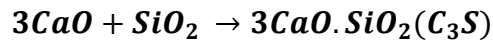
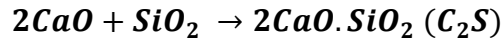
Overall, PPC is a special blend of portland cement and pozzolanic materials that offers improved physical and chemical properties compared to ordinary Portland cement (Gupta et al., 2020; Hariyadi et al., 2019; Li et al., 2007; Sathyan et al., 2018). It is used for the production of concrete and mortar and provides better resistance to chemical and physical attacks, higher hydration rate, and improved workability. The PPC is a mixed cement. It has between 15 and 35 percent pozzolanic material, 4 percent gypsum, and the remainder clinker (Bahurudeen et al., 2014). The table 1.3 shows the compared chemical composition between PPC and OPC.

1.4.1.1 Composition of Cement

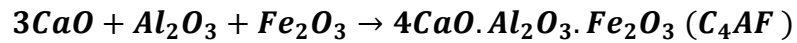
At high temperatures, the raw materials react with each other in a kiln. The molecular composition is restructured in the kiln by calcination. As a result, a series of complex chemical compounds are formed. The raw materials of the cement are mainly calcareous or argillaceous. The calcareous materials such as calcium oxide (e.g., chalk and limestone, etc.) and argillaceous materials such as silica, aluminium oxide, and ferric oxide (e.g., clay and blast furnace slag, etc.) are taken appropriate manner in grounded form and are mixed. The cement clinker is obtained by feeding the crushed raw mixture into the rotary kiln at 1300-1450°C (Trout, 2019). The mixture is fed into the upper end of the cylindrical kiln, where it undergoes a range of reactions with increasing temperature as it descends downwards:

- a) Drying Zone:** Drying takes place within a discrete zone, the size of which depends on the moisture content of the grain and the temperature, humidity and velocity of the air. This is the uppermost part of the kiln with a temperature in the range of about 100-400°C.
- b) Preheating Zone:** The upper middle part of the kiln has temperatures between 400 and 750°C. Clay and magnesium carbonate (MgCO_3) breakdown occurs in this region.
- c) Calcining Zone:** In this lower central part of the kiln decomposed CaCO_3 into CaO and CO_2 with a temperature range of 750-1000°C are known as calcining zone.

d) Burning Zone: Burning zone is the hotter zone of the kiln containing 1000-1450°C temperature. The dicalcium silicate (C₂S) and tricalcium silicate (C₃S) phases of clinker are formed by partial fusion of clay (SiO₂) and lime (CaO).



e) Cooling Zone: During the cooling process, the temperature range of 1450-1300°C facilitates the formation of tricalcium aluminate (C₃A) and tetracalcium aluminoferrite (C₄AF) through the crystallisation of the melt.



Subsequent to its formation, the cement clinker, characterized by its rigid and dark granulates, undergoes a cooling process and is subsequently comminuted to a fine powder, with the inclusion of approximately 4-5% gypsum. Table 1.4 displays the four primary cement compounds.

Table 1.4 Bogue's Compounds

Compound	Composition	Mineral Name	Abbreviation
Tricalcium silicate	3CaO.SiO ₂	Alite	C ₃ S
Dicalcium silicate	2CaO.SiO ₂	Belite	C ₂ S
Tricalcium aluminate	3CaO.Al ₂ O ₃	Aluminate	C ₃ A
Tetracalcium aluminoferrite	4CaO.Al ₂ O ₃ .Fe ₂ O ₃	Celite	C ₄ AF

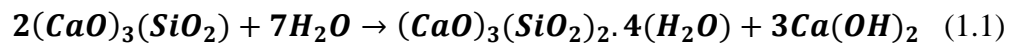
1.4.1.2 Hydration Reactions of Cement

Hydration reactions of cement refer to the chemical reactions that occur between water and the various compounds present in cement, leading to the formation of hardened cement paste. The hydration process of cement is exothermic and releases a significant amount of heat, which is why curing is necessary to prevent cracking due to thermal stress (Cheng-yi & Feldman, 1985; Huang et al., 2019; Liao et al., 2019). The main chemical compounds present in cement that undergo

hydration are tricalcium silicate (C_3S), dicalcium silicate (C_2S), tricalcium aluminate (C_3A), and tetracalcium aluminoferrite (C_4AF) (Bache et al., 1966; Bishop et al., 2003; Cheng-yi & Feldman, 1985; Feng et al., 2020). Each of these compounds contributes to the strength and setting characteristics of cement. The hydration process of cement can be divided into four stages: dissolution, nucleation, crystal growth, and interlocking. In the dissolution stage, water penetrates the surface of the cement particles and dissolves the compounds. In the nucleation stage, the dissolved compounds begin to form crystals. In the crystal growth stage, the crystals continue to grow and interlock with each other. Finally, in the interlocking stage, the crystals interlock with each other to form a hardened mass. During the hydration process, the compounds in cement react with water to form calcium silicate hydrate (C-S-H), calcium hydroxide ($Ca(OH)_2$), and other compounds such as ettringite and monosulfate. The C-S-H is the primary product of hydration and is responsible for the strength and durability of hardened cement paste (Cheng-yi & Feldman, 1985; Choi, 2022; Cui et al., 2022; Dong et al., 2022; Yoda et al., 2017). Overall, the hydration reactions of cement are complex and play a crucial role in the setting and hardening of concrete. The proper control and understanding of these reactions are essential for the successful use of mortar in construction.

- a) Tricalcium Silicate (C_3S)**, also known as alite, is the main phase (50-70%) present in the cement. Tricalcium silicate, commonly abbreviated as C_3S , is a compound that belongs to the family of calcium silicates. It is one of the main components of Portland cement, which is the most widely used cement in the world. The chemical formula of tricalcium silicate is Ca_3SiO_5 , which indicates that it contains three atoms of calcium, one atom of silicon, and five atoms of oxygen. Tricalcium silicate is a fine powder that is grayish white in color and is insoluble in water. When water is added to Portland cement, tricalcium silicate reacts with water to form calcium silicate hydrate (C-S-H) and calcium hydroxide as shown in equation 1.1. This reaction is exothermic and contributes to the hardening and strength development of concrete (Jawed, 1983; S. Meng et al., 2021). Tricalcium silicate is known for its fast reaction rate and is responsible for the early strength development in concrete. It also contributes to the long-term strength development and durability of

concrete(Bazli et al., 2020; Cheng-yi & Feldman, 1985; Delgado et al., 1996; Feng et al., 2020).



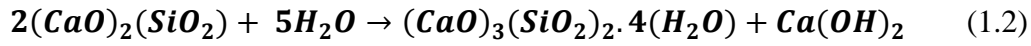
C₃S

C-S-H

C-H

b) Dicalcium Silicate (C₂S), which is also referred to as belite, yields analogous hydration byproducts, namely calcium silicate hydrates (C-S-H) and calcium hydroxide (C-H), also recognised as portlandite, as illustrated in equation 1.2. Dicalcium silicate is responsible for the progressive enhancement of strength and the appearance of strength in later stages(Hewlett, 2003). Dicalcium silicate is accountable for gradual setting reactions and acquires mechanical characteristics subsequent to a duration of one month. Tricalcium silicate and dicalcium silicate generate identical outcomes of hydration, nevertheless exhibiting variations in the quantity of portlandite produced, the heat of hydration, and the rate of hydration reaction.

The primary component is the calcium-silicate-hydrate gel, which serves as a cohesive agent and enhances the structural integrity of the material. The C-S-H gel is a non-crystalline material that exhibits limited crystallinity at the nanoscale. The tetrahedral silica chains encircle the sheets of calcium and oxygen in C-S-H. The atomic configuration exhibits notable resemblance to tobermorite, a crystalline phase characterized by a Ca/Si ratio that is comparably lower than that of C-S-H gel(Nonat & Lecoq, 1998; Richardson, 1999). C-S-H particles are generated within the nanometer scale during the process of hydration. The particles facilitate the heterogeneous nucleation of additional C-S-H sheets atop them or coalesce with the previously formed C-S-H sheets. This elucidates the limited extent of crystallinity within the C-S-H layers over a short distance (Gartner, 1997). In contrast, it can be observed that calcium hydroxide, also known as portlandite, possesses a crystalline structure. The substance is observed to exist in hexagonal plate morphology with a diameter of a few micrometers, exhibiting growth during hydration within aqueous-filled voids. The primary production of portlandite is attributed to alite, which contains a higher calcium content compared to belite(Gartner, 1997).

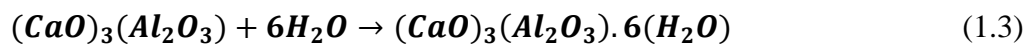


C₂S

C-S-H

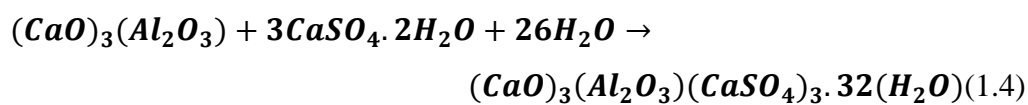
C-H

c) **Tricalcium Aluminate (C₃A)** is a chemical compound with the molecular formula Ca₃Al₂O₆. It is one of the four main components of cement, along with tricalcium silicate (C₃S), dicalcium silicate (C₂S), and tetracalcium aluminoferrite (C₄AF)(Hewlett, 2003; Trout, 2019). C₃A is known for its high reactivity and contributes to the early strength development in cement. However, it can also cause some problems, such as flash setting and rapid hardening, if present in high amounts. C₃A can react with water to form calcium aluminate hydrates, which are responsible for the initial set and early strength development of cement. It is also involved in the formation of ettringite, a calcium aluminum sulfate hydrate, which can cause expansion and cracking in concrete if formed in excessive amounts. The compound exhibits swift setting reactions when exposed to water and sulphate ions found in gypsum, resulting in the formation of the ettringite phase (AFt; aluminoferrisulphate) characterised by needle-shaped crystals during the initial stages of hydration, as illustrated in equations 1.3 and 1.4. Upon depletion of the majority of sulphate ions present in the solution, ettringite undergoes an additional reaction with the residual tricalcium aluminate, ultimately resulting in the formation of monosulphate (AFm; monosulphoaluminate)(Borštnar et al., 2021; H. Cui et al., 2017; Ylmén & Jäglid, 2013), as depicted in equation 1.5. Overall, C₃A plays an important role in the properties and performance of cement, but its content and reactivity must be carefully controlled to ensure the quality and durability of concrete structures.



C₃A

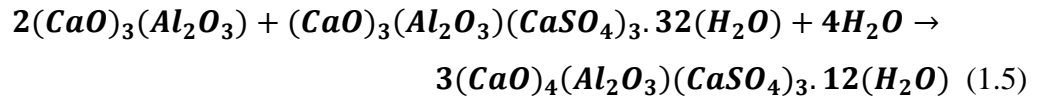
C-A-H



C₃A

Gypsum

AFt needles



C₃A

AFt needles

Calcium monosulfoaluminate (AFm)

a) Tetracalcium aluminoferrite (C₄AF) can be hydrated by reacting with water to form various hydration products, depending on the temperature, pH, and other conditions. The hydration of C₄AF is an important process in the hydration of cement, as C₄AF is one of the main components of cement clinker. When C₄AF is hydrated, it reacts with water to form calcium aluminoferrite hydrates (C-A-F-H) and calcium hydroxide (Ca (OH)₂). The C-A-F-H phase is a complex solid solution that contains a mixture of aluminum, iron, and silicon ions, and its exact composition depends on the specific conditions of the hydration reaction. The hydration of C₄AF can be influenced by various factors, such as the fineness of the cement, the curing temperature, and the pH of the water used. In general, the reaction rate of C₄AF hydration is slower than that of other cement components, such as tricalcium silicate (C₃S) and dicalcium silicate (C₂S). Overall, the hydration of C₄AF plays an important role in the development of the strength and durability of concrete, and understanding this process is essential for optimizing the performance of cement-based materials. The formation of AFt occurs subsequent to the hydration reaction, through which C₄AF reacts with gypsum in the presence of water, followed by the emergence of AFm (Beaudoin & Odler, 2019). The effect of hydration on the various mineralogical phases of cement at the initial to 48-hour time interval is schematically illustrated in Figure 1.5 (Zhu et al., 2020).

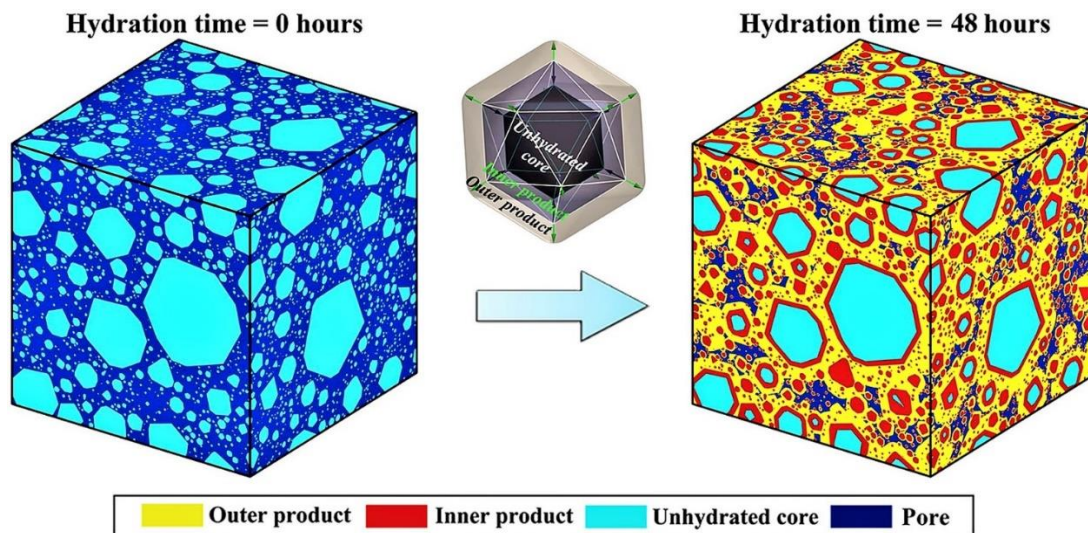


Figure 1.5 Schematic diagram of hydration reaction at initial to 48hrs interval(source (Zhu et al., 2020))

1.4.1.3 Chemical Admixtures for Cement

Chemical admixtures are materials added to concrete during mixing to modify its properties in various ways. There are several types of chemical admixtures for cement, including:

- 1 **Water-Reducing Admixtures:** The amount of water needed for the necessary concrete workability is lessened by these admixtures. High-performance concrete frequently contains water-reducing admixtures since they improve the concrete's strength and life expectancy(Barbudo et al., 2013).
- 2 **Corrosion Inhibitors:** These additives aid in preventing corrosion of the reinforcing steel in concrete, which can result in the early collapse of structures. The use of corrosion inhibitors is widespread in parking garages and marine buildings(Jain et al., 2020).
- 3 **Retarding Admixtures:** These additives postpone the time that concrete takes to set, which is beneficial in hot weather or when extended placement durations are required. Large concrete constructions like bridge decks and tall buildings frequently use retarding admixtures(Ke & Zhang, 2020).
- 4 **Air-Entraining Admixtures:** The concrete's resistance to freeze-thaw is increased by these admixtures, which create tiny, stable bubbles in the

concrete. In chilly climates, air-entraining admixtures are frequently utilised(Tunstall et al., 2021).

- 5 ***Superplasticizers:*** These admixtures are high-range water reducers that can significantly reduce the water content of concrete while maintaining workability. Superplasticizers are used in high-strength concrete, self-consolidating concrete, and precast concrete. Superplasticizers can be categorised as sulfonated naphthalene formaldehyde condensates, sulfonated melamine formaldehyde condensates, lignosulfonates, and polycarboxylates based on their composition as chemicals. The most recent generation of superplasticizers are those based on polycarboxylate ether (PCE-SP). It has a polymeric structure with side chains that are made of polyethylene oxide (PEO) and negatively charged carboxylate groups on the main carbon chain. For a certain use in concrete, the superplasticizer's qualities are determined by the density of carboxylate groups, the length, and the quantity of side chains(Lin et al., 2021; Takigawa et al., 2022).
- 6 ***Shrinkage Reducing Admixtures:*** These admixtures help to minimise cracking by reducing the drying shrinkage of concrete. Admixtures that reduce shrinkage are routinely utilised in concrete slabs and walls(Kioumars et al., 2020; Zhan & He, 2019). Chemical admixtures are an important part of current concrete technology, and their application can increase the performance and durability of concrete/mortar structures greatly.

1.4.1.4 Supplementary Cementitious Materials (SCMs)

Supplementary cementitious materials (SCMs) are the materials that are utilized to replace Portland clinkers in cement to produce PPC or can be added separately into the OPC during casting of concrete or mortar mixture(Gupta et al., 2020; Hossain et al., 2021; Liao et al., 2019; Lu et al., 2018; Skibsted & Snellings, 2019). This partial replacement can lead to sustainable green construction as it lessens the CO₂ emissions by 30-40% without significantly affecting mechanical strength and durability performance. They are normally added in small amounts to the mixture and react with the cement in the mixture to increase the performance and durability of the concrete. SCMs come in a variety of forms, but among of the most common are fly ash, slag cement, and silica

fume(Aziminezhad et al., 2018; Pitroda et al., 2012; Ren et al., 2022; Richardson, 1999; Verma & Srivastava, 2017; Wetwet et al., 2023). These elements are frequently mixed with Portland cement, which serves as the major binding agent in concrete(Zhu et al., 2020).

Pozzolans: The pozzolanic reaction is distinguished by its gradual nature, which consequently leads to a delayed heat of hydration and a gradual development of strength. The chemical reaction entails the utilization of Ca(OH)_2 rather than its generation. The enhancement of cement paste durability can be achieved through the densification and impermeability of the paste, which can be facilitated by the reduction of Ca(OH)_2 (Skibsted & Snellings, 2019; Tobón et al., 2015). Pozzolanic materials can be divided into two groups: natural pozzolana and artificial pozzolana as follows in Figure 1.6.

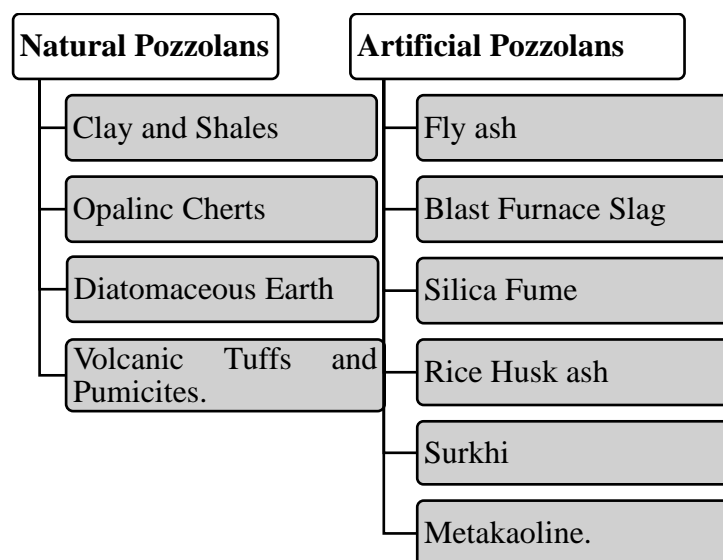


Figure 1.6 Some examples of natural pozzolana and artificial pozzolana

Natural Pozzolans

The activation of natural pozzolans, including diatomaceous earth, clay and shale, pumicites, and opaline cherts, often requires additional grinding and, in some cases, calcination to exhibit pozzolanic properties. The Hirakud dam construction in Orissa (India) utilised Talabara clay, a naturally occurring substance, as a pozzolanic material. The decreased utilisation of natural pozzolans can be attributed to the prevalence of more potent synthetic pozzolans.

Artificial pozzolans

Artificial pozzolans are substances that resemble natural pozzolans but are synthesized through a commercial method. In the manufacturing of cement, concrete, and other building materials, they serve as a substitute for natural pozzolans. Examples of artificial pozzolans include:

a) **Fly ash:** Fly ash is a fine powder produced as a byproduct of burning pulverized coal in electric power plants. It is the most commonly used artificial pozzolan in concrete production(Provis et al., 2015). The Fly ash have no self-cementitious properties(Ahmaruzzaman, 2010; Saha, 2018).

At this temperature, the mineral matter derived from coal undergoes a transition into a fluid state, potentially leading to subsequent processes such as oxidation, fusion, decomposition, agglomeration, or disintegration. The process of rapid cooling of mineral matter in the post-combustion zone results in the formation of amorphous, spherical fly ash particles, accompanied by residues such as quartz, hematite, mullite, char, and other crystallization phases, as illustrated in Figure 1.7.

b) **Blast Furnace Slag:** Ground granulated blast-furnace slag is a non-metallic material that is mainly comprised of silicates and aluminates of calcium and other bases. The rapid cooling of molten slag through the process of quenching in water induces the formation of a granulated material that exhibits a glassy texture comparable to sand. After undergoing additional grinding to achieve a particle size of less than 45 microns, it is anticipated that the granulated material will demonstrate a specific surface area within the range of 400 to 600 m²/kg, as determined by the Blaine method(Skibsted & Snellings, 2019; Sotiriadis et al., 2020).

c) **Silica Fume:** Silica fume is an additional byproduct generated during the smelting process, wherein coal is utilised to reduce highly pure quartz to silicon in electric arc furnaces. This process is commonly employed in the production of silicon and ferrosilicon alloys. Silicon vapours are generated in a furnace by heating quartz to a temperature of around 2000°C with the aid of coal(Akkaya et al., 2007; Aldahdooh et al., 2013; Wetwet et al., 2023). These vapours subsequently undergo oxidation and condensation to form microspheres, which are then gathered through the utilisation of

filters. Silica fume, commonly referred to as micro-silica, is primarily composed of amorphous silica. This material is comprised of silicon dioxide particles (SiO_2), which account for approximately 85%-90% of the constituents found within silica fume. Silica fume exhibits a surface area of approximately 20,000 cm^2/g and may undergo agglomeration due to its high surface area. According to Mitchell et al. (1998), the average diameter of silica fume microspheres falls within the range of 20-250 nm, with a mean diameter of approximately 150 nm (Mitchell et al., 1998).

Silica fume is supplied to the construction sector as a water-based slurry or a densified powder by SCM to mitigate the hazards of silicosis. The utilisation of slurry form in concrete/mortar matrix is responsible for ensuring a homogeneous dispersion of silica fume, which in turn contributes to improved quality control. In order to attain enhanced strength coupled with decreased permeability, it is recommended to employ silica fumes as a substitute for cement at a proportion of 7-9%. The incorporation of silica fumes into cement pastes results in increased mechanical strength and durability, attributed to the densification of the paste. The improvement of strength is significantly dependent on the particle size distribution of microspheres, as noted by Panjehpour et al. (2011) and Sanjuán et al. (2015) (Panjehpour et al., 2011; Sanjuán et al., 2015).

d) **Rice Husk Ash:** Rice husk ash (RHA) is a byproduct of the controlled combustion of rice husk, which is achieved without any adverse impact on the environment. When subjected to appropriate combustion, it exhibits a substantial proportion of SiO_2 and can serve as an effective additive for concrete (Della et al., 2002; Yu et al., 1999). The utilisation of rice husk ash in concrete has been found to possess significant pozzolanic properties, resulting in enhanced strength and impermeability of the material.

The composition of RHA is primarily comprised of amorphous silica (90% SiO_2), with 5% carbon and 2% K_2O . The surface area of RHA falls within the range of 40 to 100 square metres per gramme. Annually, the paddy production in India amounts to approximately 122 million tonnes. Approximately 40 kg of rice husk ash (RHA) is generated from the production of one metric tonne of paddy. The utilisation of RHA as a

pozzolanic material has significant potential to confer comparable properties to those of microsilica. Agrosilica, a trade name for highly pozzolanic rice husk ash, is patented and marketed in the United States. Agrosilica demonstrates superpozzolanic characteristics when utilised in a limited amount, specifically 10% by weight of cement, resulting in a significant improvement in the workability and impermeability of concrete. Concrete admixtures have the potential to become a significant material in the future.

According to Al-khalaf and Yousift (1984), the incorporation of RHA as a 40% replacement for cement clinker does not result in any adverse impact on the mechanical strength. Research has shown that incorporating rice husk ash into cement-based materials such as concrete or mortar can enhance the microstructure of the interfacial transition zone (ITZ) between the cement phases and the aggregates. According to previous studies (Chindaprasirt et al., 2008; Van Tuan et al., 2011; Rodrigues et al., 2010), the utilisation of rice husk ash in cement-based materials results in a reduction of Ca(OH)_2 levels due to pozzolanic reaction, leading to increased resistance against sulphate attack.

e) **Surkhi:** Surkhi was a frequently utilised pozzolanic material in India. Prior to the widespread use of modern Portland cement in India, lime was commonly utilised in the construction of traditional structures. Despite the emergence of Portland cement in the construction industry, surkhi continued to be utilised as an admixture to address certain limitations of cement concrete. Surkhi was a significant component utilised in waterproofing treatments, often combined with lime and occasionally with cement, to enhance the valuable pozzolanic action and render the treatment impervious. Surkhi is a type of artificial pozzolana that is produced by pulverising bricks or burnt clay balls. In certain significant works, the production of surkhi on a large scale involves the specialised burning of clay balls for this specific purpose, which are subsequently pulverised. Due to its inherent characteristics, this material exhibits a high degree of complexity and significant variations in its properties and capabilities. The properties of the substance in question are significantly impacted by the mineral composition of the soil from which it originates, as well as the

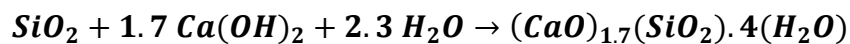
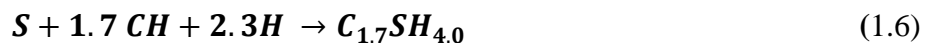
extent of its combustion and the level of refinement achieved through grinding (Cecchin et al., 2017; Du et al., 2014). The complexity of the problem has led to significant confusion due to the divergent findings reported by different researchers. Historically, the nomenclature "surkhi" has been applied to a substance that exhibits significant variability in terms of its constituent composition, combustion temperature, and degree of grinding fineness. The contemporary nomenclature for surkhi, a construction material, is calcined clay pozzolana. This updated terminology denotes the distinct characteristics and composition of the material. The specification for calcined clay pozzolana intended for use in mortar or concrete is addressed in IS 1344 of 1981. The standard IS 1727 of 1967 pertains to the techniques employed in the examination of pozzolanic substances.

f) **Metakaolin:** Metakaolin belongs to the category of pozzolans, characterised by their siliceous or siliceous and aluminous composition. These materials have the ability to undergo a reaction with calcium hydroxide in the presence of water at ambient temperature, resulting in the formation of compounds that exhibit cementitious properties. Metakaolin is generated through a calcination process of kaolin clay, wherein the clay is subjected to high temperatures ranging from 500 to 800 degrees Celsius. This process facilitates the elimination of water and crystalline structures from the clay. Metakaolin exhibits a significant degree of pozzolanic reactivity, which enables it to undergo a chemical reaction with calcium hydroxide, leading to the formation of compounds characterised by superior strength and durability. The incorporation of this substance into cement and concrete mixtures has been found to be advantageous due to its ability to enhance compressive strength, reduce permeability, and improve other properties of the resultant material. Metakaolin has the potential to serve as a filler in various materials, including coatings and plastics (Ahmad et al., 2022; Ma et al., 2022)..

Metakaolin has been reported to exhibit significant pozzolanic activity, leading to enhanced strength at early stages of development (Snelson et al., 2011; Wild et al., 1996). According to Dinakar et al. (2013), it has been

determined that the most effective amount of metakaolin as a replacement for cement is approximately 10%. Beyond this point, the strength of the material decreases due to the agglomeration of metakaolin particles.

Typically, SCMs do not react with water by themselves. They instead react with the calcium hydroxide in the cement mixture to form additional cementitious compounds that contribute to the concrete's strength and durability. SCMs stay inert after being introduced to the concrete mixture until they come into contact with the calcium hydroxide (primary hydration product from cement) that is produced when the cement is hydrated. At this time, the SCMs combine with the calcium hydroxide to generate new cementitious substances like calcium silicate hydrate (C-S-H) gel, which improves the concrete's mechanical strengths. This combination was carried out by reaction in between then, termed as 'pozzolanic reaction,' and such materials are termed as 'pozzolans.' The reaction of pozzolanic SCMs materials results shown in equation 1.6.



Silica Calcium hydroxide Calcium silicate hydrate gel

OR



The reaction mechanism between SCMs and calcium hydroxide is contingent upon the particular SCM employed. The reaction between fly ash and calcium hydroxide results in the formation of additional C-S-H gel and calcium aluminate hydrate (C-A-H) gel, whereas the reaction between slag cement and calcium hydroxide primarily yields C-S-H gel. Furthermore, the utilization of SCMs as a substitute for cement clinker can result in a noteworthy reduction of anthropogenic carbon dioxide (CO₂) emissions by 30-40%, while maintaining the mechanical strength and durability of the concrete or mortar (Skibsted & Snellings, 2019).

Figure 1.7 shows the ternary diagram, which depicts the contents of CaO, Al₂O₃, and SiO₂ for portland or other supplementary materials. The figure revealed that the fly ashes contain higher amount of silica (SiO₂), and lower amount of calcium (CaO) than portland. SCMs possessing higher calcium content, present cementitious properties of their own. In the sections below, there is information about some SCMs that are often used.

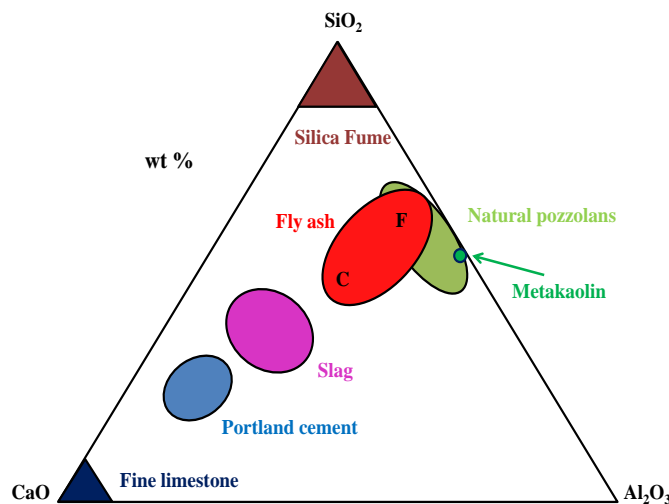


Figure 1.7 CaO-Al₂O₃-SiO₂ Ternary Illustration of Cement and Supplementary Cementitious Materials (Lothenbach et al., 2011)

1.4.2 Nano-Modification of Pozzolana Portland -Fly Ash based Cementitious Matrixes

The modification of cement-based materials at the nano-scale level can be categorized into two main areas: nanoscience and nano-engineering. The field of nanoscience primarily encompasses the methods used to characterize and measure the nano and micro-scale constituents of cementitious materials, as well as the investigation of their impact on the properties and performance of cement structures at the macroscopic level.

In contrast, the practice of incorporating nano-sized building components into cement composites, whether or not SCMs are present, enables the manipulation of material behaviour and the creation of innovative characteristics through nano-engineering. The process of attaching nano-sized molecular structures onto cement, aggregates, additives, and other related materials has been explored by Sanchez and Sobolev (2010). The efficacy of the nano-engineered composite is significantly influenced by the mechanisms transpiring at the nanoscale, as

evidenced by Garboczi and Bentz (1996), Xi et al. (2000), and Scrivener and Kirkpatrick (2008). At the nano-scale, the bottom-up approach involves conceptualizing a cementitious nanocomposite as a collection of numerous molecules, aggregates, fibers, and chemical bonds that arise from diverse intermolecular forces and chemical reactions.

The field of nanotechnology in construction and building materials has garnered significant interest in recent times. The researchers demonstrated that nano-modification of cement-based materials provided a priceless opportunity to improve features such as rheology, hydration behavior, microstructure, mechanical strength, durability, and compactness, among others (Ali et al., 2021; Singh, Bhattacharyya & Ahalawat, 2012; Singh et al., 2015). The incorporation of nanomaterials in cement composites, with or without supplementary cementitious materials, results in modification effects such as the filling effect, seeding effect, and thixotropy-modifying effect. The incorporation of diverse nanomaterials, including zero-dimensional (0-D) nanoparticles, one-dimensional (1-D) nanofibers, and two-dimensional (2-D) nanosheets, has facilitated the mitigation of most of the limitations associated with cement-based materials, thereby enabling the creation of sustainable cement-based construction materials. The incorporation of nanomaterials, including nano-clays, nano-biochar, nano-alumina (nano- Al_2O_3), nano-silica (nano- SiO_2), and nano-titanium oxide (nano- TiO_2), has been extensively studied in cement-based and fly ash-cement based cementitious composites (Cecchin et al., 2017). Despite zero-dimensional nano-particles have an excellent filling effect, one-dimensional nano-fibers such as carbon nanotubes (CNTs) and two-dimensional nano-sheets such as graphene oxide (GO) bridge the pores and cracks in cementitious nanocomposites by acting as reinforcing materials. According to Shah et al. (2015) and Chuah et al. (2014), the enhancement of the mechanical strength is achieved through the transfer of load from the matrix to the reinforcing agent. Moreover, the oxygen functional groups located on the surfaces of carbon nanotubes (CNTs) or graphene oxide (GO) sheets promote the adhesion between the hydration products and the reinforcing agent (i.e., CNTs or GO) at the interface. The incorporation of oxygen functional groups in carbon-based nanomaterials facilitates the enhancement of pore structure in

cementitious nanocomposites and fly ash-based cementitious nanocomposites. The process of pore refinement enhances the microstructure of the cement matrix through the compaction of the hydration products within the matrix. The outcome of this phenomenon is the enhancement of characteristics such as electrical conductivity, resilience, and mechanical robustness.

Figure 1.8 illustrates the correlation between the particle size (measured in nm) and the specific surface area (measured in m^2/kg) of different raw materials employed in cementitious matrices.

According to the information presented in Figure 1.8, the nomenclature "High-performance concrete" was coined subsequent to the inclusion of finely ground reactive mineral additives, such as fly ash, metakaolin, silica fume, etc., into the previously established "Conventional Concrete." The incorporation of specific dosages of nanomaterials, including nano-particles, CNTs, graphene oxide, and graphene, resulted in a further improvement of the performance of the concrete. The term used to describe it was "Nano-Engineered Concrete." The concrete and mortars that were engineered at the nano-scale level demonstrated improved mechanical and physico-chemical properties.

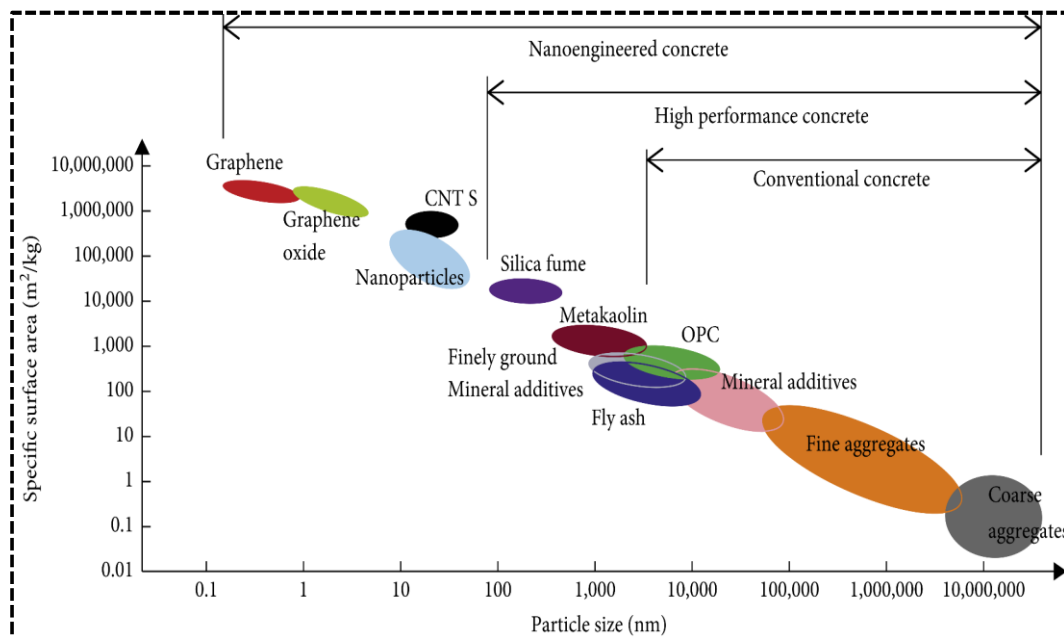


Figure 1.8 The Particle Size versus Specific Surface Area for Different Raw Materials of the Cementitious Matrix (Sanchez & Sobolev, 2010)

The nanomaterials utilized in nano-engineered concrete/mortar range in particle size from 10-70 nm, as shown in Figure 1.8, giving them reactive properties and

enabling efficient filling inside the cement matrix. Additionally, they display pozzolanic properties, which deplete calcium hydroxide (C-H), causing more C-S-H gel to develop and improving the interface structure.

Table 1.5 Advantages and Disadvantages of Nano-particles in Cementitious Composites

Sr. No	Reinforcing phase	Positive effect on cementitious (with or without fly ash) matrix	Matrix Phase	Disadvantages
1	Nano- Al_2O_3	At 28 days after curing, the addition of nano- Al_2O_3 (in 1 wt%) increased compressive strength by 16.7%. (Nazari & Riahi, 2011a)	Cement concrete	Lesser strength improvement as compared to carbon nanomaterials
2	Nano- CaCO_3	When nano- CaCO_3 (in a weight percentage of 1 wt%) was added, compressive strength increased by 108.6% after 28 days of curing, making it an inert filler and hydration product nucleation substrate(X. Liu et al., 2012).	Cement mortar	Shortened setting time; decreased flowability of cement paste
3	Nano- SiO_2	Incorporation in dosages of 3% and 5% resulted in compressive strength improvement by 13.8% and 17.5%, respectively (G. Li, 2004)	Cement mortar	Low aspect ratio as compared to carbon nanomaterials; lung toxicity due to silicosis (Napierska et al., 2010)

The filling effect of nanoparticles is stronger at greater dosages. For instance, even after C-H is depleted, the addition of nano-silica at dosages of 3% to 6% participates in pozzolanic processes and functions as a filler at the same time (Said et al., 2012). The characteristics of SCMs, mixed cement-based composites, are likewise improved by these nanoparticles when introduced in the suitable proportions.

There are some restrictions on their use, as shown in Table 1.5, despite the fact that the characteristics of cement-based materials have improved. In light of the aforementioned limitations associated with nano-particles, carbon-based nano-fibers, specifically carbon nanotubes and graphene oxide nano-sheets, present a promising alternative that addresses these shortcomings.

One-dimensional nano-fibers and two-dimensional nano-sheets serve as reinforcement agents in cementitious nanocomposites, effectively bridging pores and cracks. Furthermore, the transmission of stress from the matrix to the reinforcing agent enhances the overall mechanical strength (Chuah et al., 2014a; Shah et al., 2016).

Carbon nanotubes (CNTs) and graphene oxide (GO), which are two well-known carbon nanomaterials (CNMs), have been widely employed in cement-based composites due to their remarkable properties such as high specific surface areas, tensile strength, elastic modulus, and high aspect ratios. One-dimensional carbon nanotubes (CNTs) demonstrate exceptional tensile strength ranging from 11 to 63 GPa and an elastic modulus of 1 TPa. Furthermore, the possession of a high aspect ratio and surface area renders them highly reactive, thereby enabling them to serve as a reinforcing agent for enhancing the mechanical strength of cementitious materials. GO is a layer of hexagonally arranged carbon atoms with oxygen functional groups including hydroxyl, carboxyl, epoxide, and carbonyl. This 2-D carbon nanomaterial provides a large surface area for C-S-H nucleation during the hydration of cement. Therefore, it has the potential to be a candidate for use as a reinforcing agent due to its high surface area and hydrophilic functional groups, in addition to its tensile strength of 130 MPa and elastic modulus of 23-42 GPa (Chuah et al., 2014b; Walters et al., 1999).

The high surface area of carbon nanomaterials is advantageous for the nucleation of hydration products over it, but the strong van der Waal forces at the nano-scale lead to the agglomeration of these nanomaterials, thereby limiting their reinforcing efficacy in the cementitious matrix. In addition, additional water is required for wetting such expansive surfaces, compromising the workability of the cement. The mechanical strength of pozzolana portland based cementitious nanocomposites can be enhanced by carbon-based nanomaterials (CNMs).

Therefore, these difficulties can be mitigated by employing techniques such as ultrasonication of nanomaterials in the presence of polycarboxylate ether-based superplasticizers (PCE-SP), functionalization of the FCNTs, or by the integration of GO with FCNTs to form a 3-D hybrid framework due to the π - π stacking interactions of FCNTs over graphene sheets, thereby preventing FCNTs from aggregating (Kharisov et al., 2014; Hanif, et al., 2017a)

1.4.3 Carbon Nanomaterials/Hybrid Carbon Nanomaterials (CNMs/HCNMs) as Reinforcing Phase

The research being presented here uses graphene oxide and carbon nanotubes as the reinforcing phase of the material.

1.4.3.1 Carbon Nanotubes (CNTs)

Carbon nanotubes (CNTs) are unique one-dimensional carbon structures made by rolling up single or multiple concentric sheets of graphene into a hollow tubular structure. On the other hand, graphene is a 2D sheet composed of carbon atoms fixed in a hexagonal pattern through sp^2 hybridization. The rolling-up of a graphene sheet to form carbon nanotubes has been presented in Figure 1.9.

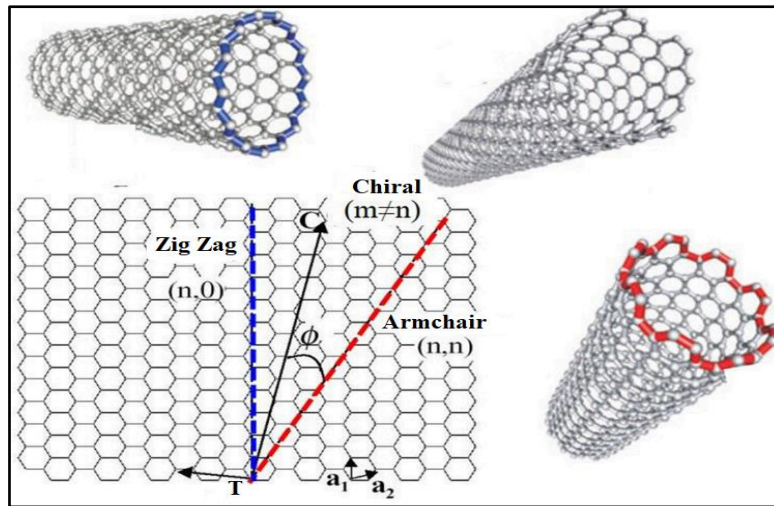


Figure 1.9 Wrapping of Graphene Sheet into Armchair, Zigzag and Chiral CNTs (Tilmaciu & Morris, 2015) Reproduced with permission)

The number of walls in carbon nanotubes classifies them. Single-walled carbon nanotubes (SWCNT) are rolled from a graphene sheet. However, concentric rolling of several graphene sheets creates multi-walled carbon nanotubes (MWCNT). CNTs typically have a diameter of 0.4 to 3 nm and a length of μm (Iijima, 1991; Thess et al., 1996).

(a) Synthesis Methods of CNTs

The synthesis of carbon nanotubes can be done by different methods such as the Arc-Discharge method, Laser Ablation method, and Chemical Vapor Deposition (CVD) method.

- ✓ **Arc-Discharge Method** in an arc produced from the high current of 100 amperes results in the formation of carbon nanotubes from the soot of the graphitic electrode. The approximate yield of CNTs produced by this method is 30% (by weight), and both SWCNTs and MWCNTs are produced with approximate length up to 50 micrometers (Eatemadi et al., 2014).
- ✓ **Chemical Vapor Deposition (CVD)** technique is considered the best technique for the large-scale production of CNTs at low temperatures. The carbon-rich precursor such as acetylene, carbon monoxide, or methane decomposes, and CNTs are formed onto the surface of a metal catalyst such as Cu, Ni, Co, or Fe, etc. The substrate is heated in the carbon-rich gaseous environment within a temperature range of 500-1000 °C. Along

with precursor, processing gas such as nitrogen, hydrogen, or ammonia is also fed into the reactor. The size and diameter of the CNTs can be controlled by the size of the metal catalyst used. CVD is mainly a two-step process. The first part involves the catalyst preparation, and the second consists of the synthesis of CNTs (Banerjee et al., 2008; Ishigami et al., 2008)

- ✓ **The Laser Ablation Method** involves a pulse laser that vaporizes the graphitic target in inert gas-filled reactor kept at high temperature. This method is quite an expensive method and produces mainly SWCNTs with a high-yield of 70% (Collins & Avouris, 2000; Guo et al., 1995).

(b) Properties of CNTs

CNTs could be used as reinforcing in a variety of nanotechnology uses because of their unique qualities, which are shown below:

1. **Electrical Properties:** The electrical characteristics of CNTs are strongly impacted by the structure of CNTs due to the unique electronic structure and symmetry shown by graphene sheets. CNTs in the armchair ($n = m$) form are metallic, while zig-zag and chiral nanotubes ($n-m$ multiple of 3) are semiconductors (Lu & Chen, 2005). Metallic CNTs have an electrical current density of $4 \times 10^9 \text{ A/cm}^2$ in theory, which is 1000 times more than silver or copper metals (Hong & Myung, 2007). CNTs are referred to as one-dimensional electrical conductors because the flow of conducting electrons occurs only in one direction, namely along the axis of the CNT (Charlier et al., 2007).
2. **Mechanical Properties:** CNTs are very strong and have great mechanical characteristics. The tensile strength of multi-walled CNTs was said to be 63 GPa, which was much higher than the 1.2 GPa tensile strength of high-carbon steel. The tensile strength of single-walled CNTs was said to be 100 GPa (Peng et al., 2008; Yu et al., 2000). CNTs have a high elastic stiffness of 1 TPa, even higher than that of aluminium (70 GPa). CNTs buckle when they are exposed to compression, twisting, or bending stress. This is because the tubes have a high aspect ratio and are hollow. They can withstand pressure up to

25 GPa without plastic deformation, which is lasting deformation. On the other hand, when they are pulled in a tensile direction, they change shape permanently and can withstand pressures up to 55 GPa (Popov et al., 2002).

3. **Thermal Properties:** Along the axis of the tube, CNTs are excellent heat conductors, and the conduction occurs by a process referred to as "ballistic conduction". They are, on the other hand, thermally insulating when seen laterally to the CNT axis. SWCNTs at room temperature show a thermal conductivity of $3500 \text{ Wm}^{-1}\text{K}^{-1}$, whereas MWCNTs show a value of $3000 \text{ Wm}^{-1}\text{K}^{-1}$ (Pop et al., 2006). Comparatively, an excellent thermal conductor such as metallic copper depicts thermal conductivity of $385 \text{ Wm}^{-1}\text{K}^{-1}$. At room temperature, SWCNTs along the radial axis exhibit a thermal conductivity of $1.52 \text{ Wm}^{-1}\text{K}^{-1}$ (Sinha et al., 2005). Thermal conductivity in the carbon nanotubes is shown to be due to the phonons rather than the electrons. Thermal conductivity for an individual CNT due to phonons has been calculated by various researchers. The peak value obtained was found to be $37,000 \text{ Wm}^{-1}\text{K}^{-1}$ which was comparable to the value of $41,000 \text{ Wm}^{-1}\text{K}^{-1}$ shown by pure diamond isotopically at a temperature of 104 K. However, at room temperature, the value for CNT was $6600 \text{ Wm}^{-1}\text{K}^{-1}$, even higher than the thermal conductivity of pure diamond (Berber et al., 2000; Hone et al., 2000).
4. **Hydrophobicity:** Although the graphite used to make CNTs has a contact angle of 90 degrees, the CNTs themselves have a contact angle of more than 160 degrees, which makes them very hydrophobic. However, by applying a voltage of around 1.3V, hydrophobic CNTs may be converted to hydrophilic CNTs (Wang et al., 2007).

1.4.3.2 Graphene Oxide (GO)

Graphene is a two-dimensional sheet of carbon made up of hexagonally organised sp^2 hybridised carbon atoms (Lambert et al., 2009). Oxygen functional groups, such as hydroxyl and epoxide groups on the basal planes and carboxyl groups on the edges, make GO, a two-dimensional nanomaterial, highly dispersible in water. Functional groups in GO make it an amorphous material,

but its hydrophilic properties and high dispersibility and stability in water (Gholampour et al., 2017; Qureshi et al., 2019) are particularly noteworthy. Graphene oxide, formerly known as "graphitic oxide" or "graphitic acid," is produced by high-temperature oxidation of graphite, a material that is both abundant in nature and very inexpensive to produce. Benjamin C. Brodie originally synthesized GO in 1860 by treating a graphite precursor with fuming nitric acid and potassium chlorate (Brodie, 1860). Exfoliation into single or few-layered GO in water and other polar solvents by physical techniques including ultrasonication, etc. was aided by the formation of an important number of groups onto the graphitic sheets, including hydroxyl, epoxide, and carboxylic acid.

(A) Synthesis of GO

There are mainly four methods for the synthesis of graphene oxide, which are discussed below:

- ✓ **Brodie and Staudenmaier Method:** By exposing graphite to an oxidising combination of fuming nitric acid and potassium chlorate, British scientist B.C. Brodie (1860) was the first to successfully synthesise graphitic oxide (Brodie, 1860). Unfortunately, this approach was shown to be risky and tedious. L. Staudenmaier introduced the first change to Brodie's approach (Staudenmaier, 1898). The two modifications were made to the existing method. To make the first adjustment more acidic, sulfuric acid was added to the concentrated nitric acid (63%). The second change included adding potassium chloride to the reaction mixture while it was being cooled very slowly over the course of about a week. These adjustments resulted in a highly oxidised end product, but the reaction was still explosive and time-consuming.
- ✓ **Hummers and Modified Hummer's Method:** About sixty years later, two experts named Hummers and Offeman altered Staudenmaier's method. The new method involved oxidising graphite in a mixture of sulfuric acid, potassium permanganate, and sodium nitrate that did not contain water (Hummers & Offeman, 1958). The response happened over a two-hour time, and the temperature was kept below 45°C. Even though

this method produced a product with a good amount of oxidation, it was found to be incomplete. Kovtyukhova and others did a great deal in 1999 to improve this method and fix its problems(Kovtyukhova et al., 1999). Researchers have since tried to improve Hummer's method by making changes that are smart and good for the environment. One change is to swap sodium nitrate with phosphoric acid, which keeps gases like dinitrogen tetroxide and nitrogen dioxide from escaping(Chen et al., 2013; Orasugh et al., 2023)

- ✓ **Tour Method:** Professor Tour of Rice University originally published on this strategy in 2010. Through the use of this approach, the reaction mixture did not need the addition of sodium nitrate. Potassium permanganate was utilised at high concentrations while phosphoric acid was used at very low amounts. Because this technique does not use sodium nitrate, it eliminates the emission of hazardous gases including di-nitrogen tetra-oxide and nitrogen dioxide, resulting in a more ecologically friendly approach.

(B) Properties of GO

The properties and structure of the GO are highly determined by the extent of oxidation and the synthesis route utilized for GO preparation(Tang et al., 2012). After oxidation of graphite, the layered structure of graphene in graphite remains maintained, but the interlayer spacing among the layers increases from ~0.34 to ~0.70 nm or even larger. The basal sheets of the graphene oxide get decorated with the functional groups such as hydroxyl (-OH), carbonyl (>C=O), epoxy (-O-) and sulfonic groups (-SO₃H), etc. and the edges are functionalized with carboxyl and carbonyl groups(Mkhoyan et al., 2009; Pandey et al., 2008)

- ✓ **Mechanical Properties:** The original single-layered graphene sheet has a break-strength of 42 Nm⁻¹, a tensile strength of 130.5 GPa, and a Young's modulus of 1.0 TPa(Lee et al., 2008). However, when functionalized, the Young's modulus of GO with a thickness of 0.7 nm drops to about 207.6 23.4 GPa, which is still a very high value. Cao et al. (2015) found that when a monolayer of GO has a high carbon to oxygen ratio (4:1),

its mean break strength is 17.3 Nm^{-1} , which is equal to 24.7 GPa (Cao et al., 2015).

- ✓ **Electrical Properties:** Graphene is a two-dimensional layer of one atom thick sp^2 bonded carbon atoms and is highly electrically conductive with a conductivity value of 6500 Sm^{-1} and electron mobility of $25 \text{ m}^2\text{V}^{-1}\text{s}^{-1}$. However, the conversion into GO renders it electrically resistive with a value of $1.64 \times 10^4 \text{ } \Omega \text{ m}$. This is attributed to the disruption of sp^2 bonding orbital networks between the adjacent carbon atoms due to the functionalization of sheets, which inhibits electrical conductivity(Novoselov et al., 2012; S. Park & Ruoff, 2009).
- ✓ **Hygroscopicity:** Due to the presence of oxygen functionalities such as hydroxyl, carbonyl, carboxyl, and epoxide groups, GO sheets are hydrophilic, resulting in the absorption of water on both the sheets and the interlayer cavities. GO is hygroscopic due to this property(Buchsteiner et al., 2006; Dikin et al., 2007). The quantity of water absorbed is affected by environmental humidity and other variables. The water molecules present in the interplanar spacing of GO sheets, in conjunction with the functional groups, establish a network of hydrogen bonding, which has a profound effect on its mechanical, structural, and other properties(Jung et al., 2008; Lerf et al., 2006).

1.4.4 Challenges Arising from Carbon Nanomaterial Usage and Potential Remedies

The dispersion of carbon nanomaterials in water is a significant concern because it reflects the manner in which these nanomaterials are dispersed within the cement matrix(Pan et al., 2011). Consequently, this section provides an exhaustive analysis of the dispersion properties of CNTs and GO. In addition, it investigates various techniques for enhancing the dispersion efficiency of CNTs and GO.

Despite the fact that CNTs and GO are superb nano-additives for cementitious matrices, they are associated with a few drawbacks. A disadvantage is the limited dispersion of CNTs as a reinforcing agent in the cement matrix due to its agglomeration as a result of its high surface energy. Similarly, GO in an

alkaline cement solution re-stacks, limiting its full use as a reinforcing material(Hanif, et al., 2017a). Opting methods, as detailed in Table 1.5, may be used to deal with this problem.

Table 1.6 A Summary of Physical & Chemical Dispersion Approach (Kharisov et al., 2014)

S. No.	Technique	Observations
1.	Functionalization	Functionalization of CNTs surface through the introduction of oxygen functional groups improves dispersion efficacy in polar solvents compared to that of CNTs in their natural state.
2.	Ultrasonication	Ultrasonication is one of the most common techniques for dispersing carbon nanomaterials, with or without the use of surfactants or chemical modification.
3.	Surfactants/ Superplasticizers	Surfactant/SP molecules function by adsorption at the interface, causing CNTs or GO dispersion through their electrostatic charges; steric stabilization.
4.	Combining various carbon allotropes and their derivatives (such as CNTs and GO)	GO can be utilized to enhance CNT dispersions. GO containing hydrophilic oxygen functional groups and multiple aromatic regions can adsorb CNTs onto its surface via non-covalent - stacking interactions, resulting in stable dispersion in aqueous media.

To enhance the dispersion of nanomaterials, a number of methods can be employed. These methods involve ultrasonication of nanomaterials in water with polycarboxylate ether-based superplasticizers (PCE-SP). In addition, functionalization of carbon nanotubes or the combination of GO with CNTs to form a three-dimensional composite structure utilizing the - stacking interactions between CNTs and graphene sheets are employed. This framework effectively prevents CNT agglomeration(Fuji et al., 2007; Kharisov et al., 2014; Takai et

al., 2007; Zhang et al., 2010). The chemical modification of CNTs and GO by covalent bonding with the -COOH groups of superplasticizers also provides steric stabilization. Consequently, these nanomaterials have exceptional dispersion properties, even in the alkaline cement pore solution (Hanif, et al., 2017b; Zhao, Guo, Liu, Ge, et al., 2018a). Table 1.6 provides a comprehensive explanation of the various dispersion methods, encompassing physical approaches like ultrasonication and chemical methods such as functionalization.

Ultrasonication: Under the influence of used ultrasound energy, particles in an aqueous solution vibrate during ultrasonication. To accomplish the dispersion of nano-particles in an aqueous medium, ultrasonic baths or ultrasonic probe sonicators (also known as horn sonicators) are typically employed. This method is based on the scientific theory that ultrasonic waves, when subjected to a succession of compressions, cause the induction of waves that are attenuated in the molecules or particles of the solution or medium through which they are travelling. This is the fundamental idea behind the approach. The shock waves generated 'tear apart' particles that were present on the outer side of the nanomaterial bundle or aggregates, resulting in the separation of nanoparticles into individual form from aggregates.

Nonetheless, ultrasonic frequencies decline at the gas-liquid interface of the solution, rendering this technique occasionally less reliable (Kharisov et al., 2014; Ma et al., 2010). Ultrasonication is an efficient technique for dispersing agglomerates of carbon nanotubes, graphene oxide, etc. in water for incorporation into cementitious nanocomposites. Lab ultrasonicators that operate at 20-23 kHz typically have a power range of 100W or less. In comparison, professional probe sonicators with a power range of 100–1500 W have varying amplitudes that run from 20–100%. The instruments of these sonicators are made of titanium.

The ultra-sonicator's base unit is coupled to the probe, concentrating all of the energy on the probe tip and supplying it with a high magnitude of intensity. This configuration generates a significant amount of heat during the sonication process. In order to avoid heat, the dispersion must be performed in brief intervals and deposited in an ice bath or cool water. The surface of CNTs has

been observed to deteriorate under severe or protracted sonication, particularly when a probe sonicator is used. The increase in D band intensity illustrates the formation of defects on the graphene sheets of CNTs or GO. In extreme situations, the graphene layers of CNTs are obliterated and transformed into amorphous carbon nanofibers. This diminishes both the mechanical and electrical properties of nanocomposites (Lu et al., 1996; Mukhopadhyay et al., 2002).

Covalent Functionalization: Due to the exceptionally large surface area of CNTs with an aspect ratio greater than 1000, it is challenging to disperse the entangled pristine CNTs in water due to the high surface energy (Ji et al., 2016; Purty et al., 2019). It has been demonstrated that treating CNTs with varying proportions of various inorganic acids or their compounds is an effective strategy for increasing their dispersion in water. CNTs surface modified with polar groups such as $-OH$ or $-COOH$ can improve the interfacial contact amid the reinforcing agent (i.e., CNTs) and the matrix (i.e., cement). The inorganic acids used individually as well as in a mixture to treat CNTs are mainly of five forms, i.e., H_2SO_4 , HNO_3 , H_2O_2 , $H_2SO_4 + HNO_3$, $HCl + HNO_3$, etc. Each acid or acid mixture has shown a significant effect on the structure, dispersion efficiency, surface chemistry, and homogeneity of the CNTs dispersion in water (Moraes et al., 2011). Nitric acid is the kind of inorganic acid that is used the most often. The functionalization of carbon nanotubes results in the formation of hydroxyl ($-OH$) and carboxyl ($-COOH$) groups onto the surface of the CNT. This improves the capacity of carbon nanotubes to be dispersed in water, and the dispersion remained stable up to $60^\circ C$ temperatures. The repulsion that exists between negatively charged functions was sufficient to overcome the van der Waals attractions that existed between the CNTs (J. Singh et al., 2011). The MWCNTs have also been purified and functionalized using a sulfuric acid and nitric acid combination. CNT length was shown to decrease with increasing functionalization time (Farbod et al., 2011).

Superplasticizer Stabilization: The most recent advancement in superplasticizer technology is polycarboxylate ether-based superplasticizers (PCE-SP). It has a polymer structure, with carboxylate groups on the main carbon chain and polyethylene oxide on the side chains, both of which are

negatively charged. The proportion of carboxylate groups, the length, and the amount of side chains define the qualities of the superplasticizer for a specific use in concrete (Kong et al., 2016; Yamada et al., 2000). In general, superplasticizers are used to improve the flowability of concrete and mortar and to minimize the ratio of water to cement in concrete. In addition to enhancing workability, PCE-SPs have emerged as a candidate for enhancing the stability of carbon nanomaterials for use in cementitious nanocomposites. FCNTs and GO are quite stable in the aqueous medium but agglomerates in cement solution. This can be attributed to the fact that the charged ions in the cement pore solution interact (Ca^{2+} , Na^+ , K^+ , OH^-) with the negatively charged GO sheets and hence, disturbing the electrostatic repulsion between the sheets. It has been reported that in the presence of Ca^{2+} containing solutions, the aggregation of GO takes place immediately. This can be acknowledged to the cross-linking caused by the Ca^{2+} ions with $-\text{COO}^-$ oxygen functional groups present at the edges (Li et al., 2016; Zhao et al., 2020). Due to electrostatic interactions, GO is initially stable in alkaline solutions (OH^-) for a few hours. However, as time passes, de-oxygenation of GO occurs in the alkaline cementitious environment, causing its agglomeration (Chuah et al., 2018; Ghazizadeh et al., 2017). The aggregation of GO not only reduces its reinforcing capacity, but also creates voids and defects in the cement matrix (Babak et al., 2014; Shamsaei et al., 2018). MWCNTs exhibited similar responses to an alkaline environment (Mendoza et al., 2013). Even though the mechanical properties can still be enhanced by agglomerated carbon nanomaterials, the mechanical properties can be enhanced to a greater extent if the agglomeration can be mitigated in a manner that ensures the well-dispersed and uniform distribution of FCNTs and GO in the cement matrix (Lu, and Li, et al., 2017). The functional groups and dispersibility of carbon nanomaterials stabilized with PCE-SP by chemical modification or superplasticizer usage are preserved in the alkaline environment, allowing for their successful application as reinforcements. Covalent interaction between oxygen functional groups of GO and carboxyl groups of PCE-SP, for instance, allows for the grafting of PCE-SP onto GO sheets (Mendoza et al., 2013; Zhao, Guo, Ge, et al., 2017a).

Hybrid materials: Hydrogen bonding between GO functional groups and the surface silicate calcium hydroxyl and calcium hydroxyl groups of C-S-H gel is responsible for improved hydration behaviour and pore structure refinement and, in turn, improved mechanical performance. The GO's functional groups also make them easier to disperse in water (Li et al., 2008; Qiu et al., 2010). The mechanical characteristics of GO have been reduced however, and sheet defects develop during the functionalization process of graphene into GO (Gong et al., 2015; Kudin et al., 2008). Therefore, the use of hybrid nano-reinforcements of carbon nanomaterials may provide a superior option to these issues.

For instance, a combination of CNTs and GO has excellent dispersibility in addition to the better mechanical capabilities of CNTs. Additionally, stable dispersion in aqueous conditions is accomplished by π -stacking non-covalent contacts of CNTs over GO sheets, as seen in Figure 1.10. (Min et al., 2018).

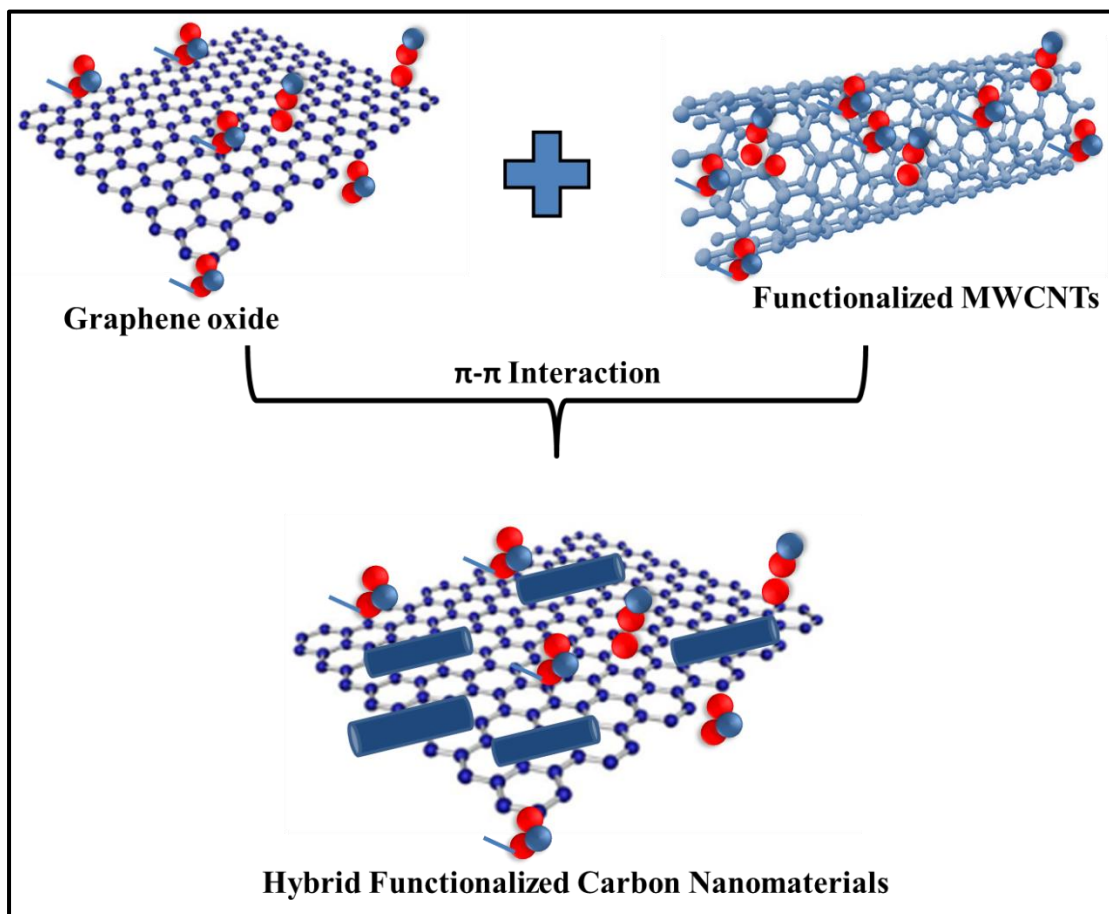


Figure 1.10 Schematic Representation of Hybrid Carbon Nanomaterials (HCNMs)

1.4.5 HYBRID CARBON NANOMATERIALS (HCNMs)

The fusion of 2D graphene oxide (GO) with 1D carbon nanotubes (CNTs) results in a flexible and adaptable 3D hybrid network that harnesses the beneficial characteristics of both CNMs. By introducing area between the stacked sheets of GO and preventing restacking and agglomeration, the potential of graphitic nanostructures can be fully realized through their interaction with CNTs, which share a similar structure (Badhulika et al., 2015). Extensive research has demonstrated that this 3D hybrid system, known as hybrid carbon nanomaterials (HCNMs), exhibits superior surface area, catalytic activity, electrical conductivity, and mechanical strength compared to individual GO or CNTs (Guo et al., 2010; Zhang et al., 2012; Zhu et al., 2011).

The graphitic nanostructures, such as CNTs and GO, exhibit an aromatic nature, allowing them to mutually stabilize each other in aqueous solutions through non-covalent interactions. The CNTs might be intercalated between the sheets of GO through π - π non-covalent interactions. This arrangement effectively prevents the re-agglomeration of CNTs and the restacking of GO sheets. A range of topological nano-architectures can result from the hybrid of nano-allotropes, as shown in Figure 1.11.

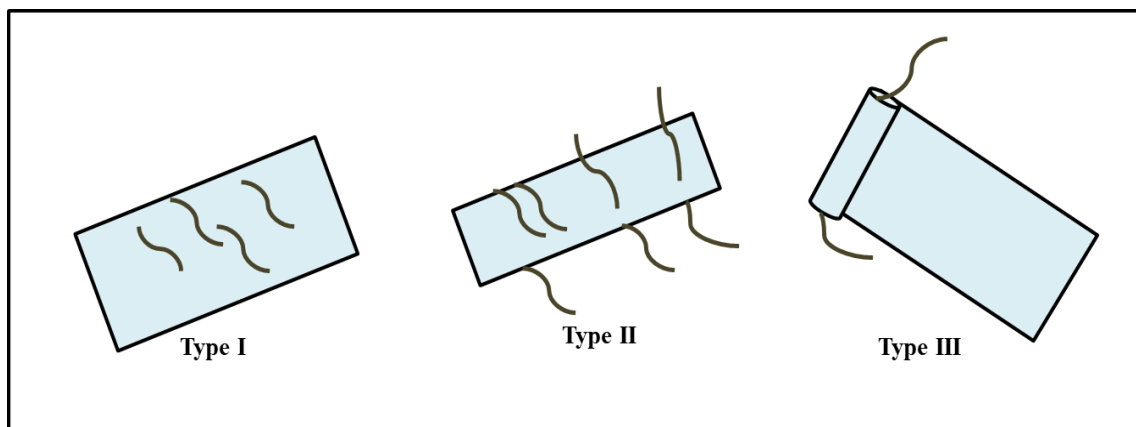


Figure 1.11 Various Orientations of CNTs over Graphene Sheets (Fan et al., 2017)

As a result, the hybridization of on the diverse topologies of the nanostructures. Firstly, there is a horizontal arrangement where carbon nanotubes are adsorbed onto the graphene sheets of GO. Secondly, the CNTs are positioned vertically over the graphene sheets of GO. Finally, there is a configuration where the CNTs are enclosed within the layers of GO, produce a wrapping effect.

Methods of Preparation: Hybrid carbon nanomaterials are composite materials that combine carbon-based materials with other components, such as metals, polymers, or inorganic compounds. These hybrid materials often exhibit unique properties and synergistic effects derived from the combination of different materials. Here are some common techniques used to fabricate hybrid carbon nanomaterials:

1. **Chemical Vapor Deposition (CVD):** CVD is a widely used technique for synthesizing carbon nanomaterials, such as CNTs and graphene. By introducing precursor gases containing carbon atoms, along with other desired components, onto a suitable substrate and under controlled conditions, hybrid carbon nanomaterials can be grown directly (Chaipanich et al., 2017; Mathur et al., 2008; Moraes et al., 2011; Pathak et al., 2016; Sharma et al., 2019; Sharma, Pathak, et al., 2018).
2. **Solution Mixing:** This method involves combining carbon nanomaterials (such as graphene oxide or carbon nanotubes) with other substances in a liquid solution. To ensure an even distribution of the solution's components, it is first mixed and then perhaps sonicated. The resultant hybrid material may then be refined in subsequent steps to get the required structure, such as filtering or drying (Alharbi et al., 2018).
3. **Electrospinning:** Electrospinning is a way of producing nanofibers from a mix of polymer. Hybrid carbon nanofibers can be made by adding carbon nanomaterials to the polymer mix. In the process, a drop of the solution is given a high voltage, which causes a tiny jet to form. As the jet moves towards a collection, it forms into nanofibers (Huan et al., 2018).
4. **Layer-by-Layer (LbL) Assembly:** LbL assembly is a versatile technique for building up multilayered structures with alternating materials. In the case of hybrid carbon nanomaterials, it involves the sequential deposition of carbon-based materials (e.g., graphene oxide) and other components, such as polymers, nanoparticles, or metals, onto a substrate. This layering process can be repeated to achieve the desired thickness and compositions (Bishop et al., 2003).
5. **In situ Growth:** This method allows for the synthesis of carbon-based materials to be supplemented with the formation of hybrid carbon

nanomaterials. Adding catalyst nanoparticles during CNT development, for instance, may speed up the production of CNTs doped with the required metal or oxide nanoparticles (Saafi et al., 2015; Wegner & Janiak, 2017).

- 6. Physical Mixing:** This method produces a heterogeneous hybrid material by mechanically combining carbon nanomaterials (such as CNTs or graphene) with other components. Some examples of physical mixing techniques are ball milling, ultrasonication, and high-shear mixing (Ke & Zhang, 2020; Kothiyal & Kaur, 2021; Praseeda & Rao, 2022; Yaghobian & Whittleston, 2022b).

These methods provide many avenues for developing carbon nanoparticles that combine desirable characteristics from both types of nanomaterials. The hybrid carbon nanomaterials' features, uses, and materials dictate the method of production.

1.5 SIGNIFICANCE OF THE RESEARCH

The present research holds following significance:

1.5.1 Enhanced Overall Performance

The shortcomings discovered in cementitious matrices over time emphasize the need for advanced reinforcements as opposed to conventional fiber-based reinforcements. Carbon nanomaterials have emerged as a focus of current research in these circumstances. These nanomaterials are intriguing candidates for augmenting the performance of cementitious matrices due to their exceptional mechanical properties, high aspect ratios, and large surface areas.

The dispersibility of carbon nanomaterials can be enhanced through steric stabilization techniques and the use of hybrid carbon nanomaterials to assure their practical applicability. This method enables the complete and efficient incorporation of carbon nanomaterials as nano-reinforcements into the cement matrix. In addition, it assists in addressing issues such as low mechanical strength, quasi-brittle behaviour, and the generation and propagation of cracks in building materials.

During hydration reactions, the mechanical strength of the cement matrix depends on the formation of needle-shaped, hexagonal-shaped, flat, elongated, and rod-shaped hydration products. Unlike traditional reinforcements, which only function at the micro- and macro-scales, nano-reinforcements affect hydration products at the nanoscale owing to nano-scale contact. Consequently, nano-reinforcements regulate the microstructural features and crystallization patterns at the nanoscale, resulting in an increase in the cement matrix's overall strength. This is due to the construction of a dense, rigid, low-porosity C-S-H polymer, which contributes to high strength.

Furthermore, the utilization of pozzolanic material-based cement enhances numerous properties of pure cement-based concrete or mortars, such as rheology, durability, and strength at later stages. Additionally, the slower rate of pozzolanic reactions in concrete and mortars helps to limit the amount of heat created during early hydration. This helps to avoid any damage to the mortar structure, such as cracking that is caused by temperature differentials.

1.5.2 Economic Sustainability

Furthermore, the increasing emphasis on construction sustainability has led to a demand for cost-effective construction materials. Incorporating pozzolanic materials-based cement in construction materials offers advantages both from economic and technical perspectives. Moreover, the utilization of waste materials in concrete brings additional benefits. It reduces bleeding and segregation, improving the workability of the concrete. However, in the present study, the limitations associated with the pozzolanic portland cement, such as poor early-age mechanical strength gain during hydration, have been overcome by employing sterically stabilized carbon nanomaterials, specifically GO, FMWCNTs, and HCNMs. Consequently, the overall utilization waste materials, and the implementation of cost-effective construction materials.

1.5.3 Environment-friendly Approach

The production of cement is responsible for approximately 5-7% of global anthropogenic CO₂ emissions (Goswami et al., 2011; Madloul et al., 2011; Onaizi et al., 2021). Considering these concerns, the current research offers a

dual benefit in terms of an environmentally friendly approach by utilizing SCMs based cement. The utilization of pozzolanic materials presents a promising avenue for cleaner production in the construction industry, as it helps reduce CO₂ emissions and waste generated during the manufacturing and mining processes of construction materials (Prasad et al., 2021).

1.6 AIM AND OBJECTIVES OF THE RESEARCH

1.6.1 Aim of the Research

The primary objective of this research is to investigate the impact of carbon nanomaterials, both individually and in hybrid forms, on cementitious nanocomposites. Consequently, this research aims to provide a sustainable approach towards developing environmentally friendly and cost-effective construction materials based on pozzolanic materials-based cement composites, which can rival the performance of PPC matrix in all aspects.

1.6.2 Objectives of the Research

Possible improvements in properties of PPC based cementitious composites will be made by use of Carbon Nanomaterials-CNMs (Individually or as hybrid). Incorporation of Carbon-based nanomaterials, which have exceptional mechanical properties, could improve various properties of PPC based cement mortar. Incorporation of these materials could also alter or modify setting and hardening behaviour of PPC based cement matrix from conventional mechanism by providing large surface area.

The prime objective of the proposed work would be to study the efficacy of hybrid carbon nanomaterials (HCNMs) as composite material to improve physico-mechanical properties of Pozzolana Portland Cement-based matrix. Supplementary cementing materials (SCMs) could also be tried with carbon-based material towards improvement of the properties.

Main objectives of the study will be as follows:

1. Synthesis of MWCNT (Multi walled carbon nanotubes) from hydrocarbon source by CVD method.
2. Functionalization of MWCNT and ball milled graphite powder.

3. Characterization of Raw Carbon Nanomaterials and Functionalized Nanomaterials using FT-IR, SEM/EDS, TEM, XRD, AFM, TGA/DTA, Raman Spectroscopy and BET Surface Area, etc.
4. Studies on dispersion behavior of individual and Hybrid Carbon Nanomaterials (HCNMs) using various polycarboxylate ether-based Superplasticizers/surfactants using ultrasonication by UV-Visible Spectrometry.
5. Effects of variation of CNMs dosages (% by weight of cement) in Pozzolana Portland cement mortar Nanocomposites and its effect on properties:
 - i. Compressive strength/ tensile strength using IS 4031-1988 and IS 5816-1999, respectively.
 - ii. Microstructural behavior by SEM
 - iii. Crystallization behavior by XRD
 - iv. Electrical resistivity using the wernner method.
 - v. Durability studies

1.7 OVERVIEW OF CHAPTERS

The work done in the current research has been classified into five chapters.

Chapter 1-Introduction: This chapter contains a comprehensive description of the basic cementitious materials and carbon nanomaterials utilized in the research. This chapter also contains the significance, purpose, and objectives of the present study.

Chapter 2-Literature Review: This chapter examines the literature concerning the effect of carbon nanomaterials/hybrid carbon nanomaterials on the various properties of cementitious nanocomposites, including mechanical properties, microstructural, crystalline, and durability properties.

Chapter 3-Experimental Methodology: This chapter describes in details the materials and methods utilized to conduct the research experiments.

Chapter 4- Results and Discussion: This chapter is classified into four sections as follows:

Section I-Characterization & Dispersion Studies of Carbon Nanomaterials:

This chapter summarizes the findings of several characterization approaches used to characterize the carbon nanomaterials and hybrid carbon nanomaterials. It also discusses dispersion studies of carbon nanomaterials and hybrid carbon nanomaterials using UV-Visible spectroscopy.

Section II-Compressive and Tensile Strength: This chapter includes the compressive and tensile strength results for the cementitious nanocomposites (CNCMs) after incorporation of CNMs/HCNMs.

Section III-Microstructural and Crystallization Behavior Studies: In this chapter, the efficiency of various reinforcing agents (i.e., FMWCNTs, GO and HCNMs) in enhancing the physico-mechanical strength of the mortars has been accessed in terms of microstructural and crystalline studies by field emission-scanning electron microscope (FE-SEM) and Powdered X-ray diffraction (PXRD), respectively.

Section IV-Durability Studies: In this chapter, the effect of carbon nanomaterials (CNMs) and hybrid carbon nanomaterials (HCNMs) on the hydration rate and microstructure of the cementitious nanocomposites (CNCMs) has been interpreted in terms of durability studies.

Chapter 5-Conclusions and Scope for Future Research: This chapter provides the important findings of the current study as well as the scope of the current work for future research.

2.1 HISTORY OF CARBON NANOMATERIALS IN CONSTRUCTION MATERIALS

Nanotechnology may have been inspired by Richard Feynman's December 29th, 1959 lecture "There is Plenty of Room at the Bottom" (Junk & Riess, 2006). The lecture was deemed science fiction at the time since he discussed the idea of changing materials "atom by atom." According to Feynman's concept, numerous inventive advancements have been made to control and transform matter at the nano-, atomic, and molecular levels. Norio Taniguchi coined the word "nanotechnology" for the very first time in 1974 (Mansoori & Soelaiman, 2005). The word was first used in the context of semiconductor manufacturing, which often involves altering materials at the molecular or atomic level. In 1981, Eric Drexler used the word "nanotechnology" once more to describe a new technique that he called "bottom-up". This was in contrast to the "top-down" approach that Feynman and Taniguchi had explored before (Mansoori & Soelaiman, 2005).

A year later, in the 1960s, people began experimenting by adding fibers of various sizes (macro or micro-sized) to cementitious materials like mortar and concrete in an effort to boost their performance. The incorporation of fibers undoubtedly aided in the reduction of huge cracks into a system of denser microstructure occupying only micro cracks; nevertheless, the fibers failed to work at the nano-scale. Several studies have demonstrated that nanotechnology uses could enhance conventional construction and building materials. Using carbon nanomaterials like carbon nanotubes (CNTs) and carbon fibers can improve the mechanical strength and durability of cement-based materials in a promising way (Silvestro & Gleize, 2020). Researchers have been looking for cheaper carbon-based nanomaterials (CNMs) due to the prohibitive expense of producing pure CNTs on a wide scale for industrial purposes. Among the various CNMs, graphene oxides (GO) act as a cost-effective reinforcing material and exhibits extraordinary properties relevant to CNTs. CNTs and GO have

presented a highly promising method for enhancing the strength, durability, and other features of cementitious nanocomposites (CNCMs).

Researchers have tried to stabilize sterically the carbon nanomaterials in the alkaline cement matrix with the help of superplasticizers (Chuah et al., 2018; Hanif, et al., 2017c; Mendoza & Filho, 2017; Wang et al., 2016; Zhao, Guo, Ge, et al., 2017a). In addition, the reinforcing effect of hybrid carbon nanomaterials (HCNMs), i.e., CNTs and GO, on the cement matrix was considered; since the hybrid of CNTs and GO combines the outstanding physico-mechanical properties of CNTs with the good dispersion capacity of GO. However, studies on the application of supplementary cementitious materials (SCMs) like fly ash to reduce the costs and provide an eco-friendly solution are also included in the literature study. The current era of cement industries in world-wide shows their attention in producing Pozzalona Portland Cement (PPC). If by-products from industries (such as fly ash from thermal power plant) and agriculture waste have the potential to replace cement for production of blended cement, the cement industries would conserve energy and lower the cost of production. This will intern results in low CO₂ emission of, sustainable, as well as low cost of production. Fly-ash present in the PPC leads to lesser binding properties but contributes strength to PPC. Pozzolanic materials react with calcium hydrates during hydration reaction in order to make impermeable and denser materials (Sharma & Kothiyal, 2015).

In the literature review part of current work have been discussed in depth, and the following sections provide a brief summary of other studies. Figure 2.1 shows a summary of the literature review.

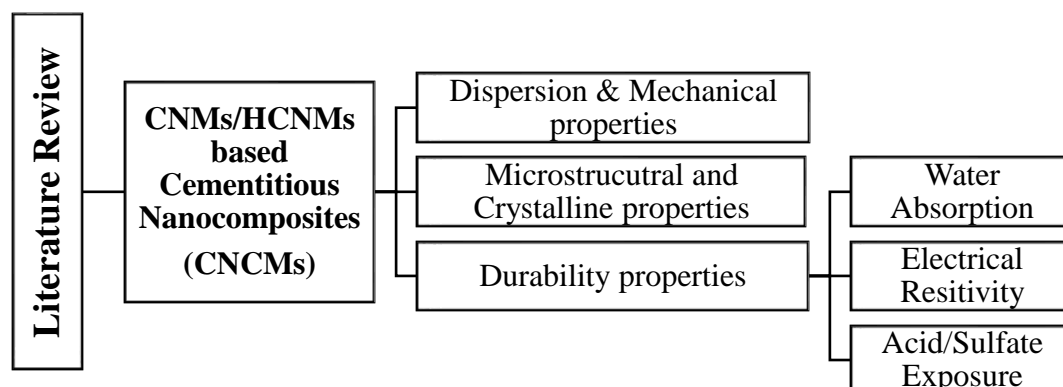


Figure 2.1 A Systematic Overview of the Literature Review

2.2 CARBON NANOMATERIALS BASED CEMENTITIOUS NANOCOMPOSITES (CNCMs)

Carbon Nanomaterials (CNMs) have a high reactivity because they influence chemical processes and behaviour inside the mortar. The addition of CNMs/HCNMs improves both the fresh and hardened characteristics of cement mortar/concrete (Paul et al., 2018; Rehman et al., 2017). In addition to this, CNMs/HCNMs fill the voids and pores in the cement matrix, leading to a compact microstructure and reduced porosity of the CNCMs (Gao et al., 2019a; G. Jing et al., 2020; S. Lv, Ting, et al., 2014; S. H. Lv et al., 2016; Parveen et al., 2015; Sobolkina et al., 2012a; Torabian Isfahani et al., 2016a; B. Wang et al., 2013; L. Zhao, Guo, et al., 2020). It was discovered to be challenging to fully exploit the capabilities of carbon nanomaterials (CNMs/HCNMs) due to the aggregation of reinforcing agents in the alkaline cement matrix. Surfactants such as gum arabic (GA), cetyltrimethylammonium bromide (CTAB), Triton X-100 (TX), sodium lauryl sulphate (SLS), sodium dodecylbenzene sulphonate (SDBS), air-entraining admixtures (Microair 905), and melamine-, naphthalene-, and polycarboxylate-based superplasticizers, etc have been used to disperse solution of CNMs/HCNMs in cementitious matrix (Chuah et al., 2018; Liu et al., 2019; Sindu & Sasmal, 2017; Sobolkina et al., 2012a; Wang et al., 2013). Other

additives, such as silica fume or silica nanoparticles etc., have also been used to improve the dispersion of CNMs/HCNMs throughout the cementitious matrix (Ali et al., 2021; Chaipanich et al., 2017; Indukuri et al., 2019; Kim, Nam, et al., 2014; Lu et al., 2018; Singh et al., 2015; Zhao, Guo, Ge, et al., 2017a). The polycarboxylate-ether based superplasticizers have been found to be the most effective of all surfactants/superplasticizers in sterically stabilizing the CNMs/HCNMs. Studies in the past have shown that CNMs and HCNMs have different effects on the mechanical and other properties of cementitious nanocomposites (CNCMs). These findings will be discussed extensively in upcoming section. Table 2.1 gives a concise overview of dispersion behaviour in presence of superplasticizers.

2.2.1 Mechanical Properties of CNCMs

Konsta-Gdoutos et al. (2010) used ultrasonication and surfactant-assisted dispersion to stabilize MWCNTs (0.025% to 0.08%) of different lengths in water. It was found that ultrasonication and the right ratio of surfactants are needed to disperse the MWCNTs in water. The surfactant-dispersed CNTs could increase the mechanical strength of cement composites by 30–40% and increase the Young's modulus by 35% compared to the control sample. To achieve a similar level of reinforcement in cement composites, high doses (around 0.08%) of short-length CNTs and low dosages (0.025% to 0.048%) of long-length CNTs were required (Konsta-Gdoutos et al., 2010).

Sobolkina et al. (2012) investigated the effects of using two distinct types of CNTs (specifically, a mixture of single-, double-, and multi-walled CNTs, as well as nitrogen-doped CNTs (N-CNTs)) on the mechanical strength of the cement composites. In order to successfully disperse CNTs, ultrasonication was utilized in presence of anionic (SDS) and non-ionic (Brij 35) surfactants were present. The optimal dispersion of CNTs was achieved with ultrasonication for 120 minutes at surfactant to CNTs ratio 1:1 to 3:2. The surfactant Brij 35 greatly enhanced the dispersion of N-CNTs by evenly covering the CNTs walls, hence enhancing dispersion. Nevertheless, CNTs were harmed with increasing sonication time. It was found that Brij 35 improved the compressive strength of cement composites with mixed CNTs and N-CNTs by 40% and 30%,

respectively. On the other hand, SDS decreased the strength of cement composites due to the fact that the porosity of cement composites got increased after addition of SDS was added(Sobolkina et al., 2012a).

Collins et al. (2012) tested the mechanical strength of cement paste mixed with CNTs at 0.5%, 1.0%, and 2.0% concentrations. The CNTs were spread out using different agents, such as polycarboxylates, lignosulfonates, naphthalene sulfonate, styrene-butadiene, and air entertainers. Use of a polycarboxylate superplasticizer enabled uniform dispersion of CNTs. With use of polycarboxylate superplasticizer, adding 0.5% CNTs, increased the compressive strength by 25%. In a similar way, Han et al. (2012a) used superplasticizers to disperse CNFs and CNTs instead of any other dispersing agent that could affect the rate of hydration of the cement composite(F. Collins et al., 2012).

Mendoza et al. (2013) investigated the influence of ultrasonication and superplasticizer (superplasticizer was utilized four times the weight of CNTs) on the dispersion of functionalized CNTs (-OH groups). Raman spectroscopy analysis revealed that extreme ultrasonication of CNTs led to fragmentation of CNTs. In addition, the addition of $\text{Ca}(\text{OH})_2$ to the dispersion of CNTs disrupted the steric repulsion between CNTs and SP molecules, resulting in CNT aggregation. $\text{Ca}(\text{OH})_2$ interaction with the negatively charged -OH groups on CNTs eliminated the electrostatic repulsion between the SP and -OH groups(Mendoza et al., 2013).

Wang et al. (2013) altered the dispersion of MWCNTs using the surfactant Gum Arabic (GA) and an ultrasonication procedure. Thereafter, the flexural toughness and fracture energy of cement paste samples modified with CNTs were evaluated. With a CNT dose of 0.08%, flexural toughness was increased by 57.5%, and fracture energy was increased to a value of 312.2 N/m, both of which were the highest values found(Wang et al., 2013).

Lv et al. (2013) used graphitic oxidation and ultrasonication to develop an aqueous GO dispersion with 29.75% oxygen content. With GO concentrations of 0.01% to 0.05% (by weight of cement), the effect of GO nanosheets on improvement of mechanical properties of cement composites were studies. At a GO concentration of 0.03%, the tensile strength, compressive strength, and

flexural strength of cement composites all increased by 78.6%, 38.9%, and 60.7%, respectively(Lv, Ma, Qiu, & Zhou, 2013).

Kim et al. (2014a) used silica fume as an additive to make CNTs disperse out more evenly and improve their effect on the mechanical and electrical properties of the cement matrix. The amounts of CNTs used were 0.15% and 0.30% by weight of cement, while the amounts of silica fume used were 10%, 20%, and 30%. (By weight of cement). When silica fume was added to composites, it tends to make them stronger until a dose of 20%. The re-agglomeration of dispersed CNTs resulted in a decrease in strength when the concentration of silica fume was increased to 30%(Kim, Nam, et al., 2014).

Lv et al. (2014) examined the impact of GO with different sheet sizes and dosages (from 0.01% to 0.06% by weight of cement) on the compressive and flexural strength of the cement paste. GO was dispersed with ultrasonication for times duration from 0 to 60 minutes. After 60 minutes of ultrasonication, GO nanosheets with a thickness of 3.4 nm and a size of 72 nm were produced. At dosage 0.04%, the maximum increase in flexural strength was found to be 52.9%, and the maximum increase in compressive strength was 38.2%(Lv, Liu, et al., 2014).

Parveen et al. (2015) reported the mechanical performance of cement mortar strengthened with SWCNTs and stabilized with Pluronic F-127 (as dispersant). In comparison to the control sample, the flexural modulus of the mortar containing 0.1% SWCNTs increased by 72%. Compressive and tensile strength was increased by 23% and 17%, respectively, after 56 days of curing. The even distribution of CNTs was seen, which held the hydration products together(Parveen et al., 2015).

Horszczaruk et al. (2015) investigated the influence of graphene oxide in a 3.0% (by weight of cement) dosage on the mechanical strength of cement composite. The Young's modulus distribution for the reference sample was found to be between 1 and 10 GPa. After GO was added, this range grew to 5 to 20 GPa(Horszczaruk et al., 2015).

Zou et al. (2015) studied the effect of ultrasonication energy on CNT dispersion. The CNT to PC mass ratio of 1:8 proved beneficial for homogeneous CNT dispersion in the cement matrix. Furthermore, considerable improvements in Young's modulus, fracture toughness, and flexural strength were discovered. This was attributed to crack-bridging as well as the nano-scale reduction in porosity by the CNTs(Zou et al., 2015).

Lu et al. (2015) evaluated the mechanical performance of cement paste with GO/CNTs and individual GO and CNTs. Employing any dispersant, the CNTs dispersion was stabilised by adding GO solution to it. UV-visible spectroscopy and optical microscopy revealed that the absorption degree of the GO/CNTs dispersion was three times that of the aqueous dispersion of CNTs. This was explained as improved electrostatic repulsions in the GO/CNT dispersion. Control, 0.05% GO, 0.05% CNTs, and 0.025% GO/ 0.025% CNTs cement paste samples were produced (by weight of cement). The maximum improvements in flexural strength, compressive strength, and Young's modulus were determined to be 24.2, 21.1, and 27.2% for GO/CNTs-based samples, respectively(Lu, Hou, Meng, Sun, Lu, et al., 2015).

Similarly, Li et al. (2015) reinforced cement mortar samples with a CNT/GO mixture distributed with polycarboxylate superplasticizer. CNT/GO-cement composite exhibited a 72.7% increase in bending strength, whereas CNTs and GO-based composites exhibited only 26.3% and 51.5% improvements, respectively(Li et al., 2015).

Lv et al. (2016) developed a co-polymeric product (PC/GON) by co-polymerizing GO nanosheets (GON) with the superplasticizer's (PC) monomeric units. After co-polymerization with PCE-(PC/GON) SPs monomer units, uniform dispersion of GO nanosheets in cement composites was achieved, resulting in flower-like and polyhedron-shaped regulated hydration products that filled cracks and voids. The enhancement in flexural and compressive strength for 0.22% PC/GON incorporation was found to be 77.6% and 56.5%, respectively(Lv et al., 2016).

Torabian Isfahani et al. (2016) investigated the mechanical properties of cement mortar using pristine and functionalized CNTs (p-CNT and f-CNT) in dosages

of 0.22% and 0.45% (by weight of cement). Ultrasonication for various time periods of 0, 30, 60, and 120 minutes were used to prepare CNT dispersions in aqueous solution. The maximum dispersion for p-CNT and f-CNT was obtained after 60 and 120 minutes of sonication, respectively. Increased CNT dosage or dispersion strategy did not significantly improve compressive, flexural, or fracture toughness. This could be due to the aggregation of CNTs within the cement matrix (Torabian Isfahani et al., 2016b). Sindu et al. (2017) investigated the effect of several surfactants and sonication settings on the dispersion of carbon nanotubes in order to get the best dispersion. The surfactant stabilised CNTs produced the best dispersion when sonicated for 1 hour at a power of 70 W. Gum Arabic (GA), cetyltrimethyl ammonium bromide (CTAB), Triton X-100 (TX), sodium lauryl sulphate with defoamer (SLS), and sodium dodecyl benzenesulphonate (SDBS) were the various surfactants employed. The dosage of CNTs added ranged from 0.02% to 0.3% by weight of cement. The most successful method for CNTs dispersion was the surfactant SLSD. Tensile strength and compressive strength were maximum for CNTs dosages of 0.08% and 0.1% with GA, by 10% and 80%, respectively. Maximum fracture energy was observed in GA-based cement mortars including CNTs at a ratio of 0.06–0.1% (Sindu & Sasmal, 2017).

Chaipanich et al. (2017) investigated the effects of as-prepared carbon nanotubes (in dosage of 0.5% and 1%) and silica fume (10% by weight) on the mechanical strength of cement-based mortars. With 0.01% CNTs in the cement mortar, the maximum compressive strength was found to be 17% and the maximum tensile strength was 10% (Chaipanich et al., 2017).

Zhao et al. (2017) used polycarboxylate superplasticizer (PC) to change the GO sheets into PC@GO. Through covalent bonds between the oxygen functional groups of GO and the carboxyl groups of PC. The PC molecules alter the shape of the GO sheets. This weakens the van der Waals interactions present between the GO sheets. When ultrasonication is used on PC@GO, the exfoliated GO sheets are distributed evenly and are kept apart by the side chains of PC. On the basis of the compressive strength, the hybrid effect of PC@GO sheets adorned with SiO₂ nanoparticles was investigated. At 28 days of curing, the hybrid-based mortar sample had a 38.9% increase in compressive strength, which was better

than the increases caused by either SiO₂ nanoparticles or PC@GO(Zhao, Guo, Ge, et al., 2017b).

Zhao et al. (2018) modified GO with water-reducing agents (anionic surfactants) including lignosulfonates, naphthalene sulfonates, and polycarboxylate-ether based superplasticizers to enhance its dispersion in the cement pore solution. It was found that the polycarboxylate-ether-based superplasticizer was more effective of enhancing the distribution of GO compared to the others. The stable dispersion of GO by superplasticizer can be explained by its ability to stop Ca²⁺ ions from linking GO sheets together and by covering the GO sheets with steric hindrance. In addition to this, the addition of superplasticizers to GO led to an improvement in the fluidity of cement paste, which was caused by the adsorption of anionic anchors on the cement particles. The mechanical strength of mortar containing superplasticizer-modified GO was greater than that of mortar containing unmodified GO. This proves that the superplasticizer can disperse the GO evenly throughout the cement matrix(Zhao, Guo, Liu, Ge, et al., 2018a).

Li et al. (2018) used X-ray photoelectron spectroscopy and X-ray computed tomography to study the distribution of GO in the cement paste. Very few GO platelets were found to be absorbed by the hydration products and cement particles in the GO agglomerates. But because GO sheets are strong and have a unique shape, cement paste with 0.04% (by weight) of GO added made the flexural strength better by 83.0%(Wang, et al., 2018).

Lu et al. (2018) used ultrafine particles of silica fume as a dispersant for graphene oxide (GO) in both a neutral aqueous medium and an alkaline cement matrix. Studies of Zeta potential and UV-visible spectroscopy shows that silica fume made it easier for GO to distribute in matrix by forming hydrogen bonds and covering the silica fume particles. The silica fume contains more negatively charged overall, which leads to better dispersion through electrostatic interactions. But in the cement pore solution, GO and silica fume work together to make a bad effect. The interlocking of GO and silica fume by divalent Ca²⁺ ions produce aggregations(ZLu, Hou, et al., 2018).

Chuah et al. (2018) used different surfactants to treat GO, like air-entraining admixtures (Microair 905), polycarboxylate superplasticizers (Sika Visocrete 6

and ADVA 210), and Gum Arabic. Using the above-mentioned surfactants, the dispersion of GO in the ionic environments of NaOH, KOH, NaCl, and CaCl_2 solutions was studied. At a pH of 13.0, the electrostatic interactions between GO molecules were found to be weaker, so they clumped together. But the Ca^{2+} ions made the GO in the cement pore solution immediately aggregate together. When 0.03% GO was added to a cement composite with Gum Arabic as a surfactant, the flexural strength of the cement matrix increased by 67.0% (Chuah et al., 2018).

Gao et al. (2018) investigated the influence of ultrasonication and polycarboxylate superplasticizer on the dispersion of GO/CNT hybrid. It was found that increasing the sonication strength and time can considerably improve the dispersion of GO/CNT hybrid up to the point where a plateau is reached. After that, increasing the ultrasonication power further may damage the dispersion efficiency. However, increasing the duration of the ultrasonication process has only a marginal impact on the dispersion achieved. The findings of testing the mechanical strength of GO/CNT-paste samples show that the plateau in sonication power and time was achieved at 81-94 W and 15 minutes, respectively. It was determined that an increase of 78.8% in flexural strength, 53.2% in Young's modulus, and 62.3% in fracture energy provided the best possible results (Gao et al., 2019b).

Indukuri et al. (2019) examined the influence of silica fumes on the dispersion of graphene oxide (GO) within the cement matrix paste. The dispersion of GO was enhanced as a result of the reaction between silica fume and portlandite, which produced calcium silicate hydrate gel. This process reduces the concentration of Ca^{2+} ions surrounding GO nano-sheets in cement pore solutions, hence preventing their aggregation. GO was added to the cement composite at concentrations of 0.01%, 0.02%, 0.03%, and 0.04% by weight of cement. At 28 days of curing, the flexural strength of the sample containing 0.03% GO increased by 65.2% in comparison to the control sample. For 0.04% GO dosages, compressive strength increased by 46.9% after 28 days of curing (Indukuri et al., 2019).

Liu et al. (2019) investigated the mechanical characteristics of cement pastes containing graphene at concentrations of 0.01 wt%, 0.025 wt%, and 0.05 wt%. Graphene sheets were dispersed using ultrasonication and several surfactants, including sodium dodecyl benzene sulfonate (SDBS), sodium dodecyl sulphate (SDS), Triton X-100 (TX10), and polycarboxylate superplasticizer, etc. Using ultraviolet-visible (UV-vis) spectroscopy, the dispersion level was measured. At 28 days, the compressive strength was improved by 13.5% with 0.01% graphene introduction compared to the control. However, the increase in flexural strength and tensile strength was 16.0% and 15.2% at 28 days and 7 days, respectively, for a 0.025% dosage (Liu et al., 2019).

Wang et al. (2019) reinforced cement composites using graphene nanoplatelets (GNPs) modified with Melamine, Naphthalene, and Polycarboxylate superplasticizers (MS, NS, and PS). The dosage of GNPs varied between 0.03% and 0.12% (by weight% of cement). The integration of 0.06 percent GNPs resulted in a fluidity improvement equivalent to that of the control sample when water reducers were used. Melamine superplasticizers with 0.06% GNPs inclusion had the highest compressive and flexural strength. At 28 days, the increase in flexural strength for MS, NS, and PS was determined to be 20%, 13%, and 16%, whereas the increase in compressive strength was 11.2%, 5%, and 8% (Wang et al., 2019).

Arrechea et al. (2020) examined the mechanical properties of cement mortar reinforced by MWCNTs, MWCNT-COOH, and MWCNT-Thiazol at dosages of 0.01%, 0.03%, and 0.05%. (By weight of cement). The best dispersion was achieved with dispersion ratios of 1:16, 1:20, and 1:40 MWCNT to SP. Maximum dispersion was observed with a MWCNT:SP ratio of 1:20 and an SP:MW-COOH ratio of 40:1. At 7 days, the compressive strength increased by 5.3% for 0.01% MWCNTs compared to the control. Also, the maximum compression resistance was found at 28 days for 0.01% MWCNTs, which was 17.6% more than for the control (Arrechea et al., 2020).

Zhao et al. (2020) studied the effect of Ca^{2+} ions and OH^- ions individually and in combination on the aggregation of GO in the cement pore solution and its stabilization in an alkaline environment using a polycarboxylate-ether-based

superplasticizer. Optical microscopy, scanning electron microscopy, and X-ray photoelectron spectroscopy were used to examine the dispersion of GO in NaOH, CaCl₂, and Ca(OH)₂ solutions. Ca²⁺ ions generating cross-linking of GO sheets, rather than OH⁻ ions causing deoxygenation of GO, were the most important factor in the aggregation of GO in the alkaline cement solution. The GO was stable in an OH⁻ ionic environment for a few hours, but after six hours it tended to form smaller aggregates due to decreased electrostatic repulsions. However, the dispersion was stabilised using a polycarboxylate-ether based superplasticizer that adsorbs onto the GO sheets, delaying agglomeration through the steric hindrance mechanism. As a result, Ca²⁺ ions were discovered to be the primary cause of fast agglomeration in the alkaline environment, rather than the alkalinity of the cement pore solution (Zhu, et al., 2020).

Qureshi et al. (2020) investigated the influence of graphene, graphene oxide, and reduced graphene nanoplatelets (G, GO, rGO; utilised at concentrations of 0.01-0.16% by weight of cement) on the mechanical, microstructural, and electrical resistivity of cement paste. It was discovered that the flexural and compressive strength increases for G, GO, and rGO were 38% and 39%, 81% and 28%, and 84% and 30%, respectively. The variation in improvement induced by various graphene derivatives is attributable to the differing physical strengths and defining features of two-dimensional sheets (Qureshi & Panesar, 2020a).

M. Mansouri Sarvandani, et al. (2021) examine the impact of employing multi-walled carbon nanotubes (MWCNTs) functionalized with COOH on the mechanical properties and durability of cement mortars. This study analyzed the behaviour of nanocomposites modified with well-dispersed MWCNTs at 0.05, 0.1, 0.2, 0.3, and 0.4 wt. percent of cement using compressive and flexural strength tests exposed to environmental conditions of combined sodium-magnesium sulphate and limestone-saturated water for up to 960 days. By refining pores and altering the microstructure, a filler increased compressive strength in the two mentioned condition by 25 and 39 % respectively (Sarvandani et al., 2021).

K. Chintalapudiah et al. (2021) reinforced the PPC with GO at a 0.02%, 0.04%, 0.06%, 0.08%, and 0.1% concentration by weight of cement to examine the impacts of GO addition and to validate their performance improvement. PPC

composites with 0.04% GO dosage increased compressive strength by 40.41 percent compared to the 28-day-hydrated reference mix. Incorporating GO at the quantifiable way resulted in the formation of dense hydrated crystals that strengthened ITZ, which in turn significantly improved the compressive strength of fly ash-based cement composites(Chintalapudi & Pannem, 2021a).

D. Praseeda and K. S. Rao (2022) investigated the resistance to sulphate attack of the control mix (M 30 grade), the optimum blended concrete mix with cement, vitrified tile powder, silica fume, and fly ash, and the blended concrete mix reinforced with Multi-Walled Carbon Nano Tubes. The reinforced blended mixes were produced by introducing well dispersed Multi Walled Carbon Nano Tubes at 0.01%, 0.02%, 0.03%, 0.05%, and 0.1% by weight of binder content. At the end of the immersion period, the reinforced blended mix containing 0.05% carbon nanotubes had the greatest compressive strength value of about 54 MPa, which was about 23% higher than that of control mix(Praseeda & Rao, 2022).

2.2.2 Microstructural Properties of CNCMs

Konsta-Gdoutos et al. (2010) have been conducted on the rheological properties, macro- and nanoscale mechanical properties, as well as the nanostructure of cement nanocomposites reinforced with Multi-Walled Carbon Nanotubes (MWCNTs). The effective dispersion was successfully achieved through the application of ultrasonic energy, along with the utilization of a surfactant. The microstructural study depicted the fracture surface of samples reinforced with short and long Multi-Walled Carbon Nanotubes (MWCNTs) at two distinct concentrations, at a scale of 1 μm . Notably, the images reveal that in all instances, the MWCNTs appear to be effectively dispersed within the cement paste, with only isolated MWCNTs being identifiable on the fracture surface(Konsta-Gdoutos et al., 2010).

Nochaiya and Chaipanich (2011) investigated the microstructure of cement paste strengthened by pristine CNTs at 0.5% and 1.0% concentrations (by weight of cement). SEM images showed that CNTs were distributed uniformly throughout the hydrates of cement paste, resulting in reduced porosity and mesopores(Nochaiya & Chaipanich, 2011).

Sobolkina et al. (2012) studied the influence of two different kinds of CNTs (i.e., a mixture of single, double, and multi-walled CNTs and nitrogen-doped CNTs, N-CNTs) at the dosage of 0.05% on the microstructural aspects of the cement composites. Anionic (SDS) and non-ionic (Brij 35) surfactants were used to achieve the dispersion of CNTs. At 3 days of curing, mixed CNTs formed a net-like arrangement over the C-S-H gel surface, while N-CNTs can be seen successfully bridging the C-S-H phases. Mixed CNTs were found to bridge only 1 micrometre distances but failed to hold larger cracks together, whereas N-CNTs bridged the hydration products via uniform CNT distribution(Sobolkina et al., 2012a).

Collins et al. (2012) examined whether polycarboxylate-based superplasticizers were superior to other dispersing agents for uniform CNT dispersion. This was confirmed by SEM micrographs of the cement slurry after 28 days of curing(Collins et al., 2012).

Wang et al. (2013) used the surfactant, Gum Arabic (GA) and an ultrasonication method to disperse the MWCNTs. The effect of MWCNTs at concentrations varying from 0.05% to 0.15% on the morphology of cement pastes was investigated. The modified MWCNTs were deeply incorporated within the hydration products, enhancing the interfacial bonding between the cement paste and MWCNTs. MWCNTs also bridged the pores and voids, moving load from the cement matrix to the MWCNTs(Wang et al., 2013).

Lv et al. (2013) examined the effect of GO sheets on the microstructural properties of cement composites at concentrations ranging from 0.01% to 0.05% (by weight percentage of cement). It was discovered that GO nanosheets provided a template effect for controlling the morphology of cement hydrates. Specific shapes of hydration products, such as rod-shaped and flower-shaped crystals, were developed. When compared to the control sample(without GO added), the densification of these hydration products over time reduced brittleness to make cement composites with high toughness and mechanical strength(Lv, Ma, Qiu, & Zhou, 2013).

Lv et al. (2014) investigated the impact of GO in various dosages (ranging from 0.01% to 0.06% (by weight of cement)) on the microstructural properties of the

cement paste after 28 days of curing. SEM images revealed that specific morphology hydration products were produced as a result of various GO dosages. Lower GO dosages of 0.01% and 0.02% cause flower-shaped hydration products to appear from the voids in the cement paste, which becomes denser as GO dosages increase. The crystal pattern changed to rod-shaped and polyhedral crystals as the dosages were raised to 0.03% and 0.04%, respectively. Lamellar-shaped crystals were formed at higher GO dosages of 0.05% and 0.06%. Finally, the hydration products resulted in a dense and compressed microstructure, which decreased porosity and increased the compressive and flexural strength of the cement paste(Lv, Liu, et al., 2014).

Kim et al. (2014a) used SEM to investigate the microstructural and morphological properties of cement mixtures containing varying amounts of CNTs and silica fume. Low silica fume dosages evenly distributed the CNTs inside the cement matrix as individual strands. However, large dosages of silica fume resulted in CNT re-agglomeration(Kim, Nam, et al., 2014).

Horszczaruk et al. (2015) investigated the microstructures of cement mortar reinforced with 3.0% graphene oxide (by wt. of cement). SEM micrographs revealed that no agglomerates of GO had developed in the cement matrix. The curing of GO-mixed cement mortar was similar to that of the reference sample(Horszczaruk et al., 2015).

Torabian Isfahani et al. (2016) compared the effects of pristine and functionalized carbon nanotubes (p-CNT and f-CNT) at concentrations of 0.22% and 0.45% (by weight of cement) on the microstructural properties of cement mortar. SEM pictures showed that sonication improved the dispersion of p CNT and f-CNT into the cement mortar, but only to a limited extent. CNTs embedded within and interconnecting the cement hydration products can be observed. However, the reason for the CNTs' modest strength increases was revealed to be the poor adhesion between the CNTs and the hydration products(Isfahani et al., 2016b).

Lv et al. (2016) examined the microstructural behaviour of cement paste incorporating superplasticizer that exfoliated GO sheets (PC/GON), which was made by co-polymerizing GO with PCE-SP monomers. PC/GON was

incorporated into the cement mixture at 0.01%, 0.02%, 0.03%, and 0.04% concentration by weight (by weight of cement). With the production of regular hydration products that bridged the fissures and voids, PC/GON had a significant impact on the microstructural properties of cement composites, resulting in a reduction in overall porosity(Lv et al., 2016).

Chaipanich et al. (2017) analyzed the co-effects of as-prepared carbon nanotubes (0.5% and 1%) and silica fume (10% by weight) on the microstructural properties of cement-based compounds. Due to the filling effect and pozzolanic effect of the silica fume, SEM images of cement mortars showed a dense C-S-H gel formation(Chaipanich et al., 2017).

Lu et al. (2017) stabilised the GO dispersion by adding the polycarboxylate ether-based copolymer (PCE) to it before adding GO to the cement solution. PCE's hydrogen bonding and steric hindrance stabilised the GO dispersion in an alkaline cementitious environment and prevented it from clumping together (the ratio of PCE to GO was 15% by weight). For the study, 0.14 and 0.02% (by weight% of cement) of GO and PCE were used, respectively. Four cement composites were made, including PCE-Cement, GO-Cement, GO-Cement-PCE, and GO-PCE-Cement. GO-PCE-Cement was found to have the highest compressive strength of 27.2 MPa and the highest flexural strength of 14.6 MPa. Before the cement solution was added to this cement composite, PCE was used to stabilise the GO (Lu, Hanif, et al., 2017c).

Zhao et al. (2017) stabilized the GO by formation of covalent force between the macromolecules with the help of polycarboxylate superplasticizer (PC). It helps to prevent the GO from aggregation in alkaline environment otherwise the ions possess positively charge (Na^+ , Ca^{2+} , Mg^{2+}) interacts with negatively charged GO surface. The combined effect of PC@GO and SiO_2 nanoparticles analyzed in the microstructural behavior of mortars. The combination shows the efficient pozzolanic activity in mortar via consumption of portlandite by PC@GO and SiO_2 nanoparticles providing better densification of C-S-H gel(Zhao, Guo, Liu, et al., 2017).

Gao et al. (2018) studied the dispersion of GO/CNT hybrids under the influence of various ultrasonication parameters and polycarboxylate superplasticizer.

Power and time of sonication were observed to substantially enhance the dispersion of GO/CNT hybrid until a plateau was reached. At 81-94 W and 15 minutes, the power and time plateaus for sonication were reached, respectively. Poor sonication of GO/CNT resulted in increased porosity and pore size, whereas uniform dispersion led to the refinement of pore structure.

Liu et al. (2019) investigated the microstructure of the cement mix material reinforced with graphene. The SEM micrographs at 7 days of curing depict graphene sheets in the cement material. However, compactly organized hydration products were discovered after 28 days of curing. For the control sample, a loose structure of hydration products with defects was observed, whereas graphene exhibited a crack-bridging mechanism at a concentration of 0.025% due to the construction of a mesh shaped framework by graphene sheets (Liu et al., 2019).

Indukuri et al. (2019) studied the enhanced dispersion of graphene oxide (GO) by silica fumes within the cement matrix paste. GO was provided at concentrations of 0.01%, 0.02%, 0.03%, and 0.04%. (By weight of cement). The microstructural observations revealed that the enhanced toughness was a consequence of the modified cement paste's improved microstructural characteristics. The polyhedral and flower-shaped hydration products were observed, resulting in increased compressive and flexural strengths (Indukuri et al., 2019).

Wang et al. (2019) reinforced cement composites with graphene nanoplatelets (GNPs) modified with Melamine, Naphthalene, and Polycarboxylate superplasticizers (MS, NS, and PS). The GNP dosage ranged between 0.03% and 0.12% (by weight% of cement). The microstructural investigations revealed that GNPs filled pores in the cement composite. After incorporating nanometer-sized GNPs, the overall porosity of the cement matrix decreased as a result. Moreover, due to the large surface area of 2-D graphene sheets, GNPs enhanced the internal interface between hydration products and nanosheets (Wang et al., 2019).

Qureshi et al. (2020) investigated the influence of graphene, graphene oxide, and reduced graphene nanoplatelets (G, GO, rGO; used at concentrations of 0.01-

0.16% by weight of cement) on the mechanical, microstructural, and electrical resistivity of cement material. Ettringite, C-S-H, and C-H hydration phases are visible in the SEM images of the control sample. Micropores in samples containing graphene materials were substantially reduced due to the dense microstructure. Among the three graphene materials, the C-S-H gel structure was discovered to be most compact with GO. This was attributed to the nucleation sites provided by the GO to facilitate the formation of C-S-H and C-H hydration products at the interface of cement phases and reinforcement(Qureshi & Panesar, 2020b).

Kaur and Kothiyal (2020) compares the reinforcing ability of superplasticizer stabilized carbon nanomaterials hybrid, i.e., FCNT@GO, to individual carbon nanomaterials, i.e. graphene oxide (GO) or functionalized carbon nanotubes (FCNTs), on fly ash blended cement mortars (FCMs). Microstructural studies using FE-SEM and MIP revealed that the incorporation of FCNT@GO resulted in the densification of the mortar C-S-H gel network, resulting in reduced porosity of the mortar system(Kaur & Kothiyal, 2020).

Du et al. (2020) investigates the impact of hybrid graphene oxide (GO)/carbon nanotubes (CNTs) on the mechanical and microstructural properties of magnesium potassium phosphate cement (MKPC) paste. The morphology findings showed that the addition of hybrid GO/CNTs improved the microstructure, accelerating the formation of Struvite-k crystals and decreasing the amount of unreacted MgO particles(Du et al., 2020).

Mousavi et al. (2021) investigate the samples contains nanomaterials shows increased amount of C-S-H gel. The materials also show dense and compact nanostructure. The nanotubes functioned as embedded materials in the cement matrix in order to prevent the cracks. It reduces the cracks propagation and inhibition in the paste of cement. By filling the pores at nanoscale and creating the bridging mechanism forms stronger bond between the hydration products. The interaction between COOH functional group and the cement also shown in the article(Mousavi et al., 2021).

K. Chintalapudiah and Pannem (2021) both found that the GO reinforcing phase shows enrichment of hydration products (CSH, CH and Aft) in the cementitious

matrix. The reinforcing phase showed eliminating pores or lesser micro cracks in the cementitious matrix. The higher amount of hydration products such as CSH supported by the FESEM microstructures(Chintalapudi & Pannem, 2021a).

D. Praseeda and K. S. Rao (2022) found the better dispersed carbon nanotubes and shows outstanding performance in the resistance of sulphate attack. The optimum blended mix (0.05%) of carbon nanotube shows higher dispersion as well as more resistance due to bridging effect formed dense microstructure. Also, the MCNT5 matrix has been shown cracks due to agglomeration of carbon nanotube(Praseeda & Rao, 2022).

Verma, Chowdhury, and Chakrabarti (2023) examined the effect of rGO nanosheet into OPC. The results show that the incorporation of nanosheet into cement matrix could be leads to filling the pores with hydration products. The compact microstructure corresponds to higher hydration products. A flower shaped crystal structure has been observed in FESEM analysis. The results were supported the physico-mechanical strength as well(Verma et al., 2023).

2.2.3 Crystallization Properties of CNCMs

Horszczaruk et al. (2015) examined the crystallinity of cement mortar phases reinforced with graphene oxide at a concentration of 3.0% (by weight of cement). XRD patterns revealed a decrease in the unhydrated alite (C_3S) and belite (C_2S) peak intensities of GO-reinforced cement mortars as the curing time increased. In general, no significant differences were observed between the crystalline phases of reference and nanocomposite samples(Horszczaruk et al., 2015).

Li et al. (2015) investigates the effect of reinforcing materials (carbon nanotubes and graphene oxide), dispersed with polycarboxylate superplasticizer, on cement mortar samples was investigated. The crystalline phases of cement mortar samples were analysed using X-ray diffraction, with a focus on the impact of GO, CNTs, and CNT/GO mixture. The Debye-Scherrer equation was utilised to calculate the particle size of crystal SiO_2 in CNTs and GO composites, and it was observed that the particle size increased in comparison to the control

sample. The composite consisting of a mixture of CNT and GO demonstrated a notable increase in the size of SiO_2 crystal, indicating an enhanced reinforcing effect on mortars through the co-action of CNTs and GO(Li et al., 2015).

Zhao and colleagues (2017) modified graphene oxide (GO) sheets using polycarboxylate superplasticizer (PC) through the establishment of covalent interactions between the two macromolecules. The investigation shows the impact of SiO_2 nanoparticle-decorated PC@GO sheets on the reinforcement of mortars, taking into account the hybrid effect. The hybrid-based mortars exhibited enhanced pozzolanic activity due to the consumption of portlandite by silica nanoparticles, resulting in the formation of a compact C-S-H gel. The said assertion was substantiated by the reduction in the maximum magnitudes of portlandite (C-H) observed at $2\theta = 18.3^\circ$, relative to the reference specimen, after 28 days of the curing process(Zhao, Guo, Ge, et al., 2017c).

Liu et al. (2019) investigated the effects of graphene sheets at doses of 0.01%, 0.025%, and 0.05% (by weight of cement) on the crystallinity of cement paste samples. With the help of the surfactant sodium dodecyl benzene sulfonate (SDBS), the graphene sheets were evenly spread. During the hydration process, hexagonal portlandite (C-H) crystals grow according to the orientation index in XRD studies, and XRD was used to track the impact of graphene incorporation on the orientation of C-H crystals. The low orientation index represents the high compactness of the hydration products and hence high mechanical strength. The orientation index for the reference sample and graphene reinforced sample at 28 days of curing was found to be 1.63 and 1.43 for 0.025% dosage. Hence, the lowering of the orientation index represents the improved interfacial properties of the cement paste(Liu et al., 2019).

Indukuri et al. (2019) conducted a study by involved the addition of GO sheets into the cement matrix, alongside silica fume and fly ash. The crystalline investigations have confirmed the existence of multiple hydration products, including but not limited to ettringite, portlandite, and calcium silicate hydrate gel. It was hypothesized that the quantity of hydration products might increase as the duration of the curing process increased. The above observation indicates that the addition of GO has the potential to control the development of hydration

products, thereby exerting an advantageous effect on the mechanical characteristics of the cementitious matrix(Indukuri et al., 2019).

Liu et al. (2019) in their study, looked at how the orientation index reflects the formation of $\text{Ca}(\text{OH})_2$ crystals during cement hydration and how the effect of graphene sheets on CH orientation may be identified by an XRD pattern. Usually, a lower orientation index corresponds to a more densely packed and hardened cement paste. The incorporation of 0.025 weight percent graphene sheets resulted in a notable reduction in the orientation index of CH crystals, thereby improving the interfacial characteristics of cementitious materials(Liu et al., 2019).

Qureshi et al. (2019) examined the XRD depicted the CH phases increases with increasing the amount of carbon nanomaterials (GO and rGO) in the matrix along with the period. With time and hydration, the intensity of the ettringite phases diminishes, while it is greater in the rGO composites. With a rise in GO and rGO concentration, the crystalline phases likewise increase. Since XRD cannot identify amorphous phases directly, a quantitative analysis using Rietveld software was performed on the composites that had been hydrated for 28 days in order to determine how much amorphous C-S-H gel and other hydration products were present(Qureshi & Panesar, 2019).

Kaur and Kothiyal (2020) conduct the PXRD study of the cementitious compound after 7 and 90days. The carbon nanomaterials added in very lower amount to the matrix, since no peaks were identified corresponding to carbon nanomaterials. Various hydrations products were found such as tricalcium silicate (C_3S), dicalcium silicate (C_2S), ettringite (AFt), calcium hydroxide (CH), tetracalcium aluminoferrite (C_4AF), and quartz (Q). The major products responsible for strength of matrix was C-S-H gel. As a result of the pozzolanic reaction, FA particles were consumed by the freely accessible portlandite (CH), after 90 days of curing for all FCMs mixes as compared to the control (cement) sample(Kaur & Kothiyal, 2020).

Praseeda and Rao (2022) present X-ray diffraction (XRD) patterns of the control mix, blended mix, and nano-engineered mixes both pre- and post-immersion for a period of 180 days. In control mix the $\text{Ca}(\text{OH})_2$ exhibited a significantly higher

intensity in comparison to the other products, namely CSH and ettringite. Upon analysis of the blended mixture, it was noted that the degree of Ca(OH)_2 formation was reduced. This phenomenon can be ascribed to the utilization of Ca(OH)_2 in the generation of a secondary hydration product referred to as CSH. CSH is a primary hydration product that fills the pores within the matrix, resulting in a denser structure (Praseeda & Rao, 2022).

Verma, Chowdhury, and Chakrabarti (2023) shows the XRD pattern of rGO-based mortar samples after curing for 7 and 28 days. The findings indicate that a rise in the concentration of rGO led to a corresponding escalation in the portlandite phase's intensity, relative to the control specimen. The correlation between the rise in intensity and the increased quantity of phase within the sample is observed (Verma et al., 2023).

2.2.4 Durability of CNCMs

2.2.4.1 Electrical Properties of CNCMs

Han et al. (2012a) evaluated the electrical characteristics of pressure-sensitive composites reinforced with -COOH functionalized MWCNTs while they were compressed. It was discovered that improved CNT dispersion in composites created effective conductive networks, which therefore resulted in reduced resistance values. As a result, the composites with 0.50% CNT incorporation had lower resistance values than those with 0.10% CNT (Han et al., 2012a). In other study the Han et al. (2012b) fabricated cement composites based on CNF/CNTs, and they employed polycarboxylate superplasticizer to effectively disperse the carbon nanomaterials, as shown by the low electrical resistivity values. Additionally, the cement composite's piezoresistive response was examined, and it was discovered that the superplasticizer was crucial to produce piezoresistive cement composites (Han et al., 2012b).

Kim et al. (2014a) found the electrical resistivity properties of carbon nanotubes based cementitious composites consisting silica fume. In the presence of silica fume the electrical resistance reduced significantly. It could be attributed by the uniform distribution of carbon nanotubes, in silica contain matrix (Kim, Nam, et al., 2014). In another study, Kim et al. (2014b) investigated the electrical resistivity in mortar fabricated with dispersed (addition of probe method) CNTs

at low w/c ratio. The piezoresistive sensitivity and stability were reduced for a low w/c ratio (Kim, Park, et al., 2014).

Li et al. (2018) examined the electrical resistivity properties of cement paste through the probe method. The study also involved the incorporation of graphene oxide (GO) at varying weight percentages of 0.01%, 0.02%, 0.03%, and 0.04%. The findings of this investigation indicate that the electrical resistivity displays an increase in comparison to the control sample after a 28-day curing period. The electrical resistivity demonstrated an initial increase up until the point of GO dosage reaching 0.02%, thereafter it remained relatively constant with the incorporation of 0.04% GO. The elevated electrical resistivity measurements exhibited by the cement paste that has been strengthened with GO curtails its capacity to generate self-sensing cement matrices (Li et al., 2018).

Kaur and Kothiyal (2019) investigated the control sample exhibited electrical resistivity values of 7.4, 11.2, and 13.5 K ohms-cm at 7, 14, and 28 days of curing, respectively. The inclusion of SP@GO and SP@FCNT in the mixes resulted in increased electrical resistivity. Among the SP@GO-CNCs, the highest electrical resistivity was observed with a 0.02% SP@GO content. Compared to the control sample, the electrical resistivity increment was 79%, 71%, and 67% for curing periods of 7, 14, and 28 days, respectively. However, after reaching a concentration of 0.02% SP@GO, the resistivity exhibited a decreasing trend until 0.16% SP@GO. Conversely, among the SP@FCNT-CNCs, a dosage of 0.08% SP@FCNT demonstrated the highest electrical resistivity at all curing ages (Kaur & Kothiyal, 2019a).

Qureshi et al. (2020) studied the impact of pure graphene, graphene oxide, and reduced graphene nanoplatelets (G, GO, rGO; employed in concentrations of 0.01-0.16% by weight of cement) on the electrical resistivity of cement paste. The study involved measuring the electrical resistivity of samples over a period of 24 hours to 28 days during the curing process. The results indicated a positive correlation between increased curing age and electrical resistivity. The incorporation of 0.02% GO resulted in the highest electrical resistivity, exhibiting a 13% increase compared to the control after 28 days. However, the electrical resistivity decreased as the dosage of GO was further increased. The electrical resistivity values of cement pastes containing reduced graphene oxide

(rGO) and graphene (G) exhibited an increase with higher dosages, attributed to the conductive properties of graphene(Qureshi & Panesar, 2020b).

2.2.4.2. Water absorption

Gingos (2011) conducted a study on mortar mixes of 0.3w/c, 0.4w/c, and 0.5w/c ratios with 10%, 20%, and 30% PFA replacements. The amount of PFA replacements in the mortar has an enormous effect on the strength development and water absorption rate of the mortar. Results show that 20% PFA mortars with a 0.5w/c ratio are the best mix to lower the rate of water absorption and get a higher compressive strength(Gingos, 2011).

Najimi et al. (2012) found that after 24 hours, concrete with 30% (NZ30) natural nano zeolite by weight of cement absorbed 7.75% more water than reference concrete (NZ0). The porous structure of zeolites is responsible for this. Water also penetrate NZ30, though to a shallower depth of 10 mm compared to NZ0's 15 mm(Najimi et al., 2012).

Jalal et al. (2013) investigated water absorption and capillary water absorption in concrete mixes containing varying percentages of TiO₂ nanoparticles for up to 168 hours. When 5% nano-TiO₂ was added to the mix, water absorption and capillary water absorption of concrete were found to be reduced by roughly 15% and 25%, respectively. It should be noted that in both instances, the specimens were cured in water for up to 90 days. As a result, it is inferred that the longer curing time and older age of the concrete specimens containing TiO₂ nanoparticles lower the permeability gaps(Jalal et al., 2013).

Rajkumar et al. (2016) studied the water absorption capacity of nano-SiO₂ concrete. 1.5% of the cement in the concrete mix was replaced with nano-SiO₂. The cylindrical specimens were immersed in water for water absorption tests. Significantly less water absorption was found in the concrete with nano-SiO₂ than reference concrete. After 7 days, the reference concrete had 275% greater water absorption. Though the authors did not explain why this difference exists, it is possible that the interaction of nano-SiO₂ with Ca(OH)₂ densifies the matrix, making it harder for water to permeate(Rajkumar et al., 2016).

Prabayathy et al. (2020) added 0.1% rGO in cementitious matrix which enriches the compactness by pore filling ability where rGO attributes clogging of micropores by forming Nanoplatelets. This compactness of cement matrix

results in enriched properties such as carbonation effects, resistance against acid penetration and water absorption(Prabavathy et al., 2020).

Zhang et al. (2021) investigates the influence of nano-SiO₂ (NS) and nano-Al₂O₃ (NA) with 0.5%, 1.0%, 2.0%, and 3.0% in cement concrete (w/b = 0.5). Via introducing of 0.5% NS + 0.5% NA powders in matrix, it shows 1% reduced capillary permeability coefficient of concrete samples compared to that of 0.5%NS and 0.5%NA samples(Zhang et al., 2021).

2.2.4.3. Acid and sulphate attack

Sathyan et al. (2019) investigated the durability properties of fly ash-based cement concrete. It was discovered that PPC and OPC (with 25% FA) samples performed better when PCE-SP was added compared to the control sample without a superplasticizer. Compared to the control sample, a reduction in sorptivity, resistance to acid, and chloride ion penetration was observed(Sathyan & Anand, 2019a).

Sharma and Arora, (2018) investigated the influence of graphene and recycled aggregates on the mechanical properties and sulfate attack resistance of cement-FA based mortar. The incorporation of 0.05% graphene (with FA used as 30% partial replacement to cement) enhanced the flexural strength and compressive strength by 13% and 8%, respectively, in comparison to control sample. Also, a significant resistance to sulfate attack was obtained for 0.05% graphene composite(Sharma & Arora, 2018).

In a study by Xu et al. (2018) an enhanced degree of polymerization of Si-tetrahedrons in GO reinforced fly ash geopolymer was found. With 0.02% incorporation of graphene oxide (by weight of fly ash), compressive strength improvement from 33.6 MPa to 41.4 MPa was found at 28 days of curing. In this study, the combined effect of fly ash and PCE-SP stabilized GO was studied on the durability properties of fly ash-cement based mortars(Xu et al., 2018).

Muthu and Santhanam (2018), added nanoparticles of rGO, alumina, and silica were each added into the paste mixes at concentrations of 0.02%, 0.2%, and 4% correspondingly, based on the weight of the cement. The results showed that the presence of reduced graphene oxide and nano alumina decreased the amount of capillary pores (10 nm–10 µm) by up to 46% and 51% than the control paste after storage in acidic solution for 28 days(Muthu & Santhanam, 2018).

Ranckel son et al. (2022) concentrates on the initial phase of the degradation of various cementitious materials in phosphoric acid. Comparisons are made between three varieties of cementitious materials: OPC (100 percent cement), slag-blended OPC (slag/cement mass ratio of 65/35), and alkali-activated slag/fly ash pastes (slag/fly ash mass ratio of 50/50). Samples were exposed to phosphoric acid solution with a constant pH at 2.0 ± 0.2 for 44 days. The results indicate that the alkali-activated slag/fly ash binder has the lowest degradation rate among the cement-based binders. Changes in the kinetics of degradation are brought about by the intrinsic properties of the compounds(Ren et al., 2022).

Samimi and Zareechian (2022), examine the effect of pumice and zeolite as natural pozzalona in cement paste that has been created by water-dispersed graphene that has been synthesized from graphite and surfactant. The cement paste is being tested for its resistance to an acid attack. In the mixes that included graphene, the findings showed that pumice and zeolite both lowered the compressive strength at an early age by 15.5% and 20.4%, respectively. On the other hand, as shown by the MIP and XRD data, this decrease was somewhat offset by an increase in the rate of pozzolanic reaction with time. When compared to the reference paste, zeolite was able to minimize the amount of weight loss and compressive strength loss that occurred as a consequence of acid attack by 251.72% and 239.4%, respectively(Samimi & Zareechian, 2022).

There have been previous studies depicting the mixed results of GO, FMWCNTs, and HCNMs on the mechanical and other properties of the cementitious nanocomposites (CNCMs), which are briefly discussed below. A brief tabular discussion of the same has been shown in Table 2.1.

Table 2.1 A Literature Overview of Mechanical, Microstructural, Crystallization, and Durability Properties of CNMs/HCNMs-CNCMs

S. No.	Type of CNMs and its dosage (by wt.% of cement)	Type of cement matrix & w/c ratio	Dispersion methods used	Properties examined	Major findings	Reference
1	(0.048% and 0.08%) Pure MWCNTs	Cement paste (w/c = 0.50)	Ultrasonication + Surfactant	Dispersion, Young's modulus, and Flexural strength (3, 7 and 28 days)	According to the results of the scanning electron microscopy (SEM), the dispersion of CNTs requires both ultrasonication and an appropriate ratio of surfactant to CNT. In comparison to the control sample, the mechanical strength increased up by 30–40%, and the Young's modulus increased up by 35%.	(Konstantinos et al., 2010)
2	(0.5% and 1.0%) Pristine CNTs	Cement mortar (w/b = 0.50)	Ultrasonication + PCE-SP + Fly ash (20% by weight)	Compressive strength and Microstructure (7, 28 and 60 days)	At 28 days, the compressive strength of the mortar is almost 100% higher than that of cement-based mortar. CNTs were able to interact favorably with a cement matrix that was based on fly ash and served the function of filler inside the matrix.	(Chai et al., 2010)

3	(0.5% and 1.0%) Pristine CNTs	Cement paste (w/c = 0.5)	Ultrasonication +Polycarboxylate superplasticizer	Microstructure s, and Porosity (28 days)	CNTs were found to be distributed consistently throughout the hydration products of cement paste, according to both SEM and MIP investigations, which led to a decrease in porosity and mesopore size.	(Nochaiya & Chaipanic h, 2011)
4	(0.05% and 0.25%) Pure CNTs (Mixed and N-doped)	Cement paste (w/c = 0.5)	Ultrasonication + Sodium dodecyl sulphate (SDS) or Brij-35	Dispersion, Compressive, Tensile strength, Microstructural and Porosity studies (3 and 28 days)	The use of Brij-35 led to an increase in compressive strength of 40% for mixed CNTs and 30% for N-doped CNTs respectively. Mixed CNTs formed a net-like structure on the surface of the C-S-H gel, while N-CNTs effectively connected the C-S-H phases. SDS increased the porosity of cement composites, whereas Brij 35 had no effect on porosity.	(Sobolkina et al., 2012b)
5	Pure MWCNTs	Cement mortar (w/c = 0.4)	Ultrasonication + SP + Magnetic stirring	Electrical resistivity, Compressive (30 days)	Superplasticizer uniformly disperses CNFs and CNTs owing to its double dispersion effect on cement and carbon nanomaterials. Low electrical resistivity improves piezoresistivity.	(Han et al., 2012b)

6	(0%, 0.5%, 1.0%, and 2.0%) Pure MWCNTs	Cement paste (w/c = 0.4, 0.5, 0.6)	Ultrasonication + Polycarboxylates or Lignosulfonates or Air entrainers	Dispersion, Workability and Compressive strength (28 days)	Polycarboxylate superplasticizer dispersed uniformly CNTs. Consistency have been decreased in the paste due to CNTs. Polycarboxylate superplasticizer stabilized 0.5% CNTs improves compressive strength by 25%.	(Collins et al., 2012)
7	(0.01% to 0.05%) Synthesized GO	Cement mortar (w/c = 0.36)	Ultrasonication + SP	Mechanical, Microstructure	Tensile, flexural, and compressive strength were increased by 78.6%, 60.7%, and 38.9%, respectively, in 0.03% GO reinforced cement mortars.	(Lv, Ma, Qiu, Sun, et al., 2013a)
8	Functionalized CNTs	-	Ultrasonication + SP (CNT to SP ratio 1:4) + Ca(OH) ₂	Dispersion studies of FCNTs under effect of SP and Ca(OH) ₂	CNTs were dispersed using SP and ultrasonication. The presence of Ca(OH) ₂ in a CNT dispersion disrupts the steric repulsion between CNTs and SP molecules, resulting in CNT aggregation.	(Mendoza et al., 2013)

9	(0.05%, 0.08%, 0.10%, 0.12% and 0.15%) Pure MWCNTs	Cement paste (w/c =0.35)	Ultrasonication + Surfactant (Gum Arabic-GA)	Flexural, Fracture energy, Microstructure and Porosity	The flexural toughness index for CNTs at the 0.08% level was increased by GA modification by 57.5%. The addition of CNTs at 0.08% resulted in the highest fracture energy (312.2 N/m).	(Wang et al., 2013)
10	(0.01% to 0.06%) Synthesized GO	Cement paste (w/c = 0.3)	SP (0.2% (by weight of cement))	Flexural and Compressive strength, Microstructure (3, 7 and 28 days)	Using ultrasonication for 60 minutes to disperse GO led to a dense microstructure and decreased porosity, which in turn increased compressive and flexural strength by 38.2% and 52.9%, respectively. Microstructural investigations revealed the formation of many crystalline shapes, including rod-like crystals.	(Lv, Liu, et al., 2014)
11	(0%, 0.15%, and 0.30%) Pure MWCNTs	Cement mortar	PCE based SP & Silica fume (0%, 10%, 20%, and 30%)	Dispersion, Mechanical and Electrical Microstructure (1 and 28 days)	SEM pictures reveal that silica fume improved CNT dispersion in cement composites. In terms of compressive strength, a cement composite containing 0.15 percent CNTs and 30 percent silica fume performed the best.	(Kim, Nam, et al., 2014)

12	(0%, 0.1%, 0.3%, and 0.5%) Pure MWCNTs	Cement mortar (w/c = 0.4, 0.5 & 0.6)	Superplastic izer	Compressive strength and Electrical resistance	Compressive strength was increased for the lowest w/c ratio. At the lowest w/c ratio the maximum reduction for electrical resistivity was found.	(Kim, Park, et al., 2014)
13	(3%) GO	Cement mortar (w/c= 0.6)	Ultrasonication	Young's modulus, Microstructure studies (7 days)	Enhanced Young's modulus between 5 and 20 GPa; scanning electron microscopy (SEM) evidence for homogenous GO dispersion in a cement matrix; decreasing peak intensities of alite and belite with extended curing time (XRD).	(Horszczaruk et al., 2015)
14	(0.01%, 0.03% and 0.06%) GO	Cement mortar (w/c = 0.34)	Water reducing agent	Porosity & Water absorption (28 days)	Chloride ion penetration resistance. Improved microstructure and water sorptivity due to an increase in the number of gel pores.	(Mohammed et al., 2015)
15	(0.05-1.0%) SWCNT/GO	Cement mortar (w/c = 0.3)	Ultrasonication + Polycarboxylate	Bending strength and Crystalline studies (7 days)	Bending strength was enhanced by 72.7% for CNT/GO-cement composite, whereas gains for CNTs and GO-based composites were 26.3% and 51.2%, respectively. When compared to the control sample, XRD revealed an increase in	(Li et al., 2015)

			superplasticizer		SiO ₂ particle size in the CNT/GO hybrid composite.	
16	(0.08%, 0.10% and 0.20%) Pure SWCNTs and MWCNTs	Cement mortar (w/c = 0.5)	Ultrasonication + Magnetic stirring + Pluronic F-127 (3 and 5%)	Compressive, and Flexural strength (28, 42 and 56 days), Microstructure studies	The flexural modulus of 0.1% SWCNTs-cement mortar was increased by 72%. At 56 days of curing, compressive and tensile strength increased by 23% and 17%, respectively. SEM examines revealed that CNTs were dispersed uniformly inside the cement matrix.	(Parveen et al., 2015)
17	(0.025%) FCNT & (0.025%) GO Hybrid	Cement paste (w/c = 0.4)	Ultrasonication	Dispersion, Flexural and Compressive strength (14 days)	Optical microscopy and UV-visible spectroscopy confirmed the stable dispersion of CNTs in GO solution. The compressive strength (21.1%) and flexural strength (24.2%) found to be increased in comparison to control sample.	(Lu, Hou, Meng, Sun, & Li, 2015)
19	(0.01%, 0.02%, 0.03% and 0.04%) Synthesized GO	Cement paste (w/c = 0.29)	Ultrasonication + Co-polymer of	Flexural and Compressive strength (3, 7 and 28 days)	The fluidity has been decreases via uniform dispersion of GO (PC/GON) in the cementitious composites leads to increase in compressive and flexural strength was 56.5% and 77.6%.	(Lv et al., 2016)

			GO & PCE-SP			
20	(0.5% and 1.0%) CNTs	Cement mortar (w/b = 0.5)	Ultrasonication + Polycarboxylate superplasticizer + Silica fume (10% by weight)	Compressive, and Flexural strength (28 days), Microstructural studies	0.5% of CNTs and 10% SF leads to improve the compressive strength by 17% and for both (0.5% and 1.0%) CNTs shows improvement by 10% in flexural strength as compared to control. The filler effect in cementitious matrix owing to dense microstructure revealed by SEM microstructure.	(Chaipanic h et al., 2017)
21	(0.02%, 0.04%, 0.06%, 0.08%, 0.1% and 0.3%) Pure CNTs	Cement mortar (w/b = 0.4)	Ultrasonication Surfactants (GA, CTB, etc.)	Dispersion, Compressive & Tensile strength	The CNTs with GA dosages of 0.08% and 0.1% obtained compressive strength 10% and tensile strength increased by 80% from control. The 0.06-0.1% ration of CNTs shows maximum fracture energy in GA based cementitious mortar.	(Sindu & Sasmal, 2017)
22	(0.14%) GO	Cement paste (w/c= 0.35)	Polycarboxylate ether (0.02%)	Dispersion, Flexural and Compressive	From preventing the agglomeration of GO in the alkaline environment of cementitious matrix, it was priory stabilized in the presence of PCE. In	(Lu, Hanif, et al., 2017b)

				Strength (14 days)	case of GO-PCE-mortar the increased compressive and flexural strength was found to be 27.2 and 14.6 MPa, respectively.	
23	(0.01-0.06%) Hybrid of GO and (0.1-2.0%), SiO ₂ nanoparticles	Cement mortar (w/c=0.45)	Ultrasonication & Polycarboxylate (PC)	Compressive Strength, & Microstructural studies (3, 7 and 28 days).	The GO was decorated with the PC and SiO ₂ nanoparticles. The increased compressive strength was found to be 38.9% at 28 days of curing ages.	(Zhao, Guo, Ge, et al., 2017b)
24	GO-CNT hybrid	Cement paste (w/c=0.4)	Ultrasonication & Polycarboxylate superplasticizer (PC)	Dispersion, Flexural Strength, Young's Modulus, Fracture Energy, Microstructure and Porosity	The uniformity of GO/CNT in the solution was improved by modifying sonication energy, time and power. Enhancement in flexural strength, Young's modulus, and fracture energy was found to be 78.8, 53.2, and 62.3%, respectively. SEM studies revealed that poor sonication of GO/CNT resulted in increased porosity and pore size, while uniform dispersion led to the pore structure refinement.	(Gao et al., 2019a)

25	(0, 0.01%, 0.03% and 0.05%) Ball-milled GO	Cement paste, (w/c= 0.3)	Ball-milling	Compressive strength, Microstructure, and Porosity (3 and 28 days)	9.0% increased compressive strength found at the age of 28days of curing via addition of 0.03% GO, in the cement paste in comparison to control sample. Reduction in total porosity by 1.68% for 0.03% GO addition as compared to plain sample.	(Jing et al., 2019)
26	(0.05%) Superplasticizer modified GO	Cement mortar (w/c= 0.5)	Water Reducing Agents (WRA), WRA:GO mass ratio = 5:1, 10:1, and 20:1	Fluidity, Mechanical Strength, (7 days)	At 24 hours the cross-linking GO-Ca ²⁺ was prevented by steric hindrance of high PCE-SP concentration. The compressive and fluidity were improved at the 7 days of curing ages.	(Zhao, Guo, Liu, Ge, et al., 2018b)
27	(0.01%, 0.02%, 0.03% and 0.04%) Synthesized GO	Cement paste (w/c = 0.36)	Silica fume (0%, 1%, 3% and 5%) and	Dispersion, Compressive, and Flexural Strength(3, 7	In FA-cement paste, silica fume improved the uniformity of GO (at 3.0 and 5.0% (by weight of cement)) The microstructure of GO added cementitious matrix shows, polyhedral and flower-shaped	(Indukuri et al., 2019)

			Polycarboxylate (SP)	and 28 days), Microstructure	hydration products lead to enhanced compressive and flexural strength, respectively.	
28	(0.03%, 0.06%, 0.09% and 0.12%) Graphene nanoplatelets	Cement Paste (w/c= 0.3)	Ultrasonication+ MS, NS and PS; Melamine, Naphthalene	Dispersion Studies, Mechanical Strength, Microstructural Studies and Porosity (7 and 28 days)	The incorporation of 0.06% GNP, improved fluidity equal to the water reducer added control sample. Compressive strength and flexural strength was found maximum for MS by 11.2%, and 20%, in comparison to control. Microstructural and porosity studies revealed that the introduction of GNPs refine the smaller pores with improved hydration degree of the matrix.	(Wang et al., 2019)
29	(0.01%, 0.025% and 0.05%) Graphene	Cement paste (w/c= 0.6)	Ultrasonication + Surfactants (SDBS = sodium dodecyl benzene sulfonate)	Dispersion studies, Compressive, Flexural & Tensile Strength and Porosity (3, 7 and 28 days)	Graphene:SDBS =1:6 (by weight) achieved maximum dispersion. The addition of 0.01% the improved compressive strength was found to be 13.5% at the age of 28 days of curing. And for 0.025%, the flexural and tensile strength was found to be 16 and 15.2% at the age of 28days respectively, in comparison to control sample.	(Liu et al., 2019)

30	(0.01%, 0.02%, 0.03%, and 0.04%) GO	Cement paste (w/c= 0.4)	---	Electrical Resistivity, and Flexural strength (28 days)	GO added samples shows improved electrical resistivity as compared to control sample. The flexural strength enhanced by 83.0% for addition of 0.04% GO.	(Li, Wang, et al., 2018)
31	(0%, 0.005%, 0.01%, 0.02%, 0.03%, and 0.04%) GO	Cement paste (w/c= 0.4)	Ultrasonication + Surfactants (ADVA 210, Gum Arabic, Sika Visocrete 6, Microair 905)	Dispersion, and Flexural Strength (28 days)	The ionic studies were conducted for GO dispersion in the presence of KOH, NaOH, NaCl, and CaCl ₂ . With 0.03% (by weight of cement) incorporation of A ball milling strategy to disperse graphene oxide in cement composites GO improved the flexural strength by 67.0%.	(Chuah et al., 2018)

32	(0.01%, 0.03% and 0.05%) MWCNTs, MWCNT-COOH	Cement mortar	Ultrasonication + PCE-SP (MasterGlenium ACE 30-0.2% w/w)	Dispersion and Compressive strength (7 and 28 days)	Maximum dispersion was obtained for SP: MWCNT ratios of 20:1 and SP: MWCNT-COOH ratios of 40:1. At 7 days, compressive strength increased by 5.3% for 0.01% dosage over control.	(Arrechea et al., 2020)
33	(0%, 0.02%, and 0.04%) GO	Cement mortar (w/c = 0.5)	Ultrasonication + Superplasticizer	Dispersion, Flexural and Compressive Strength, Microstructural Studies (3, 7 and 28 days)	Sika-PCE provided the best GO dispersion (SP to GO ratio was 1:1), even in extreme alkaline circumstances. At 3 days of curing, the flexural (0.02%) and compressive (0.04%) strengths were increased by 15.5% and 14.4%, respectively. Lower GO dosage densified the mortars, however, greater GO dosage increased the ITZ of cement mortar.	(Yan et al., 2020)
34	(0.05% in a weight ratio of 1:4, 2:3, 3:2 and 4:1) Hybrid of GO and CNTs	Cement mortar (w/c = 0.3)	Ultrasonication + Superplastic	Dispersion, Flexural and Compressive Strength,	UV-visible spectroscopy indicated that a GO to CNT ratio of 3:2 (by weight) resulted in the greatest dispersion.	(Du et al., 2020)

			izer (0.1 wt%)	Porosity and Microstructure (28 days)	Compressive strength increased by 45.2% when the hybrid ratio was 3:2 (by weight). Flexural strength was increased as a consequence of the hybrid structure's effective load transmission.	
35	(0.02%, 0.04%, 0.06%, 0.08% and 0.1%) GO	Cement mortar (w/c = 0.4)	Ultrasonicat ion + Superplastic izer (1%)	Compressive, and Microstructure (28 days)	The functional groups have been revealed by the use of NMR, FTIR, and FESEM in the characterization of GO's. After 28 days of hydration, PPC cement composite with 0.04 % GO had 40.41% compressive strength.	(Chintalap udi & Pannem, 2021b)
36	(0.01%, 0.02%, 0.03%, 0.05% and 0.1%) Multi walled Carbon Nano Tube	Cement concrete (w/b = 0.45)	-	Compressive, and Microstructure (28 days)	After immersion, the 0.05% mix had the greatest compressive strength of 54 MPa, 23% greater than the control mix. The SEM-EDX and XRD to determine the morphology and the formation of the crystalline phases of the matrix.	(Praseeda & Rao, 2022)
37	(0.03 %, 0.05 %, 0.07 %, and 0.09 %) rGO	Cement mortar (w/b = 0.45)	-	Compressive, Microstructure nalysis(28 ays)	When compared to the other mixes, the compression strength is best when 0.09% rGO is	(Verma et al., 2023)

					added. FE-SEM showed that rGO's pore-filling characteristic produced dense microstructures.	
38	(0.05, 0.1, 0.2, 0.3, and 0.4 wt percent of cement) MWCNTs	Cement mortar (w/b = 0.45)	Ultrasonic homogenizer, Surfactant (0.3%)	Mechanical, Microstructural analysis (28 days)	The mix with 0.05% of the carbon nano tubes have shown highest strength at the end of the immersion period by about 23% higher than the control	(Sarvanda ni et al., 2021)
39	(0.05%, 0.1%, 0.15%, and 0.2%) rGO	Cement mortar (0.75kg water)	Probe sonicator (SONICS, US) + dispersing agent	Compressive strength, Water absorption, and Acid-Sulphate attack	Compressive strength by increased by 36.23MPa as compared to control via addition of 0.1% rGO CMC. The incorporation of reduced graphene oxide is found to expedite the process of compactness enhancement, leading to alterations in various properties such as water absorption, carbonation, ultrasonic pulse velocity, fire resistance, and resistance to acid penetration.	(Prabavathy et al., 2020)
40	(0.02%), graphene oxide	Fly ash geopolymer, (w/b=0.35)	Branson digital sonifier + deionized water	Compressive strength, Durability properties	Overall, the 28-day compressive strength of fly ash geopolymer in this study was improved by 23% (from 33.6 MPa to 41.4 MPa) with GO admixed at 0.02% by mass of fly ash.	(Xu et al., 2018)

41	(0.02%, 0.2% and 4%) rGO, alumina and silica nanoparticles	Cement paste (w/b = 0.32)	Probe sonication + Polycarboxylic ether based superplasticizer at 0.05 wt%	Acid-sulphate attack, and Microstructure	The reduction in the amount of capillary pores (10 nm–10 µm) by up to 46% and 51% than the control paste. After 28 days in 0.5 M HNO ₃ solution, digital pictures, OM, X-ray CT, and SEM images helped define the degraded layer in the cementitious matrix.	(Muthu & Santhanam, 2018)
42	(0.5%, 1.0%, 2.0%, and 3.0%) nano-SiO ₂ (NS) and nano-Al ₂ O ₃ (NA)	Cement concrete (w/b = 0.5), Naphthalene superplasticizer.	ultrasonic dispersion + superplasticizer (different concentration)	Compressive strength, rapid chloride permeability and electrical resistivity test	The improvement of the flexural strength was mainly manifested in the early stage. NS after 3 days were 10.5%, 27.09%, 26.78% and 42.13%, respectively, with the increase of NS content from 0.5% to 3%. Introducing of 0.5%NS + 0.5%NA powders at 1% reduced capillary permeability coefficient of concrete samples compared to that of 0.5%NS and 0.5%NA samples.	(Zhang et al., 2021)

43	(0.05–0.1%) CNTs	Mortars with different w/c (0.35, 0.45, 0.5 and 0.55)	1.2% and 0.15% of Superplastic izer	Compressive, Flexural strength, Fracture energy, and Drying shrinkage	0.05–0.1%, effectively increased the flexural and compressive strengths at 28 days by 29% and 22%, respectively. CNTs significantly improved the mechanical strength and shrinkage at early ages, thereby increasing the hydration rate.	(Hawreen et al., 2018)
44	(0.2 and 0.23%)graphite	Cement paste (w/b = 0.4)	Surfactant	Compressive strength, Acid-sulphate attack, and Microstructure	The greatest increase was observed after 7 days of aging, which is equal to 28.66 %. Compressive strength loss induced by the G-S-Z mix is 251.72 % and 239.4% lower, respectively, then by reference paste. While it is 119.36% and 180% by G-S-P mix, respectively. The microstructure of samples immersed in acid solution confirmed the Ca(OH) ₂ phase was not visible in SEM images.	(Samimi & Zareechian , 2022)
45	(0.02 wt%, 0.05 wt % and 0.08 wt %) GO	Cement paste (w/b = 0.49)	Surfactant	Compressive Flexural and Dry shrinkage	AT 60 days, the application of GO at 0.02 wt%, 0.05 wt%, and 0.08 wt% increase of shrinkage strain by 1.99%, 5.79%, and 7.45%, respectively.	(Chen et al., 2020).

46	(1% and 2%,) nano-silica and Nano-alumina +Polypropylene fiber (PPF) added by 0.5 and 1%	Cement mortar	Mixer,+Super-plasticizer (Glenium 51)	Flexural strength , Drying Shrinkage, and Microstructure	<p>The flexural tensile strength of AAM containing PPF increases with curing time.</p> <p>PPF specimens have shown bonds between materials and fibre, and specimens with 1% NS and 1% PPF have the highest flexural strength at 90 days, 22.2 MPa.</p> <p>In SEM capture, nano-alumina expands capillary holes, strengthening the connection between reactive and pore spaces.</p> <p>Less expanded mortar contains 0.5% PPF and nanomaterials than specimens without PPF.</p>	(Dheyaaldin et al., 2022)
----	--	---------------	---------------------------------------	---	--	---------------------------

2.3 CONCLUSIONS DRAWN FROM LITERATURE REVIEW

Following a thorough review of the literature, it is clear that a substantial amount of study has been devoted to examining the use of carbon nanomaterials (CNMs) as reinforcement in cementitious nanocomposites (CNCMs). However, the main emphasis has been on using certain CNMs, such as graphene oxide (GO) or carbon nanotubes (CNTs), to improve the characteristics of CNCMs.

Extensive research literature provides substantial evidence on the benefits of incorporating GO or CNTs as reinforcing agents in cementitious matrixes at the nano-scale. However, this approach also presents certain limitations. For instance, the use of CNTs as reinforcement often leads to agglomeration, resulting in limited dispersion within the cement matrix. Similarly, GO tends to restack in alkaline cement solutions, hindering its full potential as a reinforcing material. Consequently, an alternative approach is urgently needed. One promising solution involves employing a hybrid combination of CNTs and GO, which offers a versatile three-dimensional network. This hybrid network harnesses the synergistic properties of CNMs, addressing the shortcomings of individual reinforcements and yielding superior results.

The hybridization of CNTs and GO offers a unique combination of desirable properties. By merging the superior mechanical characteristics of CNTs with the excellent dispersibility of GO, the resulting hybrid, known as (Hybrid carbon nanomaterials) HCNMs, exhibits enhanced dispersion. This improved dispersion is facilitated by the π - π stacking non-covalent interactions between CNTs and GO sheets, enabling stable dispersion in aqueous media. The three-dimensional hybrid structure of HCNMs presents several advantages, including a higher surface area, enhanced catalytic activity, and superior mechanical strength compared to individual GO or CNTs. Consequently, this study aims to investigate and compare the influence of CNMs and HCNMs on the physico-mechanical and physico-chemical properties of CNCMs.

To improve the dispersibility of GO and CNTs inside the cement matrix, researchers have often used a technique known as superplasticizer stabilization. To sterically stabilize the dispersions of these carbon nanomaterials, this method uses a variety of surfactants, air-entraining admixtures, and water reducers. According to the literature, polycarboxylate ether-based Superplasticizers (PCE-SP) have shown to be one of the most efficient anchors for enhancing the stabilization of CNM/HCNM dispersions out of all the choices investigated. On the performance of HCNMs in CNCMs under the

impact of PCE-SP stabilization, however, it is important to note that little study has been done in this area. When HCNMs are added to cement, as opposed to CNMs alone, it is anticipated that the cement's overall chemistry would alter. This shift may have a substantial effect on how well the finished nanocomposite performs.

There has been a lot of research on nanocomposites made with ordinary portland cement (OPC), but there hasn't been much done on cementitious nanocomposites made with portland pozzalona cement (PPC). This research void presents an opportunity to investigate an economically and environmentally sustainable approach. Using PPC-based nanocomposites could lower the costs of building projects and help reduce the amount of CO₂ that is released into the atmosphere when cement is made. In addition, conducting research into the impacts of pozzolanic materials, in conjunction with carbon nanomaterials such as GO and CNTs, may result in a better microstructure and an increased mechanical performance of the cementitious matrix.

The inclusion of carbon nanomaterials in combination with pozzolanic materials exhibits the potential for synergistic effects, resulting in improved secondary pozzolanic reactions. Therefore, this synergy refines the pore structure of the cementitious matrix, thereby increasing its overall physico-mechanical strength. To the best of our knowledge, no prior research has examined the effect of hybrid carbon nanomaterials (HCNMs) as reinforcing agents on the characteristics of PPC-based cementitious nanocomposites. These characteristics involve a broad variety of factors, such as the crystallization behaviour, mechanical strength, microstructure, durability, and electrical properties.

The use of waste materials provides a substantial benefit to mankind, as it provides a solution that is both cost-effective and helps offset the rising demand for Portland cement. This is an important advantage. This resource-wise utilization of waste materials lowers expenses while also promoting sustainable resource management. Taking into consideration the aforementioned concerns, the current research aims to investigate the impact of superplasticizer-stabilized CNMs and HCNMs on the physico-mechanical and physico-chemical properties PPC-based cementitious nanocomposites. Achieving improved dispersion and stability of CNMs/HCNMs is of utmost importance for their effective utilization in industrial applications of cementitious nanocomposites. Consequently, the focus of this comprehensive research investigation is to modify and manipulate cement chemistry at the nano-level, thereby offering a novel range of cementitious nanocomposites.

EXPERIMENTAL METHODOLOGY**3.1 GENERAL**

This chapter discusses in depth the experimental methodology employed in the experimental work. The experimental task was completed in the following seven steps:

Step I: Material Characterizations

Physical and chemical characteristics of the raw materials utilized in this study are determined in the first phase of the experimental technique. The materials are thoroughly analyzed before being utilized in experiments.

Step II: Preparation/ Functionalization of Carbon Nanomaterials (FCNMs)

This phase involves producing Graphene Oxide (GO) from Milled Graphite Powder (MGP) and functionalizing Multiwalled-Carbon Nanotubes. The synthesized carbon nanomaterials structural characterization has been explored.

Step III: Dispersion Studies of Carbon Nanomaterials (CNMs) and Hybrid Carbon Nanomaterials (HCNMs)

This stage includes dispersion investigations of specific carbon nanomaterials, such as GO or FMWCNTs, as well as Hybrid Carbon Nanomaterials (HCNMs), at various ratios and amplitudes of ultrasonication utilizing a probe sonicator. Following the application of superplasticizers (SPs) in order to stabilize GO and FMWCNTs, dispersion experiments were carried out.

Step IV: Preparation of CNMs/HCNMs based Cementitious Nanocomposites (CNMs/HCNMs-CNCMs)

In the fourth stage, the specifics of the cementitious nanocomposites (CNCMs) that include CNMs/HCNMs in a dosage of 0.0015% to 0.012% (by weight percentage of the cement) are outlined. In addition to this, for the purpose of comparison, control sample was also fabricated without aid of CNMs/HCNMs.

Step V: Determination of the Physico-Mechanical Strength of CNCMs

This stage involves assessing the compressive strength and tensile strength of CNCMs specimens at the curing ages of 7, 28, 56, and 90 days. It comprises information regarding the specimen size, apparatus, and the technique that was used to determine the physico-mechanical characteristics.

Step VI: Determination of Microstructural and Crystallization Studies of CNCMs

In this stage, the microstructural studies and the study of crystalline phase composition of the CNCMs are carried out with the assistance of a Field Emission-Scanning Electron Microscope (FE SEM) and Powdered X-Ray Diffraction (PXRD) analysis, respectively, at curing various curing ages of 7, 28, 56, and 90 days.

Step VII: Determination of Durability Studies of CNCMs

This step involves determining the electrical resistivity of CNCMs using the Werner Probe electrical resistivity method at 7, 28, 56, and 90 days after curing. Water absorption of CNCMs using the Capillary water absorption. It contains details regarding sample preparation and the instruments used for these two analyses. Whereas, the durability studies have been also conducted with acid/sulfate attack and water absorption of CNCMs at 28 and 90days of curing.

3.2 MATERIALS AND METHODOLOGY

As depicted in Figure 3.1, the study materials and methodology were organized and carried out according to the various phases depicted.

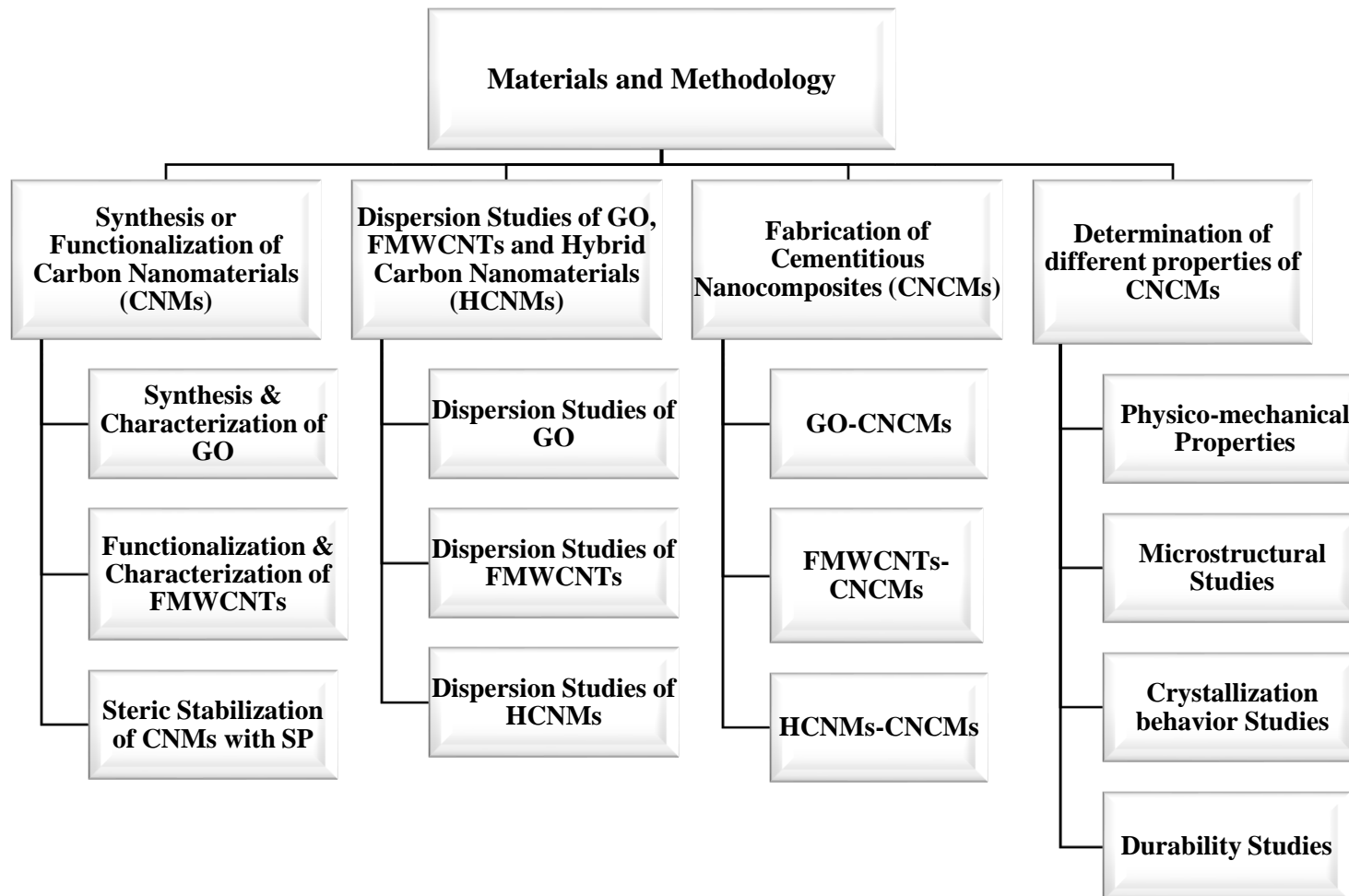


Figure 3.1 Details of the Materials and Methods Employed

3.2.1 Materials and Methodology used for Synthesis/Functionalization of Carbon Nanomaterials (CNMs)

Graphene oxide (GO) and functionalized multiwalled carbon nanotubes (FMWCNTs) were the major components of the carbon nanomaterials synthesized for this investigation. The materials used and the method of producing GO and functionalized FMWCNTs are as follows:

3.2.1.1 Materials and Methodology for Preparation of Graphene Oxide (GO)

(a) Raw Materials

Sigma-Aldrich Corp., India supplied ultrahigh purity graphite powder (GP) with a particle size of 100 microns. The Figure 3.2 shows a FE-SEM micrograph of the GP, showing the layered graphite sheets that comprise structure.

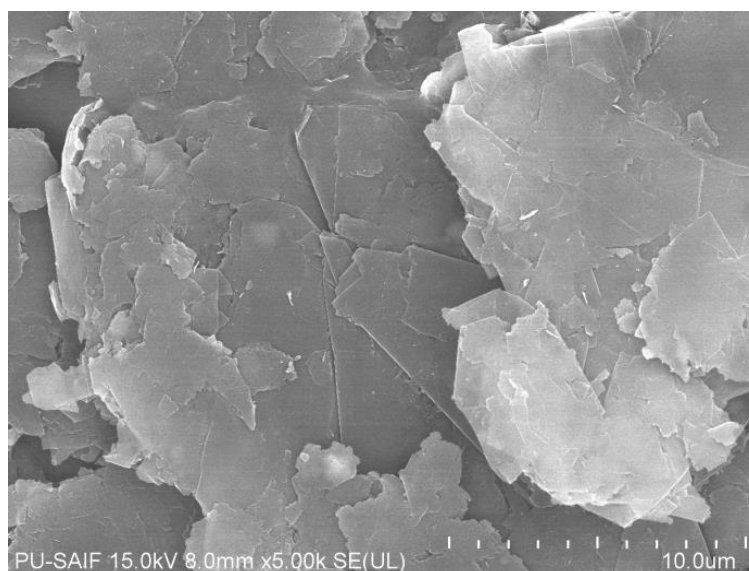


Figure 3.2 FE-SEM Image of Graphite Powder (GP)

(b) Materials and Chemicals

Loba Chemie Pvt. Ltd., located in India, was the supplier of the laboratory chemicals of analytical grade that were used in the production of GO. The chemical reagents used were sodium nitrate (NaNO_3), potassium permanganate (KMnO_4), sulfuric acid (H_2SO_4 , 98%), hydrogen peroxide (H_2O_2 , 30%).

(c) Equipment

Equipment used for the preparation of GO's a planetary ball milling machine (Retsch PM100), Hot Plate Magnetic Stirrer (Tarsons Products Pvt. Ltd., India), Ice Bath (Labco

Instruments, India), Thermometer, Conical Flask (Labco Instruments, India), Glass Rod (Labco Instruments, India), Vacuum Oven (Labco Instruments, India), and Hot Air Oven (Labco Instruments, India).

(d) Experimental Methodology for Graphene Oxide (GO) Preparation

Graphite powder (GP) was milled using a Retsch PM100 planetary ball mill. Milled graphite powder (MGP) was made by breaking down GP in a Retsch PM-100 planetary ball mill for 32 hours. Graphite powder was taken in the Jar, with 1:7 of graphite powder to the zirconia balls by weight (in dry medium). MGP was then surface functionalized with the aid of Modified Hummer's method (Hummers & Offeman, 1958). In a conical flask, 5 grams of graphite powder (GP) was combined with 114 grams of concentrated sulfuric acid (H_2SO_4 , 98%) and 2.5 grams of sodium nitrate (NaNO_3). After cooling the mixture for about two to three hours in an ice bath, 15 grams of potassium permanganate (KMnO_4) was added to the liquid in many separate batches. After that, the mixture undergoing the reaction was left to be stirred by a magnetic stirrer for another two to three hours until the reaction was finished. After that, the suspension was diluted with a total of 1000 ml of deionized water, and then 15 ml of hydrogen peroxide (H_2O_2) was added slowly to the solution. The resultant brilliant yellow suspension was subjected to centrifugation before being dried in a vacuum oven at temperatures between 35-40 °C.

(e) Characterization of Graphene oxide

Various characterization techniques were employed to analyze the characteristics of starting materials and their surface-functionalized counterparts, namely GO. The surface topography was visualized using a Field Emission-Scanning Electron Microscope (FE-SEM, NOVA Nanosem 450), while Energy Dispersive Spectroscopic analysis (EDS) provided information about the elemental compositions of the nanomaterials. For a more detailed examination of the surface morphology at higher resolution, Transmission Electron Microscopy (TEM, Tecnai G2 20 (FEI) S-Twin) was adopted. To investigate the functional group's introduction through the surface functionalization of MGP, Fourier Transform Infrared (FT-IR) spectroscopy was employed. The defect density and structural characteristics of graphene layers in both the raw and functionalized materials were assessed using the STR 500 Confocal Micro Raman spectrometer. Powder X-Ray Diffraction (PXRD) analysis, performed with the assistance of a PANalytical X'Pert PRO X-ray diffractometer, were used to evaluate the structure, crystallinity, and interplanar spacing. Finally, the thickness of GP, MGP, and

GO sheets was determined using Atomic Force Microscopy (AFM, Multimode Bruker Atomic Force Microscope) in tapping mode.

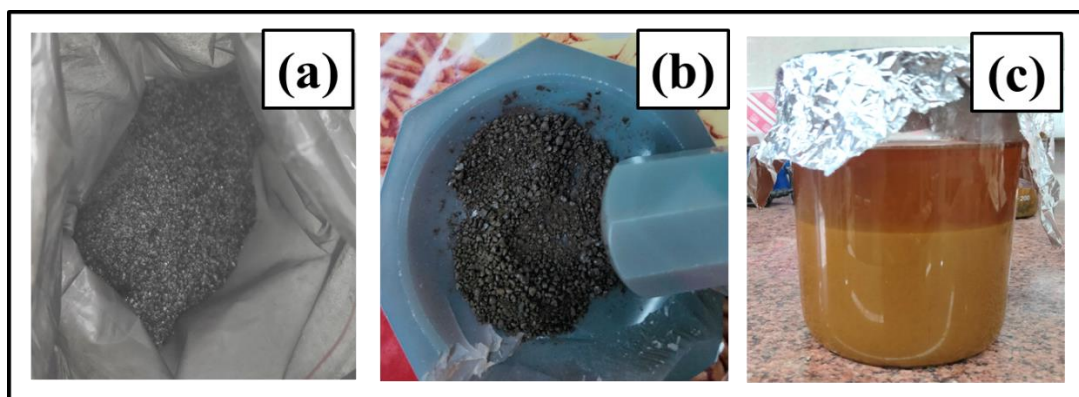


Figure 3.3 (a) Graphite Powder (GP) (b) Ball-milled Graphite Powder (MGP) (c) Graphene Oxide (GO)

3.2.1.2 Materials and Methodology for Multiwalled Carbon Nanotubes (MWCNTs)

(a) Preparation of MWCNTs

Chemical Vapour Deposition (CVD) was chosen as the approach for the indigenously synthesis of multiwall carbon nanotubes (MWCNTs). It is the most appropriate approach for the large-scale synthesis of MWCNTs. In CVD, the decomposition of hydrocarbon occurs in the presence of suitable d-block element catalysts, such as Ni, Co, or Fe. It is more cost-effective and adaptable when producing large quantities of MWCNTs. Once The hydrocarbon vapour travels via a quartz tube located beneath the high-temperature furnace zone. The temperature of the reaction zone was kept constant at 750 °C. At lower temperatures, it is necessary to use nano-sized metal particles in order to break down hydrocarbon. In general, the size of the carbon nanotube is determined by the size of the organometallic complex. The MWCNTs were generated at National Physical Laboratory New Delhi (India). FE-SEM provided in Figure 3.4., observed the multiwalled tubular like structure(Pathak et al., 2016; Sharma et al., 2019; Sharma, Pathak, et al., 2018).

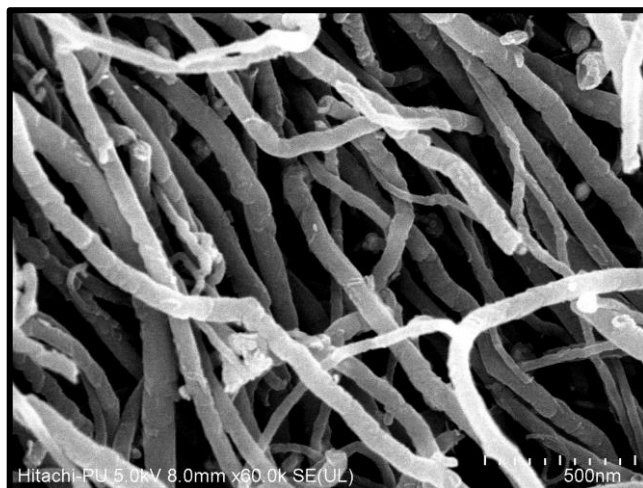


Figure 3.4 FE-SEM Image of Multi-Walled Carbon Nanotubes (MWCNTs)

(b) Chemicals and Reagents Used

Chemicals of analytical grade for the functionalization of FMWCNTs were brought from Loba Chemie Pvt. Ltd., India. The chemical reagent used was nitric acid (HNO_3 , 69%).

(c) Equipment

Equipment used for the functionalization of MWCNTs were Hot Plate Magnetic Stirrer (Tarsons Products Pvt. Ltd., India), Thermometer, Round Bottom Flask (Labco Instruments, India), Reflux Condensor (Labco Instruments, India), Glass Rod (Labco Instruments, India), Vacuum Oven (Labco Instruments, India) and Hot Air Oven (Labco Instruments, India).

(d) Experimental Methodology for Functionalization of Multiwalled Carbon Nanotubes (FMWCNTs)

In order to surface functionalize multi-walled carbon nanotubes (MWCNTs), a treatment with nitric acid was carried out. A solution was prepared by combining 69% concentrated nitric acid (HNO_3) with 5 grams of MWCNTs in a round bottom flask (RBF), resulting in a final volume of 420 ml. After having been refluxed at 80°C for ten to twelve hours, then the 800 -1000 ml of water (distilled) added to it for dilution purpose. After that, the suspension of functionalized multiwalled carbon nanotubes (FMWCNTs) was centrifuged, and then rinsed with deionized water until any and all traces of acid were eliminated entirely. After being dried in an oven, the FMWCNTs were put into a desiccator so that they may be used at a later time.

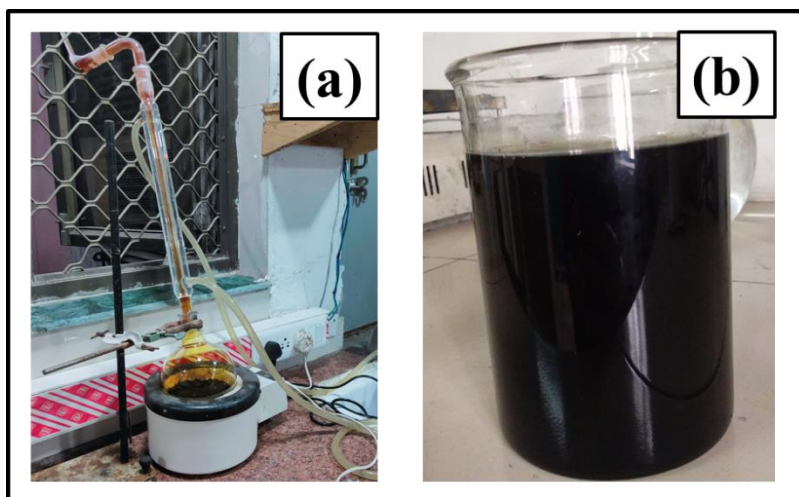


Figure 3.5 (a) Set-up for Functionalization of MWCNTs (b) FMWCNTs

(e) Characterization of FMWCNTs

The techniques used for the characterization of the MWCNTs and FMWCNTs were similar to those for GO. The characterization tools used were Fourier Transform Infrared Spectroscopy (FT-IR, Perkin Elmer RXI spectrophotometer), Field- Emission Scanning Electron Microscopy (FE-SEM, NOVA Nanosem 450) assemble with energy dispersive spectroscopy (EDS), Transmission Electron Microscopy (TEM, Tecnai G² 20 (FEI) S-Twin), Raman Spectroscopy (STR 500 Confocal Micro Raman Spectrometer), and Powdered X-Ray Diffraction (PXRD, X'Pert PRO X-ray Diffractometer).

3.2.2 Steric Stabilization of Carbon Nanomaterials (CNMs) using Superplasticizers (SP) and their Dispersion Studies

(a) Raw Materials

Graphene oxide (GO) and functionalized multiwalled carbon nanotubes (FMWCNTs) were used as a raw material for their steric stabilization using superplasticizers (SP).

(b) Chemicals and Reagents Used

SP was used for the steric stabilization of the carbon nanomaterials (FMWCNTs and GO).

(c) Equipment

Equipment used were Probe sonicator (VCX-750W, Sonics & Materials Inc, USA), UV-Visible Spectrophotometer (Agilent Pro), Hot plate magnetic stirrer (Tarsons

Products Pvt. Ltd., India), Beaker (Labco Instruments, India) and Measuring cylinder (Labco Instruments, India).

(d) Experimental Methodology

Steric stabilization of CNMs was done with the help of SP. The aqueous medium has been observed to facilitate effective dispersion of GO and FMWCNTs. The charged ions found, namely Ca^{2+} , Mg^{2+} , Na^+ , and OH^- , in the alkaline cement pore solution has been observed to result in the agglomeration of GO and FMWCNTs. Consequently, this has a noteworthy influence on their capacity to disperse. The optimal approach to address this issue involves the utilization of superplasticizer-based stabilization, whereby the oxygen functionalities of both graphene oxide (GO) and FMWCNTs undergo a chemical reaction with the $-\text{COOH}$ groups located on the main chain of superplasticizers (SP).

All dispersion processes have been carried out with the help of an Ultra-probe sonicator (Pci Analytical PKS-900F) with a diameter of the tip of the probe is 10 mm. The probe sonicator run with different ultrasonic power (in %) as 15, 20, 25, and 30. The sonicated solution was further subjected to a UV-Visible spectrophotometer (UV-1800 240V). The spectra take in the range of 250 to 700nm.

3.2.3 Materials and Methodology for Fabrication of Control samples and CNMs/HCNMs based CNCMs

3.2.3.1 Raw Materials

(a) Carbon Nanomaterials and Hybrid Carbon Nanomaterials (CNMs/HCNMs)

As raw materials for the creation of the Control samples and CNMs/HCNMs based CNCMs the superplasticizer stabilised carbon nanomaterials, i.e., GO, FMWCNTs, and HCNMs, were employed.

(b) Binder (Pozzolana Portland Cement)

Binder material used for the casting of cementitious nanocomposites were Pozzolana Portland Cement (PPC). All mixes were prepared by 350 m²/kg (Specific Surface Blaine) PPC. As per IS1489:2015, 15–35% fly ash shall be present in PPC procured from Shree Cement Ltd., India. The FE-SEM images of Cement in the anhydrous state are given in Figure 3.6.

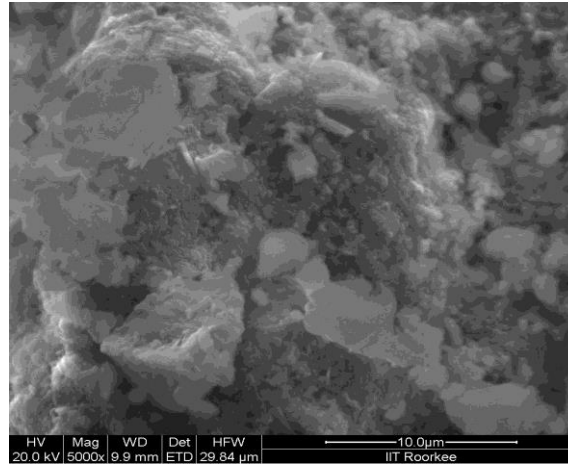


Figure 3.6 FE-SEM Images of Cement

X-Ray Fluorescence (XRF) was used to investigate the chemical composition of cement is given in Table 3.1.

Table 3.1 Oxide Analysis of Cement

Oxides	SiO ₂	Al ₂ O ₃	Fe ₂ O ₃	CaO	MgO	SO ₃	LOI
PPC (%)	29.25	8.52	5.26	42.5	1.85	2.62	3.52

(c) Indian Standard Sand

Indian standard sand, according to IS 650:1991, is available in three grades: Grade I, Grade II, and Grade III. Three sand grades were employed in an equal amount (33.33% of each grade) to fabricate cement mortar nanocomposites. Table 3.2 depicts the distribution by particle size, extent of their use and other specifications for the three categories of grades.

Table 3.2 General Specifications of Sand

Sands Grade	Grade I st	Grade II nd	Grade III rd
Type	Coarse	Medium	Fine
Particle size (mm)	2.45 to 1.18	1.18 to 0.600	≤0.600
Extent used (%)	33.33	33.33	33.33

(c) Superplasticizer (SP)

The SP was acquired from BASF India Ltd. The utilization of SP was implemented to enhance the workability of the cement mortar paste, while also providing steric stabilization to the carbon nanomaterials within both the aqueous medium and the alkaline cement matrix(Lv et al., 2014; Lu et al., 2017; Zhao et al., 2017).

(e) Water

Throughout the study, potable water was utilized for the casting of both the control and CNCMs specimen.

3.2.3.2 Equipment

The Hydraulic & Engineering Instruments (HEICO, India) cubic moulds of dimensions (70.6 mm × 70.6 mm × 70.6 mm) were used to fabricate the standard-compliant cubic specimen. The vibration table and curing tank were also bought from HEICO, India. The vibration table was used to compact the samples of cubic mortar, and the curing tank was used to cure the samples in water.

3.2.3.3 Experimental Methodology for Fabrication of Mortar Samples

The current investigation involved the preparation of a total of 13 mix designs of cementitious nanocomposites (i.e., Control, GO-CNCMs, FMWCNTs-CNCMs and HCNMs-CNCMs) as shown in Table 3.4 and were further tested following various test procedures. GO, FMWCNTs and HCNMs were incorporated in the CNCMs in the dosages of 0.0015%, 0.003%, 0.006%, and 0.012%, for each mix. Control (cement) sample comprised of 100% cement (along with sand) without any carbon nanomaterial additives. The CNCMs contained 12 mix designs each, with superplasticizer stabilized GO, FMWCNTs and HCNMs in the dosages ranging from 0.0015% to 0.012% (by the weight percentage of cement). The HCNMs dispersions were prepared by dispersing GO and FMWCNTs in ratio 4:1 in the SP at 30% sonication amplitude. All mixes were prepared at different concentrations of CNMs in PPC mortars (CNCMs), as mentioned in Table 3.3. To fabricate the CNCMs, the sand and cement were mixed in a ratio of 3:1. A planetary mixture was used to obtain the homogeneous mixture. The Vicat apparatus was used for the determination of the water-to-cement ratio, i.e., 0.42. The ultra probe sonicator (Pci Analytical PKS-750F) was adopted for the dispersion of CNMs in SP solution. SP-stabilised GO and FMWCNTs were added in an appropriate percentage to cementitious mortars. Then the fresh mortar with dispersed carbon nanomaterial mixtures was poured into a cube (70.6 mm × 70.6 mm × 70.6 mm) as shown in Figure 3.7 (a), and the compaction was done by using a vibrating table as shown in Figure 3.7 (b). All the sample then place in a curing tank at 27°C±5°C after demoulding. Four curing days were considered: 7, 28, 56, and 90 days. The pictorial images of demolded cubes and water tank used for curing has been shown in Figure 3.8. Figure

3.8(a) presents the pictorial view of cubic mortar samples demolded from the cubic mold after the time period of 24 hours and Figure 3.8(b) depicts the water curing tank.



Figure 3.7(a)Standard Cubic Mould (70.6 mm × 70.6 mm × 70.6 mm) (b) Vibration Table

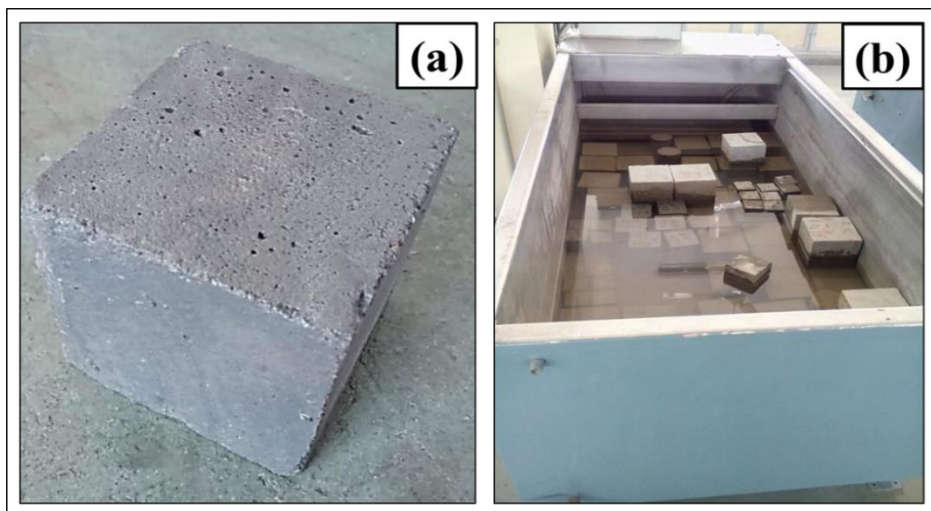


Figure 3.8(a) Demolded Cubic Specimen after 24 Hours of Molding (b) Curing Tank with Standard Temperature Regulator

Table 3.3 Mix Designs for CNCMs

*Superplasticizer; SP, CNMs and HCNMs were taken by weight percentage of cement

<i>Mix</i>	<i>Sand (g)</i>	<i>Cement (g)</i>	<i>GO</i>	<i>FMWCNTs</i>	<i>SP</i>	<i>Ratio w/b</i>
<i>Control</i>	600	200	-	-	0.2	0.42
<i>0.0015% GO-CNCMs</i>	600	200	0.0015	-	0.2	0.42
<i>0.003% GO-CNCMs</i>	600	200	0.003	-	0.2	0.42
<i>0.006% GO-CNCMs</i>	600	200	0.006	-	0.2	0.42
<i>0.012% GO-CNCMs</i>	600	200	0.012	-	0.2	0.42
<i>0.0015% FMWCNTs-CNCMs</i>	600	200	-	0.0015	0.2	0.42
<i>0.003% FMWCNTs-CNCMs</i>	600	200	-	0.003	0.2	0.42
<i>0.006% FMWCNTs-CNCMs</i>	600	200	-	0.006	0.2	0.42
<i>0.012% FMWCNTs-CNCMs</i>	600	200	-	0.012	0.2	0.42
<i>0.0015% HCNMs-CNCMs</i>	600	200	0.0012	0.0003	0.2	0.42
<i>0.003% HCNMs-CNCMs</i>	600	200	0.0024	0.0006	0.2	0.42
<i>0.006% HCNMs-CNCMs</i>	600	200	0.0048	0.0012	0.2	0.42
<i>0.012% HCNMs-CNCMs</i>	600	200	0.0096	0.0024	0.2	0.42

3.2.4. Materials and Methodology for Determination of Physico-Chemical Behavior of Control samples and CNMs/HCNMs based CNCMs

The determination of various physico-chemical properties included the evaluation of compressive strength, tensile strength, microstructural and crystalline studies, electrical resistivity and durability studies. The detailed materials and methodology used for determination of above-mentioned properties has been discussed below.

The information pertaining to specimen dimensions and curing time period opted for determination of various physico-mechanical and physico-chemical properties is shown in Table 3.4.

Table 3.4 Test Procedures, Specimen Details and Curing Time for CNCMs

S. No	Test Procedure	Specimen Details	Curing Time (days)
1	Compressive Strength	Cube, 70.6 x 70.6 x 70.6 mm	7, 28, 56, 90 days
2	Split Tensile Strength	Cube, 70.6 x 70.6 x 70.6 mm	7, 28, 56, 90 days
3	Microstructural Studies	Semi-solid samples	7, 28, 56, 90 days
4	Crystalline Behavior Studies	Powder samples	7, 28, 56, 90 days
5	Electrical Resistivity Studies	Cylinder, 100 x 200 mm	7, 28, 56, 90 days
6	Water Absorption	Cylinder, 100 x 50 mm	Till saturation
7	Dry Shrinkage	Bar, 25 mm × 25 mm × 285 mm	Till Saturation
8	Acid-Sulfate Attack	Cube, 70.6 mm x 70.6 mm x 70.6 mm	56, 90 days

3.2.4.1 Materials and Methodology for Determining Compressive Strength and Tensile Strength of Control Samples and CNMs/HCNMs based CNCMs

(a) Raw Materials

The compressive and tensile strengths of control and CNCMs mortar samples were measured using cubic specimens with dimensions of 70.6 x 70.6 x 70.6 mm.

(b) Equipment

The compressive and tensile strengths of the control and CNCMs samples were assessed using a Universal Testing Machine (UTM) with a 200-ton capacity (Model No. HC 44.95, Heico Hydraulic & Engineering Instruments, India Ltd.).

(c) Experimental Methodology

The Universal Testing Machine (UTM) with a capacity of 200 tonnes (Model no. HC 44.95, Heico Hydraulic & Engineering Instruments, India Ltd.) was used to test the compressive strength and tensile strength of the cubic mortars as illustrated in Figure 3.9. At cure ages of 7, 28, 56, and 90 days, respectively, the surface-dried cubic specimen measuring 70.6 mm x 70.6 mm x 70.6 mm was evaluated for compressive strength and tensile strength in accordance with IS 4031 (Part 6)-1988 and IS 5816-1999. The cubic specimen was subjected to a rising force of 3.5 kN/s and 0.5 kN/s, until the sample failed in the compressive strength and split tensile strength tests respectively. To reduce the inaccuracy, the physico-mechanical strength values for three specimens were determined, and the mean value was used as the strength indicator.



Figure 3.9 Compression Testing Machine (HC 44.95, Heico)

3.2.4.2 Materials and Methodology for Microstructural Studies of Control Samples and CNMs/HCNMs based CNCMs

(a) Raw Materials

After compressive strength testing, the shattered pieces from the cubic specimens were removed and used for the microstructural examination of the control and CNCMs samples.

(b) Equipment

The control and CNCMs samples were subjected to microstructural analysis using a field emission scanning electron microscope (Nova Nano FE-SEM 450), as depicted in Figure 3.10.

(c) Experimental Methodology

A Field Emission-Scanning Electron Microscope (Nova Nano FE-SEM 450) was used to better investigate the microstructure of the hydration products inside the cubic mortars. Samples from cracked mortar cubes that had undergone compressive strength testing at curing ages of 7, 28, 56, and 90 days were used for the analysis. Each sample obtained gold coating by sputtering before the FE-SEM investigation, while a copper stub was firmly attached to it using carbon tape.

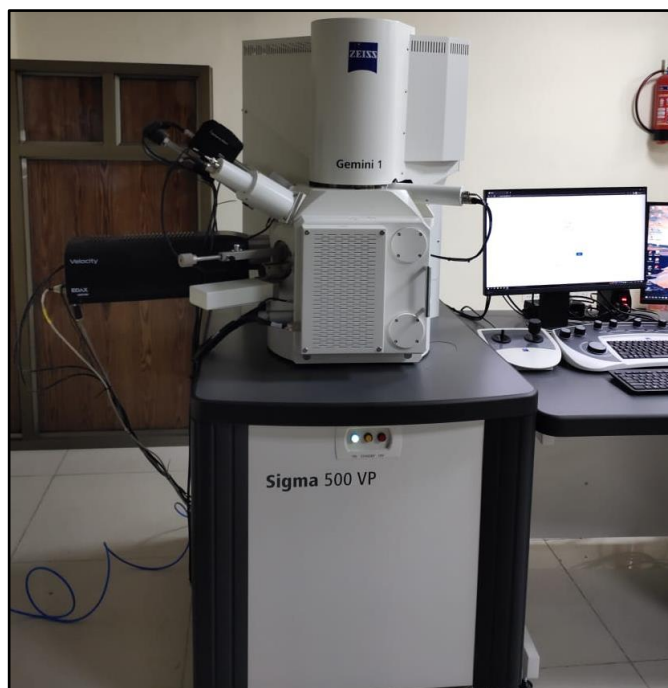


Figure 3.10 Pictorial View of Field Emission-Scanning Electron Microscope (FE-SEM)

3.2.4.3 Materials and Methodology for Determining Crystalline Behavior of Control samples and CNMs/HCNMs based CNCMs

(a) Raw Materials

The crystalline phase composition of the control and CNCMs samples was examined using the powdered samples from cubic specimens that were obtained following compressive strength testing.

(b) Equipment

X-Ray Diffractometer (PANalytical X'Pert PRO) (Figure 3.11.) was used for the analysis of crystalline phase composition of control and CNCMs samples.

(c) Experimental Methodology

X-ray diffraction (PXRD) analyses were conducted on cementitious nanocomposites (CNCMs) including carbon nanomaterials (CNMs) and hybrid carbon nanomaterials (HCNMs) that had been modified using a superplasticizer. The purpose of these analyses was to examine the impact of the modified carbon nanomaterials on the qualitative and quantitative mineralogical compositions of the cementitious nanocomposites after a 90-day curing period. The PXRD patterns were obtained using a PANalytical X'Pert PRO X-Ray Diffractometer equipped with Cu K α irradiation ($\lambda = 1.54 \text{ \AA}$), operating at 40 mA and 45 kV. The sample were initially pulverized into a fine powder using a pestle and mortar.



Figure 3.11 Pictorial View of Powder X-Ray Diffractometer (PXRD)

3.2.4.4 Materials and Methodology for Determining the Electrical Resistivity of Control samples and CNMs/HCNMs based CNCMs

(a) Raw Materials

The cuboidal shaped specimens with dimensions approximately Cylinder, 100 x 200 mm were used for the electrical resistivity test.

(b) Equipment

ResiPod Proceq instrument was used for the analysis of electrical resistivity of the control and CNCMs samples.

(c) Experimental Methodology

Electrical resistivity of the CNCMs was tested with cylindrical specimens of dimensions 100 mm × 200 mm by using Wenner's four probe method at the curing ages of 7, 28, 56. and 90 days. Electrical resistivity has been used as a measurement for the density of mortar composites, with a greater resistance indicating a denser microstructure. The samples prior testing was oven dried to remove the excess moisture entrapped. Electrical resistivity measurements were carried out using the four-point probe Wenner technique, illustrated in Figure 3.12. This method assesses the electrical resistivity of a structure or test body's surface. In accordance with the Wenner method, four equally-spaced electrodes are positioned on the mortar surface. An alternating current I (in Amperes) is passed through the outer two electrodes, while the voltage V (in Volts) is measured across the inner two electrodes. The apparent resistivity ρ_a (in $k\Omega \cdot cm$) is then calculated using Ohm's law, as shown in Equation (3.1).

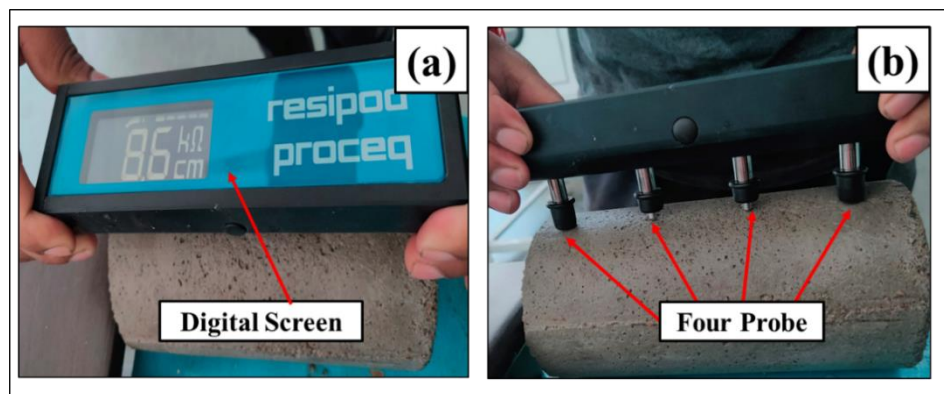


Figure 3.12 Set-up for Electrical Resistivity Measurement of Mortar Samples (a) Top view (b) Side view

The electrical resistivity was subsequently determined using the provided equation

$$\rho = R \cdot A / l \text{ K-ohm-cm} \quad (3.1)$$

where R stands for electrical resistance in ohms (Ω) and A is space between the probe in cm^2 .

RESULTS AND DISCUSSION

4.1 GENERAL

The primary goal of this study to stabilized superplasticizer stabilized Carbon Nanomaterials (CNMs) and Hybrid Carbon Nanomaterials (HCNMs) and investigate their effects on the physicochemical properties of cementitious nanocomposites (CNCMs). To improve dispersion in the cement pore solution, SPs was employed to sterically stabilize the CNMs and HCNMs. A detailed experimental approach was discussed in Chapter 3 to achieve the objectives of the current study, as shown in Chapter 1. This chapter is organized into four sections that comprise all of the results collected from the current investigation and their discussion in a systematic manner. Figure 4.1 shows the general outline of the results and discussion.

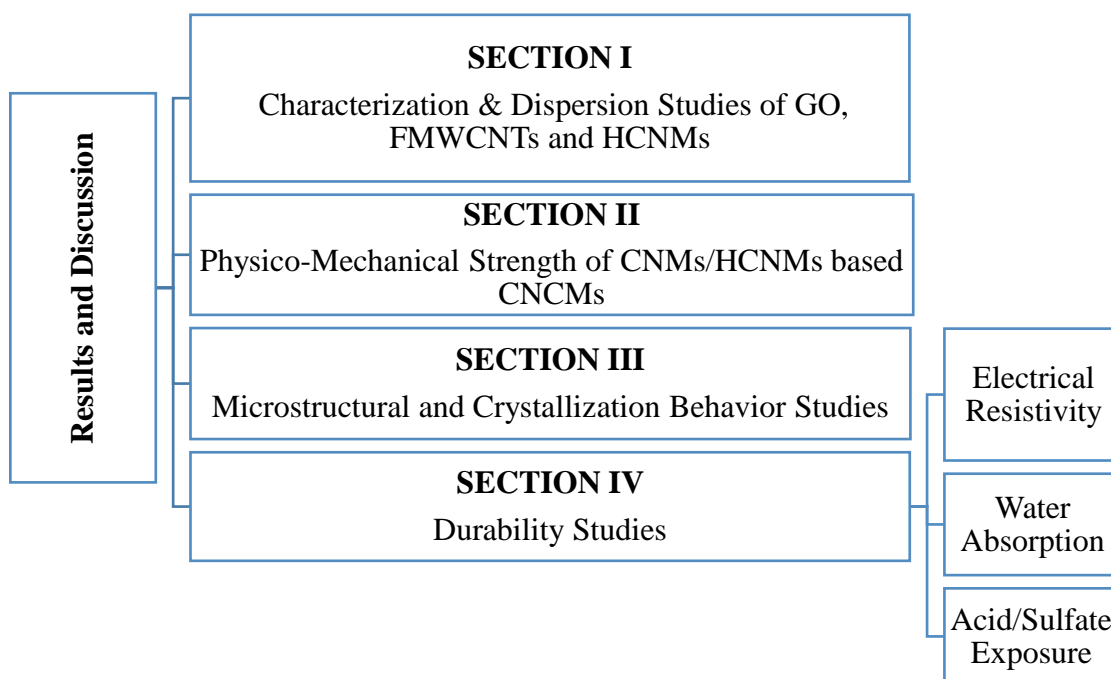


Figure 4.1 Schematic Representation of Results and Discussion

CHARACTERIZATION AND DISPERSION STUDIES

This section presents the detailed results of structural characterization of carbon nanomaterials as well as dispersion studies.

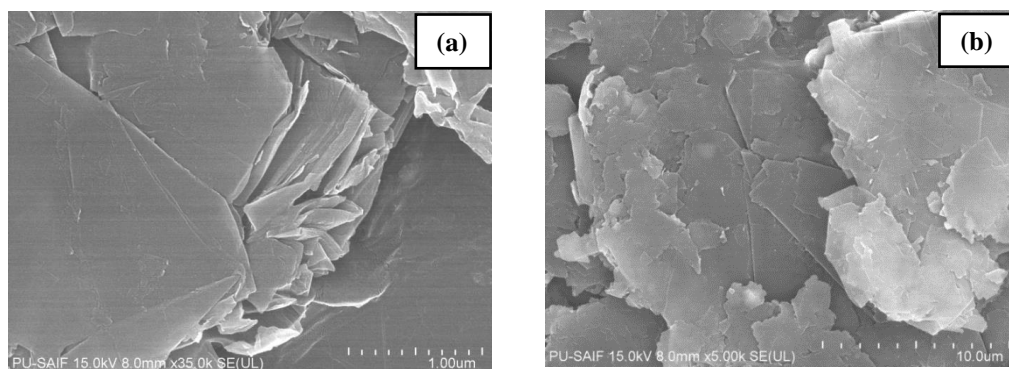
4.2 STRUCTURAL CHARACTERIZATION OF CARBON NANOMATERIALS

4.2.1 Structural Characterization of Graphite powder (GP) and Graphene Oxide (GO)

4.2.1.1 Results of FE-SEM Analysis of GP, MGP, and Graphene Oxide (GO)

Figure 4.2(a) depicts the FE-SEM micrograph of GP, while Figure 4.2(b) shows the micrograph of MGP. Additionally, Figure 4.2(c) displays the micrograph of GO.

In Figure 4.2(a), the flaky nature of GP is evident, displaying a continuous stacked sheets together morphology. Moreover, in terms of MGP as shown in Figure 4.2(b), the large sheets have undergone fragmentation due to mechanical milling. This process has resulted in the exfoliation of the graphite into smaller layers, as also confirmed by the FT-IR results mentioned in subsection 4.2.1.5. Figure 4.2(c) presents the micrograph of GO, where effectively-exfoliated corrugated graphene sheets are observed. The observed phenomenon can be ascribed to the existence of oxygen functions on the graphene sheets, resulting in the formation of a three-dimensional interconnected structure that bears resemblance to loosely stacked sheets with a sponge-like morphology.



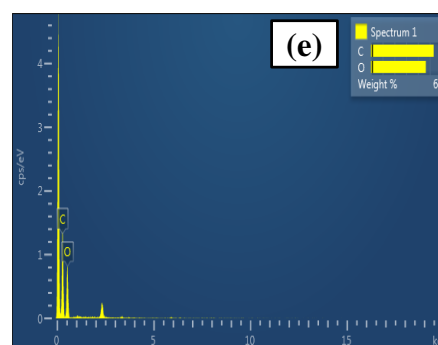
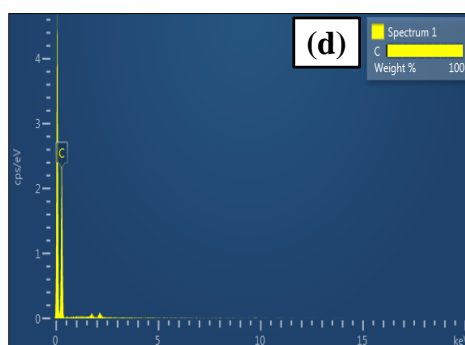
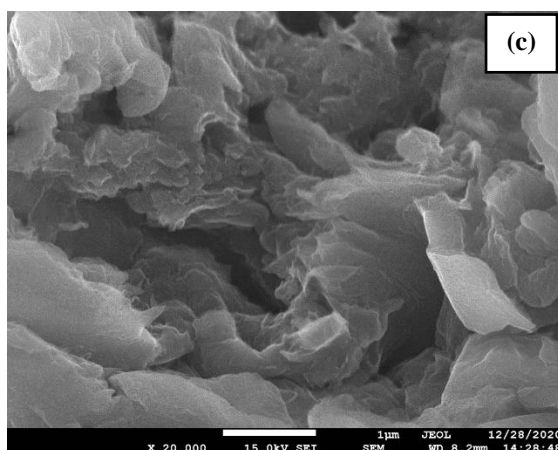


Figure 4.2 FE-SEM Images of (a) GP (b) MGP (c) GO, EDX Patterns of (d) MGP and (e) GO

The elemental compositions of Graphite Powder (GP) and Graphene Oxide (GO) are depicted in Figure 4.2(d) and 4.2(e) through the use of EDX patterns. The study of these patterns shows the presence of oxygen that comes from functionalization. This confirms that the GO sample has functional groups that contain oxygen, such as -OH, -COOH, -SO₃H, and -O-. Table 4.1 displays the atomic percentages of the elemental compositions for both GP and GO samples.

Table 4.1 Elemental Compositions of MGP and GO

S. No.	Element	Elemental Composition in Percentage (%)	
		MGP	GO
1	Carbon	100	60.35
2	Oxygen	0.00	39.65

4.2.1.2 Results of HR-TEM Analysis of MGP and GO

The surface morphology of MGP, and GO are observed in Figure 4.3 (a), and 4.3 (b), respectively, using HR-TEM. The TEM image of the MGP reveals the presence of substantial, multi-layered graphite sheets arranged in a stacked configuration, exhibiting a lack of discernible wrinkling or folding within the sheets. Also, provides a visual

representation of mechanically fragmented and corrugated sheets observed in MGP. Figure 4.3(b) displays the folded texture and wrinkled surface of GO sheets following the functionalization of MGP. The transparency reveals that the TEM image of GO sheets exhibits a distinct characteristic of being composed of multiple layers of graphene, in contrast to MGP.

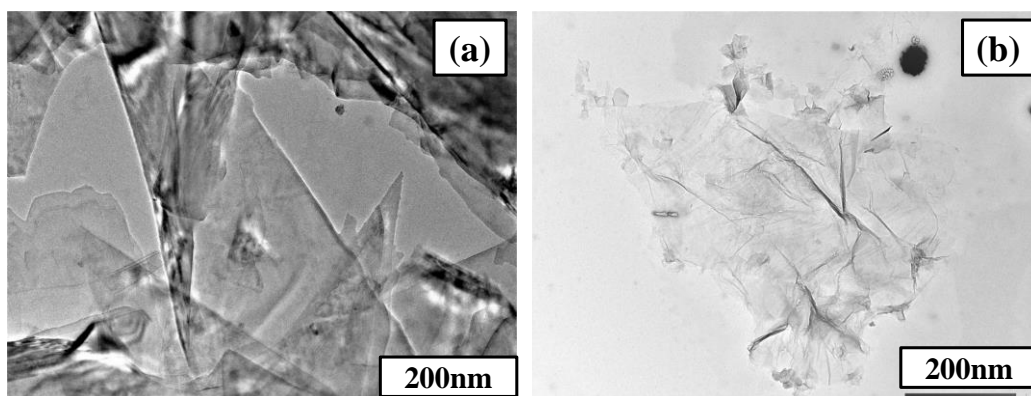


Figure 4.3 HR-TEM Images of (a) MGP (b) GO

4.2.1.3 Results of Raman Spectroscopy Analysis of MGP and GO

The study employed a Micro Raman spectrometer (STR 500 Confocal) to examine the structural characteristics and level of disorder in both the pure nanomaterials and their functionalized derivatives.

Raman spectroscopy was used to assess the defect density of raw and functionalized materials. Figure 4.4 illustrates the Raman shifts observed for MGP and GO. In the case of MGP, the G-band was observed at a wavenumber of 1584 cm^{-1} , whereas a lower wavenumber D-band was detected at 1350 cm^{-1} , suggesting the absence of defects in the graphite material. The utilization of the I_D/I_G intensity ratio is a common practice in assessing the stacking characteristics of materials. GO has a higher D-band intensity than MGP due to structural defects generated by the oxidation process, increasing the I_D/I_G ratio from 0.12 to an increased value 0.9 (Dash et al., 2016; Kaur & Kothiyal, 2019b; Xing et al., 2013). When GO is subjected to a conversion process, the sp^2 carbon atoms inside the graphene lattice are transformed into disordered sp^3 carbon atoms, leading to an increase in the intensity of the D-band. This rise in intensity indicates a reduction in the structural integrity of the graphitic carbon lattice. Therefore, an I_D/I_G ratio of 0.9 signifies a significant level of disorder and exfoliation resulting from the bonding of oxygen functions onto the graphene sheets.

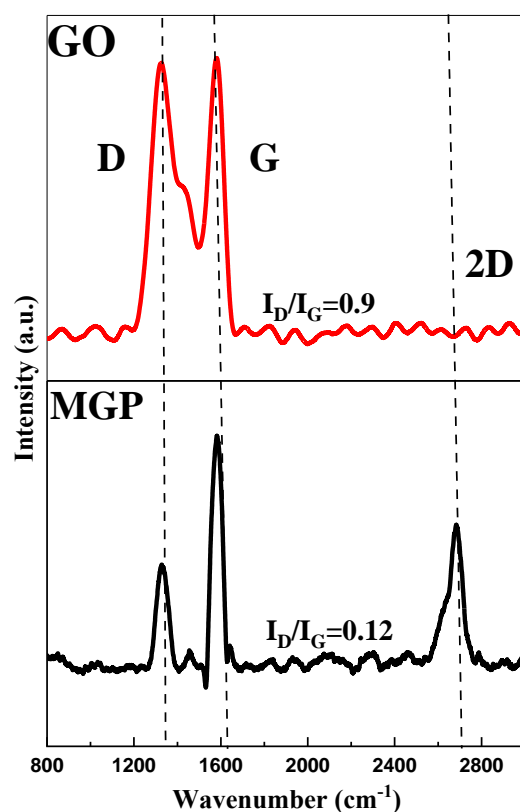


Figure 4.4 Raman Spectra of MGP and GO

4.2.1.4 Results of PXRD Analysis of MGP and GO

Figure 4.5 depicts the PXRD patterns for milled MGP, and GO. A prominent diffraction peak arises 2θ at 26.52° for MGP, corresponding to an interlayer spacing of 0.35 nm. The peak for GO shifted to the left at 2θ at 10.29° indicating an increased interlayer separation of 0.85 nm between the graphitic sheets shows the insertion of oxygenation groups on the surface of graphene sheets (Subrahmanyam et al., 2008).

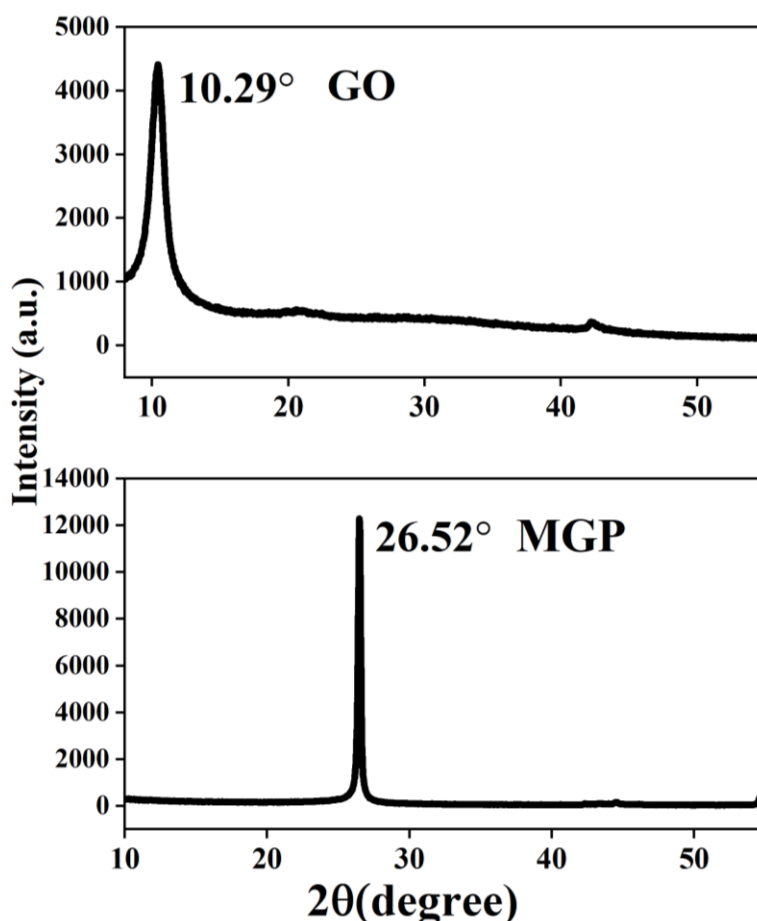


Figure 4.5 XRD Patterns of MGP, and GO

4.2.1.5 Results of FTIR Analysis of MGP and GO

Fourier-transform infrared (FT-IR) spectra were acquired by a Nicolet 5DXC FT-IR spectrometer in the range of 4000-500 cm^{-1} . After correcting for the background, the spectra were produced by averaging 10 scans with a resolution of 1 cm^{-1} . The FT-IR spectra of GO showed a strong peak at 3409 cm^{-1} (O-H stretching), indicating the presence of alcohol or carboxylic groups on the graphitic structure. The low abundance peak at 2921 cm^{-1} was caused by the asymmetric stretching of the C-H bond, whereas the peak at 1223 cm^{-1} exhibits epoxy group C-O stretching and the alkoxy group C-O stretching vibration appeared at 1050 cm^{-1} . The carbonyl C=O stretching vibration causes the peak at 1725 cm^{-1} , as shown in Figure 4.6. Additionally, a peak at 1632 cm^{-1} depicts the C=C stretching vibration of the non-oxidized graphitic domain. These spectra clearly show that oxidation of the graphite precursor resulted in graphite surface functionalization.

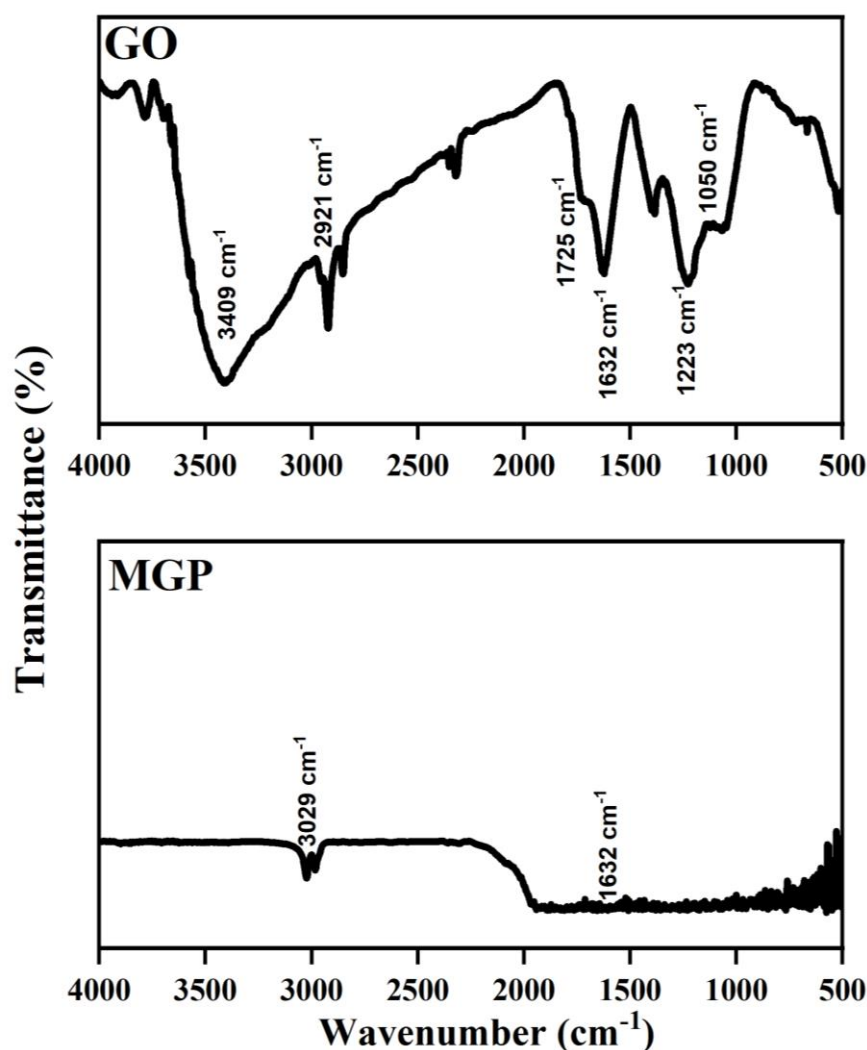


Figure 4.6 FTIR Analysis of MGP, and GO

4.2.2 Structural Characterization of MWCNTs and FMWCNTs

4.2.2.1 Results of FE-SEM Analysis of MWCNTs and FMWCNTs

Figure 4.7 (a) and (b) are observed FE-SEM of both pure and functionalized multiwalled carbon nanotubes. The MWCNTs have been shown a group of clumped nanotubes. The only difference was seen that FMWCNTs shows defects on the edges as well as on walls when the surface was modified. In subsection 4.2.2.4, Raman Spectroscopy was employed to investigate the presence of surface roughness in the in-plane sp^2 lattice of graphitic sheets in FMWCNTs. This was indicated by an increased I_D/I_G ratio, as demonstrated in the analysis.

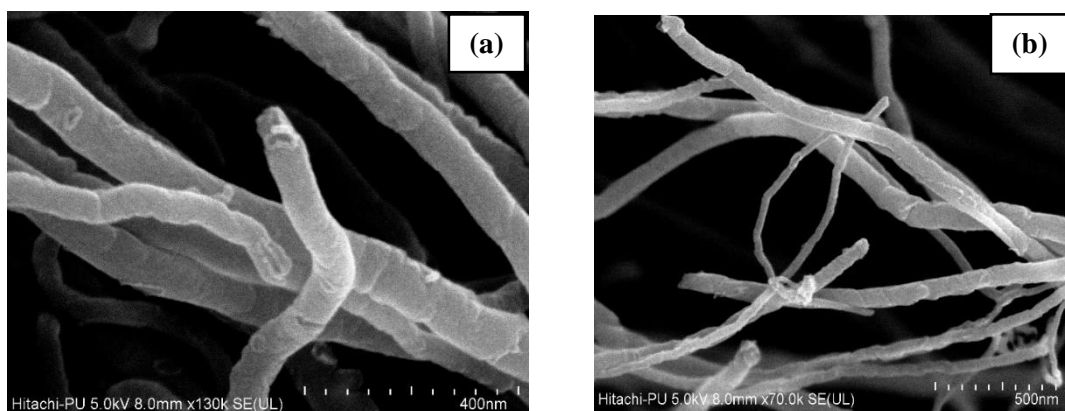


Figure 4.7 FE-SEM Images of (a) MWCNTs (b) FMWCNTs

The elemental characterization of pure and functionalized multiwalled carbon nanotubes (FMWCNTs) are depicted in Figure 4.8 using Energy Dispersive X-ray Spectroscopy (EDX) patterns. The examination of these patterns demonstrates the integration of oxygen through the addition of functional groups, specifically -COOH groups, which suggests the effective functionalization of multiwalled carbon nanotubes (FMWCNTs) via acid treatment. This discovery provides confirmation of the successful implementation of the functionalization process on the MWCNTs. The elemental compositions of MWCNTs and FMWCNTs samples (in percentages) have been depicted in tabular form in Table 4.2.

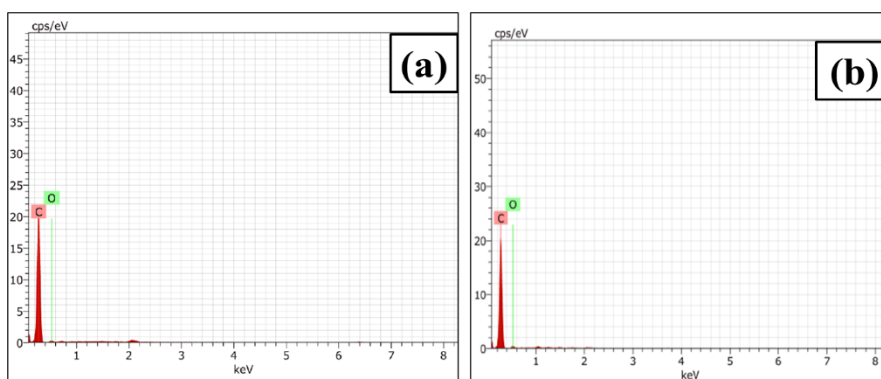


Figure 4.8 EDX Patterns of (a) MWCNTs (b) FMWCNTs

Table 4.2 Elemental Compositions of MWCNTs and FMWCNTs

S. No.	Element	Elemental Composition in Percentage (%)	
		MWCNTs	FMWCNTs
1	Carbon	100	91.43
2	Oxygen	0.00	8.57

4.2.2.2 Results of HR-TEM Analysis of MWCNTs and FMWCNTs

The High Resolution-Transmission Electron Microscope (HR-TEM; Tecnai G2 20 (FEI) S-Twin) was utilized to observe the surface morphology of Multiwalled Carbon

Nanotubes (MWCNTs) and Functionalized Multiwalled Carbon Nanotubes (FMWCNTs). Figure 4.9 (a) displays the MWCNTs, while Figure 4.9 (b) exhibits the FMWCNTs. The provided images effectively demonstrate the existence of surface imperfections on the MWCNTs, which can be attributed to the process of functional modification.

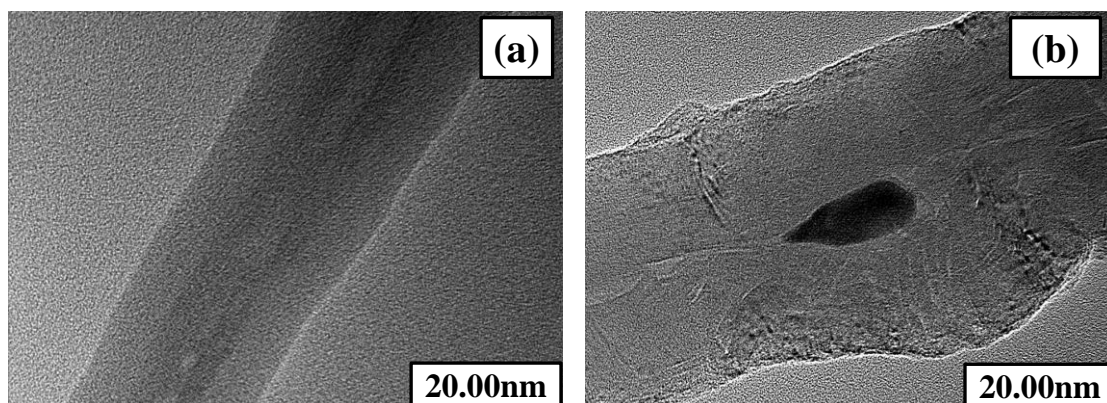


Figure 4.9 HR-TEM Images of (a) MWCNTs (b) FMWCNTs

4.2.2.3 Results of PXRD Analysis of MWCNTs and FMWCNTs

MWCNTs typically have honeycomb geometries made of single layers of graphite sheet. Furthermore, FMWCNTs have bent graphene layers with various chiralities. Figure 4.10 depicts the interplanar distance as 0.334 nm for the MWCNTs, which exhibit a prominent peak 2θ at 26.48° whereas, Figure 4.10 also, illustrates the peak for the FMWCNTs after acid treatment, which displays the same 2θ at 26.48° implying that there was no increase in interplanar distance, merely in intensity (Kaur, Kothiyal, & Singh, 2020; Mendoza et al., 2013).

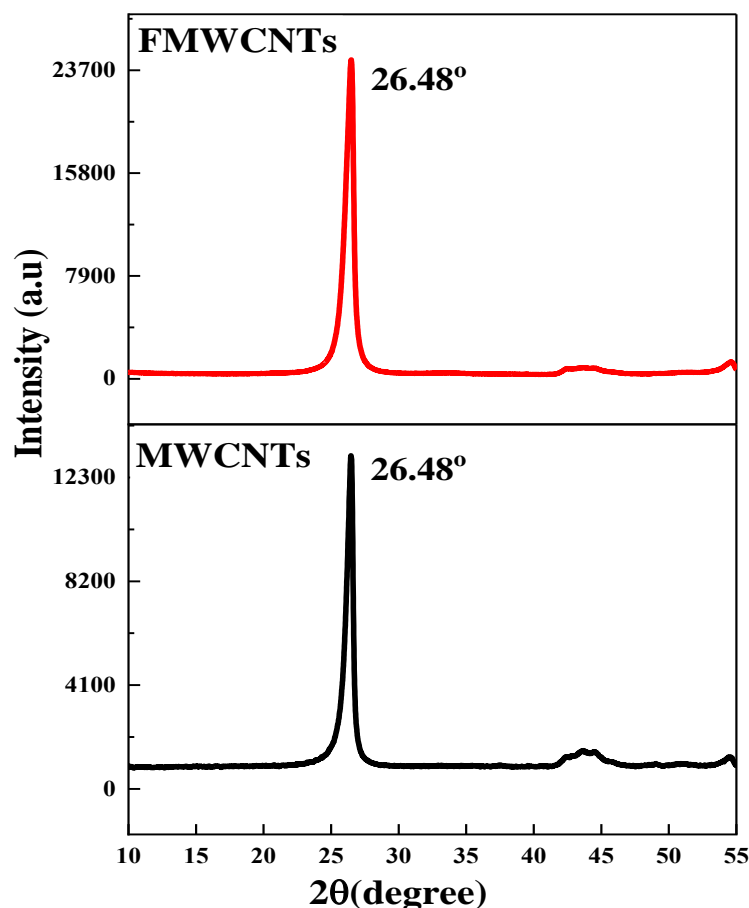


Figure 4.10 PXRD Patterns of MWCNTs, and FMWCNTs

4.2.2.4 Results of Raman Spectroscopy Analysis of MWCNTs and FMWCNTs

In order to analyze the arrangement and level of disorder in unaltered nanomaterials and their modified versions, a Micro Raman spectrometer (STR 500 Confocal) was employed. Carbon nanomaterials demonstrate two prominent vibrational modes referred to as the 'D band' and 'G band'. The D band is indicative of the level of order or disorder within the structure, whereas the G band provides information about the stacking arrangement of the structure (Wu et al., 2018; Graf et al., 2007).

The Raman spectra of Multiwalled Carbon Nanotubes (MWCNTs) and Functionalized Multiwalled Carbon Nanotubes (FMWCNTs) are presented in Figure 4.11, illustrating the presence of distinct peaks corresponding to the D-band at wave number of 1336 cm^{-1} and for the G-band at wavenumber of 1576 cm^{-1} . The observed rise in the I_D/I_G ratio, from 1.2 to 1.5, suggests the occurrence of defects on the MWCNTs surfaces as a result of functionalization.

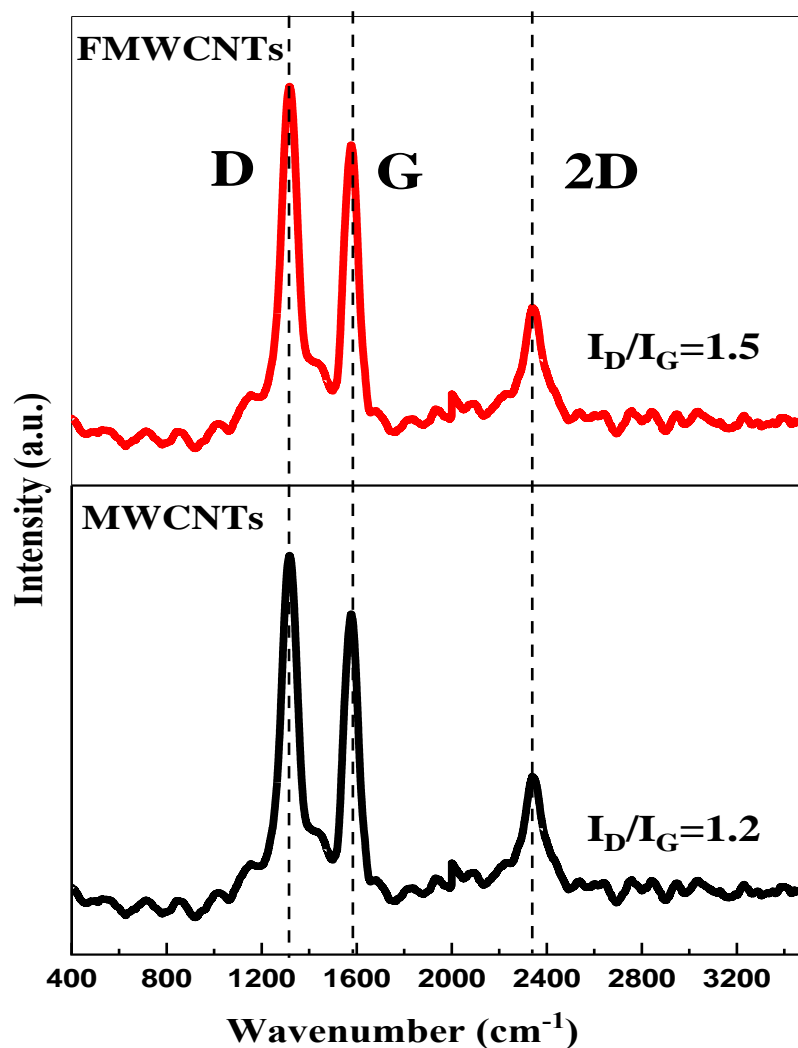


Figure 4.11 Raman Spectra of MWCNTs and FMWCNTs

4.2.2.5 Results of FTIR Analysis of MWCNTs and FMWCNTs

FTIR analysis provides valuable information about the chemical composition and molecular structure of materials. It involves the measurement and analysis of infrared absorption and transmission of samples, enabling identification of functional groups and chemical bonds present. FT-IR spectra of MWCNTs and FMWCNTs can be shown in Figure 4.12. Both have different structure entities. The conformation of FMWCNTs after the acid treatments of MWCNTs have been observed in FT-IR analysis. The low abundance peak at 2917 cm^{-1} was caused by the asymmetric stretching of the C-H bond. The absorption band at 1584 cm^{-1} is from the C=C stretching mode of MWCNTs can be shown in Figure 4.12. The FMWCNTs have three characteristic peaks such as C=C, O-H, and C-O are confirming the surface oxidation of MWCNTs. Furthermore, the peak at 715 cm^{-1} and 1385 cm^{-1} are responsible for C-O stretching and C-H bending, respectively. While the peak at 1584 cm^{-1} shows the un-oxidized C=C stretching mode

of FMWCNTs can be seen in Figure 4.12(Kaur & Kothiyal, 2019b; Raghavendra Prasad & Sitaram, 2020).

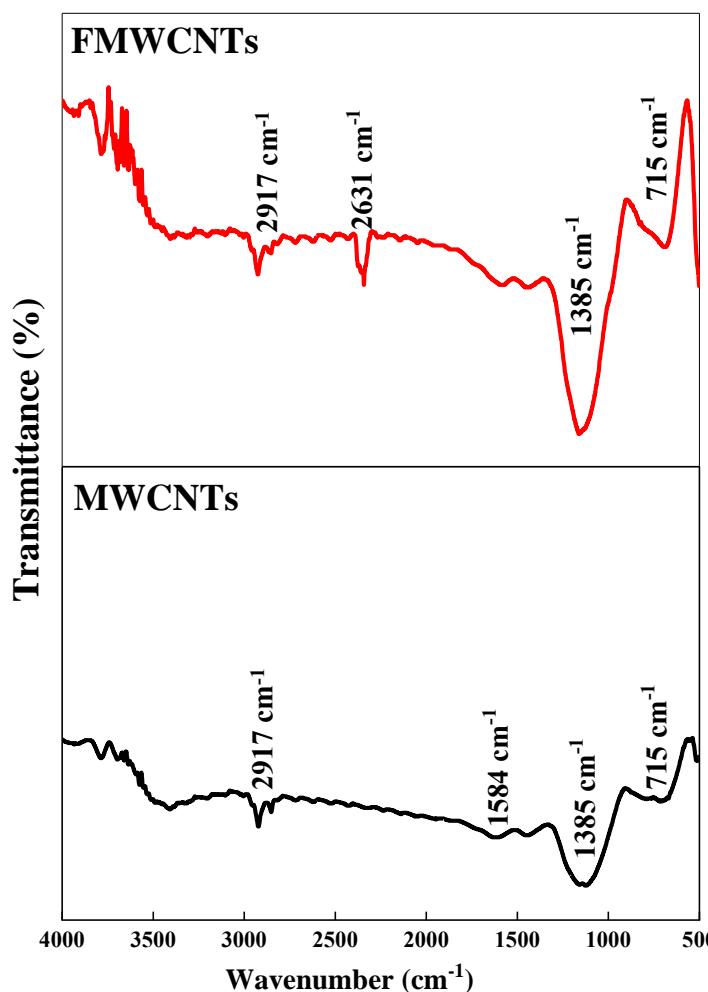


Figure 4.12 FTIR Analysis of MWCNTs, and FMWCNTs

4.3 DISPERSION STUDIES OF CARBON NANOMATERIALS

4.3.1 Structural Characterization of Superplasticizers (SP)

4.3.1.1 FT-IR Spectroscopy of SP

The SP has been utilized in this study. FT-IR spectra peak is located at 3364 cm⁻¹, 2369 cm⁻¹, and 1367 cm⁻¹ owned to O-H stretching of carbon dioxide, and stretching of alcohol respectively(Bhatrola et al., 2023). Additionally, the peak at 1187-1121 cm⁻¹ shows alcohol stretching and 1031 cm⁻¹ shows CO-O-CO strong broad stretching of the anhydride functional group can be shown in Figure 4.13(a). Based on the FT-IR data

presented above, Figure 4.13(b) illustrates the typical chemical structure and composition of commercially obtained polycarboxylate ether-based superplasticizers.

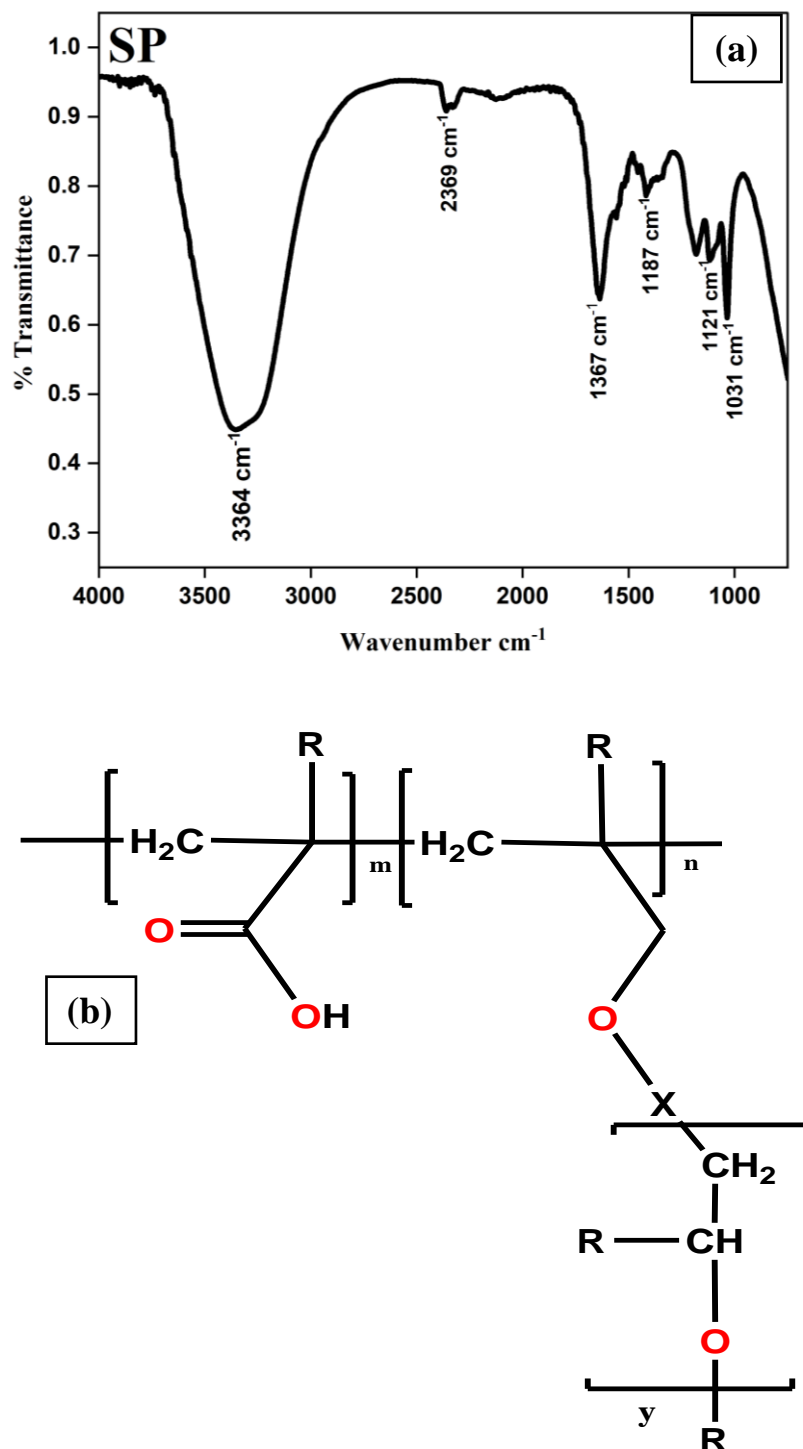


Figure 4.13 (a) FT-IR Spectra and (b) General Chemical Structure of SP

4.3.1.2 DLS analysis of SP

The Malvern Zetasizer Nano ZS instrument was employed to conduct Dynamic Light Scattering (DLS) experiments on SPs, generating the intensity versus size distribution profile as shown in Figure 4.14. The particle size distribution measured by using Malvern Zetasizer Nano ZS DLS. Measurement was carried out by dispersing superplasticizer in an aqueous solution at 500mg/L. The particle Z average size of the plasticizer is 950.6d.nm. The intensity vs size (d.nm) distribution plot is shown in Figure 4.14.

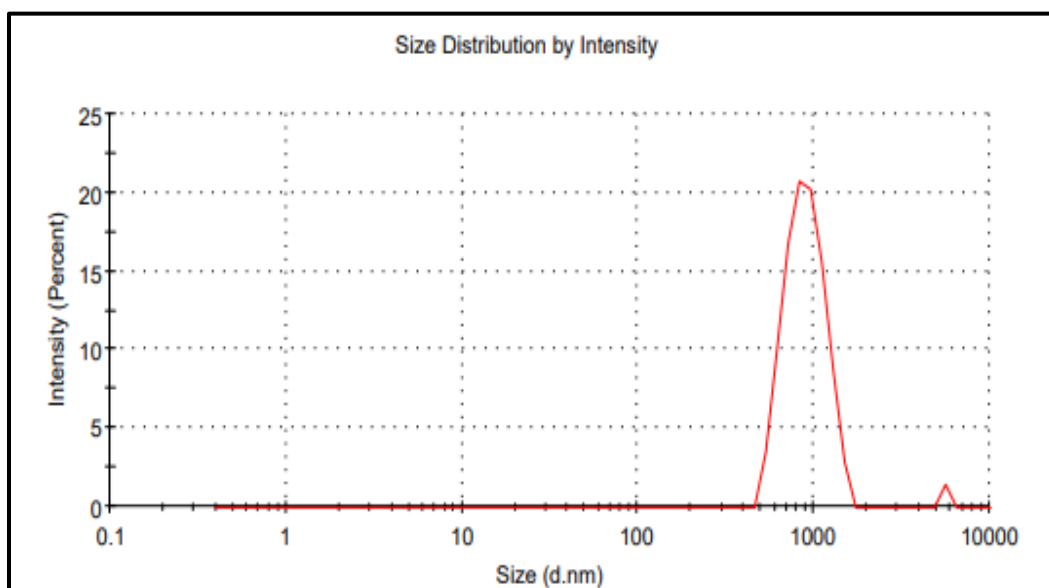


Figure 4.14 Particle Size Distribution of SP

4.3.2 Dispersion Studies of Superplasticizer Stabilized GO, FMWCNTs and HCNMs by UV-Visible Spectroscopy

The dispersion process of carbon nanomaterials in aqueous solutions is a critical aspect to address, as it provides insight into the distribution of nanomaterials inside the cementitious matrix(Cheng et al., 2010; Pan et al., 2011). The dispersion extent relies on sonication parameters, including intensity, frequency, and duration(Chuah et al., 2018). In this research, the comparison of the dispersion capabilities of GO and FMWCNTs with HCNMs, both with and without superplasticizer modification have been carried out. The comparison was done at varying amplitude intensities of 15, 20, 25, and 30%. According to Beer-Lambert Law depicted in equation 4.1, the dispersion of GO, FMWCNTs, and their Hybrid is considered better when the absorption value is higher(Calloway, 1997; Zhou et al., 2017b).

$$A = \log \frac{1}{T} = \log \frac{I_o}{I} = \epsilon cl \quad (4.1)$$

In Figure 4.15(a) and 4.15(b), the absorption values for individual GO and FMWCNTs dispersions, respectively, are presented at different amplitudes of sonication. The findings demonstrated a positive correlation between the amplitude of sonication and the absorbance levels at the 200 nm wavelength. Moreover, it is crucial to emphasize that the observed upward slope persisted consistently for both the introduction of superplasticizers in aqueous dispersions of GO and FMWCNTs. The addition of superplasticizers to the graphene oxide (GO) solution resulted in a significant enhancement in its dispersion efficiency, reaching a maximum value of 89.13% for SP when subjected to the highest sonication amplitude (30%) (Figure 4.15(a)). Similarly, variations with superplasticizer inclusion into FMWCNTs were observed, with SP showing an 80% enhancement, as depicted in Figure 4.15(b).

The improved dispersion of superplasticizer stabilized GO and FMWCNTs can be attributed to the steric stabilization caused by the polyethylene side chains of the SP. These side chains effectively turn aside the agglomeration of FMWCNTs and the GO, leading to better dispersion and stability in the aqueous solution (Yamada et al., 2000).

Indeed, it is noteworthy that the chemical alteration of GO and FMWCNTs surfaces with SP results in a reduction of π - π stacking interactions within the sp^2 hydrophobic area of GO and FMWCNTs. The primary mechanism behind this reduction is predominantly attributed to steric repulsion, which arises from the lateral chains of SP in both aqueous and cement pore solutions. The π - π stacking interactions are hindered, leading to improved dispersion and preventing agglomeration of FMWCNTs and GO in the cementitious matrix (Mani et al., 2013; L. Zhao, Guo, Ge, et al., 2017a). The figure in Figure 4.14 illustrates the size distributions of SP chain lengths, which were determined using Dynamic Light Scattering studies. The functioning mechanism of SPs is greatly influenced by various parameters, including the molecular structures of SPs themselves. These molecular structures encompass elements such as side chain polymerization degrees, densities of carboxyl groups on the main chain, and molecular weight (Kong et al., 2016; X. Y. Peng & Xia, 2013).

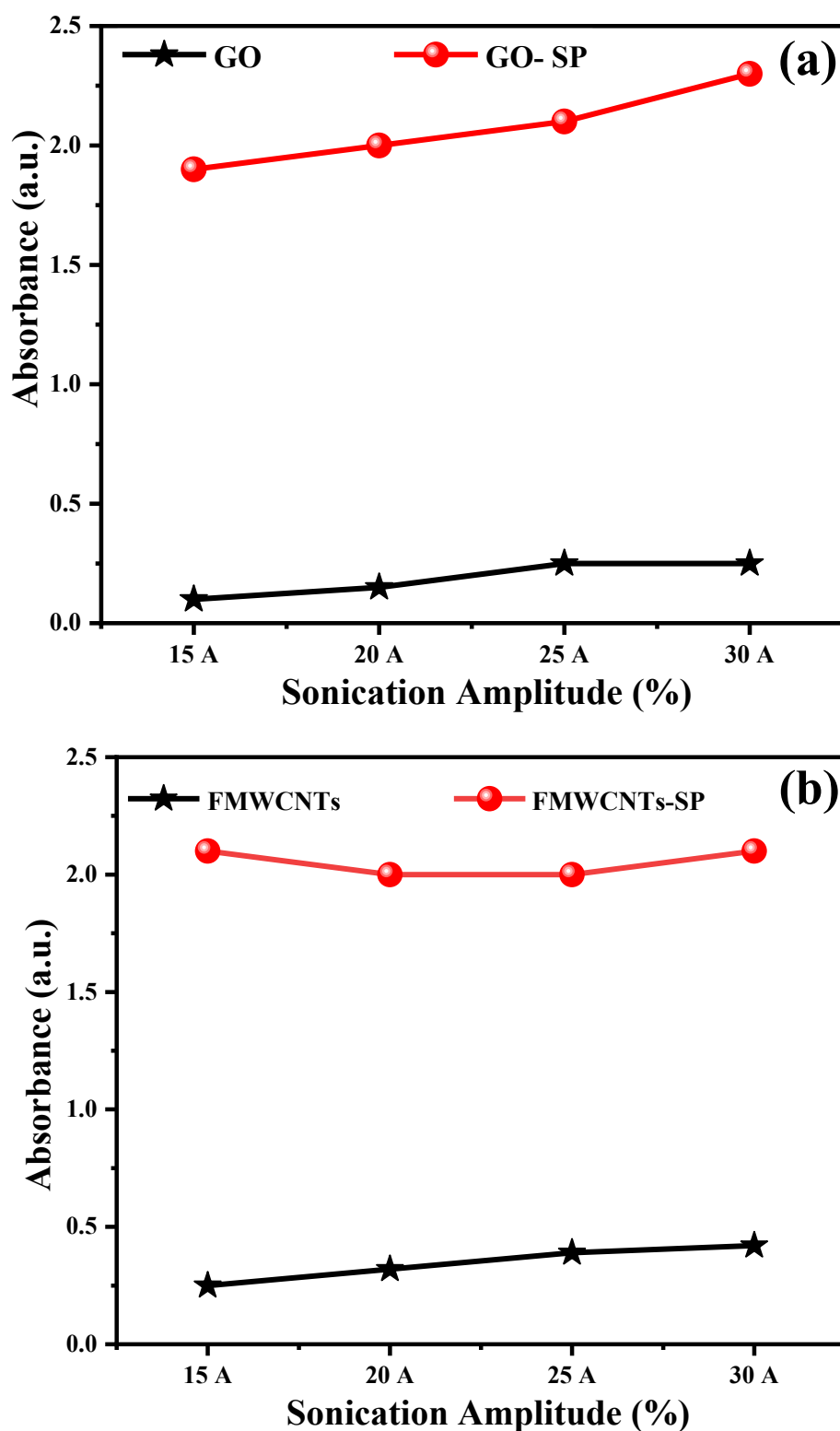


Figure 4.15 Plot of Sonication Amplitude versus Absorbance (at 200 nm) for (a) GO and (b) FMWCNTs

Dispersion studies of Hybrid Carbon Nanomaterials (HCNMs) were conducted both with and without the inclusion of superplasticizers, in addition to individual carbon nanomaterials like GO and FMWCNTs. Figure 4.16, 4.17, and 4.18 illustrate the

dispersion studies of HCNMs without any SP and HCNMs dispersed in SP. The dispersion ability of the samples increased with higher sonication amplitudes, reaching a maximum at 30% for each case. Among the different ratios of HCNMs tested, the 4:1 (GO to FMWCNTs) sample exhibited the highest dispersion at a wavelength of 200 nm. Figure 4.16(a) shows the comparison of dispersion capacity for different ratios of HCNMs; 0:5, 1:4, 2:2, 4:1, and 5:0. The dispersion degree of HCNMs was significantly greater compared to individual GO or FMWCNTs (see Figure 4.15). This improved dispersion can be attributed to the π - π stacking interactions among the sp^2 framework of FMWCNTs and GO, leading to enhanced dispersion of the hybrid nanomaterials (Mani et al., 2013; Tian et al., 2010). As a result, the prevention of re-agglomeration of FMWCNTs and re-stacking of GO sheets occurs in the aqueous solution. This is attributed to the stabilization of CNMs/HCNMs provided by the lateral chains of the superplasticizers, ensuring a stable and well-dispersed nanomaterial solution. In Figure 4.16(b), the absorbance values for HCNMs in the ratio of 4:1 (GO to FMWCNTs) are presented at different time periods after sonication. It is evident that the absorbance values for the dispersions gradually decreased with increasing time after sonication. The HCNMs dispersed at 15% of sonication amplitude showed the maximum reduction in dispersion ability. Within five hours of sonication, the absorbance of the sample at 30% amplitude approached a value similar to that of the sample sonicated at 25% amplitude. The steady reduction in the dispersion ability of the HCNMs can be attributed to the restacking of graphene sheets and re-agglomeration of FMWCNTs over time. As a result, the HCNMs dispersions may not be suitable for practical applications at construction sites after a certain time gap following ultrasonication. In Figure 4.17(a), a comparison of HCNMs dispersion ability at different ratios of 0:5, 1:4, 2:2, 4:1, and 5:0 in the presence of SP is depicted. The observation reveals that the maximum dispersion was once again achieved for the HCNMs ratio of 4:1 (GO to FMWCNTs).

The dispersion of HCNMs, facilitated by SP, exhibits two distinct differences compared to the dispersion of HCNMs in the absence of SP. Firstly, the absorption values were found to be relatively consistent across different ratios of 0:5, 1:4, 2:2, 4:1, and 5:0, which contrasts with the variability observed in HCNMs samples without SP. Secondly, the impact of varying sonication amplitudes, specifically at levels of 15%, 20%, 25%, and 30%, on each HCNMs ratio displayed remarkably similar absorption values. This

indicates that, in this particular scenario, the primary factor contributing to the improved dispersion ability of HCNMs was the electrostatic stabilization by SP rather than alterations in other factors like amplitude. Moreover, the chemical modification of -COOH groups in GO and FMWCNTs by SP leads to their steric stabilization, primarily because of the elongated lateral chains of SP(Z. Lu, Li, et al., 2017; Mendoza Reales & Dias Toledo Filho, 2017; Shang et al., 2015; L. Zhao, Guo, Liu, et al., 2017).

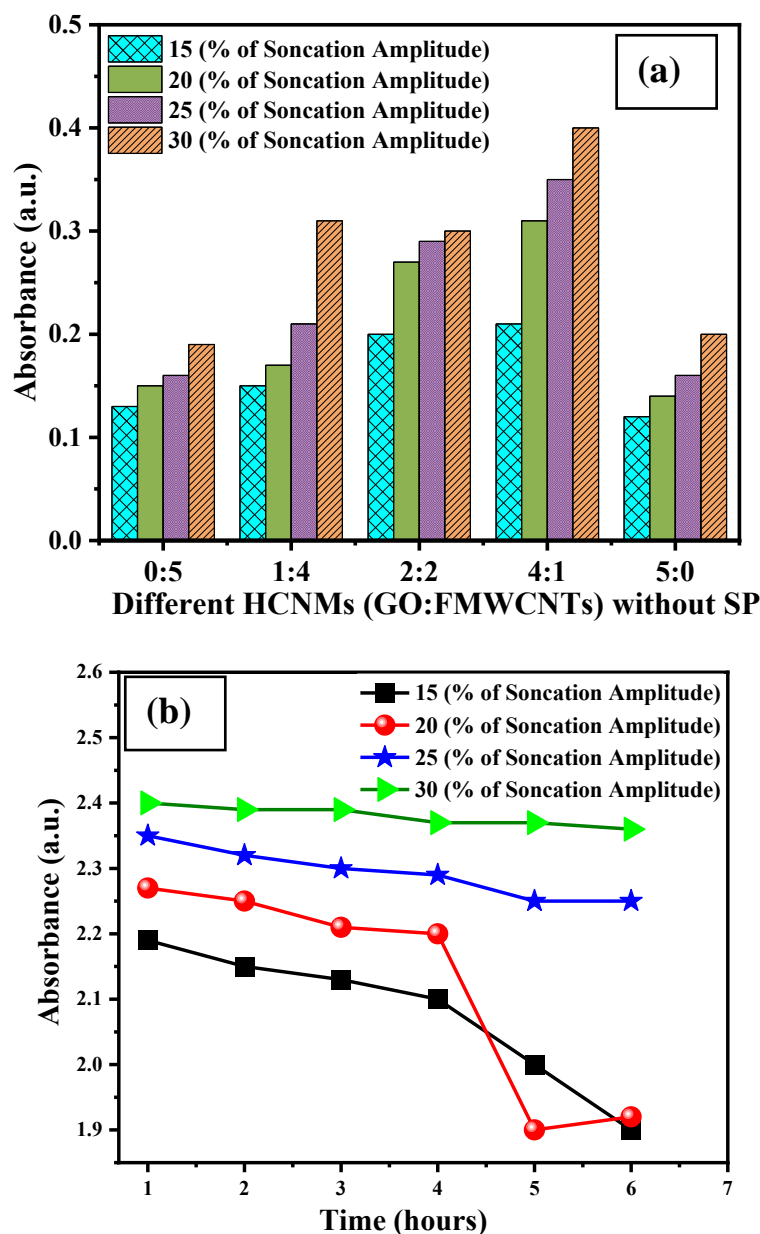


Figure 4.16 (a) Absorbance Values of HCNMs at Different Ratios and Sonication Amplitudes (b) Dispersion Stability of HCNMs (4:1) at Different Time Periods Post Ultrasonication

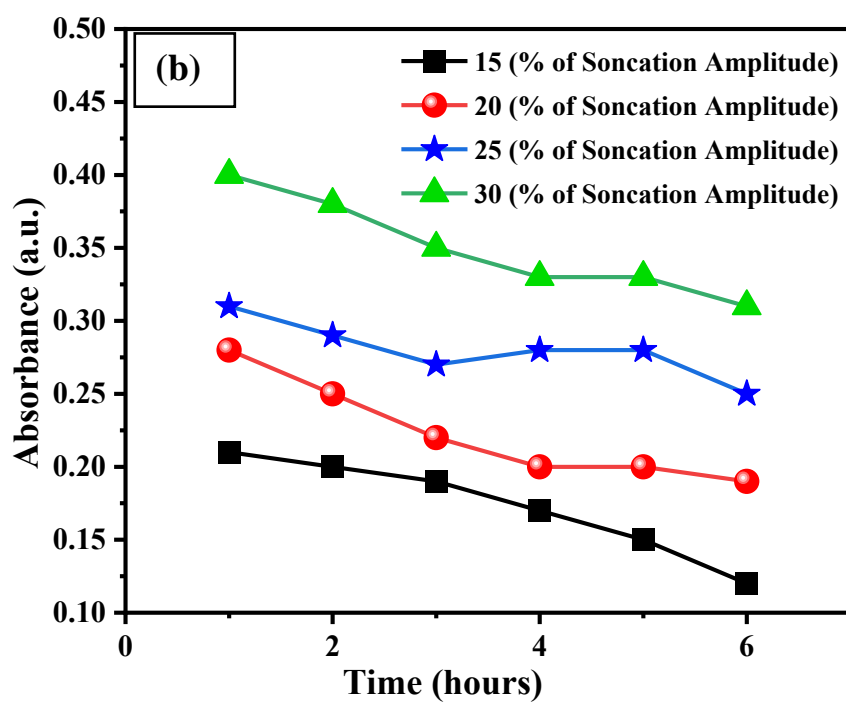
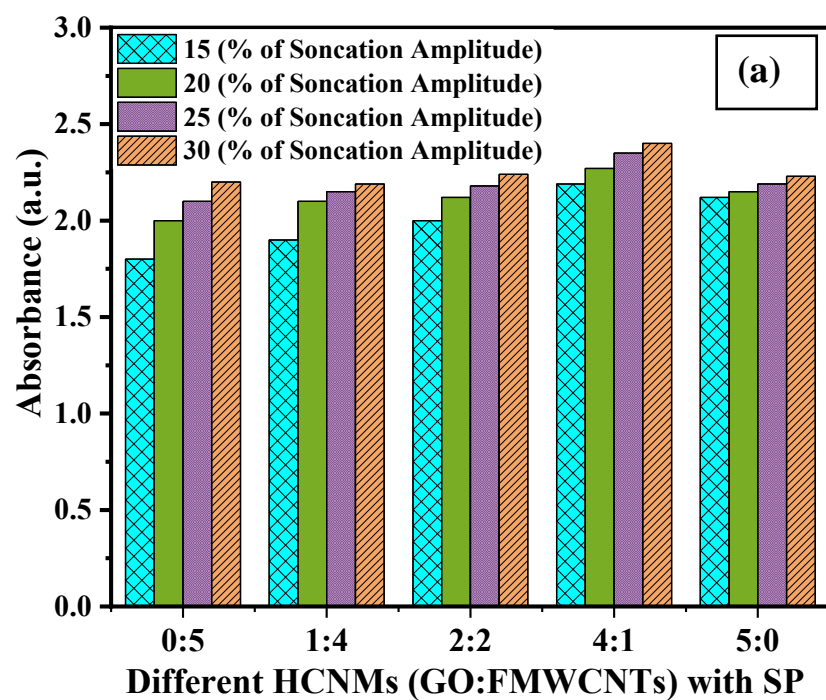


Figure 4.17 (a) Absorbance Values of HCNMs at Different Ratios (b) Dispersion Stability of HCNMs (4:1) at Different Time Periods Post Ultrasonication in SP

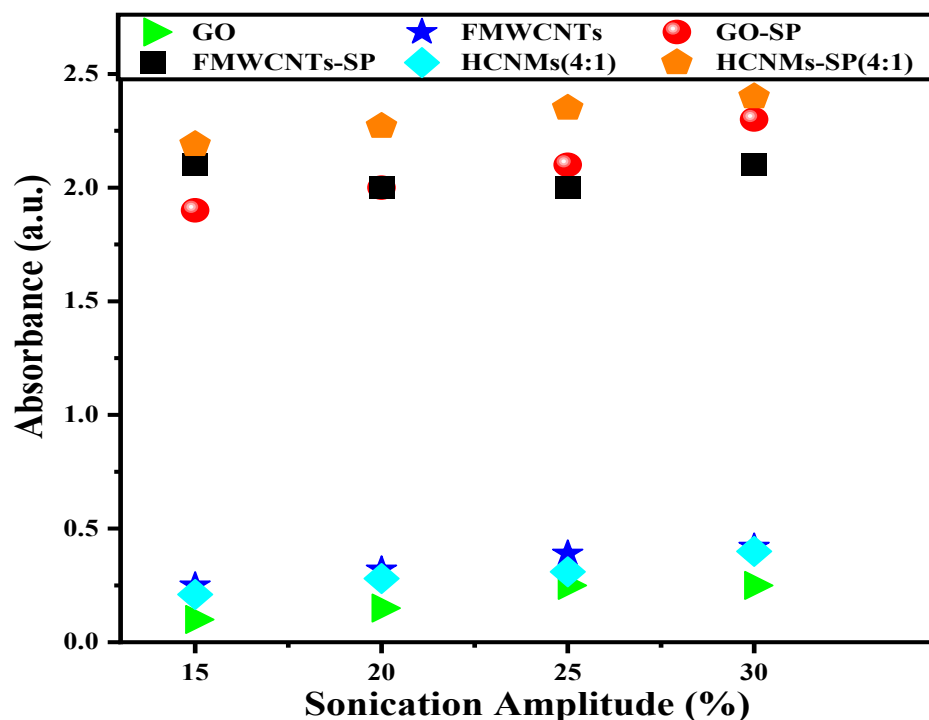


Figure 4.18 Absorbance Values of GO, FMWCNTs, and HCNMs (with and without SP) at Different Sonication Amplitudes

This is the rationale behind the enhanced stability of HCNMs dispersions stabilized by SP in comparison to HCNMs dispersions without any SP stabilization. Figure 4.17(b) illustrates the absorbance values for HCNMs in the ratio 4:1, stabilized by SP, at various time intervals after sonication. It is evident that the reduction in absorbance values was not as rapid as observed in the case of HCNMs without SP stabilization. Furthermore, the absorbance values for dispersions stabilized at 25% and 30% amplitude remained relatively stable over time. In general, the modified carbon nanomaterials and hybrid carbon nanomaterials demonstrated superior dispersion efficiency compared to their pristine functionalized counterparts. This improvement can be attributed to steric stabilization caused by covalent bonding between the oxygenated functional groups of GO/FMWCNT and SP. Moreover, this effect leads to the separation of graphene sheets and MWCNTs from each other, facilitated by the lateral chains of the SP.

In summary, Figure 4.18 provides a concise overview of the dispersion studies of CNMs/HCNMs both with and without SP. The general conclusion drawn from these studies is that HCNMs exhibited superior dispersion ability compared to individual CNMs (i.e., GO or FMWCNTs). Furthermore, the addition of SP significantly enhanced the dispersion of CNMs/HCNMs, surpassing the dispersion achieved in the absence of SP.

PHYSICO-MECHANICAL STRENGTH OF CNMs/HCNMs BASED CNCMs

In order to investigate the impact of incorporation of CNMs/HCNMs (i.e., SP stabilized GO, FMWCNTs, and HCNMs) on the physico-mechanical properties of the CNCMs mortar samples were fabricated and tested for compressive and tensile strength. The strength values were assessed at varying dosages of the reinforcing agents in the CNCMs (i.e., 0.0015%, 0.003%, 0.006%, and 0.012%; by weight of the cement) and different curing ages (7, 28, 56, and 90 days).

4.4 COMPRESSIVE STRENGTH OF CNMs/HCNMs BASED CNCMs

4.4.1 Compressive Strength of GO-CNCMs

The comparative graphical representation of the compressive strength values for control and GO-CNCMs with the varying GO dosages (i.e., 0.0015%, 0.003%, 0.006%, and 0.012%; by weight of the cement) at curing ages of 7, 28, 56, and 90 days has been presented in the Figure 4.19. The percentage increase in the compressive strength obtained for different mixes of GO-CNCMs with respect to control mortar sample is summarized in Table 4.3. The study's error bars are based on three samples per testing condition. The compressive strength results of GO-CNCMs clearly indicate that as the dosage of superplasticizer stabilized GO increases from 0.0015% to 0.012%, there is an initial increase in compressive strength up to the 0.0015% dosage level. However, beyond this point, a decline in compressive strength is observed as the GO dosage is further increased, specifically within the range of 0.003% to 0.012% for GO-CNCMs. The compressive strength values obtained for control sample and for CNCMs after GO incorporation in dosages of 0.0015%, 0.003%, 0.006%, and 0.012% are found to be 22.59MPa, 23.53MPa, 23.25MPa, 22.95MPa, and 22.88MPa, respectively, at the 7 days of curing time. Compressive strength values increase with the increase of curing age, both in the control and in each mixture of GO-CNCMs. This phenomenon can be attributed to the ongoing hydration reactions, leading to the formation of a greater amount of hydration products, thereby enhancing the interlocking of these products. The denser microstructure of cement hydrates, notably the C-S-H gel, contributes to a reduction in the porosity of the mortar matrix, consequently leading to an improvement

in compressive strength also supported by referred study(Gong et al., 2014; G. Y. Li et al., 2005). Compressive strength of control and CNCMs after addition of GO in dosages of 0.0015%, 0.003%, 0.006%, and 0.012% after 28 days of curing are found to be 29.59MPa, 31.57MPa,30.53MPa, 30.37MPa, and 30.24 MPa, respectively. As the dosage of CNMs increased from 0.0015%, there was a continuous decline in strength. Further increases curing age as 56 days the strength was found to be 36.61 MPa, 39.75MPa, 38.68MPa, 38.44MPa, and 37.54 MPa, for control, 0.0015%, 0.003%, 0.006%, and 0.012%, respectively. At the curing age of 90 days the strength was observed 38.72MPa, 43.24MPa, 41.11MPa, 40.92MPa, and 39.78MPa, for control, 0.0015%, 0.003%, 0.006%, and 0.012%, respectively. The maximum strength gain has been achieved in case of 0.0015% GO-CNCMs among all GO-CNCMs and is found to be 43.24 MPa. On the other hand, control sample showed a value of 38.72 MPa at the age of 90 days.

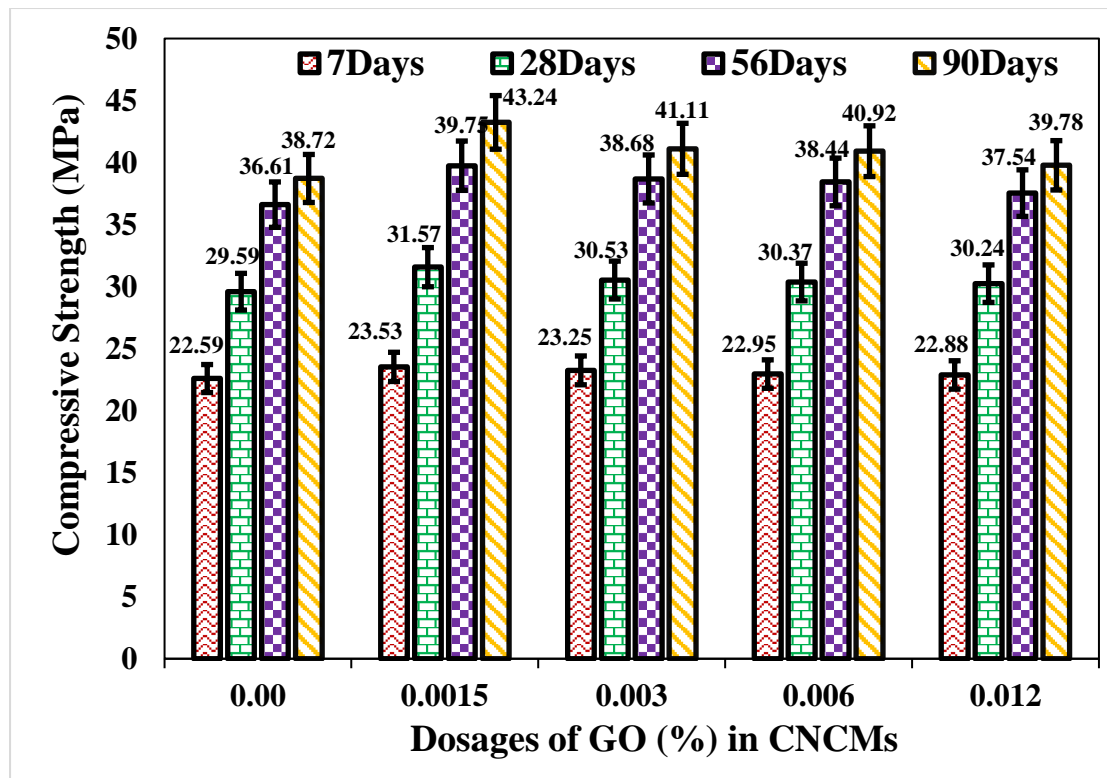


Figure 4.19 Compressive Strength for Control and GO-CNCMs at Different Dosages and Curing Ages

The reason for this additional strength enhancement for GO incorporated CNCMs can be attributed to the fact that two-dimensional GO sheets possess one extra dimension for the nucleation of the hydration products. GO possesses hydrophilic characteristics accredited to the oxygen functional groups located on the plane and edges of its

graphene sheets. This property makes GO exceptionally dispersible in water(Saafi et al., 2015). The modified surface provides an interface for the growth of cement hydration products. Moreover, the functionalization on GO enhancing the interfacial adhesion between the cement hydration product and reinforcing agent. Nonetheless, through superplasticizer stabilization, GO acquires a remarkable dispersion characteristic within the alkaline cement environment, effectively rendered the agglomeration even in the presence of various ionic species such as Ca^{2+} , Na^{2+} , K^{+} , OH^{-} , and more. Previous studies suggest that potential reasons for GO agglomeration involve the interference of electrostatic interactions among GO sheets by these ions, the interlocking of GO sheets by Ca^{2+} ions, and the deoxygenation of GO's oxygen functionalities under alkaline conditions(Z. Lu, Li, et al., 2017; L. Zhao, Guo, et al., 2020). These observations indicate that sterically stabilized GO introduces a nucleation effect to cement hydrates and contributes to the densification of the microstructure in cement-based materials.

The decrease in strength of the GO-CNCMs mixes beyond the dosage of 0.0015% (specifically at 0.003%, 0.006%, and 0.012%) can be attributed to irregular pore filling within the cement matrix due to comparatively lower dispersion when compared to the 0.0015% dosage. However, compressive strength values for dosages of 0.003%, 0.006%, and 0.012% exceed those of the control sample, suggesting successful reinforcement by CNCMs. The Table 4.3 summarizes the percentage variation in compressive strength for various GO-CNCMs mixes at curing durations of 7, 28, 56, and 90 days. The highest percentage increase, amounting to 11.67% compared to the control sample, is recorded for the 0.0015% GO-CNCMs mixture.

Table 4.3 Percentage Change in Compressive Strength for GO-CNCMs

Mix Designation	Dosage of GO incorporated (% by weight of cement)	Percentage Change in Compressive Strength with respect to Control (%)			
		7 days	28 days	56 days	90 days
GO-CNCMs	0.0015%GO-CNCMs	4.16	6.69	8.58	11.67
	0.003%GO-CNCMs	2.92	3.18	5.65	6.17
	0.006%GO-CNCMs	1.59	2.64	5.00	5.68
	0.012%GO-CNCMs	1.28	2.20	2.54	2.74

4.4.2 Compressive Strength of FMWCNTs-CNCMs

Figure 4.20 presents a comparative graphical representation of the compressive strength values for both the control and FMWCNTs-CNCMs, accounting for varying FMWCNTs dosages and curing durations. It is found that the addition of FMWCNTs tailored with SP into the mortars has resulted in improved compressive strength for all mixes (0.0015%, 0.003%, 0.006%, and 0.012% FMWCNTs-CNCMs) across all curing periods (7, 28, 56, and 90 days), surpassing the control sample. Table 4.4 represents the percentage variation in compressive strength for FMWCNTs-CNCMs in relation to the control sample at curing ages of 7, 28, 56, and 90 days. It is noteworthy to highlight that there was an increase in compressive strength observed for both the control sample and each mixture of FMWCNTs-CNCMs as the curing age increased.

At 7 days of curing ages, the most substantial enhancement in compressive strength, reaching 23.81 MPa, was achieved with the addition of 0.0015% FMWCNTs to the cementitious mortar matrix. However, beyond this point, a declining trend in compressive strength becomes evident as the dosage of FMWCNTs is further increased. This decline can be attributed to the diminished and less effective dispersion or agglomeration of the FMWCNTs nanotubes within the alkaline environment of the cement matrix as the FMWCNTs dosage continues to rise.

A similar pattern was observed for extended curing periods of 7, 28, 56, and 90 days. Specifically, at the 90day curing age, the highest compressive strength was recorded for the 0.0015% FMWCNTs-CNCMs mixture, amounting to 42.10 MPa. This marks a significant 8.72% enhancement in compressive strength compared to the control sample, which had a compressive strength of 38.72 MPa. In contrast, lesser compressive strength values were noted for CNCMs incorporating higher FMWCNTs dosages, with the compressive strength for 0.003% FMWCNTs-CNCMs, 0.006% FMWCNTs-CNCMs, and 0.012% FMWCNTs-CNCMs measured at 40.82MPa, 39.94MPa, 39.72MPa, respectively at the age of 90days of curing.

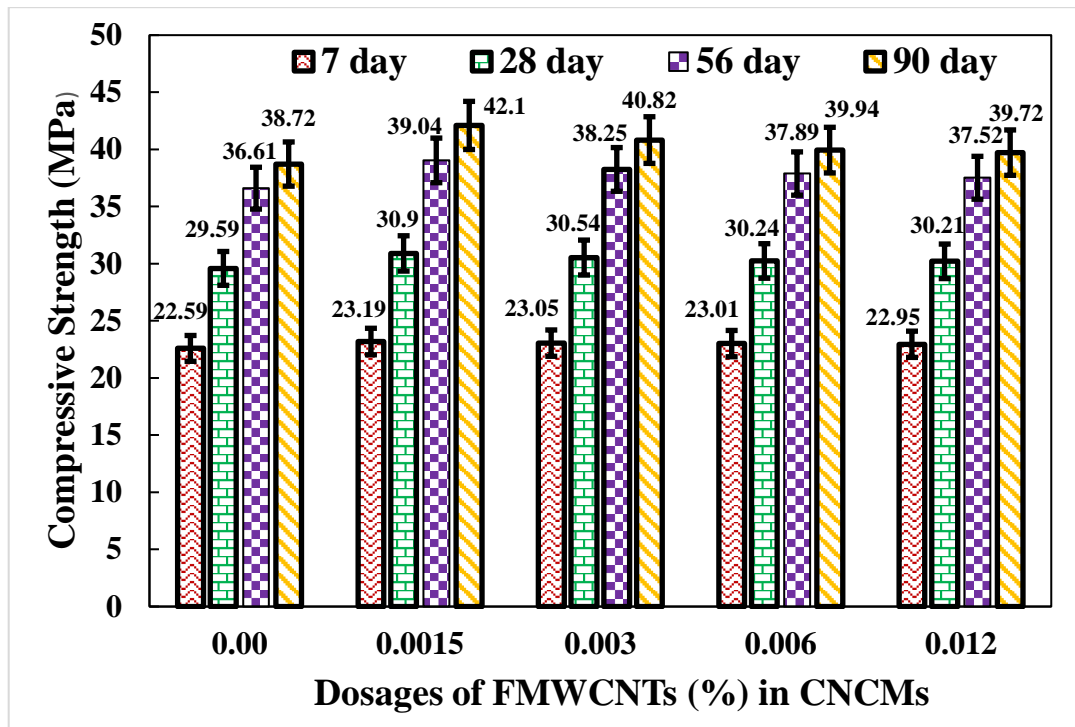


Figure 4.20 Compressive Strength for Control and FMWCNTs-CNCMs at Different Dosages and Curing Ages

Furthermore, it's important to note that the compressive strength values for GO-CNCMs have been notably higher than those of FMWCNTs-CNCMs. This additional strength enhancement observed in GO-incorporated CNCMs can be attributed to the two-dimensional nature of GO sheets, which provide an additional dimension for the nucleation of hydration products across their exposed surfaces compared to the one-dimensional structure of FMWCNTs. GO possesses inherent hydrophilic characteristics due to the presence of oxygen functional groups along the plane and edges of its graphene sheets. In the case of FMWCNTs-CNCMs, an enhancement in the formation of hydration products is observed in comparison to the control sample. This enhancement can be attributed to the presence of oxygen functionalities, specifically -COOH groups, provided by the functionalized MWCNTs. These functional groups serve as nucleation or seeding sites for hydration products such as C-S-H gel and portlandite (C-H). This interaction established robust covalent forces at the interface between FMWCNTs and the hydration products within the cement matrix. As a result, this arrangement facilitates effective load transfer from the cement mortar matrix to FMWCNTs.

Additionally, a dense and harden C-S-H structure forms, firmly bonded to the FMWCNTs. This bonding enhances the stiffness and packing density of the mortar

microstructure, effectively reducing water absorption as well (as discussed later) (Konsta-Gdoutos et al., 2010; G. Y. Li et al., 2005). However, the lesser enhancement in compressive strength observed for 0.012% FMWCNTs-CNCMs can be attributed to the clustering and agglomeration of FMWCNTs at higher dosages within the alkaline cement environment.

Table 4.4 displays the percentage increase in compressive strength for FMWCNTs-CNCMs. The most notable enhancement in compressive strength, amounting to 8.73 %, was achieved at a 0.0015% dosage compared to the control sample.

Table 4.4 Percentage Change in Compressive Strength for FMWCNTs-CNCMs

Mix Designation	Dosage of FMWCNTs incorporated (% by weight of cement)	Percentage Change in Compressive Strength with respect to Control (%)			
		7 days	28 days	56 days	90 days
FMWCNTs-CNCMs	0.0015% FMWCNTs-CNCMs	2.66	4.43	6.64	8.73
	0.003% FMWCNTs-CNCMs	2.04	3.21	4.48	5.42
	0.006% FMWCNTs-CNCMs	1.86	2.20	3.50	3.15
	0.012% FMWCNTs-CNCMs	1.59	2.10	2.49	2.58

4.4.3 Compressive Strength of HCNMs-CNCMs

Figure 4.21 illustrates the graphical representation of compressive strength values for both the control sample and HCNMs-CNCMs at various HCNMs dosage levels 0.0015%, 0.003%, 0.006%, and 0.012% across curing periods of 7, 28, 56, and 90 days. Moreover, Table 4.5 provides a tabular presentation of the percentage increase in compressive strength.

The graphical representation clearly indicates that both the control mortar and HCNMs-CNCMs, across dosages of 0.0015%, 0.003%, 0.006%, and 0.012%, exhibited their highest increase in compressive strength at the 0.0015% dosage (by the weight of cement) within the cementitious nanocomposites mortar containing Hybrid Carbon Nanomaterials (HCNMs). With the increasing of curing time, all mixes demonstrated an enhancement in compressive strength. Remarkably, each HCNMs-CNCMs mix consistently outperformed the control sample in terms of strength at all corresponding curing intervals. Similar to GO-CNCMs, and FMWCNTs-CNCMs the compressive

strength trend for HCNMs-CNCMs demonstrated its peak strength at the 0.0015% dosage, followed by a subsequent decline. This decrease in strength can be attributed to the likely reduction in nanomaterial dispersion at higher dosages.

The highest increase in the compressive strength for GO- CNCMs and FMWCNTs- CNCMs was found to be 11.67 and 8.73% at 0.0015% and 0.0015%, respectively. Comparatively, HCNMs showed a maximum enhancement of 21.32% in compressive strength at a dosage of 0.0015% compared to the control sample at 90 days of curing. So, the HCNMs proved to be better reinforcing agent for the CNCMs than individual reinforcing carbon nanomaterials, i.e., either FMWCNTs or GO.

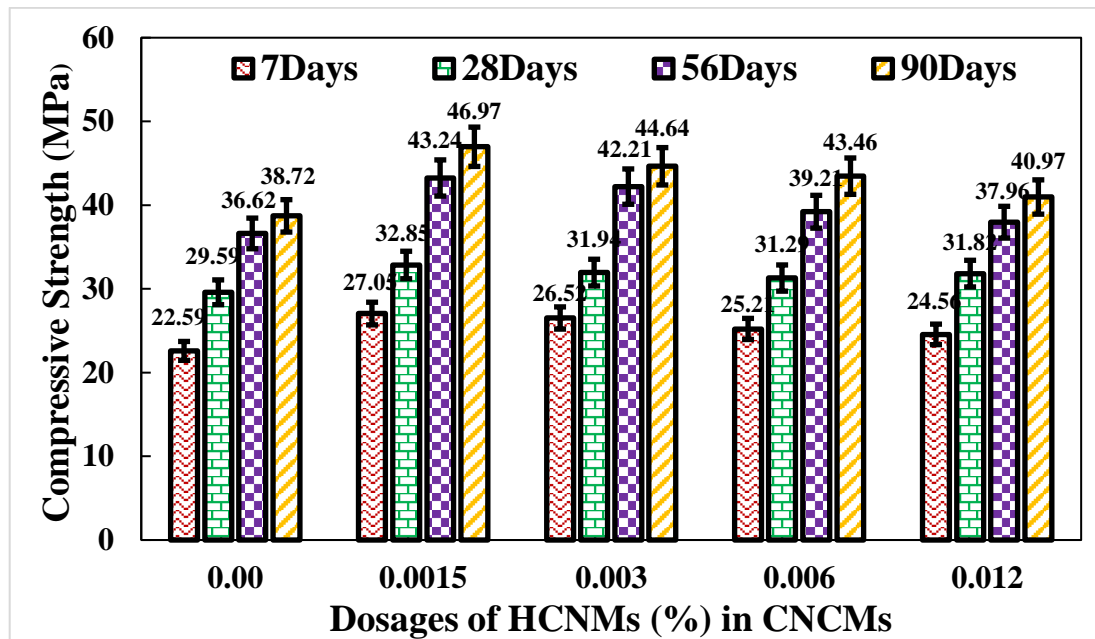


Figure 4.21 Compressive Strength for Control and HCNMs-CNCMs at Different Dosages and Curing Ages

This phenomenon can be attributed to the uniform dispersion of FMWCNTs throughout the crumpled sheets of GO, forming a three-dimensional network. This network serves as a nucleation site for the primary binding agent, namely calcium silicate hydrate (C-S-H) gel, as well as the by-product calcium hydroxide (C-H). Alongside nucleation, HCNMs also play a pivotal role in establishing interfacial adhesion between the carboxylic acid groups of GO or FMWCNTs and the C-S-H gel within the cement mortar matrix. This interaction results in the creation of a denser microstructure with reduced micro-porosity. Relevant studies support these findings (Q. Li et al., 2015; Zhou et al., 2017a).

The percentage increase in compressive strength values for CNCMs incorporating 0.0015%, 0.003%, 0.006%, and 0.012% HCNMs, relative to the control sample, at a curing time of 90 days, were determined to be 21.32%, 15.29%, 12.24%, and 5.81%, respectively. At all the corresponding curing periods, the strength was observed to increase while compared to control sample. This highlights the exceptional properties of the hybrid nanocomposites. Additionally, Table 4.5 offers a structured tabulation showcasing the percentage amplification in compressive strength values. This table presents a clear visual representation of the extent to which the compressive strength has been enhanced in relation to the control.

Table 4.5 Percentage Change in Compressive Strength for HCNMs-CNCMs

Mix Designation	Dosage of HCNMs incorporated (% by weight of cement)	Percentage Change in Compressive Strength with respect to Control (%)			
		7 days	28 days	56 days	90 days
HCNMs-CNCMs	0.0015% HCNMs-CNCMs	19.74	11.02	18.08	21.32
	0.003% HCNMs-CNCMs	17.40	7.94	15.26	15.29
	0.006% HCNMs-CNCMs	11.60	5.75	7.07	12.24
	0.012% HCNMs - CNCMs	8.72	7.54	3.66	5.81

Table 4.6 provides a concise overview of the mean compressive strength values for CNMs/HCNMs (FMWCNTs, and GO) incorporated CNCMs mortar specimens across various dosages (0.0015%, 0.003%, 0.006%, and 0.012%) and curing periods (7, 28, 56, and 90 days). Figure 4.22 displays the comparison of compressive strength values for CNCMs based on GO, FMWCNTs, and HCNMs at dosages of 0.0015%, 0.003%, 0.006%, and 0.012%, following a curing period of 90 days. In Figure 4.22, the compressive strength values of GO-CNCMs, FMWCNTs-CNCMs, and HCNMs-CNCMs are compared. Compressive strength in, GO-CNCMs is similar to FMWCNT-CNCMs, reaches its peak at a 0.0015% dosage, followed by a declining trend. This decrease is likely due to reduced nanomaterial dispersion resulting from higher concentration levels.

Table 4.6 Average Compressive Strength Values of CNMs/HCNMs based CNCMs

S. No	Mix Designation	Dosages of CNMs/HCNMs (% by weight of cement)	Compressive strength (MPa)			
			7 days	28 days	56 days	90 days
1	Control	0.00	22.59	29.59	36.61	38.72
2	GO-CNCMs	0.0015	23.53	31.57	39.75	43.24
		0.003	23.25	30.53	38.68	41.11
		0.006	22.95	30.37	38.44	40.92
		0.012	22.88	30.24	37.54	39.78
3	FMWCNTs-CNCMs	0.0015	23.19	30.9	39.04	42.1
		0.003	23.05	30.54	38.25	40.82
		0.006	23.01	30.24	37.89	39.94
		0.012	22.95	30.21	37.52	39.72
4	HCNMs-CNCMs	0.0015	27.05	32.85	43.24	46.97
		0.003	26.52	31.94	42.21	44.64
		0.006	25.21	31.29	39.21	43.46
		0.012	24.56	31.82	37.96	40.97

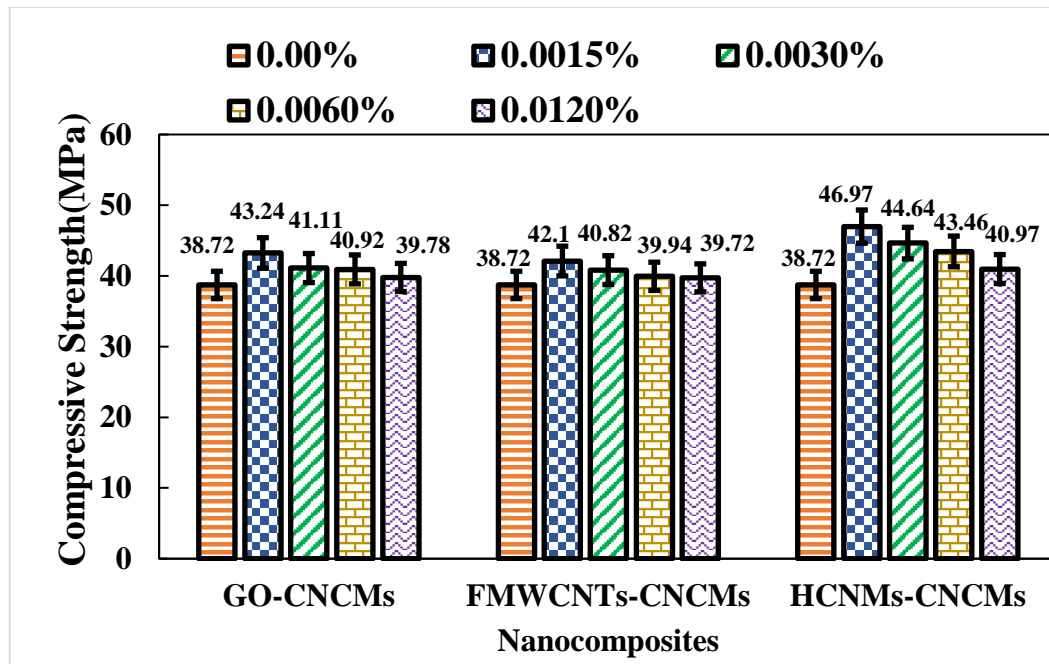


Figure 4.22 Compressive Strength Values (in MPa) for GO, FMWCNTs and HCNMs based CNCMs at 90 Days of Curing

Both GO and FMWCNTs display their maximum enhancement in compressive strength at a dosage of 0.0015%, resulting in improvements of 11.67% and 8.73% respectively, in comparison to the control mortar sample. Conversely, HCNMs-CNCMs showcase

the most substantial increase in strength at a dosage of 0.0015%, demonstrating an impressive 21.32% enhancement over the control sample.

4.5 TENSILE STRENGTH OF CNMs/HCNMs BASED CNCMs

4.5.1 Tensile Strength of GO-CNCMs

In Figure 4.23, a graphical representation signifies the tensile strength values for both the control sample and GO-CNCMs. These values are presented for different GO dosages (0.0015%, 0.003%, 0.006%, and 0.012%) and across different curing periods (7, 28, 56, and 90 days).

Among all the cement mortar nanocomposites, the highest tensile strength was observed in the 0.0015% GO-CNCMs mixture. At 7 days of curing, the tensile strength values for control sample and the GO incorporated CNCMs at dosages 0.0015%, 0.003%, 0.006% and 0.012% was found to be 2.23 MPa, 3.05 MPa, 2.95 MPa, 2.89 MPa, and 2.36 MPa, respectively. As the hydration age increased, there was a notable rise in the tensile strength for each mixture. At 90 days of curing, the tensile strength values improved to 5.16 MPa, 6.52 MPa, 5.92 MPa, 5.63 MPa, and 5.11 MPa for the respective mixes. The addition of 0.005% GO-CNCMs resulted in a significant enhancement, with a 26.35% increase in tensile strength at the 90-day curing age, when compared to the control sample.

The decline in tensile strength values after a dosage of 0.012% can be attributed to the uneven dispersion or re-stacking of GO sheets within the alkaline cement matrix, especially as the GO dosage increases. This re-stacking phenomenon might contribute to an enhancement in compressive strength, yet its potential impact on tensile strength remains constrained. Nevertheless, for GO dosages of 0.003% and 0.006%, the tensile strength values surpass those of the control sample, signifying a notable reinforcement effect at the age of 90 days of curing.

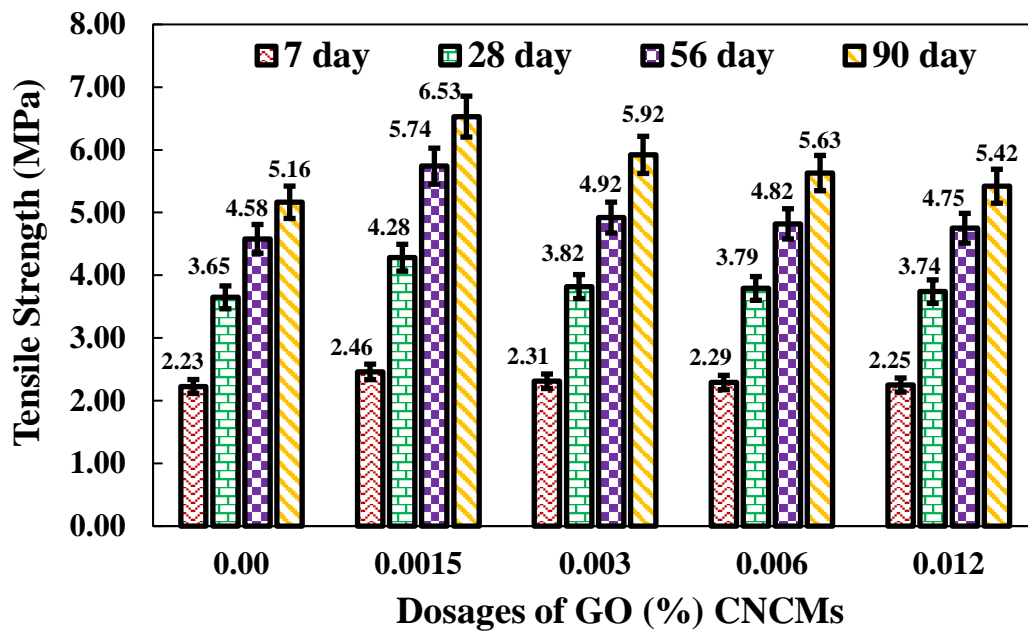


Figure 4.23 Tensile Strength for Control and GO-CNCMs at Different Dosages and Curing Ages

Table 4.7 presents the percentage change in tensile strength (%) in comparison to the control for GO incorporated CNCMs mortar specimens. This data is categorized by different dosages (0.0015%, 0.003%, 0.006%, and 0.012%) and curing durations (7, 28, 56, and 90 days).

Table 4.7 Percentage Change in Tensile Strength for GO-CNCMs

Mix Designation	Dosage of GO incorporated (% by weight of cement)	Percentage Change in Tensile Strength with respect to Control (%)			
		7 days	28 days	56 days	90 days
GO-CNCMs	0.0015%GO-CNCMs	10.51	17.31	25.30	26.35
	0.003%GO-CNCMs	3.77	4.70	7.40	14.64
	0.006%GO-CNCMs	2.88	3.88	5.22	9.02
	0.012%GO-CNCMs	1.08	2.51	3.69	4.96

4.5.2 Tensile Strength of FMWCNTs-CNCMs

Figure 4.24 illustrates the graphical depiction of tensile strength values for FMWCNTs-CNCMs across different FMWCNTs dosages and curing durations. The graph portrays

a gradual ascent in tensile strength as the FMWCNTs dosage within the cementitious matrix rises, peaking at 0.0015%. However, subsequent to this point, there is a discernible decrease in the strength values with the increment of nanomaterial dosage. Additionally, the tensile strength values are found to be more as compared to the control sample for all cases. The graphical trend for the tensile strength values of FMWCNTs-CNCMs was found to be quite parallel to that of GO-CNCMs. Like GO-CNCMs, the maximum tensile strength values were obtained for 0.0015% FMWCNTs-CNCMs i.e., by 20.61% compared to the control sample.

At 7 days of curing, the tensile strength values for control sample and the FMWCNTs incorporated CNCMs at dosages 0.0015%, 0.003%, 0.006%, and 0.012% was found to be 2.23 MPa, 2.29 MPa, 2.40 MPa, 2.59 MPa, and 2.30 MPa, respectively. With an increase in the hydration age to 90 days, the tensile strength for each mix has been found to be increased, and the tensile strength values enhanced to 5.16 MPa, 6.22 MPa, 5.97 MPa, 5.38 MPa, and 5.18 MPa, for each respective mix. The reduction in tensile strength values following the introduction of a 0.0015% dosage can be attributed to the uneven dispersion or agglomeration of nanotubes in the alkaline cement matrix.

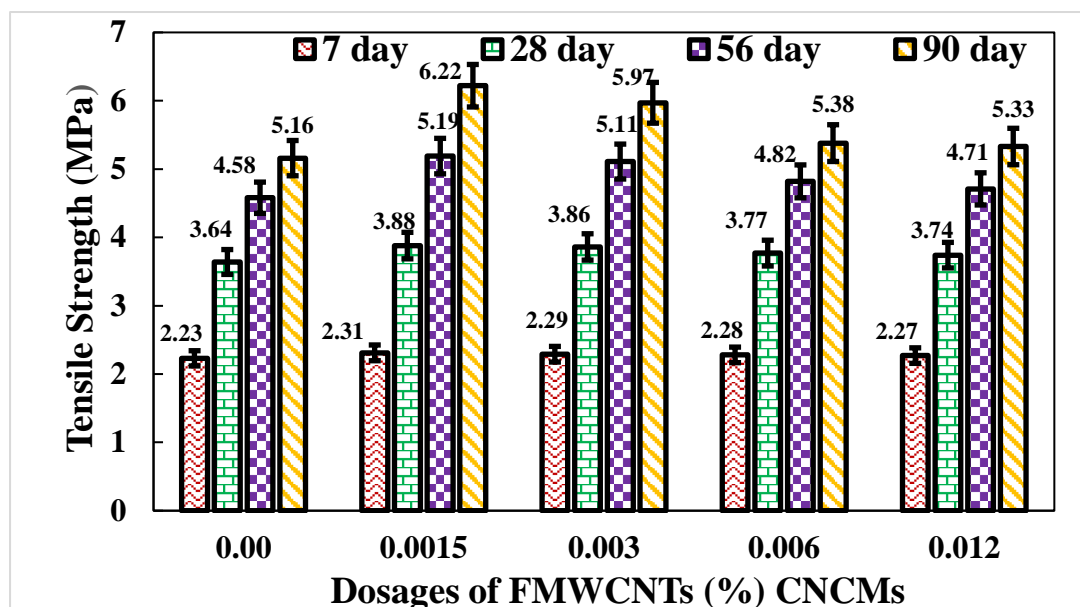


Figure 4.24 Tensile Strength for Control and FMWCNTs-CNCMs at Different Dosages and Curing Ages

Table 4.8 displays the percentage deviation in tensile strength for FMWCNTs-CNCMs concerning the control sample across curing durations of 7, 28, 56, and 90 days. The most significant percentage rise in tensile strength was recorded for 0.0015%

FMWCNTs-CNCMs, exhibiting a remarkable 20.61% increase in comparison to the control sample after 90 days of curing.

Table 4.8 Percentage Change in Tensile Strength for FMWCNTs-CNCMs

Mix Designation	Dosage of FMWCNTs incorporated (% by weight of cement)	Percentage Change in Tensile Strength with respect to Control (%)			
		7 days	28 days	56 days	90 days
FMWCNTs-CNCMs	0.0015% FMWCNTs-CNCMs	3.77	6.35	13.29	20.45
	0.003% FMWCNTs-CNCMs	2.88	5.80	11.55	15.61
	0.006% FMWCNTs-CNCMs	2.43	3.33	5.22	4.19
	0.012% FMWCNTs-CNCMs	1.98	2.51	2.82	3.22

In the case of FMWCNTs-CNCMs, the presence of oxygen functionalities (such as –COOH groups) provided by the functionalized MWCNTs leads to the formation of dense and compact C-S-H structures, a distinct contrast from the control sample. This transformation is attributed to the unique properties of functionalized MWCNTs. Additionally, the efficient transfer of loads from the cement matrix to FMWCNTs can be attributed to the robust covalent forces at the interface between MWCNTs and the products of hydration in the cementitious matrix. However, it's worth noting that at dosages of 0.003% and 0.012% of FMWCNTs, the observed lower strength values could be attributed to the challenges in achieving effective load transfers from the cement matrix to FMWCNTs at higher dosages. For further clarity, Table 4.8 compiles the percentage improvement in tensile strength for FMWCNTs -CNCMs across curing periods of 7, 28, 56, and 90 days. Remarkably, the most substantial percentage increase is attained with 0.0015% FMWCNTs -CNCMs.

4.5.3 Tensile Strength of HCNMs-CNCMs

Figure 4.25 visually represents the tensile strength values of HCNMs-CNCMs across varying dosages of HCNMs (0.0015%, 0.003%, 0.006%, and 0.012%) and different curing durations (7, 28, 56, and 90 days). Additionally, Table 4.9 provides a tabular

overview of the percentage enhancement in tensile strength for the same HCNMs-CNCMs samples.

The evaluation of tensile strength values between the control sample and HCNMs-CNCMs highlighted the most significant strength enhancement at a 0.0015% HCNMs dosage within the cementitious nanocomposites. As curing time extended, a consistent growth in strength was observed across all mix variations. Notably, every mixture exhibited greater strength values compared to the control sample, consistently observed across all curing durations.

At a hydration age of 90 days, the tensile strength measurements for the control sample and HCNMs-CNCMs at varying dosages were recorded as 5.16 MPa, 6.98 MPa, 6.19 MPa, 6 MPa, 5.74 MPa, respectively. The most significant increase in tensile strength was evident among HCN-CNCs at a 0.0015% dosage, showcasing a remarkable 35.27% surge compared to the control sample.

An important observation is that the increase in tensile strength for HCNMs-CNCMs surpassed that of GO-CNCMs and FMWCNTs-CNCMs, with improvements of 7.05% and 12.21%, respectively. For HCNMs-CNCMs, the percentage rise in tensile strength concerning the control mix was as follows: 35.27% for 0.0015%, 19.96% for 0.003%, 16.28% for 0.006%, and 11.24% for 0.012%, all evaluated at a curing age of 90 days. This improved performance can be attributed to the superior dispersion capability of HCNMs within the cement matrix, resulting in a more compact microstructure and reduced micro-porosity (T. B. He et al., 2015; Zhou et al., 2017a).

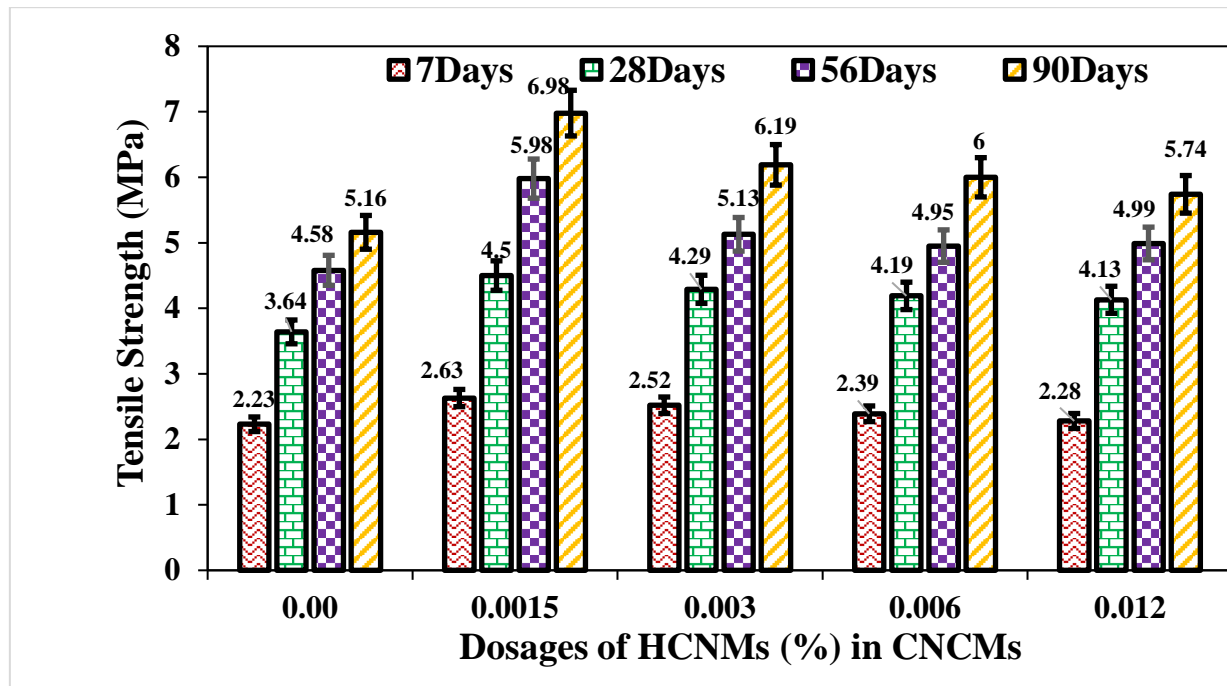


Figure 4.25 Tensile Strength for Control and HCNMs-CNCMs at Different Dosages and Curing Ages

Table 4.9 presents the percentage variation in tensile strength for HCNMs-CNCMs when compared to the control sample, across curing periods of 7, 28, 56, and 90 days.

Table 4.9 Percentage Change in Tensile Strength for HCNMs-CNCMs

Mix Designation	Dosage of HCNMs incorporated (% by weight of cement)	Percentage Change in Tensile Strength with respect to Control (%)			
		7 days	28 days	56 days	90 days
HCNMs-CNCMs	0.0015% HCNMs-CNCMs	18.47	23.41	30.57	35.27
	0.003% HCNMs-CNCMs	13.21	17.65	12.01	19.96
	0.006% HCNMs-CNCMs	7.37	14.90	8.08	16.28
	0.012% HCNMs - CNCMs	2.43	13.26	8.95	11.24

Figure 4.26 illustrates the comparison of tensile strength values for CNCMs based on GO, FMWCNTs, and HCNMs at dosages of 0.0015%, 0.006%, 0.003%, and 0.012%, all evaluated at a curing period of 90 days. This elevated enhancement in tensile strength for HCNMs at the 0.0015% dosage, compared to GO and FMWCNTs at the 0.0015% dosage, can be attributed to the more efficient dispersion of the stabilized 3-D reinforcing agent HCNMs within the cement matrix.

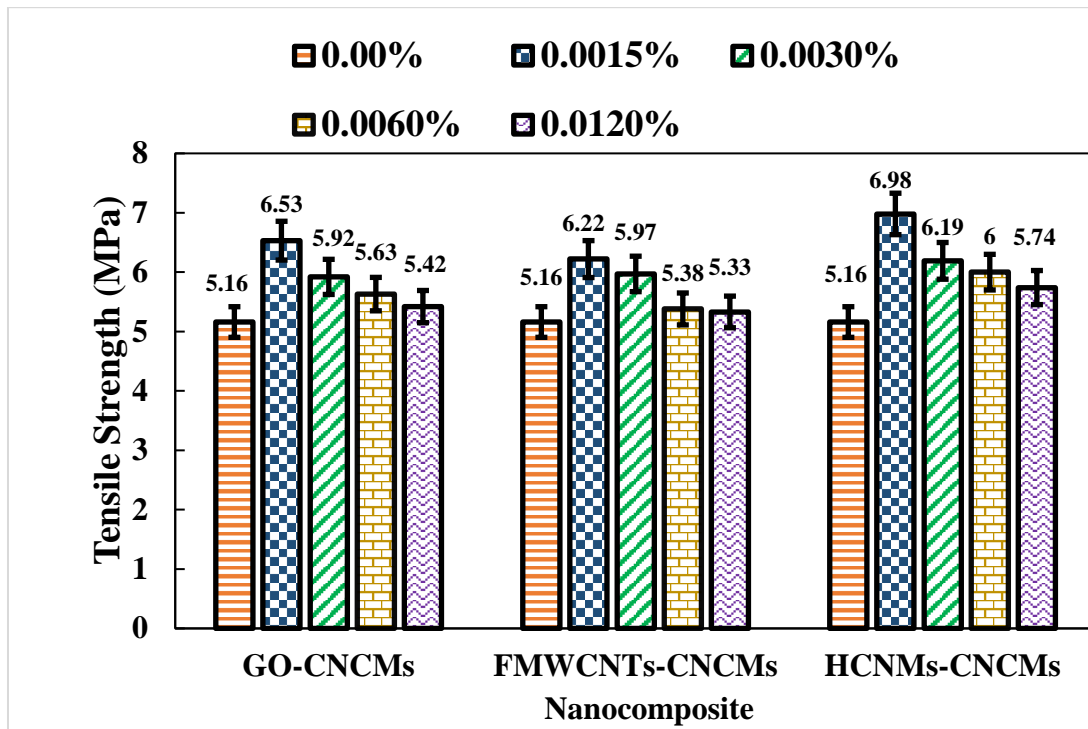


Figure 4.26 Tensile Strength Values (in MPa) for GO, FMWCNTs and HCNMs based CNCMs at 90 Days of Curing

In Figure 4.26, comparison is made among the tensile strength values of GO-CNCMs, FMWCNTs-CNCMs, and HCNMs-CNCMs. For GO-CNCMs, much like FMWCNTs-CNCMs, the highest value occurs at a 0.0015% dosage, followed by a decline, likely due to the reduced dispersion of nanomaterials resulting from higher concentrations. Both GO and FMWCNTs exhibit the greatest enhancement in tensile strength at the 0.0015% dosage, with improvements of 26.35% and 20.61%, respectively, when compared to the control mortar sample. However, in the case of HCNMs-CNCMs, a remarkable strengthening effect is observed at a 0.0015% dosage, with a significant 35.27% increase compared to the control. This notable increase in tensile strength for HCNMs at the dosages of 0.0015% as compared to GO and FMWCNTs is attributed to the improved dispersion of the stabilized 3-D reinforcing agent, HCNMs, within the cement matrix.

Table 4.10 provides a concise overview of the average tensile strength values for CNMs/HCNMs (GO, FMWCNTs, and HCNMs) based CNCMs mortar samples. These values are recorded at various dosages (0.0015%, 0.003%, 0.006%, and 0.012%) and curing durations (7, 28, 56, and 90 days).

Table 4.10 Average Tensile Strength Values of CNMs/HCNMs based CNCMs

S. No	Mix Designation	Dosages of CNMs/HCNMs (% by Weight of Cement)	Tensile Strength (MPa)			
			7 days	28 days	56 days	90 days
1	Control	0.00	2.23	3.64	4.58	5.16
2	GO-CNCMs	0.0015	2.46	4.28	5.74	6.53
		0.003	2.31	3.82	4.92	5.92
		0.006	2.29	3.79	4.82	5.63
		0.012	2.25	3.74	4.75	5.42
3	FMWCNTs-CNCMs	0.0015	2.31	3.88	5.19	6.22
		0.003	2.29	3.86	5.11	5.97
		0.006	2.28	3.77	4.82	5.38
		0.012	2.27	3.74	4.71	5.33
4	HCNMs-CNCMs	0.0015	2.63	4.5	5.98	6.98
		0.003	2.52	4.29	5.13	6.19
		0.006	2.39	4.19	4.95	6.00
		0.012	2.28	4.13	4.99	5.74

The conclusions for compressive strength of cementitious nanocomposites are as follows:

- 1 The inclusion of individual carbon nanomaterials (either GO and FMWCNTs) as well as hybrid carbon nanomaterials (GO and FMWCNTs) led to varying degrees of improvement in the compressive strength in cementitious nanocomposites. This enhancement was observed at different curing times.
- 2 For GO, the most significant enhancement in compressive strength, amounting to 11.67, was achieved with 0.0015% dosage of GO-CNCMs after a curing period of 90 days.
- 3 In the case of FMWCNTs, the highest compressive strength enhancement of 8.73 has been obtained for 0.0015% FMWCNTs-CNCMs after 90 days of curing.

- 4 The highest compressive strength for HCNMs-CNCMs was observed at the 0.0015% dosage, resulting in a remarkable 21.32% improvement compared to the control.

The summarized conclusions for tensile strength of cementitious nanocomposites are as follows:

- 1 Similar to GO-CNCMs, FMWCNTs-CNCMs exhibited their highest tensile strength at a 0.0015% dosage, with improvements of 26.35% and 20.61% compared to the control. However, a subsequent decrease in strength was observed beyond the 0.0015 dosage, likely due to reduced nanomaterial dispersion.
- 2 On the other hand, HCNMs incorporated CNCMs demonstrated the highest increase in tensile strength at a relatively higher dosage of 0.0015%, resulting in a remarkable 35.27% improvement compared to the control mortar providing a possible pathway to pozzolana Portland cementitious mortar based in application of construction building materials.

MICROSTRUCTURAL AND CRYSTALLIZATION BEHAVIOR STUDIES

The effectiveness of different reinforcing agents (FMWCNTs, GO, and HCNMs) stabilized by SP in improving the mechanical properties of the mortars has been evaluated through microstructural and crystalline analyses using field emission-scanning electron microscope (FE-SEM), Powdered X-ray diffraction (PXRD) and Fourier transform-infrared (FT-IR) techniques.

To investigate the microstructural characteristics of cementitious nanocomposites (CNCMs) at various carbon nanomaterials (CNMs) and hybrid carbon nanomaterials (HCNMs) dosages, were conducted using FE-SEM, as detailed in Chapter 3.

The dosages incorporated into the cementitious nanocomposites (CNCMs) ranged from 0.0015% to 0.012% by weight percentage of cement. FE-SEM microstructural analyses were conducted at curing ages of 7, 28, 56, and 90 days. The obtained micrographs for CNMs/HCNMs incorporated CNCMs were compared with those of the control samples to assess the impact of carbon nanomaterials on the enhanced microstructure characteristics of mortars. A detailed discussion of the conclusions drawn from these analyses can be found in Section 4.5.

Similarly, the analysis of the crystalline phases present in the hydrated mortar samples was conducted using crystallization studies via PXRD, as detailed in Chapter 3. The degree of hydration for both control samples and CNMs/HCNMs incorporated CNCMs was assessed by performing qualitative and quantitative analyses of the hydration phases formed. PXRD spectra were obtained at curing ages of 90 days. The phase analysis studies of CNMs/HCNMs (at dosages of 0.0015%, 0.003%, 0.006%, and 0.012%; by weight percentage of the cement) incorporated into CNCMs were compared to the control mortar samples to evaluate the reinforcing effects of carbon nanomaterials. A comprehensive discussion of the results obtained is presented in Section 4.6.

Along with the Microstructural and crystalline properties this study conducted Fourier-transform infrared (FT-IR) spectroscopy using a Nicolet 5DXC FT-IR spectrometer, covering the range of 4000-500 cm^{-1} . After applying background correction, we generated the spectra by averaging 10 scans at a resolution of 1 cm^{-1} . This analytical

technique was employed to scrutinize the distinctive features of hydrated cement samples at two different time points: 7 and 90 days of curing. The analysis involved collecting 2 mg samples from each mixture, followed by subjecting them to a 24-hour drying process in an oven maintained at $35^{\circ}\text{C} \pm 5^{\circ}\text{C}$. Subsequently, the samples were encapsulated in KBr pellets for further characterization. A thorough analysis and interpretation of the findings are provided in Section 4.7.

4.6 MICROSTRUCTURAL STUDIES OF CNMs/HCNMs BASED CNCMs

4.6.1 Microstructural Studies of Control sample of Mortars

Figure 4.27(a-d) shows the FE-SEM micrograph of the Control mortar sample after the curing ages of 7, 28, 56, and 90 days, respectively.

Observations from the FE-SEM images reveal distinct characteristics in the microstructure of the Control mortar sample. It exhibits loosely bound hydration products, including calcium silicates and calcium aluminates, accompanied by a substantial presence of micro-scale pores and voids. In the hydrated cement mortars, a diverse range of hydration products is discernible, exhibiting growth in various directions, which contributes to the development of a brittle cementitious matrix. Particularly in the early stages of hydration, these hydration products tend to form a loose microstructure. However, as the curing time progresses, a notable transformation is evident in the mortar samples microstructure. This transformation is marked by an increase in hardness and a reduction in pore characteristics, primarily due to the continuous formation and accumulation of hydration products over the time. The major crystalline hydration products identified include calcium hydroxide (C-H), ettringite (AFt), and monosulphates (AFm).

During the hydration process, calcium silicates, represented by C_3S and C_2S , undergo reactions that lead to the formation of calcium hydroxide. On the other hand, aluminates, such as C_3A and C_4AF , undergo hydration reactions that result in the formation of ettringite and monosulphates. C-H typically presents itself in the cement matrix in the form of hexagonal plates. In contrast, ettringite is primarily found as a network of needle-shaped crystals. It's important to note that ettringite is most prevalent during the early stages of hydration. As time progresses and the hydration reactions continue, the

simultaneous production of other hydration products can obscure or mask the presence of ettringite.

The hydration product known as calcium-silicate-hydrate (C-S-H) is of great significance, and it tends to become more prevalent at later curing ages, typically ranging from 28 to 90 days. C-S-H exists in a semi-crystalline form, and it can take on various structures, including fibrillar or gel-like forms within the cementitious matrix (L. Zhao, Guo, Liu, Zhao, et al., 2018).

Figure 4.27(a) provides a visual representation of randomly scattered ettringite needles, which was derived from tricalcium aluminate (C_3A), particularly at the early stages of hydration, such as at 7 days of curing. However, excessive ettringite formation found to be the cause of an expansion in the cement matrix, resulting in brittleness. For the control sample at hydration ages of 28 and 56 days (Figure 4.27(b) and 4.19(c)), the microstructure C-S-H gel porous structure which is loosely interacted due to the hydration of cement compounds (silicates), namely C_3S and C_2S . At the 90-day hydration age, a relatively thicker and more compact C-S-H gel framework are observed, as depicted in Figure 4.27(d) (Q. Wang et al., 2019).

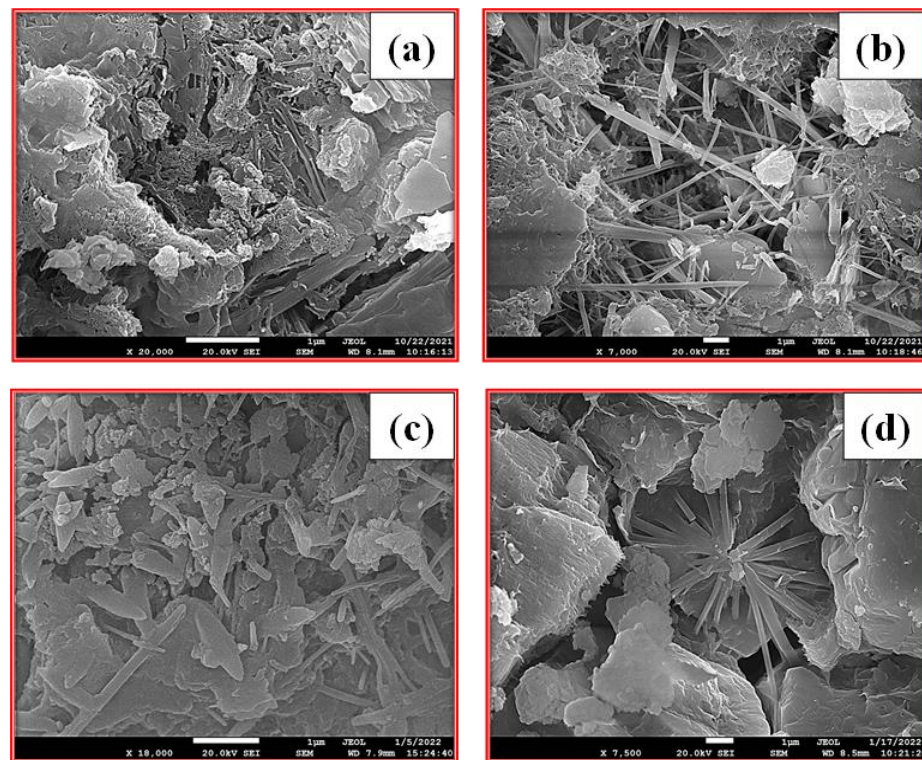


Figure 4.27 FE-SEM Images of Control specimen after (a) 7 days (b) 28 days (c) 56 days and (d) 90 days of Curing

4.6.2 Microstructural Studies of GO-CNCMs

The micrographs obtained from FE-SEM analysis of GO-CNCMs at different curing ages (7, 28, 56, and 90 days) are depicted in Figure 4.28, 4.29, 4.30, and 4.31, correspondingly. These images provide valuable insights into the microstructural changes that occurred at various stages of curing, which are discussed in detail below.

4.6.2.1 Microstructure Analysis at 7 Days of Curing

FE-SEM micrographs of GO-CNCMs at dosages of 0.0015%, 0.003%, 0.006%, and 0.012% after 7 days of curing are presented in Figure 4.28(a), 4.28(b), 4.28(c), and 4.28(d) respectively. The incorporation of superplasticizer-modified Graphene oxide (GO) improves the densification of cement hydration products in comparison to the Control mortar sample. GO facilitates the alignment of hydration products, resulting in improved microstructure.

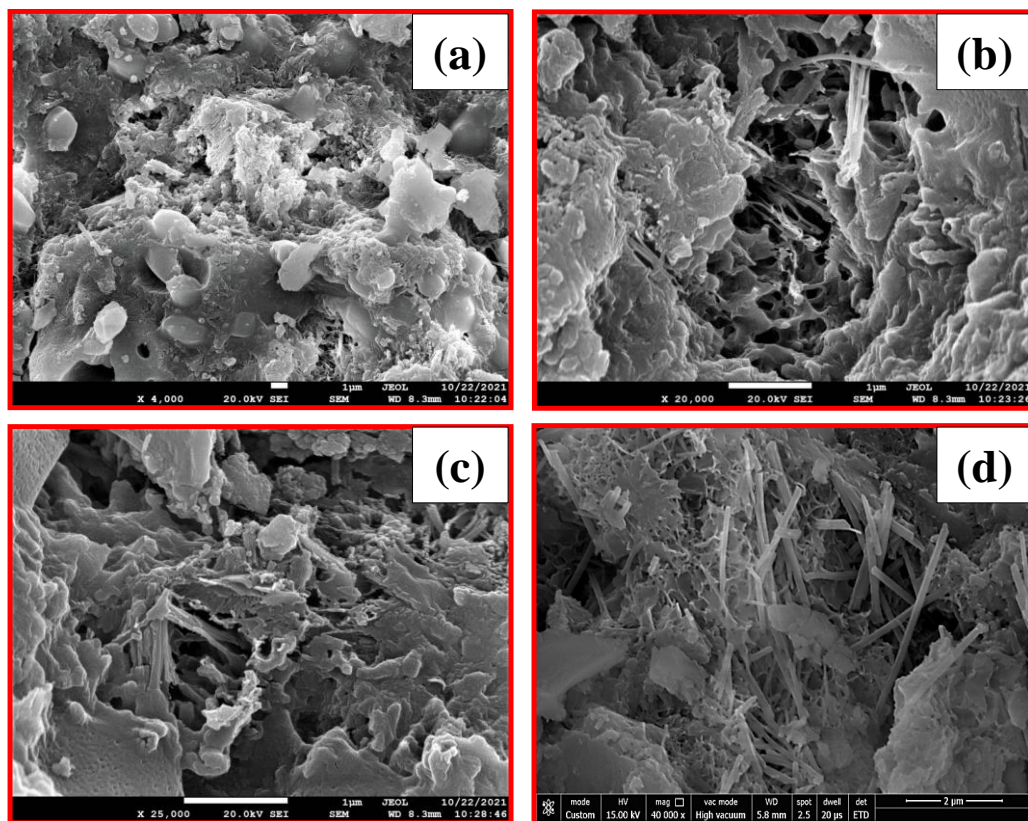


Figure 4.28 FE-SEM Images of GO-CNCMs after 7 Days of Curing (a) 0.0015% GO-CNCMs (b) 0.003% GO-CNCMs (c) 0.006% GO-CNCMs (d) 0.012% GO-CNCMs

The oxygen functionalities present on GO's corrugated graphene sheets serve as nucleation and crystallization sites for C-S-H gel, which is the major binding agent of the cementitious matrix. Figure 4.28(a) depicts the progression of the C-S-H gel

network formation resulting from the hydration process of calcium silicates, in conjunction with the concurrent existence of ettringite(Suo et al., 2020). However, at a higher dosage of GO (0.003%), the C-S-H gel structure appeared to be porous, as shown in Figure 4.28(b), consisting of loosely packed gel bars arranged regularly.

As the GO dosage increased further (Figure 4.28(c) and 4.20(d)), The presence of hydration products such as ettringite, delicate C-S-H gel structures, and hexagonal platy calcium hydroxide (C-H) crystals was observed. GO provides a significant surface area and crystallization sites for the hydration process, resulting in the production of the C-S-H binder gel. This C-S-H gel then infiltrates the cracks and voids within the cementitious matrix, effectively filling them and enhancing mechanical strength.

4.6.2.2 Microstructure Analysis at 28 Days of Curing

The FE-SEM micrographs depicting GO-CNCMs at the curing age of 28 days are presented in Figure 4.29(a-d). With the inclusion of 0.0015% GO in CNCMs, a noticeable conversion of the early hydration-produced C-S-H loose gel into densely compacted gels, as depicted in Figure 4.29(a). The accelerated hydration rate of GO-CNCMs contributes to a more consolidated microstructure in comparison to the control samples. As the dosage increases to 0.003%, as shown in Figure 4.29(b), the C-S-H gel cages expand further over the previously formed hydration masses, accompanied by only a few porous needles. This leads to the development of adhered masses of hydrates that likely thicken over time.

Figure 4.29(c) demonstrates compact C-S-H gel bars separated by porous hydration products. This increasing porosity as the GO dosage rises is linked to the decrease in mechanical strength of the cementitious nanocomposites. At a GO dosage of up to 0.012% (Figure 4.29(d)), there was an expansion of a platy arrangement of hydration products. This structure included stacked C-H crystals and C-S-H phases growing, and forming a thick but fragile structure. The likely reason for the creation of a porous C-S-H network at higher dosages could be the partial agglomeration of GO sheets(Yan et al., 2020). This agglomeration restricts the full utilization of GO's potential as a reinforcing agent in the cementitious matrix.

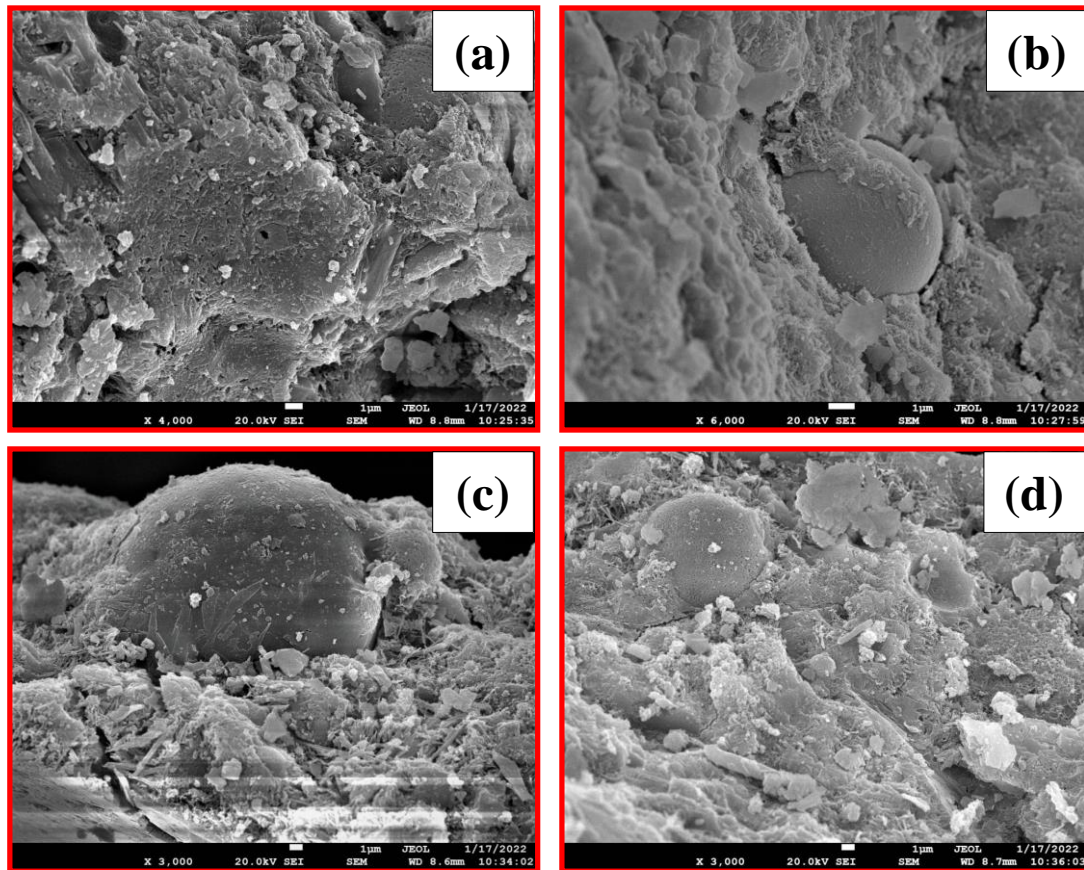


Figure 4.29 FE-SEM Images of GO-CNCMs after 28 Days of Curing (a) 0.0015% GO-CNCMs (b) 0.003% GO-CNCMs (c) 0.006% GO-CNCMs (d) 0.012%GO-CNCMs

4.6.2.3 Microstructure Analysis at 56 Days of Curing

The FE-SEM images illustrating the GO-CNCMs following a 56day curing period are displayed in Figure 4.30(a-d). Figure 4.30(a) showcases the development of robust, product bars such as polyhedral hydration, organized in a stacked configuration. This arrangement suggests that the C-S-H or C-H hydration products may arranged in a systematic way because of the chemical link between the carboxylate groups of GO and those of the C-S-H/C-H hydration products. This chemical bonding increases adhesion at the interface between reinforcement and cementitious matrix(Qureshi & Panesar, 2019).

In the case of CNCMs incorporating 0.003% and 0.006% of GO, well-aligned C-S-H gel bars can be observed, but with reduced cohesion among the C-S-H bars compared to CNCMs with 0.0015% GO (Figure 4.30(b and c)). Figure 4.30(d) depicts an irregularly arranged, granular form of C-S-H hydration products, which contributes to its lower compressive strength compared to the other three GO dosages.

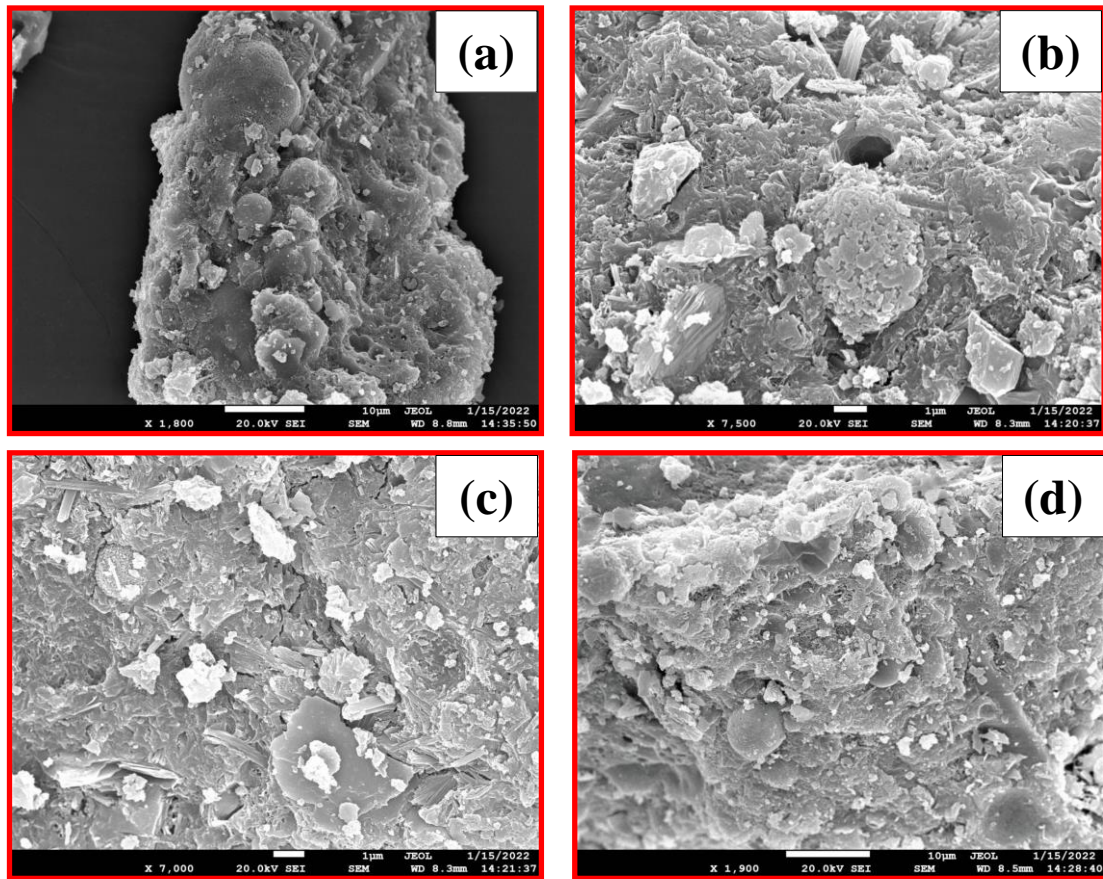


Figure 4.30 FE-SEM Images of GO-CNCMs after 56 Days of Curing (a) 0.0015% GO-CNCMs (b) 0.003% GO-CNCMs (c) 0.006% GO-CNCMs (d) 0.012%GO-CNCMs

4.6.2.4 Microstructure Analysis at 90 Days of Curing

The FE-SEM micrographs, illustrating the impact of different GO dosages on the hydration process of CNCMs at the 90-day curing mark, are presented in Figure 4.31(a-d). Over the course of 90 days, the overall compactness of the cementitious structure has enhanced. The hydrophilic characteristics of GO sheets have played a pivotal role in addressing the cracks observed at the 28-day mark. These two-dimensional GO sheets have effectively bridged the gaps, establishing an interconnected network within the hydration(S. Meng et al., 2021; Xu et al., 2019). In the instance of incorporating 0.0015% of GO dosage, the polyhedral C-S-H hydration products, organized in a regular pattern, progress into even more compact hydration products, displaying a notable level of adhesion compared to other GO dosages can be observed in Figure 4.31(a). This clearly highlights that the robust, polyhedral-shaped hydration products contribute to superior compressive strength, whereas granular-shaped hydrates play a role in enhancing tensile strength in GO-CNCMs. This progression underscores the

development and arrangement of hydration crystals for various GO-CNCMs over the course of increased hydration time. The expansion of hydration products into previously vacant voids and cracks at later stages contributes to the refinement of the microstructure within the cementitious matrix(Gong et al., 2014; D. Lu & Zhong, 2022; Makar, 2011). Moreover, when a higher amount of GO is introduced i.e., 0.003, 0.006 and 0.012% into the mortar, there is a potential for agglomeration, resulting in the clustering of GO sheets. This clustering can generate voids or pores within the material, ultimately contributing to the formation of a porous microstructure can be depicted in Figure 4.31(b, c and d).

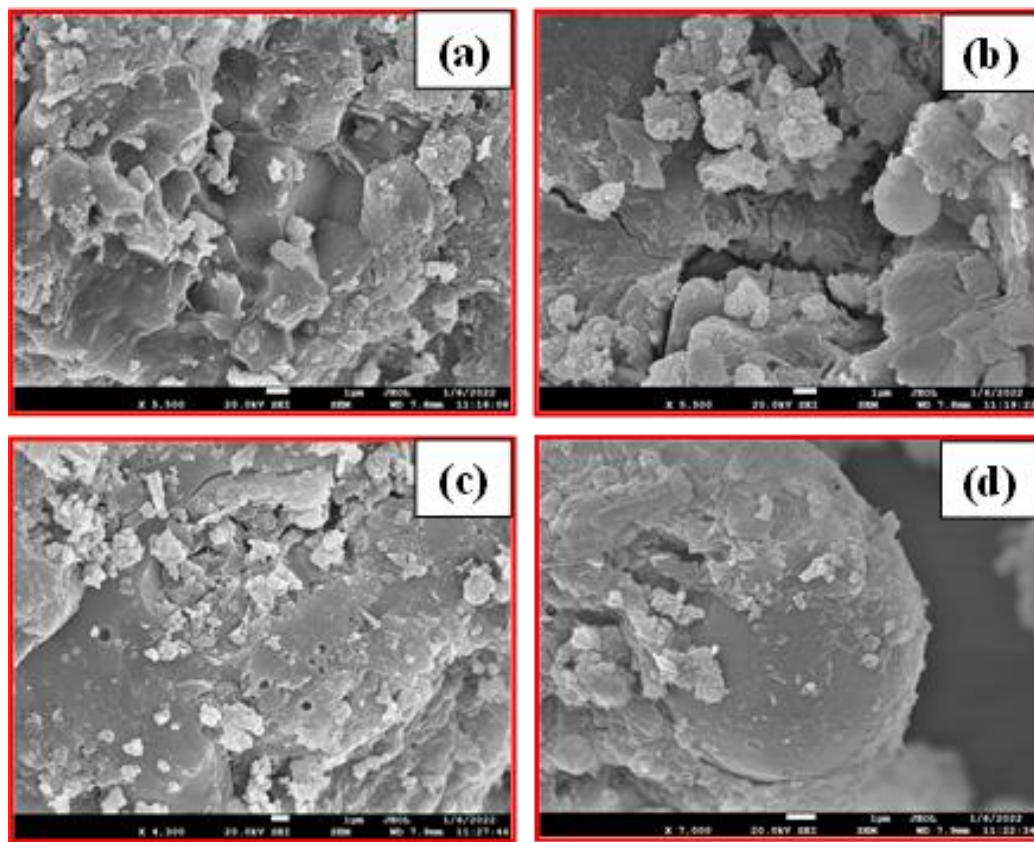


Figure 4.31 FE-SEM Images of GO-CNCMs after 90 Days of Curing (a) 0.0015% GO-CNCMs (b) 0.003% GO-CNCMs (c) 0.006% GO-CNCMs (d) 0.012%GO-CNCMs

4.6.3 Microstructural Studies of FMWCNTs-CNCMs

The FE-SEM images depicting FMWCNTs-CNCMs at curing intervals of 7, 28, 56, and 90 days are presented in Figures 4.32, 4.33, 4.34, and 4.35, respectively. The subsequent sections delve into an in-depth microstructural analysis following varying curing durations.

4.6.3.1 Microstructure Analysis at 7 Days of Curing

The FE-SEM images of FMWCNTs-CNCMs taken at the 7day curing stage exhibit significant distinctions compared to the Control samples. Specifically, at the 7-day hydration age, the micrograph for 0.0015% FMWCNTs-CNCMs reveals the emergence of hydration products, including ettringite, alongside less dense C-S-H gel structures exhibiting limited integrity. These granular C-S-H gel structures are notably present within the cementitious matrix, as evidenced by Figure 4.32(a). It's important to highlight that as the dosage of FMWCNTs is progressively increased up to 0.0015%, there is a noticeable improvement in the hydration products with compactness.

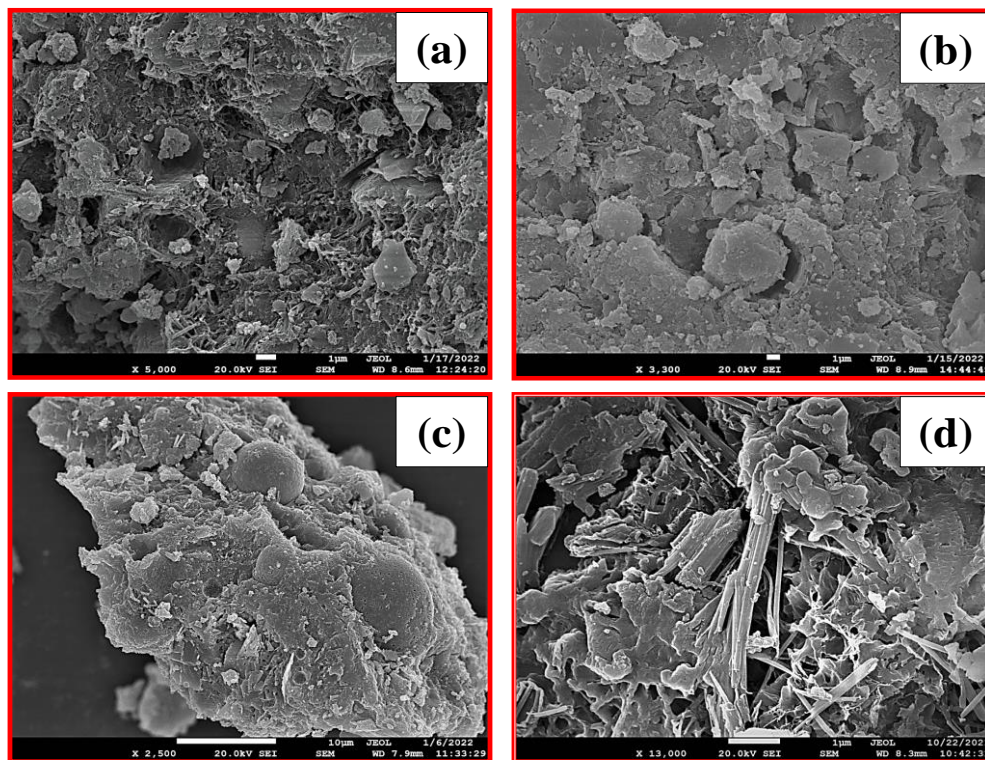


Figure 4.32 FE-SEM Images of FMWCNTs-CNCMs after 7 Days of Curing (a) 0.0015% FMWCNTs-CNCMs (b) 0.003% FMWCNTs-CNCMs (c) 0.006% FMWCNTs-CNCMs (d) 0.012%FMWCNTs-CNCMs

Figure 4.32(b) clearly showcases the development of the C-S-H gel network alongside a sparse presence of ettringite needles across the cement phases. This observation underscores the progression of hydration products. It's important to highlight that the functional groups present on the walls of FMWCNTs serve as nucleation sites for the burgeoning hydration products. This phenomenon is related to the establishment of great covalent interactions at the interface between FMWCNTs and the emerging hydration products, similar studies conducted by Chuah et al. (2014) and Sharma et al. (2016). As increase in the dosage of FMWCNTs dosage in the cementitious matrix to

0.003% an irregular yet dense C-S-H gel structure with less evident voids or pores can be visualized in Figure 32(c). However, when the dosage of FMWCNTs was raised to 0.012% (as shown in Figure 4.32(d)), a small amount of C-S-H gel was observed along with hexagonal C-H plates. The observed phenomenon can be ascribed to the poor dispersion of FMWCNTs within the cementitious matrix when greater dosages are used, notwithstanding their stabilization through the addition of a superplasticizer.

4.6.3.2 Microstructure Analysis at 28 Days of Curing

The FE-SEM analysis for FMWCNTs-CNCMs at the 28day curing stage are displayed in Figure 4.33(a-d). It is important to note that as the curing period extends from 7 to 28 days, there is a noticeable expansion in the growth of hydration products, attributable to the increased hydration reactions.

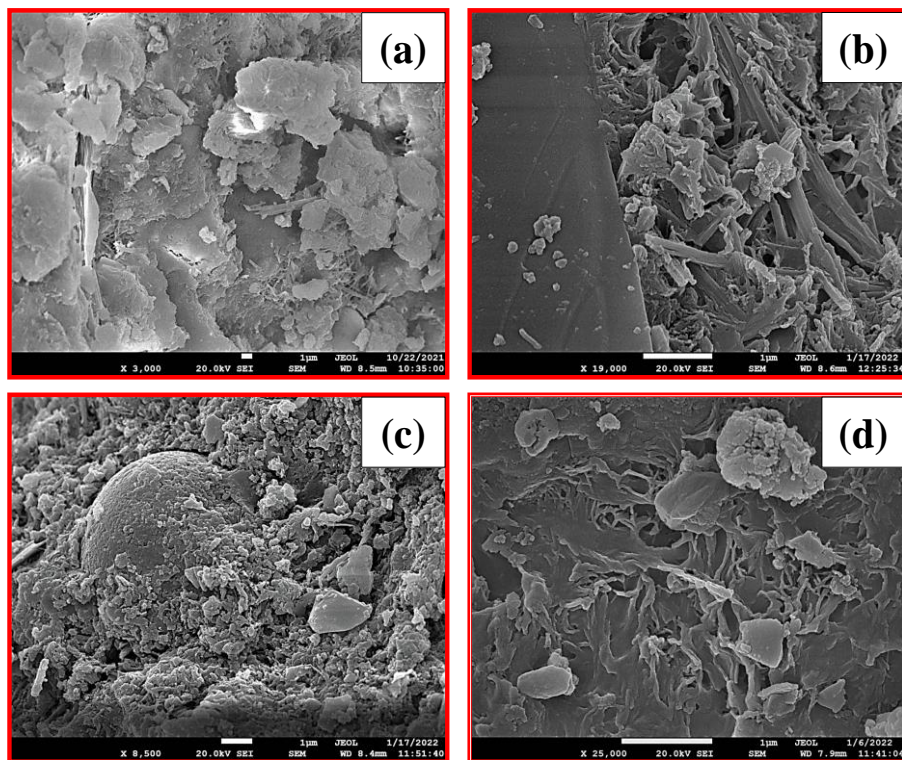


Figure 4.33 FE-SEM Images of FMWCNTs-CNCMs after 28 Days of Curing (a) 0.0015% FMWCNTs-CNCMs (b) 0.003% FMWCNTs-CNCMs (c) 0.006% FMWCNTs-CNCMs (d) 0.012%FMWCNTs-CNCMs

In the case of a 0.0015% incorporation of FMWCNTs, there is a distinct observation of relatively thicker C-S-H gel structures, accompanied by a limited presence of ettringite needles when compared to the FMWCNTs-CNCMs at the 7-day hydration stage. Figure 4.33(a) provides a clear depiction of stacked sheets of C-S-H gel structures layered upon each other, forming during the hydration process.

On further increasing the FMWCNTs dosage up to 0.003%, comparatively more rigid hydration products are obtained with reduced empty voids, as shown in Figures 4.33(b). However, for 0.006% and 0.012% FMWCNTs incorporation into the cement matrix, a relatively loose and porous microstructure was obtained even after 28 days of curing as shown in Figures 4.33(c) and 4.33(d).

4.6.3.3 Microstructure Analysis at 56 Days of Curing

The micrographs acquired for FMWCNTs-CNCMs following a 56day curing period are featured in Figure 4.34. Notably, Figure 4.34 (a) shows significant enhancement is evident with the FMWCNTs dosage up to 0.0015%. In these images, it observed well-structured and orderly arranged C-S-H bars adhere a top one another. These structures are accountable for the heightened compressive strength and reduced water absorption observed in the cement nanocomposites.

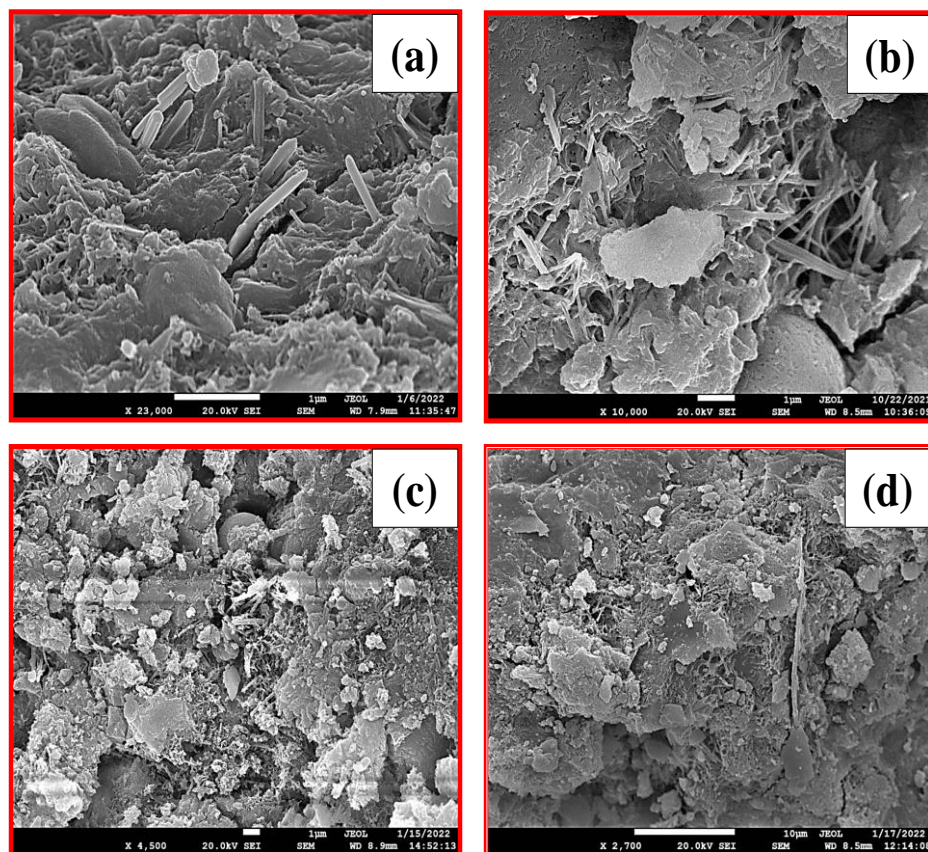


Figure 4.34 FE-SEM Images of FMWCNTs-CNCMs after 56 Days of Curing (a) 0.0015% FMWCNTs-CNCMs (b) 0.003% FMWCNTs-CNCMs (c) 0.006% FMWCNTs-CNCMs (d) 0.012%FMWCNTs-CNCMs

However, highlights the loose network nature of the C-S-H gel as illustrated in Figure 4.34(b and c). Conversely, in the case of a 0.012% FMWCNTs added cementitious

matrix, the cohesion shows these gel bars is somewhat diminished due to the clustering and agglomeration of FMWCNTs as shown in Figure 4.34(d). This results in a decline in compressive strength. However, it's worth noting that the tensile strength is maximized in the case of 0.0015% FMWCNTs-CNCMs, attributed to the efficient transfer of loads from the cement mortar to FMWCNTs, as described in the study by Konsta-Gdoutos et al. (2017)(Konsta-Gdoutos et al., 2017).

4.6.3.4 Microstructure Analysis at 90 Days of Curing

The FE-SEM micrographs showcasing FMWCNTs-CNCMs after 90 days of curing are presented in Figure 4.35(a-d). Notably, as the dosage of FMWCNTs in the CNCMs rises in case of 0.0015%, there is a discernible reduction in voids or porosity within the hydrated mortar system, as evident in Figures 4.35(a).

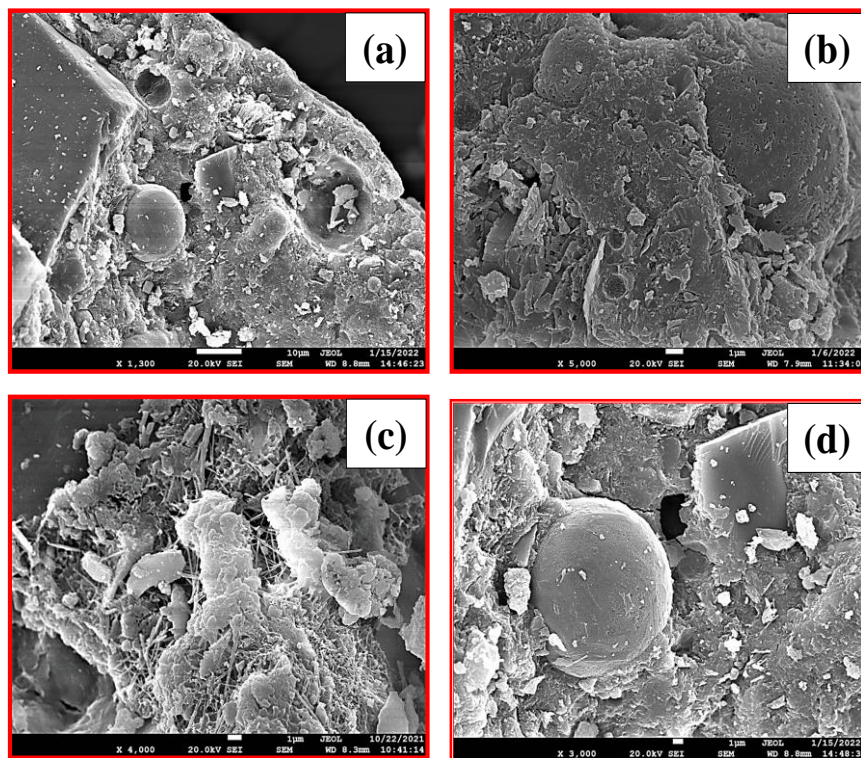


Figure 4.35 FE-SEM Images of FMWCNTs-CNCMs after 90 Days of Curing (a) 0.0015% FMWCNTs-CNCMs (b) 0.003% FMWCNTs-CNCMs (c) 0.006% FMWCNTs-CNCMs (d) 0.012% FMWCNTs-CNCMs

This phenomenon can be attributed to the progression of hydration reactions, resulting in the generation of more hydration products that interlock with one another. However, for FMWCNTs-CNCMs with a 0.003, 0.006 and 0.012% dosages of FMWCNTs, a relatively porous network of C-S-H gel is found. This can be attributed to the less efficient dispersion of SP stabilized FMWCNTs at higher dosages within the CNCMs matrix, as depicted in Figure 4.35(b-d).

The functional groups present on FMWCNTs serve as nucleation sites for the crystallization of hydration products such as C-S-H gel and portlandite (C-H), among others. Furthermore, these reactive nucleation sites facilitate robust interfacial bonding between C-S-H gel and FMWCNTs, enhancing the overall material properties, in accordance with studies by Lv et al. (2013) and Kurda et al. (2018)(Kurda et al., 2019; S. Lv, Ma, Qiu, Sun, et al., 2013b).

4.6.4 Microstructural Studies of HCNMs-CNCMs

The FE-SEM images illustrating distinct dosages of HCNMs-CNCMs across curing periods of 7, 28, 56, and 90 days are presented in Figures 4.36, 4.37, 4.38, and 4.39, respectively. The subsequent sections delve into an exhaustive microstructural analysis of HCNMs-CNCMs across varying curing durations.

4.6.4.1 Microstructure Analysis at 7 Days of Curing

The FE-SEM micrographs showcasing HCNMs-CNCMs at the 7day curing age and varying dosages of 0.0015%, 0.003%, 0.006%, 0.012% are displayed in Figure 4.36(a-d).

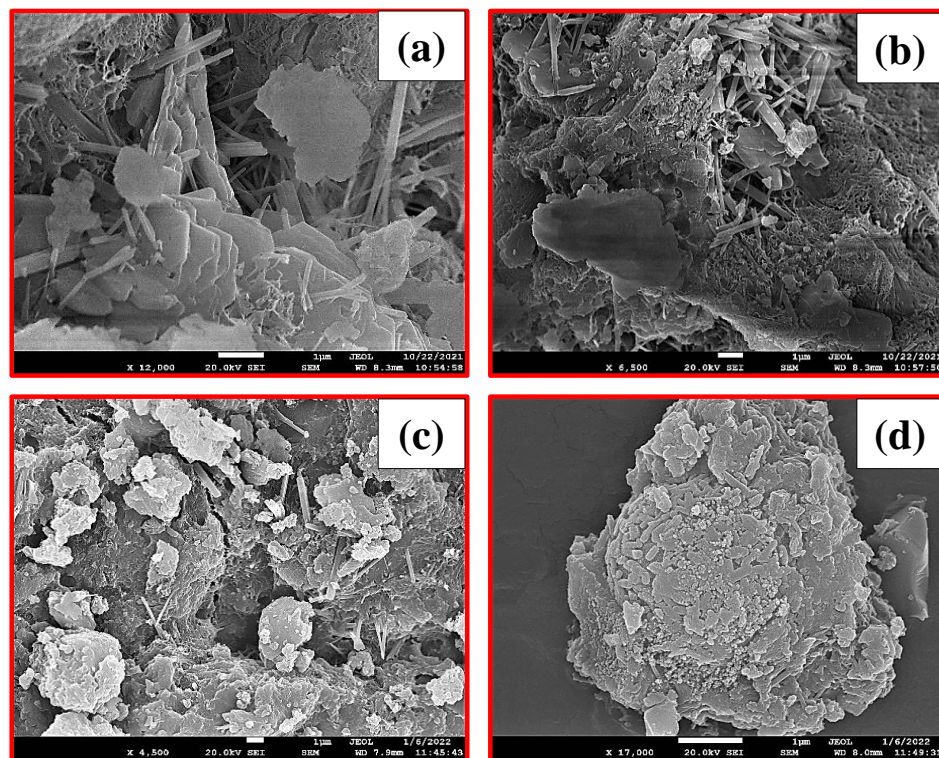


Figure 4.36 FE-SEM Images of HCNMs-CNCMs after 7 Days of Curing (a) 0.0015% HCNMs-CNCMs (b) 0.003% HCNMs-CNCMs (c) 0.006% HCNMs-CNCMs (d) 0.012% HCNMs-CNCMs

An examination of the hydration crystal morphology underscores the significant influence of HCNM dosage on the shape of cement hydration crystals. At an HCNM

dosage of 0.0015% (Figure 4.36(a)), a smooth layer of hydrated cement phases is evident, adorned with flake-like hydration crystals.

Upon increasing the HCNMs dosage to 0.006%, a sight of irregular hydration products and rod-like hydration crystals, arranged in a disorderly manner, can be observed (Figure 4.36(b)). Upon reaching a dosage of 0.003% HCNMs-CNCMs, flaky and porous cement hydration products emerge at the 7-day curing ages, as depicted in Figure 4.36(c). With higher HCNMs dosages, such as 0.012%, the micrographs reveal a porous morphology of hydration products featuring ettringite needles and low-density C-S-H gel (Figure 4.36(d))(Kaur & Kothiyal, 2019c).

4.6.4.2 Microstructure Analysis at 28 Days of Curing

The FE-SEM images displaying HCNMs-CNCMs at the 28 days curing stage are featured in Figure 4.37(a-d). Notably, at lower HCNMs dosages, one can observe flake-like crystals arranged in flower-like patterns, as depicted in Figure 4.37(a-b). However, this array of hydration products appears to be loosely interconnected.

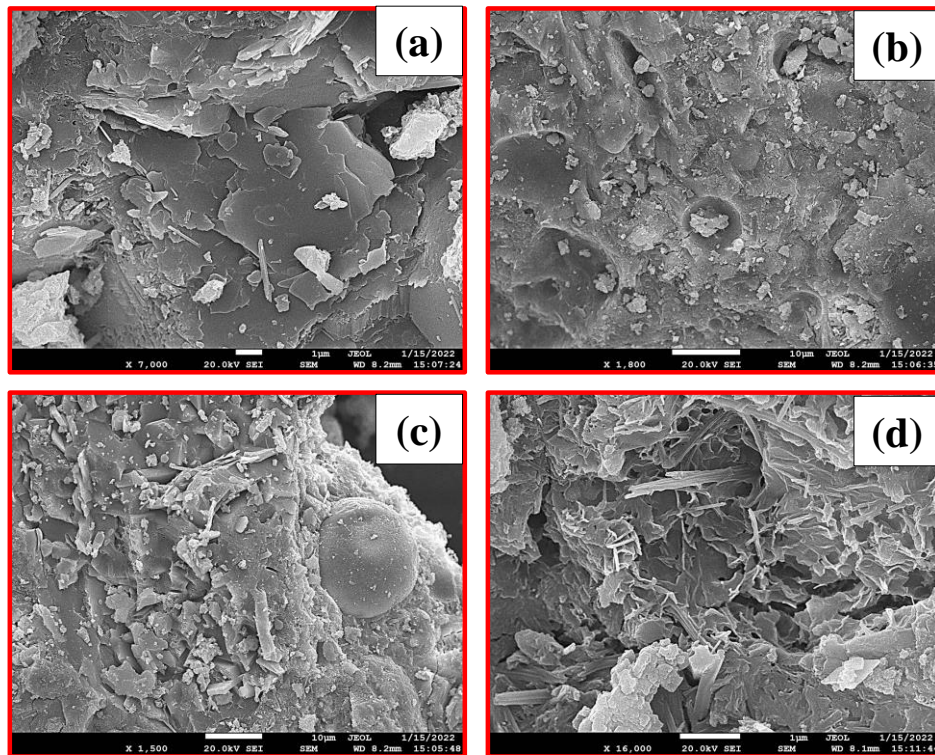


Figure 4.37 FE-SEM Images of HCNMs-CNCMs after 28 Days of Curing (a) 0.0015% HCNMs-CNCMs (b) 0.003% HCNMs-CNCMs (c) 0.006% HCNMs-CNCMs (d) 0.012% HCNMs-CNCMs

The presence of these flaky hydration products, such as C-H, is likely a result of crystallization induced by the three-dimensional arrangement of Hybrid Carbon

Nanomaterials (HCNMs). These flower-like crystals serve as crack arrestors or fillers, extending into micro-cracks or voids within the hardened cement to create a well-crosslinked structure (H. Cui et al., 2017; S. Lv, Ting, et al., 2014). At higher HCNMs dosages, the ordered arrangement of hydration products is not observed due to a relatively lower degree of dispersion of HCNMs within the cementitious matrix. Nonetheless, there is evidence of a short-range order of hydration products, surrounded by the C-S-H gel, as seen in Figure 4.37(c-d).

4.6.4.3 Microstructure Analysis at 56 Days of Curing

The FE-SEM micrographs capturing HCNMs-CNCMs at the 56 days curing ages are displayed in Figure 4.38(a-d). Across all HCNMs dosage levels within the CNCMs, a consistently ordered flower-like framework is observed, contributing to a well-connected structure. However, it is noted that the hydration products become lower dense as the HCNMs dosage increases from 0.006% to 0.012%, as reported by Lv et al. (2014). In the case of 0.0015% HCNMs-CNCMs (Figure 4.38(a)), the increased cohesion and densification of flower-like hydration patterns can be attributed to the effective dispersion of HCNMs at lower extents as compared to higher ones (S. Lv, Ma, Qiu, Sun, et al., 2013b).

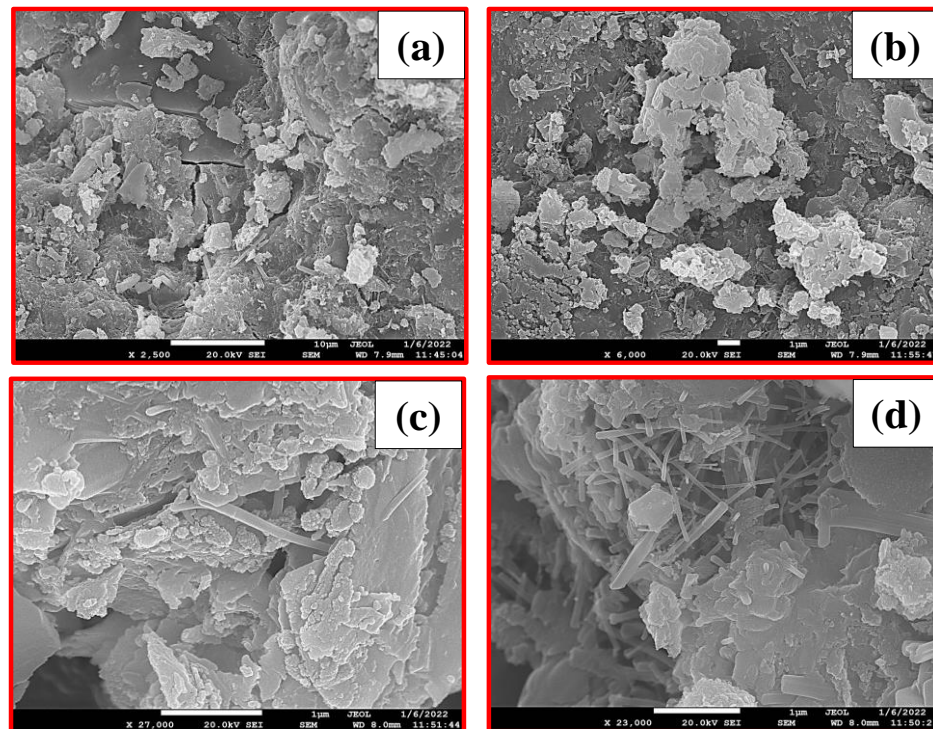


Figure 4.38 FE-SEM Images of HCNMs-CNCMs after 56 Days of Curing (a) 0.0015% HCNMs-CNCMs (b) 0.003% HCNMs-CNCMs (c) 0.006% HCNMs-CNCMs (d) 0.012% HCNMs-CNCMs

Consequently, HCNMs promote more arranged crystal growth of hydrated cements, resulting in the formation of non-porous structure when compared to GO-CNCMs and

FMWCNTs-CNCMs. However, as we progress from 0.003% to 0.012% HCNMs-CNCMs (Figure 4.38(b-d)), the uniformly distributed flower-like patterns become less substantial, contributing to a decrease in strength properties at higher dosages.

4.6.4.4 Microstructure Analysis at 90 Days of Curing

The FE-SEM images depicting HCNMs-CNCMs after 90 days of curing are showcased in Figure 4.39(a-d). Notably, for 0.0015% HCNMs-CNCMs (Figure 4.39(a)), a tightly interwoven microstructure of flower-like patterns observed at the 28-day curing stage results in a compact, dense, and smooth C-S-H gel structure. In contrast, for 0.003% HCNMs-CNCMs, one can observe polyhedral-shaped C-S-H bars, densely stacked atop one another. These polyhedral-shaped structures emerge from the transformation of the flower-shaped hydration products observed during the initial curing stages (i.e., at 56 days), evolving into a denser polyhedral form can be shown in Figure 4.39(b).

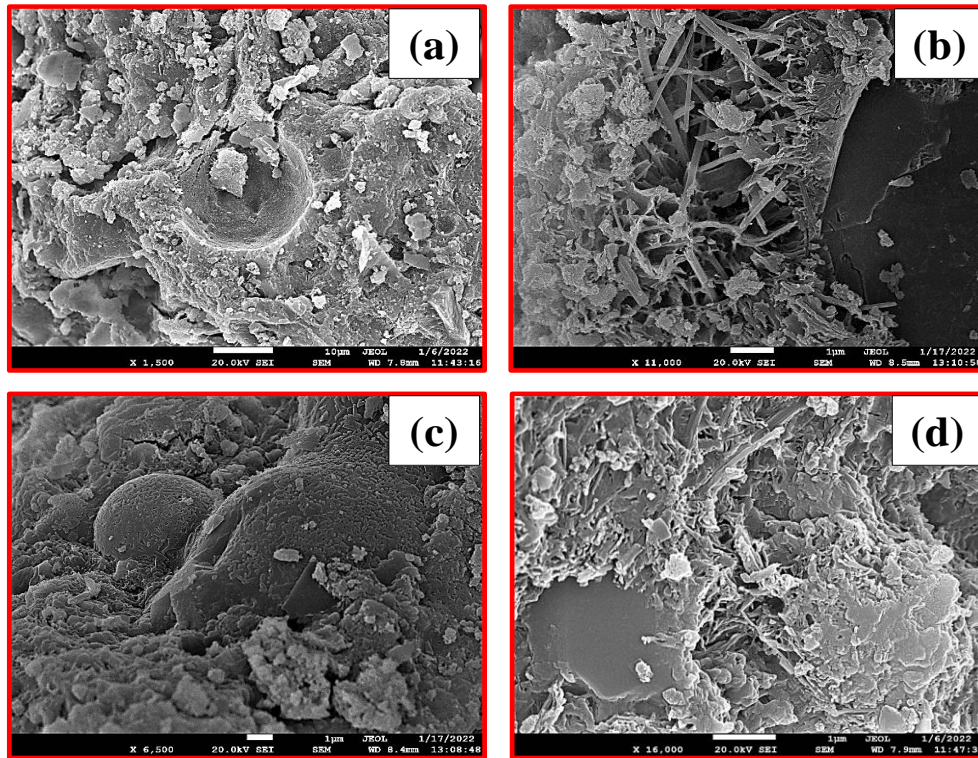


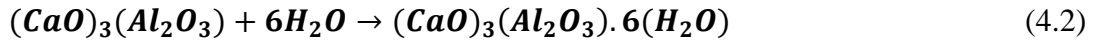
Figure 4.39 FE-SEM Images of HCNMs-CNCMs after 90 Days of Curing (a) 0.0015% HCNMs-CNCMs (b) 0.003% HCNMs-CNCMs (c) 0.006% HCNMs-CNCMs (d) 0.012% HCNMs-CNCMs

For 0.006% and 0.012% HCNMs-CNCMs, irregular blocks of high-density C-S-H gel are obtained, as illustrated in Figure 4.39(c) and 4.39(d), respectively. However, it's worth noting that the hydration products acquired in these cases exhibit a degree of porosity compared to the hydration products obtained at lower HCNMs dosages(Kaur & Kothiyal, 2019c). Overall, HCNMs contribute to the development of compact and

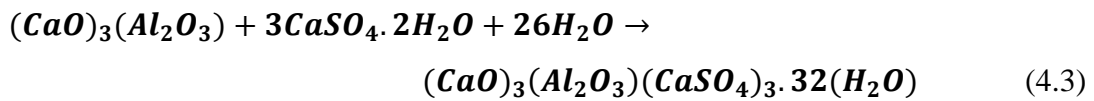
dense microstructural features within the cementitious matrices, surpassing the contributions of individual nanomaterials in CNCMs.

4.7 CRYSTALLIZATION BEHAVIOR STUDIES OF CNMs/HCNMs BASED CNCMs

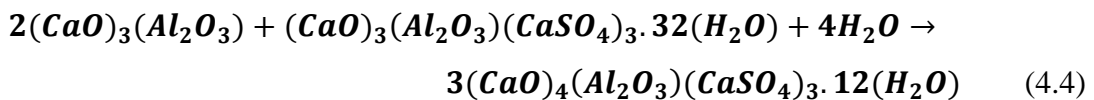
The impact of CNMs and HCNMs on alterations in the mineralogical composition of CNCMs at 90days of curing durations was investigated using Powdered X-ray diffraction (PXRD) analysis. This analytical technique yielded both quantitative and qualitative insights into the array of crystalline and semi-crystalline hydration products generated within the cement matrix during hydration reactions(S. Lv, Ma, Qiu, Sun, et al., 2013b; Qureshi et al., 2019; Qureshi & Panesar, 2020a; Skibsted & Snellings, 2019). The anhydrous composition of cement primarily consists of key reactive compounds including dicalcium silicate (C_2S), tricalcium silicate (C_3S), tricalcium aluminate (C_3A), and tetracalcium aluminoferrite (C_4AF). Upon contact with water, the most reactive phase of cement, C_3A , undergoes a reaction with water to generate aluminate gel, as depicted in equation 4.2. Subsequently, when this gel interacts with sulfate ions present in the cement solution, it forms ettringite (AFt), characterized by rod-shaped or needle-shaped structures, as shown in equation 4.3. These ettringite needles can randomly proliferate within the cement matrix, contributing to its brittleness.



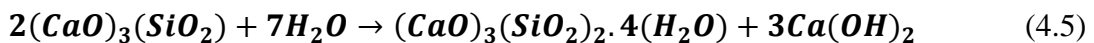
C_3A Calcium Aluminate Hydrate



C_3A Gypsum AFt rods



C_3A AFt rods Calciummonosulfoaluminate (AFm)



C_3S C-S-H gel C-H



C₂S

C-S-H gel

C-H

In the advanced stages of hydration, AFt reacts with C₃A, leading to the formation of the monosulfonate phase (AFm), as illustrated in equation 4.4. The diffraction pattern of C₃A displays prominent peaks at $2\theta = 33.1^\circ$ and $2\theta = 32.9^\circ$, corresponding to its cubic and orthorhombic polymorphs, respectively, as indicated in Jadhav and Debnath (2011)(Jadhav & Debnath, 2011).

The hydration process of C₃S and C₂S phases leads to the formation of calcium silicate hydrate gel, commonly known as tobermorite gel (C–S–H), along with the by-product calcium hydroxide or portlandite (C–H), as demonstrated in equations 4.5 and 4.6. It's noteworthy that the C–S–H gel is acknowledged as the primary contributor to the strength of the cement matrix, a fact supported by research conducted by Zhang et al. (2008), Chakraborty et al. (2013) and so on (Chakraborty et al., 2013; P. Verma et al., 2023; C. Zhang et al., 2008).

The quantitative estimation of calcium silicate hydrate (C–S–H), being an amorphous hydration product, presents challenges when relying on PXRD patterns. Therefore, the degree of hydration for silicates is assessed by observing the increased peak intensities of the side product, namely calcium hydroxide or portlandite (C–H). During the hydration of silicates, the primary crystalline phase that forms is C–H, which precipitates as large hexagonal crystals or plate-shaped prisms. Previous research has identified prominent diffraction peaks for C–H at $2\theta = 18.3^\circ$, 34.2° , 47.1° , and 50.1° (Kaur et al., 2019; L. P. Singh et al., 2015; L. Zhao, Guo, Ge, et al., 2017a). Consequently, the assessment of hydration rates for various CNCMs based on CNMs/HCNMs was carried out by comparing the quantity of the primary crystalline phase C–H formed, drawing upon insights from research by refereed references (Qureshi & Panesar, 2020a; Snellings et al., 2014).

Additionally, the increase in the production of C–S–H can be approximated by observing the reduction in peak intensities associated with the Alite (C₃S) and Belite (C₂S) phases (as discussed in (Jadhav & Debnath, 2011)). Alite is known to exist in three polymorphic forms: monoclinic, triclinic, and rhombohedral crystalline phases, with corresponding peaks appearing in the range of 51° to 52° (at $2\theta = 51.3^\circ$, 51.5° , and 51.8°). Additionally, a noteworthy peak for the monoclinic phase of alite can be found

at $2\theta = 29.3^\circ$ and 32.2° . Similarly, fluctuations in the belite phase can be deduced from diffraction peaks at $2\theta = 32.7^\circ$ in the PXRD pattern, as reported in studies by referred studies (Jadhav & Debnath, 2011; Kaur et al., 2019; Qureshi & Panesar, 2019; Sharma & Arora, 2018; L. Zhao, Guo, Liu, Ge, et al., 2018b)

The sand integrated into the cementitious nanocomposites consists of inert siliceous materials like silica (SiO_2) or quartz (Qz). Consequently, PXRD patterns of the hydrated cement matrix exhibit distinctive peaks corresponding to quartz at $2\theta = 26.6^\circ$, 36.7° , 60.0° , and 67.9° . Due to its inert nature, the peaks for quartz appear relatively more intense compared to other cement phases or hydrates, as observed in the research conducted by Lv et al. (S. Lv, Ma, Qiu, Sun, et al., 2013b).

Since sand is consistently used in equal quantities across all mixtures, any variations in the peak intensities of quartz (Qz) are not significant when evaluating the hydration levels of CNCMs. However, the relative decrease in peak intensity for Tetracalcium Aluminoferrite (C_4AF) at $2\theta = 23.3^\circ$ does indicate the accelerated hydration rates of the cementitious nanocomposites compared to the control mixture.

In CNCMs, a decline in the peak intensity at $2\theta = 18.3^\circ$ for C-H is characteristic of the onset of the pozzolanic reaction. Furthermore, the initiation of the pozzolanic reaction in the later stages of hydration can also be confirmed by the refinement of the crystal grain size of C-H. The incorporation of CNMs exerts a notable influence on both the size and quantity of C-H crystals during the later phases of hydration, although no discernible impact is observed during the early stages of hydration. The reduction in the grain size of C-H crystals enhances their adhesion to the C-S-H gel, thereby improving the microstructural characteristics and ultimate performance of the cement matrix.

To determine the crystallite size can be calculated of C-H crystals (corresponding to the peak at $2\theta = 18.3^\circ$), the Scherrer equation is employed, as shown in Equation 4.7 below:

$$D = (K \times \gamma) / (B \times \cos\theta) \quad (4.7)$$

where D is grain size of crystal in nm; K is Scherrer constant (taken as 0.89); γ is X-ray wavelength which is 0.154956 nm; B is half-width of diffraction peak in radians; θ is the diffraction angle.

The comprehensive outcomes of Powder X-ray Diffraction (PXRD) and their corresponding discussions are presented below.

4.7.1 Crystallization Behavior of GO-CNCMs

The PXRD patterns of GO-CNCMs in comparison to the control sample at 90 days of curing ages as illustrated in Figure 4.40.

4.7.1.1 Effect of GO dosage

The impact of GO on the crystallization behavior of GO-CNCMs in comparison to the control is demonstrated through the PXRD pattern acquired after 90 days of curing (Figure 4.40). Significantly, upon the inclusion of GO into the CNCMs, the diffraction peak associated with C-H in each GO-CNCMs blend exhibited declined as compared to control sample. The production of the C-H crystalline phase at 90 days of curing was minimum in the case of 0.0015% GO-CNCMs. Furthermore, the production of ettringite was lower in various GO-CNCMs compared to the control sample, even in the early stages of curing. The Aft peak intensity for GO dosages of 0.0015% was lower than in the GO-CNCMs with higher GO dosages, indicating enhanced hydration at lower GO dosages. Additionally, the peak intensities for C₂S and C₃S decreased with GO incorporation compared to the control sample, signifying increased consumption of calcium silicates. At the 90-day curing ages, the most significant hydration of cement phases among GO-CNCMs was observed in the case of 0.0015% GO-CNCMs, as indicated by lower C-H peak intensities in Figure 4.40. This improved hydration could be attributed to the larger surface area of GO sheets compared to cement particles, promoting the nucleation of C-S-H, as revealed by PXRD diffractograms.

4.7.1.2 Impact of Curing Time

Figures 4.40 reveal that an increase in curing time at 90 days lead to significant alterations in the C-H composition. Subsequently, hydration production increased with extended curing durations. Notably, a substantial C-H consumption is evident for 0.0015% GO-CNCMs at the early curing stage of 90 days.

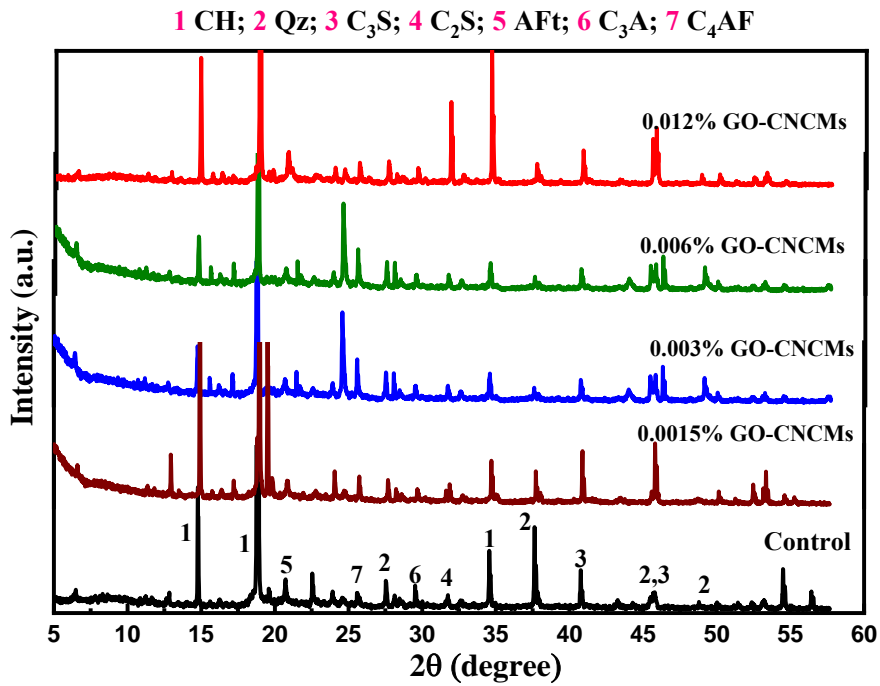


Figure 4.40 PXRD Patterns of GO-CNCMs at 90 Days of Curing

A noticeable augmentation in C-H peak intensities for GO-CNCMs, relatively lower to the control sample, is observable. The AFt peak intensity declines at 90 days of curing period. Similarly, noticeable reductions in C_3S , C_2S , and C_3A phases are easily discernible.

4.7.2 Crystallization Behavior of FMWCNTs-CNCMs

The PXRD patterns of FMWCNTs-CNCMs in comparison to the control sample are presented in Figure 4.41 for 90 days. These PXRD results will be analyzed with respect to FMWCNTs concentrations (ranging from 0.0015% to 0.012%) and curing duration (90 days).

4.7.2.1 Effect of FMWCNTs dosage

In Figure 4.41 ettringite (AFt) peak in FMWCNTs-CNCMs exhibited a decrease in peak intensities in case of FMWCNTs dosage 0.0015%. But at 0.003 to 0.012% FMWCNTs-CNCMs, it displayed a similar intensity to the control sample. This observed trend in crystallization behavior aligns well with the physico-mechanical performance, where the best results were achieved with 0.0015% FMWCNTs-CNCMs. In Figure 4.41, the primary crystalline hydration product, C-H, is evident at peak positions of $2\theta = 18.3^\circ$, 34.2° , 47.1° , and 50.1° in both FMWCNTs-CNCMs and the control sample. The C-H

peak found to be lower in case of 0.0015% FMWCNTs-CNCMs as compared to control. The diffraction peaks corresponding to Quartz (Qz) remained unchanged in all cases.

4.7.2.2 Effect of Curing Time

The gradual progression of hydration reactions in the mortar samples leads to an increase in the quantity of hydration products as the hydration age advances. This increase is a contributing factor to the development of strength in the cementitious nanocomposites over the time. Figure 4.41 displays the X-ray patterns obtained for FMWCNTs-CNCMs at curing ages of 90 days.

For FMWCNTs-CNCMs, as the curing age extended beyond 90 days, there was a notable increase in the consumption of C_2S and C_3S cementitious phases. The peak intensities corresponding to C-H also decreased, indicating a higher production of C-S-H gel compared to the control sample. This suggests that as the hydration age increased, cement compounds were increasingly consumed, leading to the simultaneous production of more hydration products.

The most substantial relative decrease in C-H peak intensity at $2\theta = 18.3^\circ$ is observed for 0.0015% FMWCNTs-CNCMs compared to the control sample at 90 days of curing. A notable reduction in the ettringite phase (AFt) is evident after 90 days of curing for all FMWCNTs-CNCMs, suggesting that ettringite is primarily formed in the early stages of hydration and becomes less prominent as other hydration products form. Additionally, the complete disappearance of the C_4AF crystalline phase was observed for all FMWCNTs-CNCMs compared to the control sample by 90 days of curing. This indicates a superior degree of hydration and desirable crystallization behavior of FMWCNTs-CNCMs compared to the control sample.

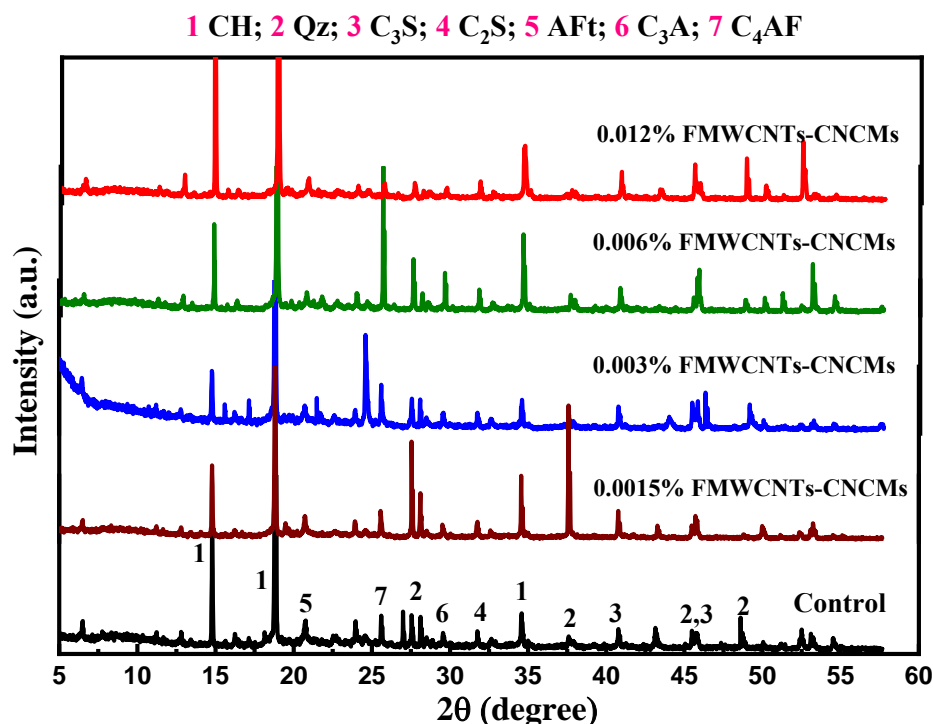


Figure 4.41 PXRD Patterns of FMWCNTs-CNCMs at 90 Days of Curing

4.7.3 Crystallization Behavior of HCNMs-CNCMs

The PXRD patterns of HCNMs-CNCMs in comparison to the control sample at 90 days of curing ages as illustrated in Figure 4.42.

4.7.3.1 Effect of HCNMs dosage

The impact of HCNMs on the crystallization behavior of HCNMs-CNCMs in comparison to the control sample is evident from the PXRD pattern obtained after 90 days of curing (Figure 4.42). However, a decrease in C-H peak intensity (at $2\theta = 18.3^\circ$) was observed as the HCNMs dosage was increased at 90 days of curing. This decline in crystallization could be attributed to the effective dispersion of 3-D hybrid networks at higher dosages as well. The uniformly dispersed FMWCNTs on corrugated GO sheets act as nucleating agents, facilitating the binding of C-S-H gel and the formation of hydration products, providing interfacial adhesion between cement hydrates and reinforcing agents. The ettringite (Aft) phase was minimal for 0.0015% HCNMs-CNCMs compared to the control sample. However, above this dosage, the Aft peak intensity noticeably increased for higher dosages of HCNMs-CNCMs at the same curing time, revealed lower hydration products as compared to the 0.0015% HCNMs-CNCMs. Additionally, there was a clear reduction in the peak intensities of C₂S, C₃S, and C₄AF phases for HCNMs-CNCMs compared to the control sample, which aligns

with the physico-mechanical properties and microstructural observations of HCNMs-CNCMs.

4.7.3.2 Impact of Curing Time

The effect of curing time on the crystallization behavior of HCNMs-CNCMs can be illustrated from the diffraction patterns as shown in Figure 4.42.

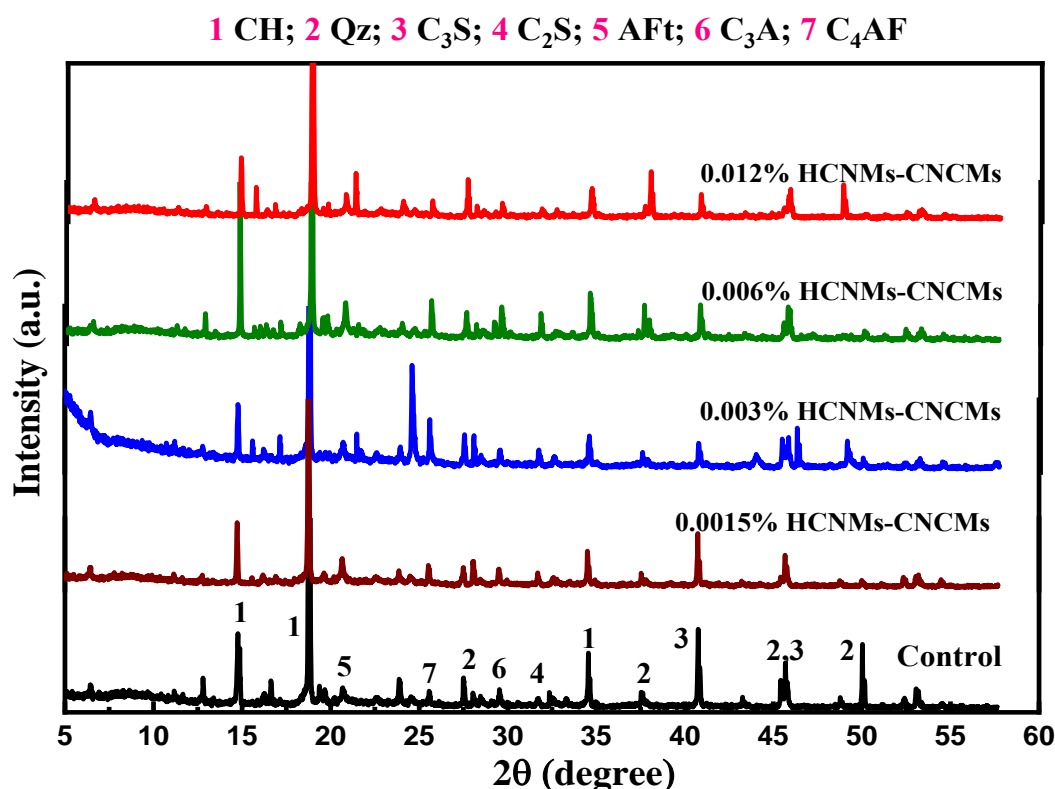


Figure 4.42 PXRD Patterns of HCNMs-CNCMs at 90 Days of Curing

A gradual progression in curing age 90 days enhanced the overall amount of hydration products. After 90 days of curing, the relative decrease in C-H peak intensity for HCNMs-CNCMs was relatively higher compared to the control. Ettringite (AFt) production was minimum for 0.0015% HCNMs-CNCMs; however, the quantity of AFt and reactive silicates dropped at 90 days for all HCNMs-CNCMs mix. Other reactant phases such as C₄AF and C₃A also diminished at 90 days of curing.

4.8 FUNCTIONAL GROUP STUDIES OF CNMs/HCNMs BASED CNCMs

Fourier transform-infrared spectroscopy (FT-IR) stands as a potent analytical method extensively applied in the realm of materials science. It serves as a window into the chemical composition, molecular structure, and bonding interactions found within a

wide array of materials. Within the domain of construction materials and cementitious composites, FT-IR has firmly established itself as a valuable instrument for delving into the intricate characteristics of carbon-based cement materials. These remarkable materials encompass a diverse family of carbon nanomaterials (CNMs), including functionalized multiwalled carbon nanotubes (FMWCNTs), graphene oxide (GO), and hybrid carbon nanomaterials (HCNMs). Their growing prominence arises from their potential to substantially elevate the mechanical, and durability attributes of cementitious composites.

FTIR spectroscopy presents researchers with a non-invasive and remarkably sensitive approach to investigate the molecular vibrations and chemical moieties inherent in these carbon-based additives, as well as their interplay with the cementitious matrix. This adaptable methodology offers a window into the alterations in structure, functional entities, and bonding mechanisms that transpire throughout the hydration and curing stages of carbon-based cement materials. FT-IR empowers researchers to monitor the evolution of cement hydration reactions and the generation of crucial hydration products like calcium silicate hydrate (C-S-H) gel and calcium hydroxide (C-H). It delivers real-time insights into the chemical changes taking place within the composite material. FT-IR has the capability to unveil the characteristics of chemical bonds established at the interface between carbon-based additives and the cement matrix. The presence of strong interfacial bonding is of utmost importance as it facilitates load transfer and contributes to enhancing the mechanical properties of the composite material.

Essentially, FT-IR spectroscopy offers a comprehensive understanding of the intricate molecular-level interactions and chemical dynamics that govern the behavior of carbon-based cement materials. This deep understanding helps improve modern construction materials, making them better for various uses in building, infrastructure, and more.

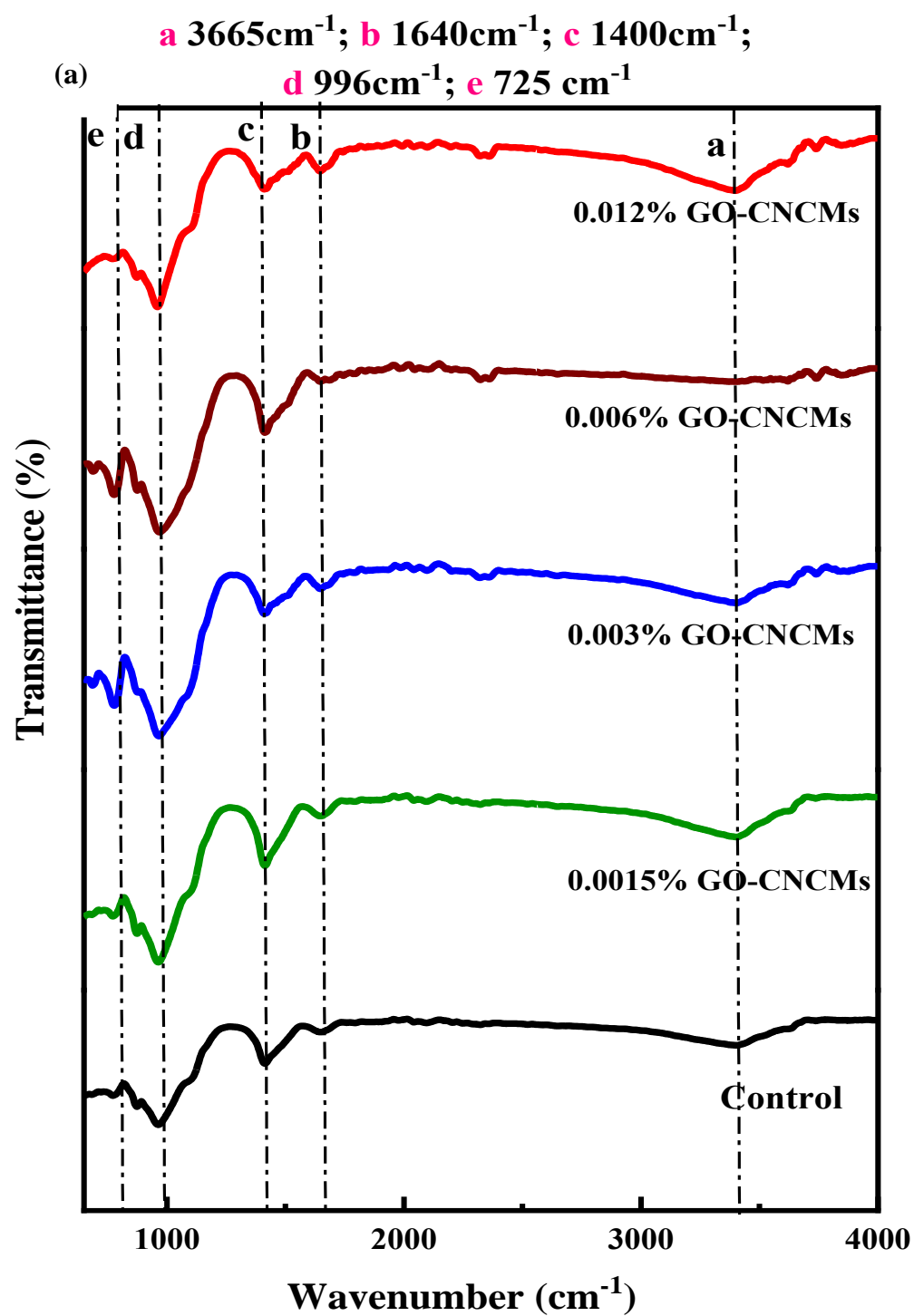
4.8.1 FT-IR studies of GO based CNCMs

Fourier-transform infrared (FT-IR) spectra were recorded using a Nicolet 5DXC FT-IR spectrometer within the range of 4000-500 cm^{-1} . Following background correction, the spectra were generated by averaging 10 scans at a resolution of 1 cm^{-1} . This technique was employed to analyze the distinctive characteristics of hydrated cement samples after 7 and 90 days of curing. For analysis, 2 mg samples from each mixture were

collected and subjected to a 24-hour drying process in an oven at $35^{\circ}\text{C}\pm 5^{\circ}\text{C}$. Subsequently, the samples were encapsulated in KBr pellets for further characterization.

The FT-IR spectra of hydrated cement and hydrated cement mixed with GO at 7 and 90 days are shown in Figures 4.43(a-b). This FT-IR investigated the types of functionalities and the bonds in the compound. The major bands are shown at approximately 3824, 3684, 3665, 3640, 1640, 1400, 996 and 725cm^{-1} in cementitious compound at the days of 7 and 90 days. At the age of 7 days of spectra, two significant bands in mixes at 3665 and 996cm^{-1} are observed. The H–O–H band is found at 996cm^{-1} showed the existence of water molecules, similar results have been found by Hussin et al. (Hussin et al., 2015). The peaks at 3640cm^{-1} (Figure 4.43(b)) correspond to CH, which was formed as silicate phases in the hydrated cement (Sharma, Susan, et al., 2018). Although, at the age of 90 days, the vibrational bands of C-A-S-H were found in the range $1100\text{--}700\text{cm}^{-1}$ in the spectra. However, major spectra show peaks at 996 and 725cm^{-1} , corresponding to asymmetric stretching vibrations of Si–O, that indicate the polymerization in C-S-H and also for H-O-H found in the compound, as observed in Figure 4.43 (a and b) (Saafi et al., 2015). The spectral bands falling within the range of 996 to 725cm^{-1} are indicative of the in-plane bending vibrations of the Si–O bonds found in C_3S and C_2S (Bache et al., 1966). As illustrated in this figure, the introduction of CNMs into the matrix led to the enhancement of the moderately absorbing band around $\sim 1400\text{cm}^{-1}$, which can be attributed to a C-H vibration.

As the curing age increased, the pozzolanic behaviour of the fly ash present in PPC started to react with $\text{Ca}(\text{OH})_2$ and continued to generate more C-S-H gel. Furthermore, the C-S-H gel led to a stronger T-O-Si band in the case of hybrid nanomaterials added to the cementitious materials, which also matched the compressive strength results as discussed in section II. However, in Figure 4.43 (a-b), no difference was observed for the characteristic peaks after the addition of GO, confirmed the absence of chemical reactions between GO and cementitious mortar.



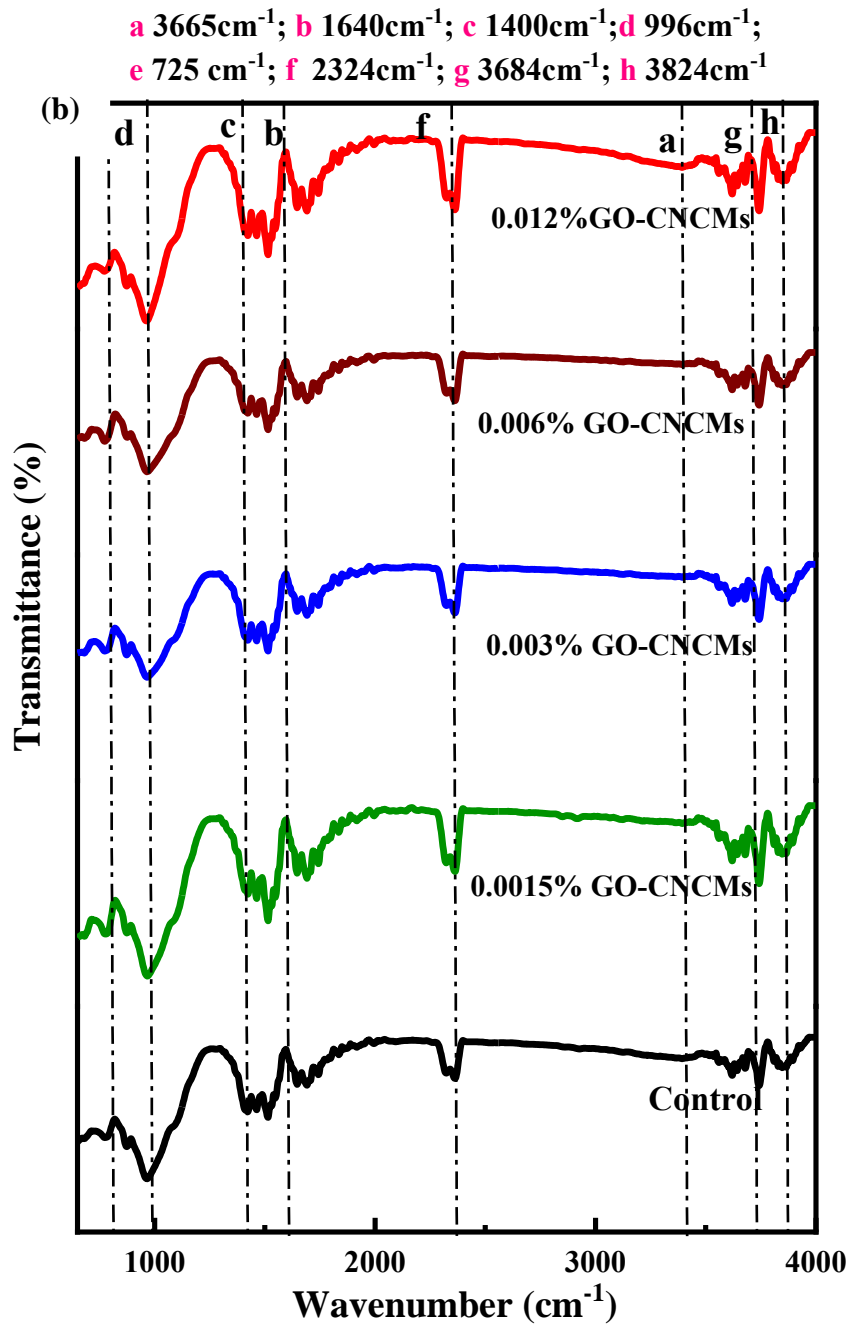


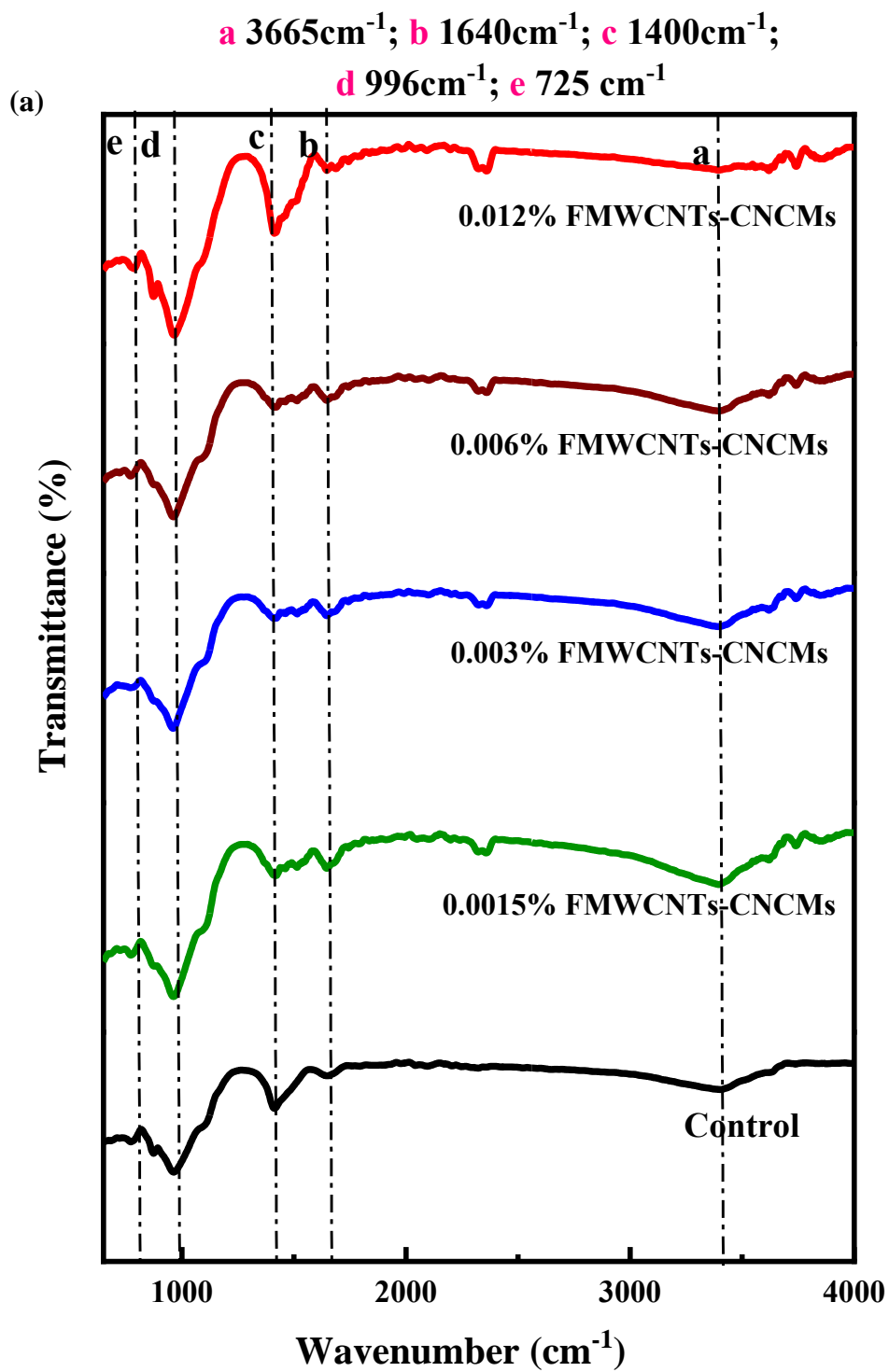
Figure 4.43 FT-IR Patterns of GO-CNCMs at (a) 7 Days of Curing, and (b) 90 Days of Curing

4.8.2 FT-IR studies of FMWCNTs based CNCMs

The FT-IR spectra of the hydrated cement and the cement mixed with FMWCNTs at both 7 and 90 days of curing are presented in Figures 4.44(a-b). These spectra provided valuable insights into the functional groups and chemical bonds present in the compounds. At the 7-day curing age, two prominent bands were observed in the spectra,

located at approximately 3665 and 996 cm^{-1} . The band at 996 cm^{-1} is attributed to the H-O-H bending mode, indicating the presence of water molecules within the cementitious compound (Shrestha, 2018). Additionally, the peaks observed at 3640 cm^{-1} (Figure 4.44(b)) are associated with CH, which is formed as silicate phases hydrate in the cement. As the curing age extended to 90 days, the FT-IR spectra revealed vibrational bands in the range of 1100–700 cm^{-1} , corresponding to C-A-S-H gel, indicating further pozzolanic reactions between the fly ash present in the PPC and $\text{Ca}(\text{OH})_2$. The spectral bands within the range of 996 to 725 cm^{-1} correspond to the in-plane bending vibrations of the Si–O bonds present in C_3S and C_2S (Z. Lu et al., 2016; Tulashie et al., 2021). As depicted in this figure, the incorporation of CNMs into the matrix resulted in the intensification of the moderately absorbing band at approximately $\sim 1400 \text{ cm}^{-1}$, attributable to C-H vibrations (Saafi et al., 2015).

Notably, the spectra prominently featured a peak at 725 cm^{-1} , which corresponds to asymmetric stretching vibrations of Si-O, indicating polymerization in the C-S-H gel (Saafi et al., 2015). However, it's important to note that, as seen in Figure 4.44(a-b), there was no observable difference in the characteristic peaks after the addition of FMWCNTs. This suggests that there were no significant chemical reactions between FMWCNTs and the cementitious mortar, highlighting the inert nature of FMWCNTs in this context.



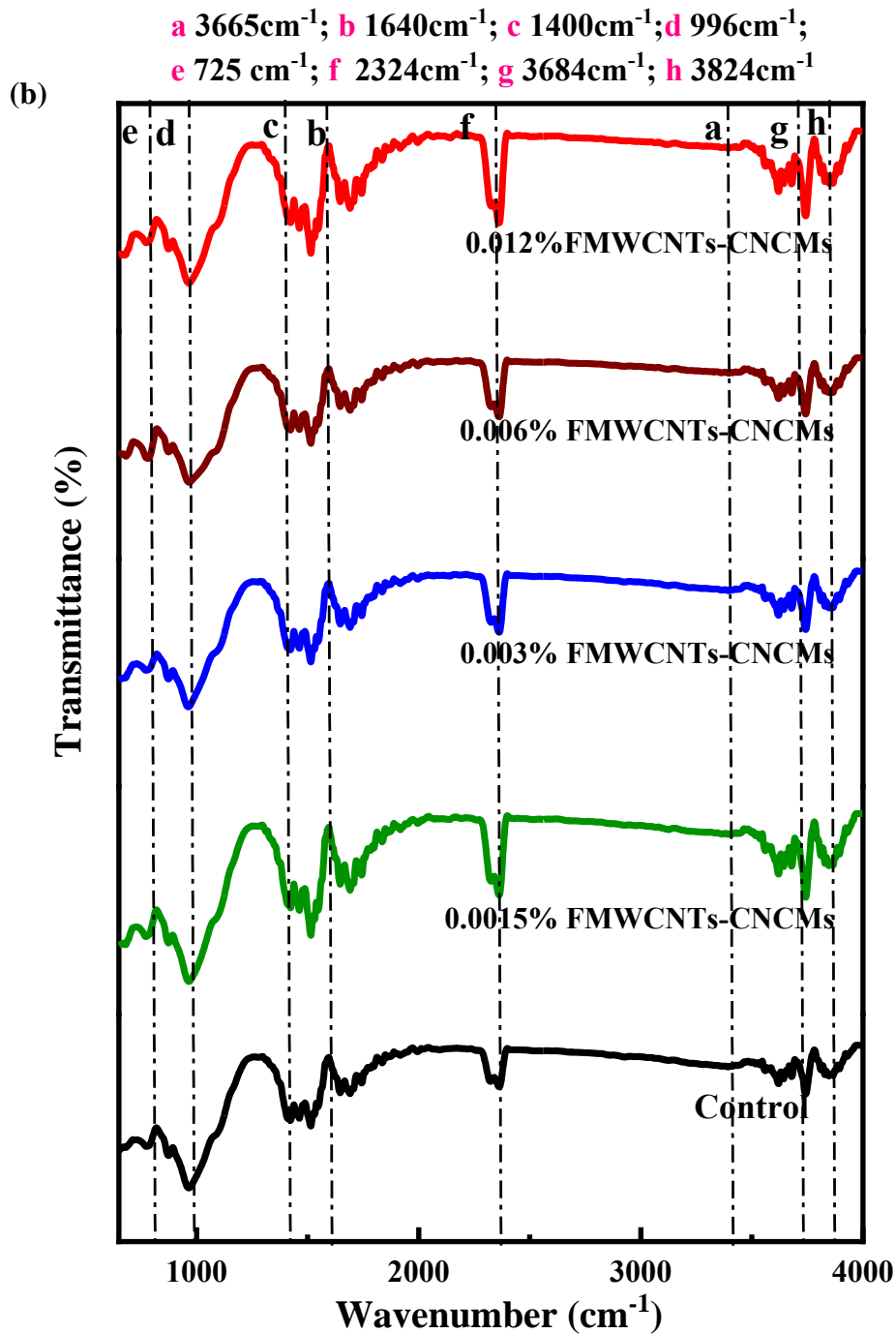


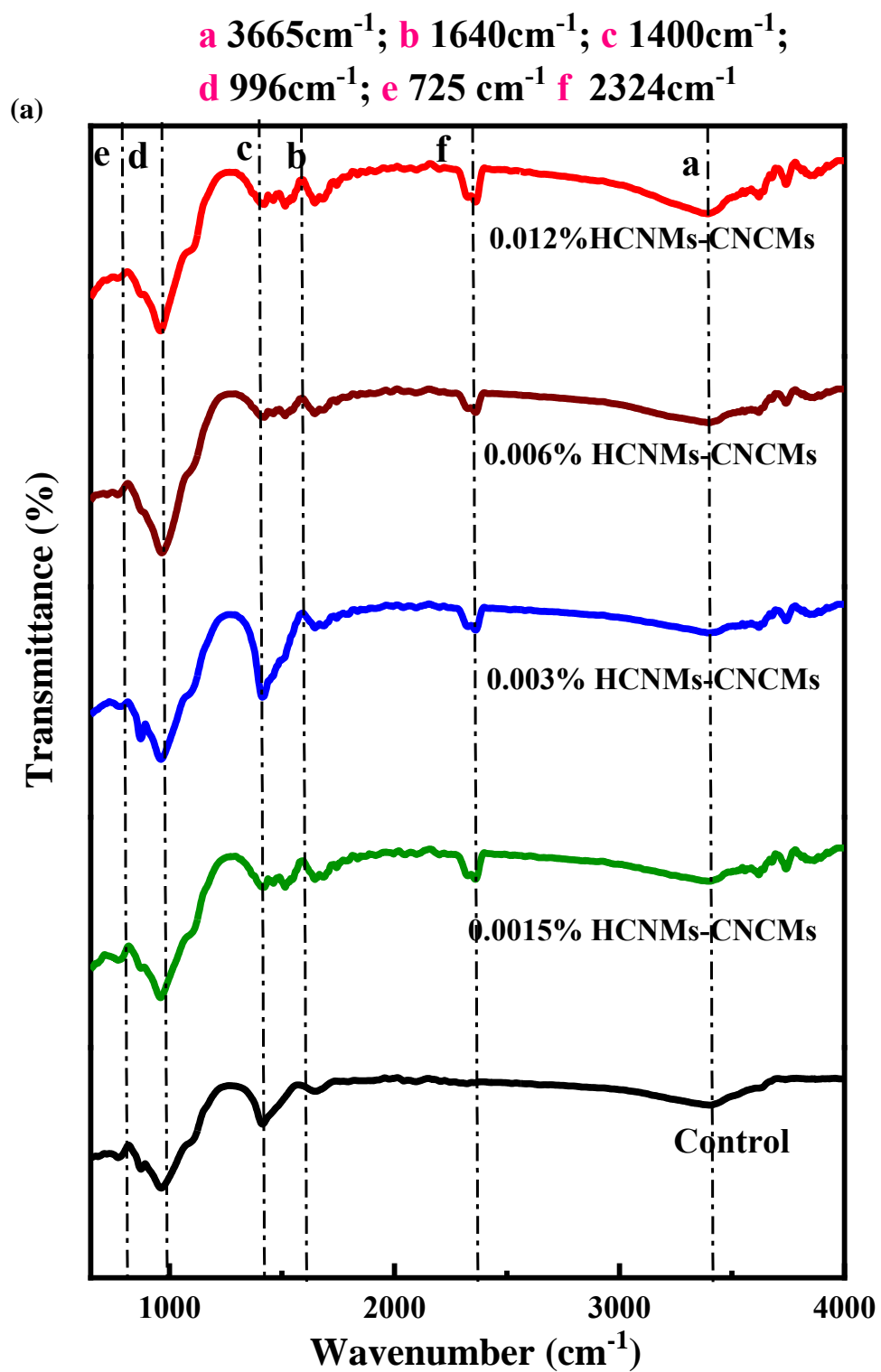
Figure 4.44 FT-IR Patterns of FMWCNTs-CNCMs at (a) 7 Days of Curing, and (b) 90 Days of Curing

4.8.3 FT-IR studies of HCNMs based CNCMs

Figures 45(a, b) showcase the FT-IR spectra of hydrated cement and cement mixed with hybrid carbon nanomaterials (HCNMs) at both 7 and 90 days of curing. These FT-IR analyses delve into the functional groups and chemical bonds present within the

compounds under investigation. Notably, the major bands in the cementitious compound are evident at approximately 3824, 3684, 3665, 3640, 1640, 1400, 996 and 725cm^{-1} for both the 7 and 90 day, samples. Specifically, at the 7 day mark, two significant bands are discernible in the spectra, located at 3665 and 996cm^{-1} . The band at 996cm^{-1} corresponds to the H-O-H bending mode, indicating the presence of water molecules. This finding aligns with results reported by Hussin et al. Additionally, the peaks observed at 3640cm^{-1} (Figure 4.45 a-b) are attributed to CH formed as silicate phases hydrate in the cement (Shrestha, 2018). Upon reaching the 90-day curing age, vibrational bands attributed to C-A-S-H gel appear within the range of $1100\text{--}700\text{cm}^{-1}$ in the spectra. Remarkably, the spectra prominently exhibit peaks at 725cm^{-1} , corresponding to asymmetric stretching vibrations of Si-O. This phenomenon indicates polymerization within the C-S-H gel and underscores the presence of H-O-H within the compound, as observed in Figure 4.45(b) (Björnström et al., 2004). As the curing age progresses, the interaction between the fly ash in PPC and $\text{Ca}(\text{OH})_2$ fosters pozzolanic behavior, leading to increased C-S-H gel formation. Moreover, this C-S-H gel contributes to a more pronounced T-O-Si band within the hybrid nanomaterials added to the cementitious materials, aligning with the results of compressive strength testing. The spectral bands within the range of $996\text{ to }725\text{cm}^{-1}$ signify the in-plane bending vibrations of the Si-O bonds present in C_3S and C_2S . As depicted in this figure, the incorporation of CNMs into the matrix resulted in the augmentation of the moderately absorbing band at approximately 1400cm^{-1} , which is attributable to a C-H vibration.

Moreover, the HCNMs incorporated cementitious mortar shows more pronounced peaks as compared to individual CNMs, referred HCNMs highly efficient. Interestingly, in Figure 4.45(a,b), no discernible differences are observed in the characteristic peaks after the incorporation of hybrid GO/FMWCNTs. This observation confirms the absence of chemical reactions between GO/FMWCNTs and the cementitious mortar, reaffirming the inert nature of these additives in this context.



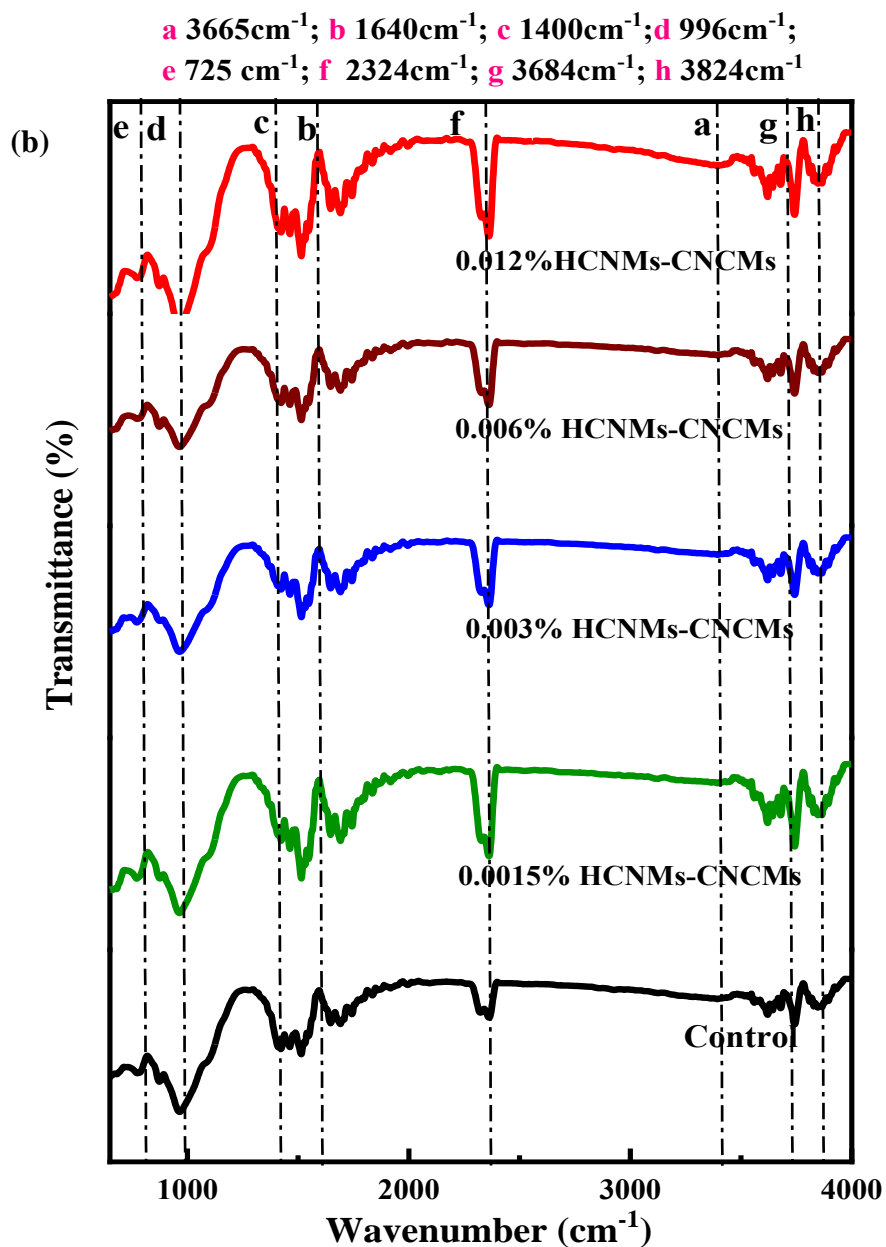


Figure 4.45 FT-IR Patterns of HCNMs-CNCMs at (a) 7 Days of Curing, and (b) 90 Days of Curing

DURABILITY STUDIES

To examine the influence of carbon nanomaterials (CNMs) and hybrid carbon nanomaterials (HCNMs) on the hydration rate and microstructure of cementitious nanocomposites (CNCMs) we conducted studies on durability.

In order to examine the impact of incorporating CNMs/HCNMs on the refinement of void structure of CNCMs, an investigation was conducted on the electrical resistivity of CNCMs using direct current electrical resistivity studies, as detailed in Chapter 3. The impact of varying doses of CNMs and HCNMs inclusion on the connectivity of pores, porosity, and conductivity of the pore solution in mortar matrices including CNCMs has been evaluated by electrical resistivity studies. The dosages utilized in this study varied between 0.0015% and 0.012% by weight percentage of cement. The electrical resistivity measurements were conducted at four different curing periods: 7, 28, 56, and 90 days. The electrical resistivity values of the various mix designations were compared to those of the control samples. To evaluate the enhanced hydration level of the CNCMs mortar samples, the density of the hydration products was quantified using electrical resistivity. This approach allows for the determination of the microstructural density of the mortar samples, with higher electrical resistivity indicating greater density. A comprehensive analysis of the findings has been elucidated in section 4.8.

In addition a capillary water absorption test was carried out according to ASTM 1585-13 (ASTM C1585-13, 2013). The standard size (100×50 mm) of the samples was taken after the curing ages of 28 and 90 days. The samples were dried in an oven at $105^{\circ}\text{C} \pm 5^{\circ}\text{C}$ and then cooled at $25^{\circ}\text{C} \pm 5^{\circ}\text{C}$ in a desiccator. The sides of the CNCMs mortar were coated with wax except at the bottom and top. All the sides of the samples were wrapped with plastic, while the bottom remained unwrapped. Then the dry weight was noted. The underside of the specimen was covered in water, and the water level was maintained at 3 mm throughout the test. The sample was removed from the pan at the end of the test period. The water on the surface of the sample was wiped off with a towel, and the sample was then weighed (Xiong et al., 2021). The whole test procedure was carried out at room temperature for the periods of 1 min, 5 min, 15 min, 30 min, 1 hr, 3 hr, 7 hr, 1

day, 2 day, 3 day, 4 day, 5 day, 6 day, 7 day, 8 day, 9 day, and 10 day. In this study, we employed dosages ranging from 0.0015% to 0.012% by weight percentage of cement. To assess the heightened level of hydration in the CNCMs mortar samples, we compared the water absorption of the different mix designs to control samples (referred to as 'Control'). A thorough examination of these results is detailed in Section 4.9.

Similarly, to explore the impact of incorporating CNMs/HCNMs on acid and sulfate attack of CNCMs the utilization of accessible acid and sulfate solution, as detailed in Chapter 3. The investigation also encompassed an examination of the impact of varying dosages of CNMs and HCNMs incorporation in CNCMs after acid and sulfate attacked solution. The dosages incorporated in this study varied from 0.0015% to 0.012% by weight percentage of cement. The chemical exposure was conducted after a curing time of 56 and 90 days. The mechanical strength and weight loss of the various mix designations were compared to the control samples (namely, Control) to evaluate the enhanced hydration level of the CNCMs mortar samples. A comprehensive analysis of the findings has been presented in section 4.10.

In this section, we delve into three extensive studies on durability, each focusing on specific facets of the material's robustness: Electrical resistivity, Water absorption characteristics, and Resistance to acid/sulfate exposure.

4.9 ELECTRICAL RESISTIVITY OF CNMs/HCNMs BASED CNCMs

4.9.1 Electrical Resistivity of GO-CNCMs

Figure 4.46 displays the outcomes pertaining to the electrical resistance of graphene oxide-based cementitious nanocomposites (GO-CNCMs) at different dosages and curing durations. The GO-CNCMs exhibit higher electrical resistivity values compared to the control due to the generation of a greater quantity of hydration products. The increased production of hydration products has the effect of filling gaps between cement grains. This, in turn, reduces porosity and elevates electrical resistivity. This effect can be attributed to the more efficient progression of hydration reactions in mortars containing GO when compared to those with control sample (Gong et al., 2014; S. Lv, Ma, Qiu, Sun, et al., 2013a). This acceleration of the hydration rate also results in the compaction of the microstructure within the mortar matrix, thereby enhancing electrical resistivity.

Following a curing period of 7 days, the electrical resistivity values were determined for the control and samples containing varying concentrations (0.0015%, 0.003%, 0.006%, and 0.012%) of superplasticizer stabilized graphene oxide (GO). The resistivity values obtained as 34.07 k-ohm-cm, 33.5 k-ohm-cm, 29.77 k-ohm-cm, 29.95 k-ohm-cm, and 27.75 k-ohm-cm, respectively.

But with increase in the curing time to 90 days the electrical resistivity values for control sample, GO-CNCMs; 0.0015%, 0.003%, 0.006%, and 0.012% was found to be 98.77 k-ohm-cm, 101.22 k-ohm-cm, 89.40 k-ohm-cm, 92.37 k-ohm-cm and 95.00 k-ohm-cm, respectively. It can be observed from the graphical trend that the maximum electrical resistivity value was found for 0.0015% GO-CNCMs, thereafter depicting a gradual decline in the electrical resistivity as continuously increasing the dosages in GO-CNCMs.

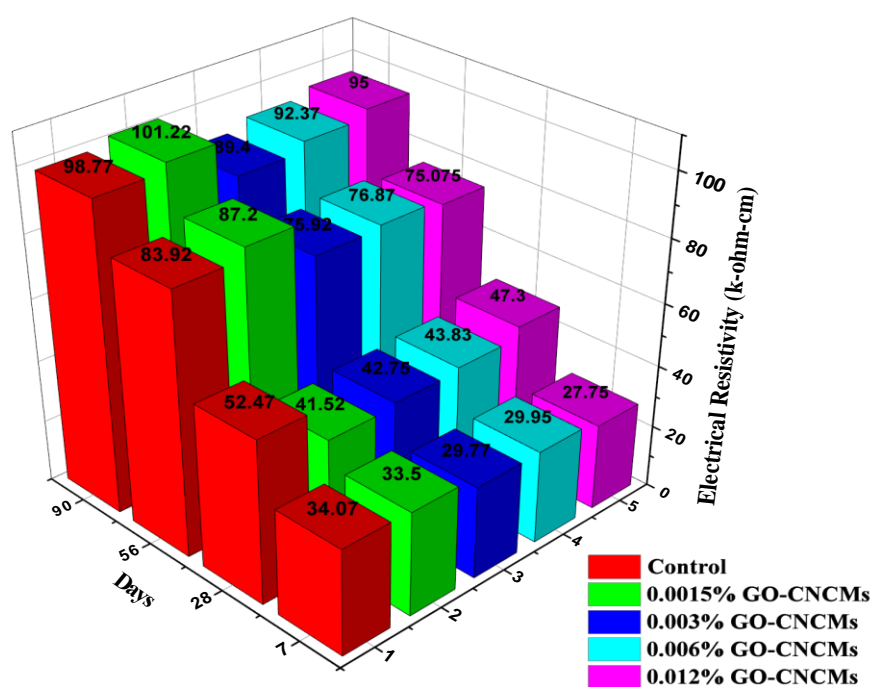


Figure 4.46 Electrical Resistivity for GO-CNCMs at Different Dosages and Curing Ages

The electrical resistivity values for graphene oxide in cementitious nanocomposites (GO-CNCMs) at various levels of graphene oxide (GO) and curing durations of 7, 28, 56, and 90 days are displayed in Table 4.11. A notable rise in electrical resistance is evident in the GO-CNCMs at various stages of curing. The tabular data reveals that the highest increase in electrical resistivity was seen for GO-CNCMs with a concentration

of 0.0015%. Subsequently, the electrical resistivity readings exhibited a declining pattern as the dosage of graphene oxide (GO) was further increased.

Table 4.11 Electrical Resistivity for GO-CNCMs

Mix Designation	Dosage of GO Incorporated (% by Weight of Cement)	Electrical Resistivity (k-ohm-cm)			
		7 days	28 days	56 days	90 days
GO-CNCMs	0.0015% GO-CNCMs	33.5	41.52	87.2	101.22
	0.003% GO-CNCMs	29.77	42.75	75.92	89.4
	0.006% GO-CNCMs	29.95	43.83	76.87	92.37
	0.012% GO-CNCMs	27.75	47.3	75.075	95

4.9.2 Electrical Resistivity of FMWCNTs-CNCMs

The results for the electrical resistivity of FMWCNTs-CNCMs at various dosages and curing times are depicted in Figure 4.47. It's evident that the incorporation of superplasticizer stabilized FMWCNTs into the cementitious nanocomposites matrix at low dosages has led to an increase in electrical resistivity compared to the control sample. This can be attributed to the densification of the mortar matrix's microstructure due to the improved hydration level in FMWCNTs-incorporated mortar samples. This, in turn, hampers the movement of ions through the pore solution, resulting in higher electrical resistivity(W. Li et al., 2017; Qureshi & Panesar, 2019).

In the case of FMWCNTs-CNCMs, the presence of oxygen functionalities (specifically, –COOH groups) from the functionalized MWCNTs contributes to the formation of improved hydration products compared to the control sample. These functional groups serve as nucleation or crystallization sites for hydration products such as C-S-H gel and portlandite (C-H). Moreover, these reactive nucleation sites establish strong interfacial bonding between the C-S-H gel and the reinforcing agents(Kurda et al., 2019; S. Lv, Ma, Qiu, Sun, et al., 2013a).

The graphical trend reveals a rise in electrical resistivity values as the hydration period advances from 7 to 90 days, observed in both control and FMWCNTs-CNCMs. This phenomenon can be attributed to the ongoing refinement of the pore structure and enhanced C-S-H gel formation during the curing process. Consequently, this densifies the microstructure of cement mortars, causing the obstruction of ionic conduction pathways through the water-filled pores in the cement mortars (Konsta-Gdoutos et al., 2017; N. Zhao & Zhang, 2009).

The electrical resistivity of the control sample was measured at 98.77 k-ohm-cm. However, when superplasticizer stabilized FMWCNTs were incorporated at dosages of 0.0015%, 0.003%, 0.006%, and 0.012%, the electrical resistivity increased to 104.67 k-ohm-cm, 91.41 k-ohm-cm, 92.15 k-ohm-cm, and 89.12 k-ohm-cm, respectively, after 90 days of curing.

As the concentration of FMWCNTs increased, electrical resistivity exhibited an upward trend, peaking at 0.0015% FMWCNTs-CNCMs. However, beyond this point, a decline in electrical resistivity values occurred, notably for the 0.003% FMWCNTs-CNCMs. This decline can be attributed to the less consistent dispersion of higher FMWCNTs dosages compared to lower ones. Consequently, this reduced the efficiency of cement phase hydration over the nucleation sites provided by FMWCNTs, ultimately resulting in lower resistivity.

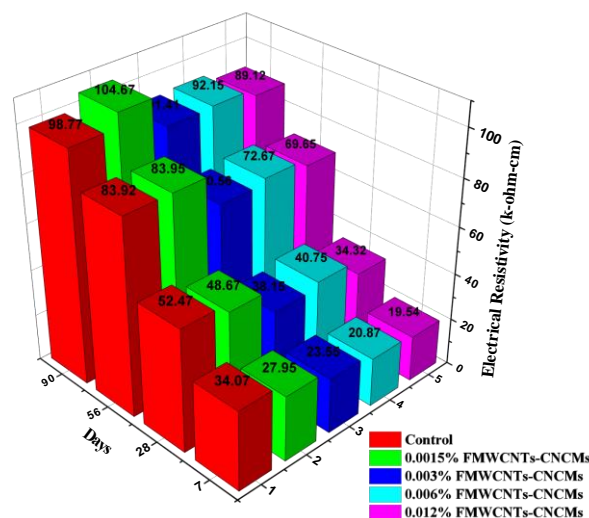


Figure 4.47 Electrical Resistivity for FMWCNTs-CNCMs at Different Dosages and Curing Ages

Table 4.12 displays the electrical resistivity values for FMWCNTs-CNCMs at various curing ages: 7, 28, 56, and 90 days. Notably, a significant increase in electrical resistivity was observed for FMWCNTs-CNCMs at each curing age. The rising trend in electrical resistivity also suggests that FMWCNTs dispersion remained uniform up to a dosage of 0.0015% in the cement mortar matrix. However, beyond this dosage, agglomerates of FCNTs began to form upon incorporation. Consequently, the enhancement in electrical resistivity values for 0.003% -0.012% FMWCNTs-CNCMs was relatively less pronounced compared to other FMWCNTs-CNCMs.

Table 4.12 Electrical Resistivity for FMWCNTs-CNCMs

Mix Designation	Dosage of FMWCNTs Incorporated (% by Weight of Cement)	Electrical Resistivity (k-ohm-cm)			
		7 days	28 days	56 days	90 days
FMWCNTs-CNCMs	0.0015% FMWCNTs-CNCMs	27.95	48.67	83.95	104.67
	0.003% FMWCNTs-CNCMs	23.55	38.15	70.56	91.41
	0.006% FMWCNTs-CNCMs	20.87	40.75	72.67	92.15
	0.012% FMWCNTs-CNCMs	19.54	34.32	69.65	89.12

4.9.3 Electrical Resistivity of HCNMs-CNCMs

The electrical resistivity results for HCNMs-CNCMs, varying in dosages of HCNMs and curing times, are presented in Figure 4.48. Notably, the electrical resistivity values for HCNMs-CNCMs exhibited a trend similar to that observed for GO-CNCMs. The highest electrical resistivity was recorded for 0.0015% HCNMs-CNCMs compared to the control. Subsequently, as the dosage of HCNMs increased, a gradual decrease in

electrical resistivity was observed. However, it's evident that the degree of electrical resistivity enhancement in HCNMs-CNCMs exceeded that of GO-CNCMs.

The introduction of HCNMs into the cement mortars resulted in higher electrical resistivity due to the development of a tightly packed C-S-H gel network, leading to densification of the cementitious microstructure. The homogeneous dispersion of FMWCNTs over the corrugated graphene sheets of GO, facilitated by π - π stacking interactions, resulted in the formation of a three-dimensional network of nucleation sites for the hydration of cementitious phases, producing C-S-H gel and C-H (Kharisov et al., 2014; Sujay et al., 2020; C. Zhang et al., 2010). This 3-D network prevents the re-stacking of graphene oxide sheets and the agglomeration of FMWCNTs, enhancing reinforcement of the cementitious matrix and maximizing the utilization of its functional groups for the crystallization of hydration products (Y. Du et al., 2020; Kaur, Kothiyal, & Arora, 2020; Kothiyal & Kaur, 2021; Z. Lu, Hou, Meng, Sun, Lu, et al., 2015; Zhou et al., 2017b).

After 7 days of curing, the electrical resistivity values for control and HCNMs-CNCMs with dosages of 0.0015%, 0.003%, 0.006%, and 0.012% were 34.07 k-ohm-cm, 16.67 k-ohm-cm, 16.57 k-ohm-cm, 12.57 k-ohm-cm, and 15.02 k-ohm-cm, respectively. With extended curing times up to 90 days, the average electrical resistivity values increased to 98.77 k-ohm-cm, 104.26 k-ohm-cm, 89.34 k-ohm-cm, 87.56 k-ohm-cm, and 87.27 k-ohm-cm, respectively. The graphical trend shows that the maximum electrical resistivity value was obtained for 0.0015% HCNMs-CNCMs, followed by a gradual decline in electrical resistivity values as the HCNMs dosage increased, reaching 0.003% HCNMs-CNCMs.

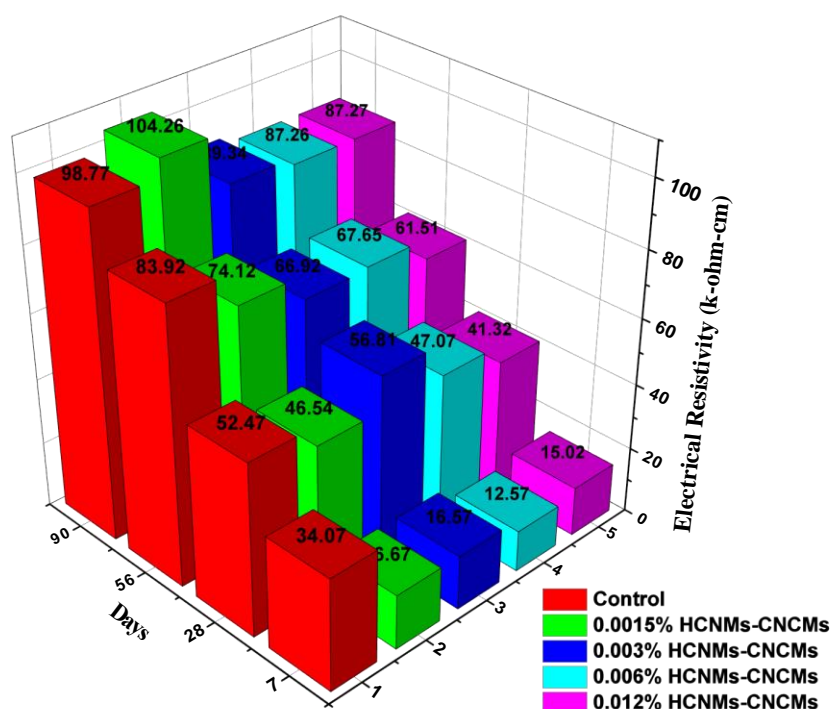


Figure 4.48 Electrical Resistivity for HCNMs-CNCMs at Different Dosages and Curing Ages

Table 4.13 displays the electrical resistivity values for HCNMs-CNCMs at curing ages of 7, 28, 56, and 90 days. Notably, the observed values exhibited a substantial increase in electrical resistivity for the HCNMs-CNCMs at each curing age.

Table 4.13 Electrical Resistivity for HCNMs-CNCMs

Mix Designation	Dosage of HCNMs Incorporated (% by Weight of Cement)	Electrical Resistivity (k-ohm-cm)			
		7 days	28 days	56 days	90 days
HCNMs-CNCMs	0.0015% HCNMs-CNCMs	16.67	46.54	74.12	104.26
	0.003% HCNMs-CNCMs	16.57	56.81	66.92	89.34
	0.006% HCNMs-CNCMs	12.57	47.07	67.65	87.26
	0.012% HCNMs-CNCMs	15.02	41.32	61.51	87.27

The most significant increase in electrical resistivity was observed for 0.0015% HCNMs-CNCMs, with a subsequent decrease in electrical resistivity as the HCNMs dosage increased at the age of 90days of curing.

In summary, the findings related to electrical resistivity indicate that:

- (a) The addition of GO, FMWCNTs, and HCNMs at different concentrations to cementitious nanocomposites leads to an increase in electrical resistivity values when compared to the control samples.
- (b) The electrical resistivity value for control sample was found to be 98.77 k-ohm-cm after 90 days of curing.
- (c) For FMWCNTs, the most significant improvement in electrical resistivity was observed in the case of 0.0015% FMWCNTs-CNCMs, with an electrical resistivity value of 104.67 k-ohm-cm.
- (d) GO-CNCMs and HCNMs-CNCMs exhibited their highest electrical resistivity values at dosages of 0.0015%, with resistivity values of 101.22 k-ohm-cm and 104.26 k-ohm-cm, respectively.

A concise summary of the electrical resistivity results for control and CNMs/HCNMs incorporated CNCMs at various dosages and curing ages is presented in Table 4.14.

Table 4.14 Average Electrical Resistivity Values of CNMs/HCNMs based CNCMs

S. No.	Mix Designation	Dosages of CNMs/HCNMs (% by Weight of Cement/Blend)	Electrical Resistivity (k-ohm-cm)			
			7 days	28 days	56 days	90 days
1	Control (Cement)	0.00	34.07	52.47	83.92	98.77
2	GO-CNCMs	0.0015%	33.5	41.52	87.2	101.22
		0.003%	29.77	42.75	75.92	89.4
		0.006%	29.95	43.83	76.87	92.37
		0.012%	27.75	47.3	75.075	95
3	FMWCN Ts-CNCMs	0.0015%	27.95	48.67	83.95	104.67
		0.003%	23.55	38.15	70.56	91.41
		0.006%	20.87	40.75	72.67	92.15
		0.012%	19.54	34.32	69.65	89.12
4	HCNMs-CNCMs	0.0015%	16.67	46.54	74.12	104.26
		0.003%	16.57	56.81	66.92	89.34
		0.006%	12.57	47.07	67.65	87.26
		0.012%	15.02	41.32	61.51	87.27

4.10 CAPILLARY WATER ABSORPTION (WATER ABSORPTION TEST) OF CNMs/HCNMs BASED CNCMs

The capillary water absorption I of mortars was calculated as per equation 4.8. The relation between I and the square root of time \sqrt{t} was obtained (Pitroda et al., 2012; Punurai et al., 2018).

$$I = \frac{mt}{a - \rho} \quad (4.8)$$

Where I is the water absorption of the specimen (mm), and mt is the difference in mass of the specimen in grams, at the time t , a is the area of the sample (mm^2), and ρ is the water density (g/mm^3) i.e., 0.001 g/mm^3 is used.

By fitting data to the curve of the relation $I \sim \sqrt{t}$, it is possible to generate two linear relations (MacLeod et al., 2020).

$$I = S \times \sqrt{t} + b \quad (4.9)$$

Where S is the rate of water absorption, measured in $\text{mm/s}^{1/2}$, t is the amount of time that the specimen takes to absorb water, and b is the constant that represents the line intercept. During the earliest phases of water absorption, the high absorption capacity of each sample causes the curves to rise swiftly and almost linearly due to the high absorption capacity (Abedi et al., 2020; Gamal et al., 2021). Initial and final water absorption rates are reduced relative to control sample. After about 5 hours (18000 seconds), the rate of water absorption gradually slows down, and after 5 days (432000 sec), the sample is nearly saturated in terms of capillary water absorption. The pores that have been discovered and have the capability of capturing free water are primarily spread throughout the cementitious mortar. In addition, Figure (49-51) demonstrates that the pores are able to rapidly absorb a significant quantity of capillary water during the first five hours (18000 seconds) of water absorption. However, after five hours (18000 seconds), only certain pores continue to absorb water, and the absorption speed decreases even further. As anticipated, the initial sorptivity within the first 0-6 hours was higher, attributed to the presence of voids within the cementitious matrix. Subsequently, the sorptivity decreased, indicating a transition to the secondary sorptivity phase, which was observed after 6 hours.

4.10.1 Water Absorption of GO-CNCMs

The water absorption values for the GO-CNCMs for various dosages incorporation after 28 and 90 days of curing are presented in Figure 4.49(a) and (b). At 28 days of curing Figure 49(a) shows the water absorption of control and GO-CNCMs is about 8.149mm, 4.966mm, 6.489mm, 6.998mm, and 6.489mm respectively at the end of the test completion. Which is about 39.06, 20.36, 14.11, and 20.36 percent lower than the control sample.

Furthermore, in Figure 49(b) shows the water absorption after 90 days of control and GO-CNCMs is about 7.177mm, 1.527mm, 3.054mm, 4.453mm, and 4.835mm respectively at the end of the test completion. Which is about 78.72, 57.45, 37.95, and 32.63 percent lower at 90 days of curing as compared to the control. This decrease is attributable to the filler action of graphene oxide in the cement matrix (Qi et al., 2021).

At both the micro- and nanoscales, the material was found to be compacted. Thus, nanomaterials help lower the vacancy at the nano level, which in turn reduces the water absorption into the cementitious mortar (Gamal et al., 2021).

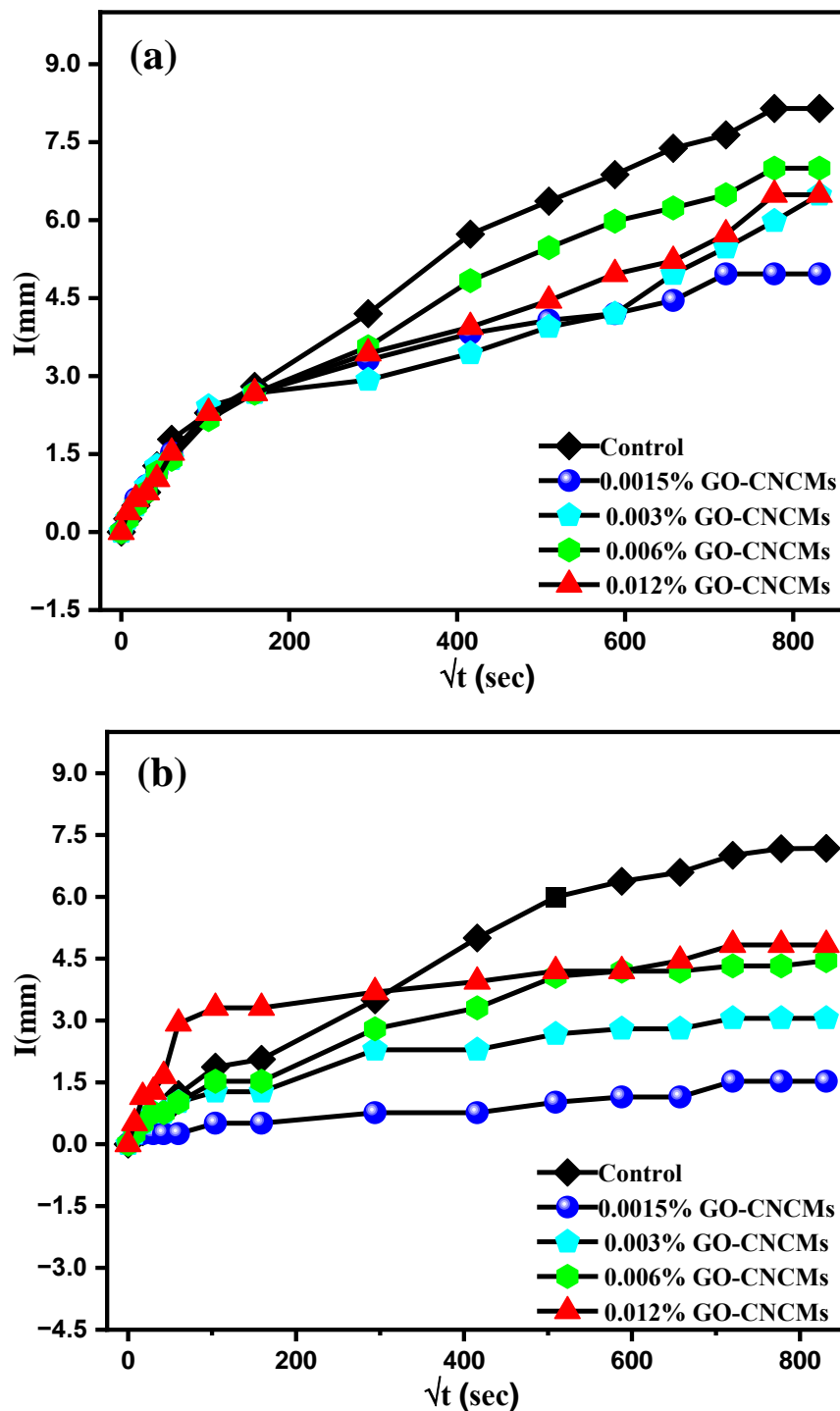


Figure 4.49 Water Absorption for GO-CNCMs after (a) 28 Days of curing, (b) 90 Days of curing

Table 4.15 presents the water absorption values for GO-CNCMs at curing ages of 28 days. Remarkably, the recorded values demonstrated a notable lower the water

absorption value for the GO-CNCMs at 28 days of curing age. The most substantial decrement in water absorption was observed for the 0.0015% GO-CNCMs, followed by a gradual increase in water absorption as the GO dosage increased, particularly at the 28-day curing age.

Table 4.15 Water Absorption for GO-CNCMs after 28 Days of curing

Mix Designation	Time (\sqrt{t})	Control	Dosage of GO Incorporated (% by Weight of Cement)			
			0.0015% GO-CNCMs	0.003% GO-CNCMs	0.006% GO-CNCMs	0.012% GO-CNCMs
			Water Absorption (I(mm))			
GO-CNCMs	7.74597	0.255	0.255	0.254	0.254	0.382
	17.3205	0.509	0.637	0.509	0.509	0.636
	30	0.764	0.891	0.891	0.763	0.763
	42.4264	1.273	1.146	1.272	1.145	1.018
	60	1.783	1.528	1.400	1.400	1.527
	103.923	2.292	2.292	2.418	2.163	2.290
	158.745	2.801	2.674	2.672	2.672	2.672
	293.939	4.202	3.310	2.927	3.563	3.435
	415.692	5.730	3.820	3.435	4.835	3.944
	509.117	6.366	4.074	3.944	5.471	4.453
	587.878	6.876	4.202	4.199	5.980	4.962
	657.267	7.385	4.456	4.962	6.235	5.217
	720	7.639	4.966	5.471	6.489	5.726
	777.689	8.149	4.966	5.980	6.998	6.489
	831.384	8.149	4.966	6.489	6.998	6.489

Table 4.16 illustrates the water absorption values for GO-CNCMs after 90 days of curing. Notably, the results showed a significant reduction in water absorption for the GO-CNCMs at this 90-day curing age. The most substantial decrease in water absorption was observed for the 0.0015% GO-CNCMs, followed by a gradual increase in water absorption as the GO dosage increased, particularly at the 90-day curing age.

Table 4.16 Water Absorption for GO-CNCMs after 90 Days of curing

Mix Designation	Time (\sqrt{t})	Control	Dosage of GO Incorporated (% by Weight of Cement)			
			0.0015% GO-CNCMs	0.003% GO-CNCMs	0.006% GO-CNCMs	0.012% GO-CNCMs
			Water Absorption (I(mm))			
GO-CNCMs	7.74597	0.190	0.254	0.254	0.254	0.509
	17.3205	0.302	0.254	0.509	0.509	1.145
	30	0.579	0.254	0.763	0.763	1.272
	42.4264	0.755	0.254	0.763	0.763	1.654
	60	1.206	0.254	1.018	1.018	2.927
	103.923	1.873	0.509	1.272	1.527	3.308
	158.745	2.059	0.509	1.272	1.527	3.308
	293.939	3.503	0.763	2.290	2.799	3.690
	415.692	5.001	0.763	2.290	3.308	3.944
	509.117	5.996	1.018	2.672	4.072	4.199
	587.878	6.378	1.145	2.799	4.199	4.199
	657.267	6.594	1.145	2.799	4.199	4.453
	720	7.008	1.527	3.054	4.326	4.835
	777.689	7.171	1.527	3.054	4.326	4.835
	831.384	7.177	1.527	3.054	4.453	4.835

4.10.2 Water Absorption of FMWCNTs-CNCMs

The water absorption of the cured samples control and FMWCNTs at the age of 28 days is about 8.149mm, 5.217mm, 6.362mm, 5.344mm, and 6.616mm, respectively at the end of the test completion and it as about 35.98, 21.92, 34.41, and 18.80 percent lower for 90 days, as shown in Figure 50(a). Moreover, after 90days of curing the control and FMWCNTs sample showed 7.177mm, 5.221mm, 1.489mm, 5.562mm, 5.557mm, respectively, which is approximately 35.93, 81.72, 31.74, and 31.81 percent lower as observed in Figure 50(b). The reduced capacity of cementitious mortar to absorb water is correlated with the bridging action of FMWCNTs. It helped refine the

voids or pores in the cementitious mortar(MacLeod et al., 2020). The microstructural behaviour, as seen in the microstructural tests, also provided support for the study.

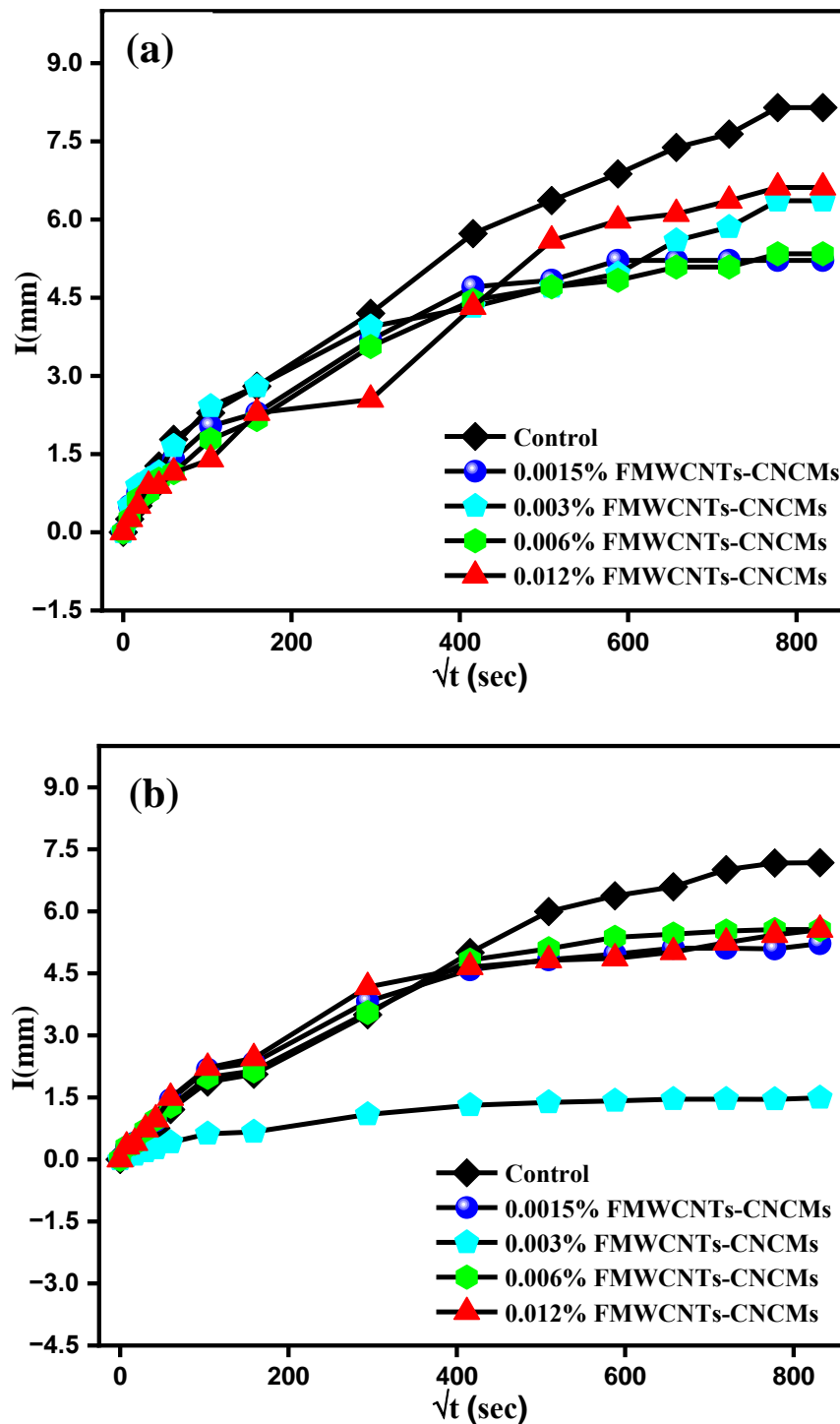


Figure 4.50 Water Absorption for FMWCNTs-CNCMs after 28 Days of curing, (b) 90 Days of curing

Table 4.17 presents the water absorption values for FMWCNTs-CNCMs at curing ages of 28days. Remarkably, the recorded values demonstrated a notable lower the water absorption value for the FMWCNTs-CNCMs at 28 days of curing age. The most

substantial decrement in water absorption was observed for the 0.003% FMWCNTs-CNCMs, followed by a gradual increase in water absorption as the FMWCNTs dosage increased, particularly at the 28-day curing age.

Table 4.17 Water Absorption for FMWCNTs-CNCMs after 28 Days of curing

Mix Design ation	Time (\sqrt{t})	Control	Dosage of FMWCNTs Incorporated (% by Weight of Cement)			
			0.0015% FMWCN Ts- CNCMs	0.003% FMWCN Ts- CNCMs	0.006% FMWC NTs- CNCMs	0.012% FMWCN Ts- CNCMs
			Water Absorption (I(mm))			
FMWC NTs- CNCM s	7.74597	0.255	0.509	0.509	0.254	0.254
	17.3205	0.509	0.763	0.891	0.636	0.509
	30	0.764	0.891	1.018	0.763	0.891
	42.4264	1.273	1.145	1.145	1.018	0.891
	60	1.783	1.400	1.654	1.145	1.145
	103.923	2.292	2.036	2.418	1.781	1.400
	158.745	2.801	2.290	2.799	2.163	2.290
	293.939	4.202	3.690	3.944	3.563	2.545
	415.692	5.730	4.708	4.326	4.453	4.326
	509.117	6.366	4.835	4.708	4.708	5.599
	587.878	6.876	5.217	4.962	4.835	5.980
	657.267	7.385	5.217	5.599	5.090	6.107
	720	7.639	5.217	5.853	5.090	6.362
	777.689	8.149	5.217	6.362	5.344	6.616
	831.384	8.149	5.217	6.362	5.344	6.616

Table 4.18 illustrates the water absorption values for FMWCNTs-CNCMs after 90 days of curing. Notably, the results showed a significant reduction in water absorption for the FMWCNTs-CNCMs at this 90-day curing age. The most substantial decrease in water absorption was observed for the 0.0015% FMWCNTs-CNCMs, followed by a gradual

increase in water absorption as the FMWCNTs dosage increased, particularly at the 90-day curing age.

Table 4.18 Water Absorption for FMWCNTs-CNCMs after 90 Days of curing

Mix Designation	Time (\sqrt{t})	Control	Dosage of FMWCNTs Incorporated (% by Weight of Cement)			
			0.0015% FMWCNTs-CNCMs	0.003% FMWCNTs-CNCMs	0.006% FMWCNTs-CNCMs	0.012% FMWCNTs-CNCMs
			Water Absorption (I(mm))			
FMWCNTs-CNCMs	7.74597	0.190	0.279	0.079	0.304	0.314
	17.3205	0.302	0.394	0.113	0.389	0.401
	30	0.579	0.683	0.195	0.711	0.729
	42.4264	0.755	0.940	0.268	0.966	0.968
	60	1.206	1.443	0.412	1.289	1.490
	103.923	1.873	2.178	0.621	1.986	2.217
	158.745	2.059	2.339	0.667	2.144	2.451
	293.939	3.503	3.822	1.090	3.553	4.170
	415.692	5.001	4.590	1.309	4.822	4.656
	509.117	5.996	4.831	1.378	5.096	4.817
	587.878	6.378	4.964	1.416	5.371	4.864
	657.267	6.594	5.110	1.457	5.450	5.016
	720	7.008	5.111	1.458	5.522	5.244
	777.689	7.171	5.093	1.453	5.562	5.429
	831.384	7.177	5.221	1.489	5.562	5.557

4.10.3 Water Absorption of HCNMs-CNCMs

The water absorption values for the HCNMs-CNCMs for various dosages incorporation after 28 and 90 days of curing are presented in Figure 4.51(a) and (b). At 28 days of curing Figure 4.51(a) shows the water absorption of control and HCNMs-CNCMs is about 8.149mm, 5.353mm, 5.953mm, 6.530mm, and 7.365mm, respectively at the end of the test completion. Which is about 39.06, 20.36, 14.11, and

20.36 percent lower than the control 34.30, 26.94, 19.86, and 9.61 percent lower for 28 days.

However, after 90days of curing the value of water absorption for control and HCNMs-CNCMs are observed at Figure 51(b), 7.177mm, 5.306mm, 6.153mm, 5.816mm, and 6.387mm, respectively. Which is about 34.88, 24.48, 28.62, and 21.61 for 0.0015% FMWCNTs-CNCMs, 0.003% FMWCNTs-CNCMs, 0.006% FMWCNTs-CNCMs, 0.012% FMWCNTs-CNCMs, percentage points lower for 90 days, respectively. This is indicative of pore network refinement as a result of microstructure densification (also supported by a Microstructural study) accompanied by the development of hydration products, most notably C-S-H gel, in the presence of hybrid carbon nanomaterials (Abedi et al., 2020). The reduction in capillary water absorption may be due to GO's strong pozzolanic reactivity, which makes the mortar denser and better packed, and FMWCNTs ultra-high strength and stiffness with extremely high aspect ratios and surface areas. As a result, incorporating a modest number of nanomaterials into mortar can significantly reduce capillary water absorption. Furthermore, GPPC has the greatest impact on improving mortar capillary water absorption.

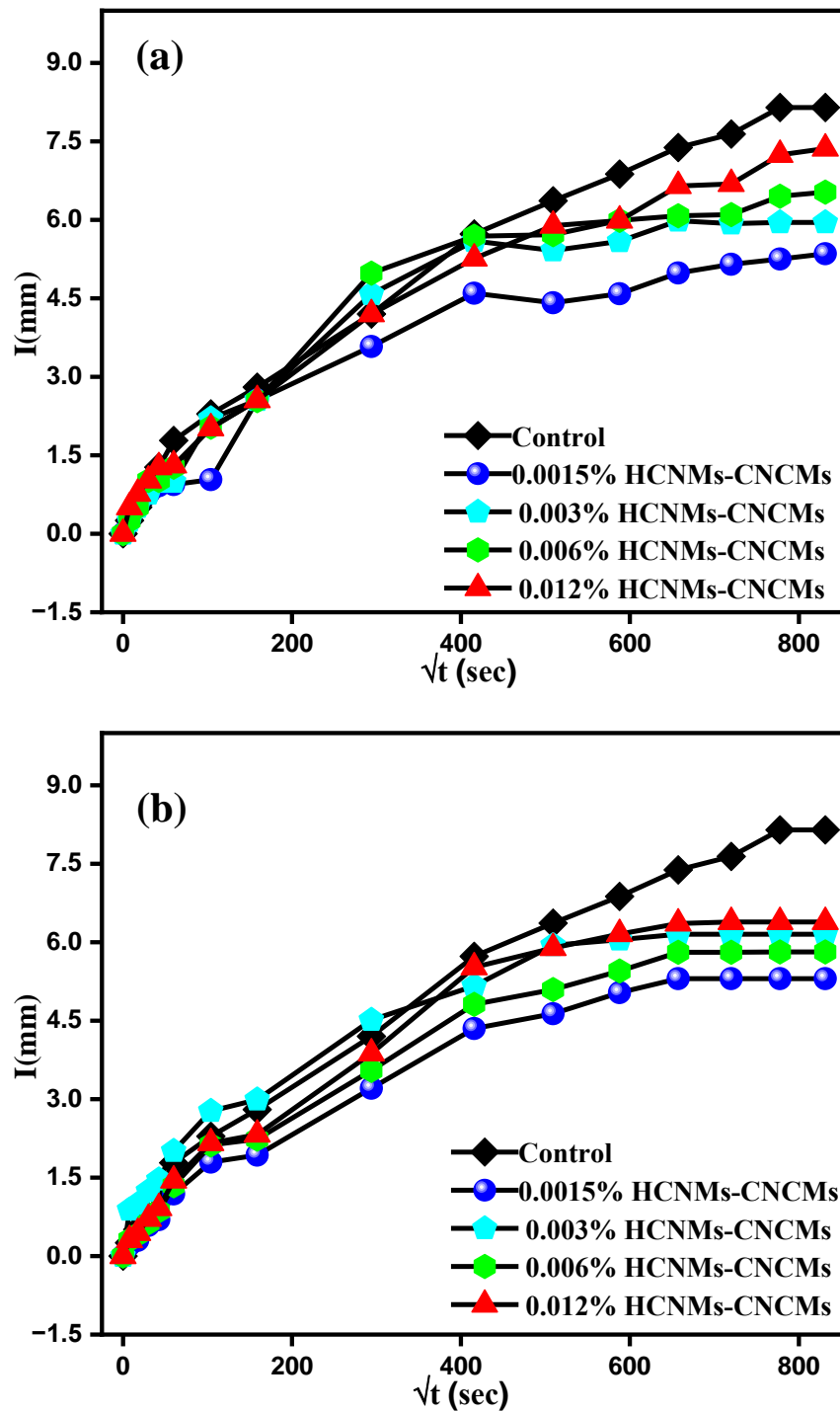


Figure 4.51 Water Absorption for HCNMs-CNCMs after (a)28 Days of curing, (b) 90 Days of curing

Table 4.19 illustrates the water absorption values for HCNMs-CNCMs after 28 days of curing. Notably, the results showed a significant reduction in water absorption for the HCNMs-CNCMs at 28 days curing age. The most substantial decrease in water absorption was observed for the 0.0015% HCNMs-CNCMs, followed by a gradual increase in water absorption as the HCNMs dosage increased, particularly at the 28 days curing age.

Table 4.19 Water Absorption for HCNMs-CNCMs after 28 Days of curing

Mix Designation	Time (\sqrt{t})	Control	Dosage of HCNMs Incorporated (% by Weight of Cement)			
			0.0015% HCNMs - CNCMs	0.003% HCNMs -CNCMs	0.006% HCNMs - CNCMs	0.012% HCNMs - CNCMs
			Water Absorption (I(mm))			
HCNMs-CNCMs	7.74597	0.255	0.254	0.245	0.254	0.509
	17.3205	0.509	0.509	0.511	0.509	0.763
	30	0.764	0.763	0.764	1.018	1.018
	42.4264	1.273	0.918	0.988	1.018	1.272
	60	1.783	0.940	0.990	1.272	1.309
	103.923	2.292	1.036	2.204	2.036	2.019
	158.745	2.801	2.554	2.554	2.545	2.554
	293.939	4.202	3.581	4.581	4.981	4.199
	415.692	5.730	4.599	5.599	5.689	5.261
	509.117	6.366	4.416	5.416	5.716	5.889
	587.878	6.876	4.590	5.590	5.990	5.989
	657.267	7.385	4.985	5.985	6.079	6.649
	720	7.639	5.153	5.930	6.100	6.689
	777.689	8.149	5.253	5.953	6.453	7.243
	831.384	8.149	5.353	5.953	6.530	7.365

Table 4.20 illustrates the water absorption values for HCNMs-CNCMs after 90 days of curing. Notably, the results showed a significant reduction in water absorption for the HCNMs-CNCMs at this 90-day curing age. The most substantial decrease in water absorption was observed for the 0.0015% HCNMs-CNCMs, followed by a gradual increase in water absorption as the HCNMs dosage increased, particularly at the 90-day curing age.

Table 4.20 Water Absorption for HCNMs-CNCMs after 90 Days of curing

Mix Designation	Time (\sqrt{t})	Control	Dosage of HCNMs Incorporated (% by Weight of Cement)			
			0.0015% HCNMs - CNCMs	0.003% HCNMs-CNCMs	0.006% HCNMs - CNCMs	0.012% HCNMs-CNCMs
			Water Absorption (I(mm))			
HCNMs-CNCMs	7.74597	0.190	0.212	0.886	0.309	0.307
	17.3205	0.302	0.300	0.994	0.414	0.444
	30	0.579	0.585	1.244	0.635	0.711
	42.4264	0.755	0.697	1.461	0.861	0.917
	60	1.206	1.188	2.008	1.345	1.444
	103.923	1.873	1.797	2.771	2.126	2.159
	158.745	2.059	1.929	2.990	2.237	2.323
	293.939	3.503	3.208	4.513	3.550	3.876
	415.692	5.001	4.350	5.166	4.813	5.522
	509.117	5.996	4.635	5.942	5.095	5.889
	587.878	6.378	5.037	6.049	5.450	6.158
	657.267	6.594	5.306	6.153	5.807	6.358
	720	7.008	5.306	6.153	5.807	6.387
	777.689	7.171	5.306	6.153	5.816	6.387
	831.384	7.177	5.306	6.153	5.816	6.387

To summarize, the results pertaining to water absorption suggest that:

- (a) The incorporation of GO, FMWCNTs, and HCNMs at various concentrations into cementitious nanocomposites results in demoted water absorption values compared to the control samples.

- (b) The water absorption value for control sample was found to be 8.149mm and 7.177mm at the end of the saturation value, after 28 and 90, days of curing respectively.
- (c) For GO, the most significant decrement in water absorption was observed in the case of 0.0015% GO-CNCMs, with a water absorption value of 4.96mm and 1.527mm for 28 and 90 days respectively.
- (d) Regarding FMWCNTs, the most notable reduction in water absorption occurred in the case of 0.003% FMWCNTs-CNCMs, with water absorption values of 6.398 mm and 1.489mm at 28 and 90 days, respectively.
- (e) In the context of HCNMs, the most significant decrease in water absorption was observed in the case of 0.0015% HCNMs-CNCMs, with water absorption values of 5.353 mm and 5.306 mm at 28 and 90 days, respectively.
- (f) GO-CNCMs demonstrated their most substantial reduction in water absorption at dosages of 0.0015%, with water absorption values of 4.966 mm and 1.527 mm at 28 and 90 days, respectively

A brief summary of the electrical resistivity results for control samples and CNCMs/HCNMs incorporated CNCMs at different dosages and curing ages is provided in Table 4.21.

Table 4.21 Average Water Absorption Values of CNMs/HCNMs based CNCMs

Mix Designation	Time (\sqrt{t})	Control	Dosage of GO Incorporated (% by Weight of Cement)			
			0.0015% GO-CNCMs	0.003% GO-CNCMs	0.006% GO-CNCMs	0.012% GO-CNCMs
			28 Days of curing			
			Water Absorption (I(mm))			
	7.74597	0.255	0.255	0.254	0.254	0.382
	17.3205	0.509	0.637	0.509	0.509	0.636
	30	0.764	0.891	0.891	0.763	0.763
	42.4264	1.273	1.146	1.272	1.145	1.018

GO-CNCMs	60	1.783	1.528	1.400	1.400	1.527
	103.923	2.292	2.292	2.418	2.163	2.290
	158.745	2.801	2.674	2.672	2.672	2.672
	293.939	4.202	3.310	2.927	3.563	3.435
	415.692	5.730	3.820	3.435	4.835	3.944
	509.117	6.366	4.074	3.944	5.471	4.453
	587.878	6.876	4.202	4.199	5.980	4.962
	657.267	7.385	4.456	4.962	6.235	5.217
	720	7.639	4.966	5.471	6.489	5.726
	777.689	8.149	4.966	5.980	6.998	6.489
	831.384	8.149	4.966	6.489	6.998	6.489
	Time (\sqrt{t})	Control	Dosage of FMWCNTs Incorporated (% by Weight of Cement)			
FMWCNTs- CNCMs			0.0015% FMWC NTs- CNCMs	0.003% FMWC NTs- CNCMs	0.006% FMWC NTs- CNCMs	0.012% FMWC NTs- CNCMs
			Water Absorption (I(mm))			
	7.74597	0.255	0.509	0.509	0.254	0.254
	17.3205	0.509	0.763	0.891	0.636	0.509
	30	0.764	0.891	1.018	0.763	0.891
	42.4264	1.273	1.145	1.145	1.018	0.891
	60	1.783	1.400	1.654	1.145	1.145
	103.923	2.292	2.036	2.418	1.781	1.400
	158.745	2.801	2.290	2.799	2.163	2.290
	293.939	4.202	3.690	3.944	3.563	2.545
	415.692	5.730	4.708	4.326	4.453	4.326

	509.117	6.366	4.835	4.708	4.708	5.599
	587.878	6.876	5.217	4.962	4.835	5.980
	657.267	7.385	5.217	5.599	5.090	6.107
	720	7.639	5.217	5.853	5.090	6.362
	777.689	8.149	5.217	6.362	5.344	6.616
	831.384	8.149	5.217	6.362	5.344	6.616
HCNMs- CNCMs	Time (√t)	Control	Dosage of HCNMs Incorporated (% by Weight of Cement)			
			0.0015% HCNMs - CNCMs	0.003% HCNMs - CNCMs	0.006% HCNMs - CNCMs	0.012% HCNMs - CNCMs
			Water Absorption (I(mm))			
	7.74597	0.255	0.254	0.245	0.254	0.509
	17.3205	0.509	0.509	0.511	0.509	0.763
	30	0.764	0.763	0.764	1.018	1.018
	42.4264	1.273	0.918	0.988	1.018	1.272
	60	1.783	0.940	0.990	1.272	1.309
	103.923	2.292	1.036	2.204	2.036	2.019
	158.745	2.801	2.554	2.554	2.545	2.554
	293.939	4.202	3.581	4.581	4.981	4.199
	415.692	5.730	4.599	5.599	5.689	5.261
	509.117	6.366	4.416	5.416	5.716	5.889
	587.878	6.876	4.590	5.590	5.990	5.989
	657.267	7.385	4.985	5.985	6.079	6.649
	720	7.639	5.153	5.930	6.100	6.689
	777.689	8.149	5.253	5.953	6.453	7.243

	831.384	8.149	5.353	5.953	6.530	7.365
Mix Designation	Time (\sqrt{t})	Control	Dosage of GO Incorporated (% by Weight of Cement)			
			0.0015% GO-CNCMs	0.003% GO-CNCMs	0.006% GO-CNCMs	0.012% GO-CNCMs
			90 Days of curing			
			Water Absorption (I(mm))			
GO-CNCMs	7.74597	0.190	0.254	0.254	0.254	0.509
	17.3205	0.302	0.254	0.509	0.509	1.145
	30	0.579	0.254	0.763	0.763	1.272
	42.4264	0.755	0.254	0.763	0.763	1.654
	60	1.206	0.254	1.018	1.018	2.927
	103.923	1.873	0.509	1.272	1.527	3.308
	158.745	2.059	0.509	1.272	1.527	3.308
	293.939	3.503	0.763	2.290	2.799	3.690
	415.692	5.001	0.763	2.290	3.308	3.944
	509.117	5.996	1.018	2.672	4.072	4.199
	587.878	6.378	1.145	2.799	4.199	4.199
	657.267	6.594	1.145	2.799	4.199	4.453
	720	7.008	1.527	3.054	4.326	4.835
	777.689	7.171	1.527	3.054	4.326	4.835
	831.384	7.177	1.527	3.054	4.453	4.835
	Time (\sqrt{t})	Control	Dosage of FMWCNTs Incorporated (% by Weight of Cement)			
			0.0015% FMWC	0.003% FMWC	0.006% FMWC	0.012% FMWC

			NTs- CNCMs	NTs- CNCMs	NTs- CNCMs	NTs- CNCMs
			Water Absorption (I(mm))			
FMWCNTs- CNCMs	7.74597	0.190	0.279	0.079	0.304	0.314
	17.3205	0.302	0.394	0.113	0.389	0.401
	30	0.579	0.683	0.195	0.711	0.729
	42.4264	0.755	0.940	0.268	0.966	0.968
	60	1.206	1.443	0.412	1.289	1.490
	103.923	1.873	2.178	0.621	1.986	2.217
	158.745	2.059	2.339	0.667	2.144	2.451
	293.939	3.503	3.822	1.090	3.553	4.170
	415.692	5.001	4.590	1.309	4.822	4.656
	509.117	5.996	4.831	1.378	5.096	4.817
	587.878	6.378	4.964	1.416	5.371	4.864
	657.267	6.594	5.110	1.457	5.450	5.016
	720	7.008	5.111	1.458	5.522	5.244
	777.689	7.171	5.093	1.453	5.562	5.429
	831.384	7.177	5.221	1.489	5.562	5.557
	Time (√t)	Control	Dosage of HCNMs Incorporated (% by Weight of Cement)			
			0.0015% HCNMs - CNCMs	0.003% HCNMs - CNCMs	0.006% HCNMs - CNCMs	0.012% HCNMs - CNCMs
			Water Absorption (I(mm))			
	7.74597	0.190	0.212	0.886	0.309	0.307
	17.3205	0.302	0.300	0.994	0.414	0.444

HCNMs- CNCMs	30	0.579	0.585	1.244	0.635	0.711
	42.4264	0.755	0.697	1.461	0.861	0.917
	60	1.206	1.188	2.008	1.345	1.444
	103.923	1.873	1.797	2.771	2.126	2.159
	158.745	2.059	1.929	2.990	2.237	2.323
	293.939	3.503	3.208	4.513	3.550	3.876
	415.692	5.001	4.350	5.166	4.813	5.522
	509.117	5.996	4.635	5.942	5.095	5.889
	587.878	6.378	5.037	6.049	5.450	6.158
	657.267	6.594	5.306	6.153	5.807	6.358
	720	7.008	5.306	6.153	5.807	6.387
	777.689	7.171	5.306	6.153	5.816	6.387
	831.384	7.177	5.306	6.153	5.816	6.387

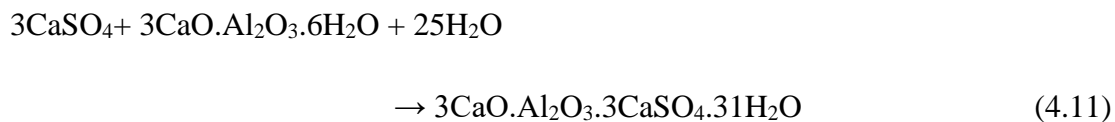
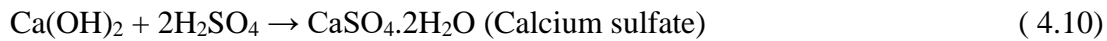
4.11 ACID AND SULFATE ATTACK OF CNMs/HCNMs BASED CNCMs

The changes in compressive strengths of cementitious nanocomposite incorporated with GO, FMWCNTs, and HCNMs on immersion in 5% solution of sulfuric acid at 28 and 90 days of curing are shown in Figure 4.52, 4.53, and 4.54 respectively. It was observed that acid attack on mortar matrix incorporated with carbon nanomaterials results in weight loss which was comparatively lower than control sample. Acid attack study was done as per ASTM C-267 (Astm, 2012). After 28 days of curing in water, the samples were removed from the curing tank and dried in a hot air oven at $105^{\circ}\text{C} \pm 5^{\circ}\text{C}$ for 24 hours, where the initial compressive strengths were measured.

Furthermore, for the test of sulphate resistance, a sodium sulfate solution (5%) was used. Then, six samples from each mixture were placed in solutions containing 5% sulfuric acid and 5% sodium sulfate. The pH of the acidic and base mediums was measured during the entire testing period. Every 30 days, the solution was renewed (Allahverdi & Skvara, 2000; Prabavathy et al., 2020; Sujay et al., 2020; Živica, 2004). After 28 and 90 days of acid and sulfate attacks, the specimens were removed and rinsed with deionized

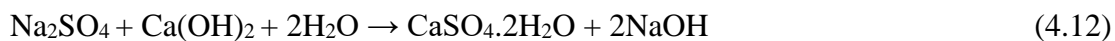
water. The specimens were then rapidly dried with blotting paper, followed by the elimination of any loose particles. In accordance with ASTM C-109, the effects of acid and sulfate attack were examined by estimating the retained weight of the specimens and then evaluating their compressive strength (Vafaei et al., 2018). In the presence of an acidic solution, soluble calcium sulfate (gypsum) may form (Vafaei et al., 2018).

Equation 4.10 and 4.11 depicts the expression of the reaction.



The reaction under consideration entails the production of expansive products, namely gypsum and ettringite. These compounds have the potential to accelerate the deterioration of building materials in acidic environments, while also contributing to the mechanisms of expansive deterioration.

In the case of a sodium sulfate attack, the formation of sodium hydroxide as a residue of the reaction (equation 4.12) ensures high alkalinity, which plays a vital role in the stability of the cementitious hydration products (Jo et al., 2017; Kanaujia et al., 2021).



The mechanical strength of specimens subjected to sulfate attack initially increases and then decreases as the concentration of CNMs increases, both at 28 and 90 days.

4.11.1 Acid and Sulfate Attack on GO-CNCMs

The Acid and Sulfate Attack results for GO-CNCMs, varying in dosages of GO and curing times, are presented in Figure 4.52 (a, b). Figure 4.52 (a) shows that, after 28 days of acid attack, the compressive strengths of 0.0015% GO-CNCMs was found to be 38.67%, greater than control sample. After 90 days of acid curing the compressive strength was determined for 0.0015% GO-CNCMs was found about 36.21% higher as compared to the control sample. It was observed that among all the GO-incorporated cementitious nanocomposites, the sample containing 0.0015% of GO was found to lose minimum weight. This is due to the production of higher C-S-H gel in carbon nanomaterials incorporated composites which assisted in enhanced hydration process.

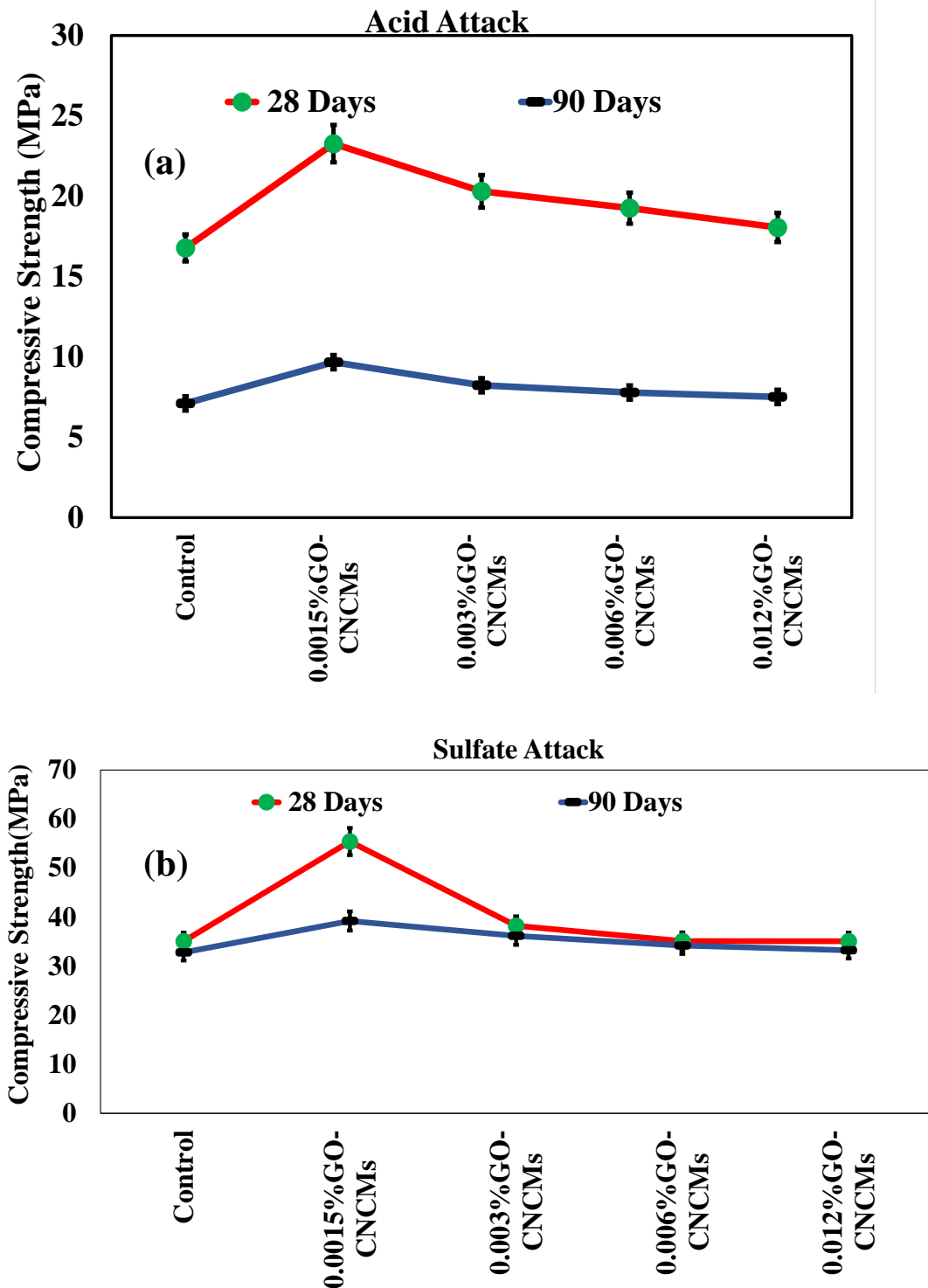


Figure 4.52 Compressive Strength after 28 and 90 Days of (a) Acid cured GO-CNCMs, (b) Sulfate cured GO-CNCMs

The mechanical strength of sulfate-attacked specimens initially increases and then decreases as the concentration of CNMs increases, at both 28 and 90 days. Figure 4.52(b) illustrates a notable increase in compressive strength compared to the control. Furthermore, 0.0015%GO-CNCMs exhibited a substantial increase in compressive strength, up by 58%, when compared to control at 28 days of curing. Similarly, at 90

days of curing, the compressive strengths of 0.0015%GO-CNCMs increased by 19.57%. The incorporation of nano materials into cement-based composites allows for the modification of the matrix by reducing porosity through their filling properties, hence improving the durability performance.

The Table 4.22 summarizes the percentage variation in compressive strength after acid and sulfate cured sample for various GO-CNCMs mixes at curing durations 28, and 90 days.

Table 4.22 Percentage Change in Compressive Strength after acid and sulfate cured for GO-CNCMs

Mix Designation	Dosage of GO incorporated (% by weight of cement)	Percentage Change in Compressive Strength with respect to Control (%)			
		Acid Cured		Sulfate Cured	
		28 days	90 days	28 days	90 days
GO-CNCMs	0.0015%GO-CNCMs	38.67	36.21	58.01	19.57
	0.003%GO-CNCMs	21.02	16.02	9.07	10.31
	0.006%GO-CNCMs	14.76	9.66	0.13	4.29
	0.012%GO-CNCMs	7.59	5.78	0.03	1.36

4.11.2 Acid and Sulfate Attack of FMWCNTs-CNCMs

The Acid and Sulfate Attack results for FMWCNTs-CNCMs, varying in dosages of FMWCNTs and curing times, are presented in Figure 53(a and b). Figure 53(a) shows that, after 28 days of acid attack, the compressive strengths of 0.006% FMWCNTs-CNCMs was found to be 43.63 %, greater than control sample. Whereas, after 90 days, of an acid attack, the higher compressive strength was found to be 47.59%, for 0.006% FMWCNTs-CNCMs relation to control. We found that among the nano-engineered CNCMs, those containing 0.006% FMWCNTs lost the least amount of weight. This is because the additional CNMs assisted in the hydration process that produced the additional C-S-H gel.

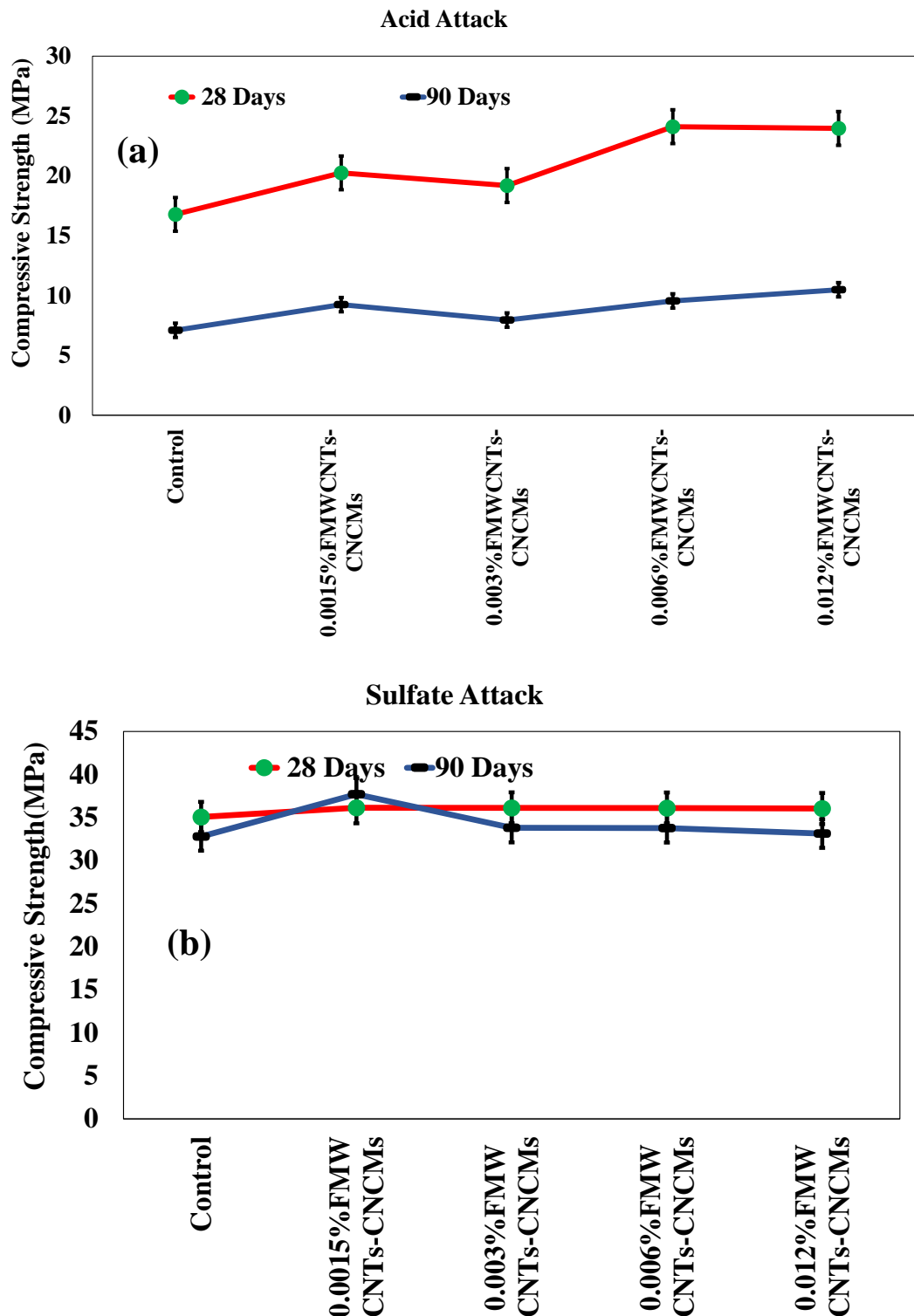


Figure 4.53 Compressive Strength after 28 and 90 Days of (a) Acid cured FMWCNTs-CNCMs, (b) Sulfate cured FMWCNTs-CNCMs

The mechanical strength of specimens subjected to sulfate attack exhibits an interesting trend as the concentration of CNMs increases. In Figures 55(b), an initial increase in compressive strength compared to the control can be observed, followed by a subsequent decrease. Furthermore, 0.0015%FMWCNTs-CNCMs displayed a

notable increase in compressive strength, up by 3.05%, when compared to the control at 28 days of curing. Similarly, at 90 days of curing, the compressive strengths of 0.0015%FMWCNTs-CNCMs increased by 14.98%.

Table 4.23 provides a summary of the percentage variation in compressive strength for FMWCNTs-CNCMs samples after exposure to acid and sulfate curing at durations of 28 and 90 days.

Table 4.23 Percentage Change in Compressive Strength after acid and sulfate cured for FMWCNTs-CNCMs

Mix Designation	Dosage of FMWCNTs incorporated (% by weight of cement)	Percentage Change in Compressive Strength with respect to Control (%)			
		Acid Cured		Sulfate Cured	
		28 days	90 days	28 days	90 days
FMWCNTs-CNCMs	0.0015% FMWCNTs-CNCMs	20.66	30.10	3.06	14.98
	0.003% FMWCNTs-CNCMs	14.35	11.94	3.03	3.08
	0.006% FMWCNTs-CNCMs	43.63	34.46	2.97	3.01
	0.012% FMWCNTs-CNCMs	42.80	47.60	2.80	1.06

4.11.3 Acid and Sulfate Attack on HCNMs-CNCMs

Figure 54(a and b) illustrates the consequences of the Acid and Sulfate Attack on HCNMs-CNCMs, with variations in the amount of hybrid CNMs and periods of curing. Figure 54(a) demonstrates that the compressive strengths of 0.0015%HCNMs-CNCMs were 55.64% greater than the control sample after 28 days of acid exposure. In a similar trend, it was shown that the compressive strength of the specimens containing 0.0015%HCNMs-CNCMs exhibited a noteworthy enhancement of 75.31% following a 90-day exposure to acid assault, as compared to the control group. Additionally, it was revealed that within CNCMs, the specimens contained a concentration of 0.0015% HCNMs exhibited the lowest degree of mass reduction. The presence of more HCNMs

can be ascribed to facilitating the process of hydration, resulting in the production of additional C-S-H gel.

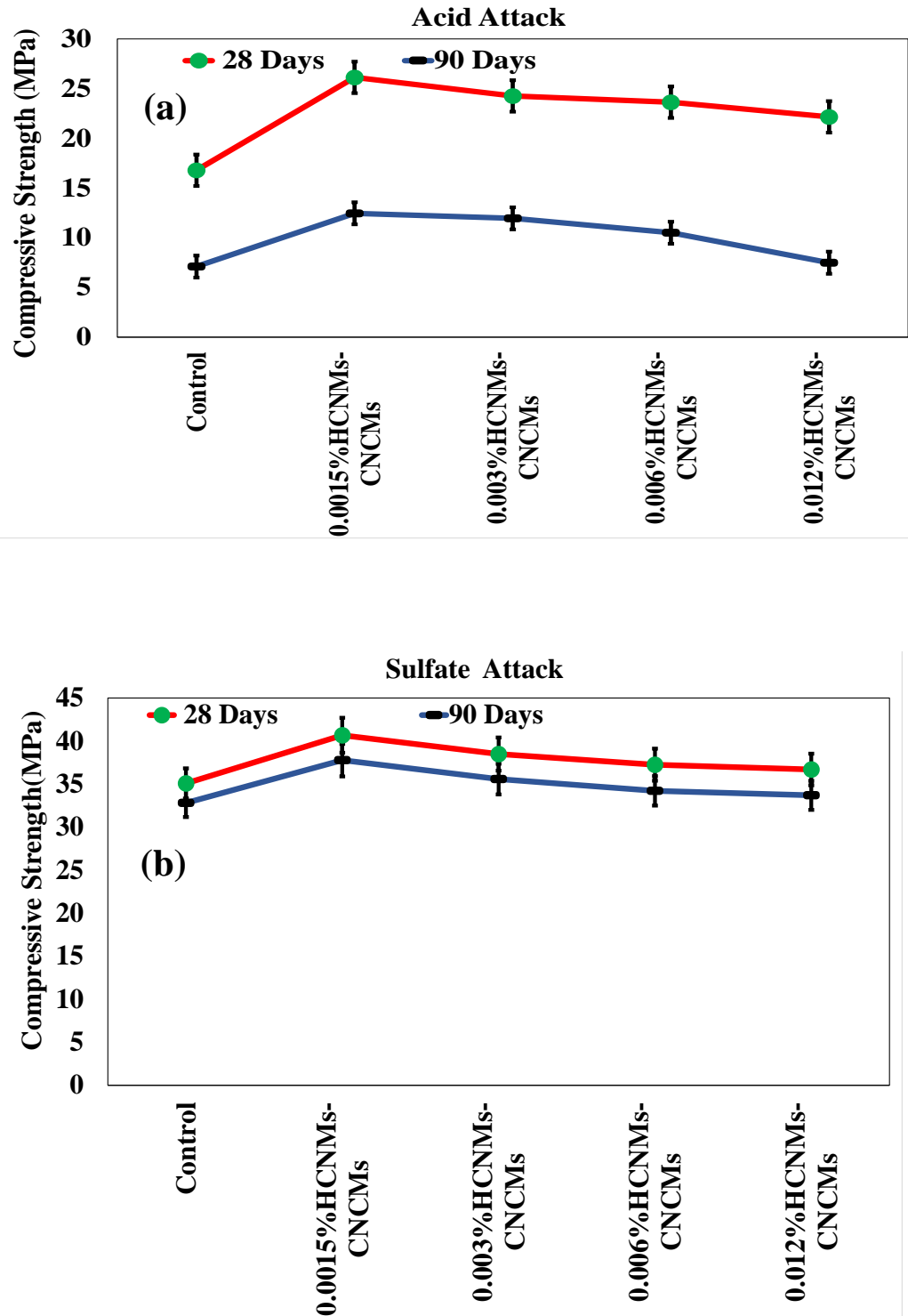


Figure 4.54 Compressive Strength after 28 and 90 Days of (a) Acid cured HCNMs-CNCMs, (b) Sulfate cured HCNMs-CNCMs

Furthermore, at 28 days of curing, 0.003% HCNMs-CNCMs exhibited a significant increase in compressive strength, up by 15.9%, when compared to control. Similarly,

at 90 days of curing, 0.003%HCNMs-CNCMs displayed a notable increase in compressive strength, up by 15.19% can be shown in Figure 54(b). These cementitious compositions containing reinforcing nanomaterials showcased a matrix with lower porosity, rendering them more resistant to Sulfate attack. This enhanced resistance can be attributed to the nucleation effect facilitated by well-dispersed CNMs stabilized by superplasticizer in the matrix. This effect promotes the secondary pozzolanic reaction of calcium hydroxide (CH) with fly ash, leading to the production of more calcium-silicate-hydrate (C-S-H) gel. This, in turn, results in reduced porosity and a denser microstructure, effectively preventing the intrusion of aggressive ions into the inner structure of the mortar.

Table 4.24 provides a summary of the percentage variation in compressive strength for HCNMs-CNCMs mixes after exposure to acid and sulfate curing for different curing durations, specifically 28 and 90 days.

Table 4.24 Percentage Change in Compressive Strength after acid and sulfate cured for HCNMs-CNCMs

Mix Designation	Dosage of HCNMs incorporated (% by weight of cement)	Percentage Change in Compressive Strength with respect to Control (%)			
		Acid Cured		Sulfate Cured	
		28 days	90 days	28 days	90 days
HCNMs-CNCMs	0.0015% HCNMs-CNCMs	55.65	75.32	15.93	15.20
	0.003% HCNMs-CNCMs	44.53	68.22	9.73	8.47
	0.006% HCNMs-CNCMs	40.77	47.88	6.19	4.29
	0.012% HCNMs-CNCMs	32.04	5.37	4.61	2.70

Table 4.25 shows a concise summary of the average compressive values after acid and sulfate attack for CNCMs mortar samples incorporating CNMs/HCNMs, including GO, FMWCNTs, and HCNMs. These values are documented at different dosages (0.0015%, 0.003%, 0.006%, and 0.012%) and curing periods (28, and 90 days).

Table 4.25 Average Compressive Strength Values of CNMs/HCNMs based CNCMs

S. No	Mix Designation	Dosages of CNMs/HCNMs (% by Weight of Cement)	Compressive Strength (MPa)			
			Acid Cured		Sulfate Cured	
			28 days	90 days	28 days	90 days
1	Control	0.00	16.78	7.10	35.08	32.80
2	GO-CNCMs	0.0015	23.27	9.67	55.43	39.22
		0.003	20.31	8.24	38.26	36.18
		0.006	19.26	7.79	35.13	34.21
		0.012	18.06	7.51	35.09	33.25
3	FMWCNTs-CNCMs	0.0015	20.25	9.24	36.15	37.72
		0.003	19.19	7.95	36.14	33.81
		0.006	24.11	9.55	36.12	33.79
		0.012	23.96	10.48	36.06	33.15
4	HCNMs-CNCMs	0.0015	26.12	12.45	40.67	37.79
		0.003	24.26	11.95	38.49	35.58
		0.006	23.62	10.50	37.25	34.21
		0.012	22.16	7.48	36.70	33.69

The conclusions derived from the investigations into compressive strength after acid and sulfate exposure are as follows:

1. The addition of individual carbon nanomaterials (such as GO and FMWCNTs) as well as hybrid carbon nanomaterials (GO and FMWCNTs) resulted in differing levels of improvement in the compressive strength after acid and sulfate attack of CNCMs. These improvements were noticeable at 28 and 90 days of curing.
2. For GO, the most notable improvement in compressive strength after acid attack, amounting to 38.67% and 36.21%, was achieved with a 0.0015% dosage of GO-CNCMs after curing for 28 days and 90 days, respectively.
3. In the case of FMWCNTs, the most significant improvement in compressive strength after acid attack, amounting to 43.63% and 47.59%, was achieved with a 0.006% FMWCNTs-CNCMs after curing for 28 days and 90 days, respectively.

4. In the case of HCNMs, the most significant enhancement in compressive strength after acid attack, amounting to 55.6% and 75.31%, was observed for 0.0015% HCNMs-CNCMs after curing for 28 days and 90 days, respectively.
5. The most significant enhancement in compressive strength following sulfate exposure was observed in the case of GO. Specifically, a dosage of 0.0015% of GO-CNCMs resulted in a noteworthy increase of 58% and 19.57% in compressive strength after a curing period of 28 days and 90 days, respectively.
6. In the context of FMWCNTs, a notable enhancement in compressive strength following sulfate attack was seen. Specifically, the addition of 0.0015% FMWCNTs-CNCMs resulted in a substantial increase of 3.05% and 14.98% after a curing period of 28 days and 90 days, respectively.
7. Following 28 and 90 days of curing, 0.003%HCNMs-CNCMs showed an improvement in compressive strength following sulfate assault, reaching to 15.93% and 15.20%, respectively.

4.12 A PROPOSED METHOD TO IMPROVE THE WAY GO, FMWCNTs, AND HCNMs BEHAVE MORE EFFECTIVELY

4.12.1 Steric stabilization of GO, FMWCNTs, and HCNMs: A proposed mechanism

Steric stabilization of GO and FMWCNTs facilitates their effective dispersion within the alkaline cement pore solution, allowing them to maximize their potential in strengthening the cementitious matrix. The suggested mechanism illustrates how ultrasonic treatment and the presence of superplasticizers enhance the dispersion of GO, FMWCNTs and HCNMs through steric stabilization.

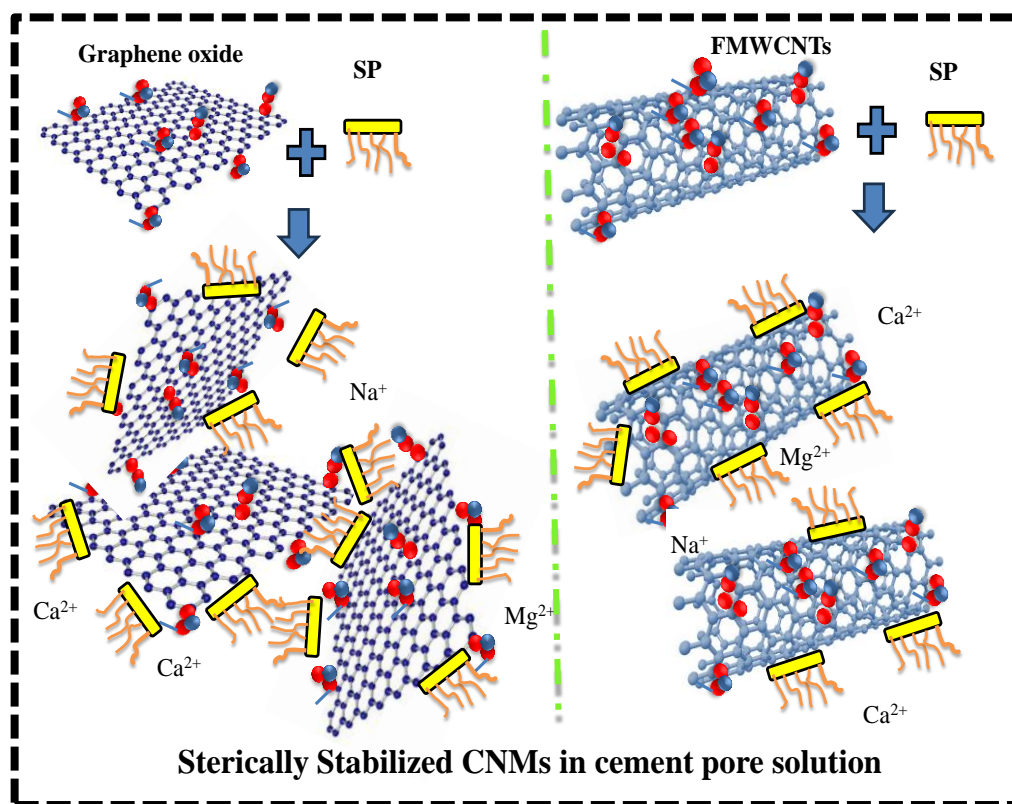


Figure 4.55 Depicting the Stabilization of using GO and FMWCNTs by Comb-Shaped SP Molecules

The agglomeration of carbon nanomaterials that were initially well-dispersed can be attributed to two primary factors: firstly, the presence of calcium ions in the cement pore solution leads to cross-linking between the -COO- functional groups of GO and FMWCNTs, resulting in agglomeration; secondly, the alkaline nature of the cement pore solution (i.e., OH^- ions) leads to deoxygenation of the oxygen functionalities over prolonged (Du et al., 2020; Lu, Hanif, et al., 2017a; Tabish et al., 2023).

The UV-visible spectroscopy studies of GO, FMWCNTs, and HCNMs have demonstrated a significant improvement in the dispersion of these carbon nanomaterials when SP is introduced. The lateral chains of SP serve to shield CNMs/HCNMs from the ionic environment and simultaneously stabilize GO and FMWCNTs or through a steric stabilization effect. Additionally, the dispersibility of GO and FMWCNTs in water is maintained through electrostatic repulsions between their oxygen functionalities (Yan et al., 2020; Lu et al., 2017). The proposed mechanism illustrating the steric stabilization of GO and FMWCNTs by SP is depicted in Figure 4.55.

The dispersion ability of HCNMs in an aqueous solution with SP is notably superior to that of either GO and FMWCNTs. This enhanced dispersion is attributed to the synergy of two factors: firstly, the effect of SP on HCNMs, and secondly, HCNMs' inherent capacity to self-disperse through π - π non-covalent stacking interactions that occur between the GO and FMWCNTs. A schematic illustrating the SP-assisted dispersion of HCNMs is presented in Figure 4.56.

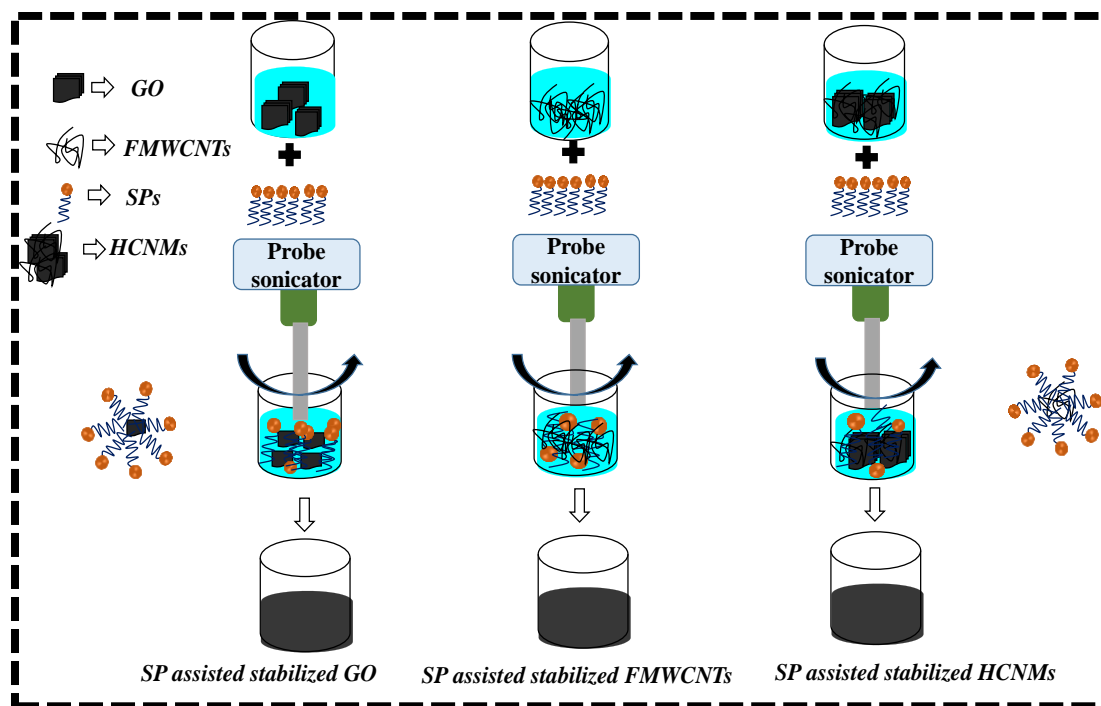


Figure 4.56 Diagram Depicting the Stabilization of CNMs and HCNMs Using SP Molecules

Moreover, dispersions stabilized by SP remain relatively stable for approximately 5 hours without significant changes. In contrast, HCNMs dispersions lacking SP tend to rapidly re-agglomerate after ultrasonication in the absence of stabilization.

4.12.2 Proposed Mechanism for CNMs/HCNMs Hydration Reaction in CNCMs

Comparing the strengthening mechanisms of individual carbon nanomaterials and hybrid carbon nanomaterials in cementitious nanocomposites, it is possible to propose that the incorporation of HCNMs into CNCMs results in greater physico-mechanical strength than FMWCNTs or GO. In addition, greater dosages of CNMs were ineffective in enhancing the strength of CNCMs, whereas the use of HCNMs alone or in combination with pozzolanic cementitious materials improved the strength values even at higher dosages of HCNMs, i.e., up to 0.012% (by weight of cement).

This is due to the physical exfoliation of carbon nanomaterials caused by the ball-bearing effect of pozzolanic materials present in cement, thereby enhancing the overall hydration mechanism. Active sites provided by GO and FMWCNTs aid in the nucleation of refined calcium hydroxide (C-H) during hydration reactions (Kaur, Kothiyal, & Arora, 2020; Kaur, Kothiyal, & Singh, 2020; Priyap & Vanitha, 2021; Sathyan & Anand, 2019b). These C-H crystallites have improved adhesion with other hydration products, such as C-S-H gel, which results in a denser microstructure (Q. Wang et al., 2019; L. Zhao, Guo, Liu, et al., 2017) (Figure 4.57).

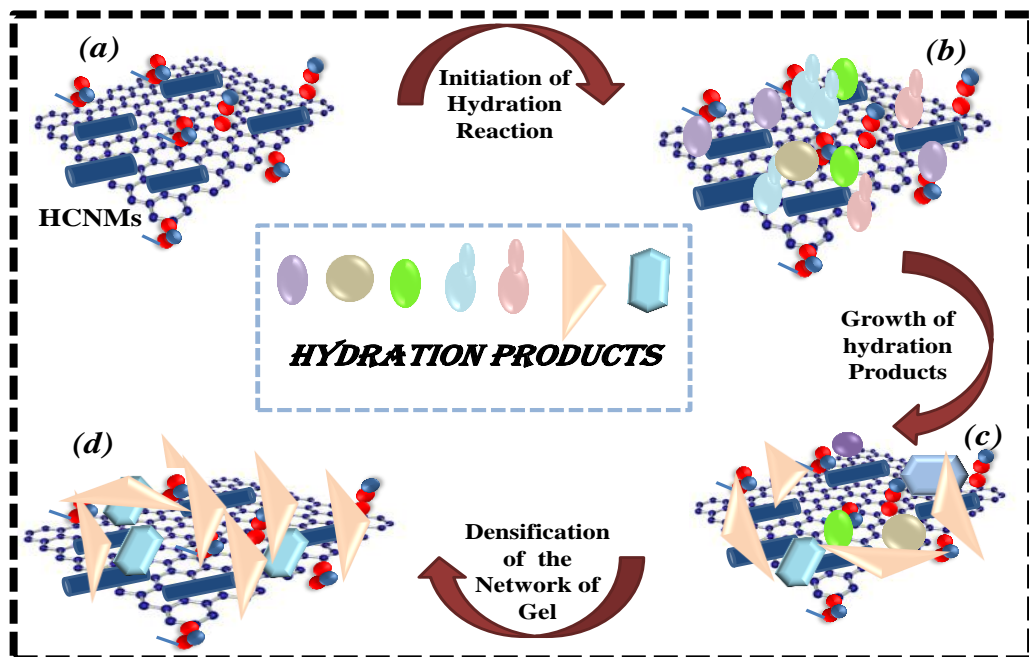


Figure 4.57 Schematic Diagram Illustrating the Growth of Hydration Products on Active Sites of HCNMs in CNCMs

CONCLUSIONS AND SCOPE FOR FUTURE RESEARCH

5.1 GENERAL

The conclusions derived from the present study have been categorized into different sections, and an overview is presented in Figure 5.1.

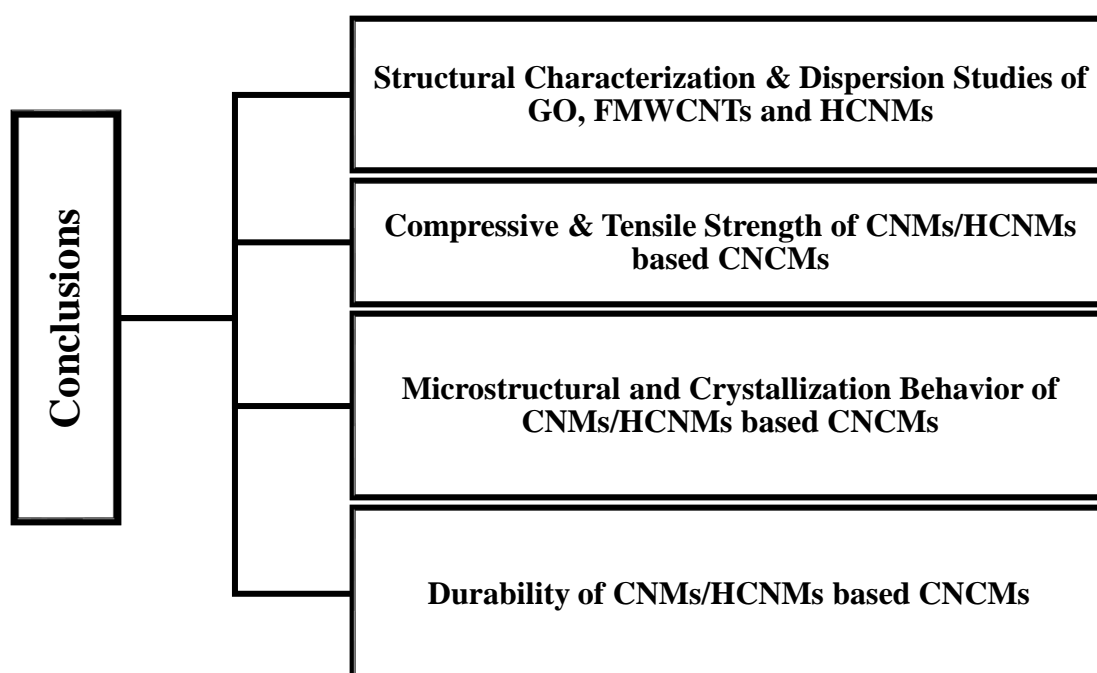


Figure 5.1 Overview of Concluding Remarks

5.2 CONCISE CONCLUDING REMARKS

The conclusions drawn from the current investigation are as follows:

5.2.1 Findings from the Synthesis/Functionalization of Carbon Nanomaterials and Dispersion Studies

1. Graphene Oxide (GO) was successfully synthesized from Ball-milled Graphite Powder (MGP) using Hummer's Method with a yield of $\geq 95\%$. The structural characterization of GO was conducted through FE-SEM-EDX, HR-TEM, Raman Spectroscopy, FT-IR and PXRD.

2. The FE-SEM and HR-TEM observations showed GO with corrugated surface morphology due to attachment of functional groups. EDX results have shown the presence of 60.35 carbon and 39.65% oxygen content in GO sheets.
3. The Raman spectroscopic results exhibited characteristic bands (i.e., D-band, G-band, and 2D-band) typical of carbon nanomaterials. The I_D/I_G ratio for GO was determined to be 0.9, indicating the successful functionalization of graphene sheets. The 2D-band for GO was nearly absent, suggesting the absence of graphene sheet stacking in GO. PXRD analysis indicated an increased interplanar spacing of 0.85nm between the graphitic sheets after functionalization.
4. The synthesis Multiwalled Carbon Nanotubes (MWCNTs) was done via CVD method and further functionalization of Multiwalled Carbon Nanotubes (FMWCNTs) was successfully achieved through nitric acid treatment, resulting in a high yield of FMWCNTs (~74%). The structural characterization of FMWCNTs was conducted using various techniques, including FE-SEM-EDX, HR-TEM, Raman Spectroscopy, FTIR, and PXRD.
5. FE-SEM and HR-TEM observations revealed the presence of defects on the outer walls of MWCNTs following the functionalization process. This was further confirmed by Raman spectroscopy, where the I_D/I_G ratio increased from 1.2 to 1.5 after functionalization. EDX results indicated the incorporation of oxygen content, accounting for 8.57% in FMWCNTs in the form of functional groups. PXRD results identified in both MWCNTs and FMWCNTs, with an interplanar spacing of 0.33 nm.
6. The general conclusion drawn from these studies is that HCNMs (GO to FMWCNTs ratio of 4:1) exhibited superior dispersion ability compared to individual CNMs (i.e., GO or FMWCNTs). Furthermore, the addition of SP significantly enhanced the dispersion of CNMs/HCNMs, surpassing the dispersion achieved in the absence of SP.

5.2.2 Conclusions derived from the analysis of Compressive Strength

The findings obtained from the examinations conducted on compressive strength can be summarized as follows:

1. The inclusion of individual carbon nanomaterials (either GO and FMWCNTs) as well as hybrid carbon nanomaterials (GO and FMWCNTs) led to varying degrees

of improvement in the compressive strength in cementitious nanocomposites. This enhancement was observed at different curing times.

2. For GO-CNCMs, the most significant enhancement in compressive strength, found to be 11.67, was achieved with 0.0015% dosage of GO-CNCMs after a curing period of 90 days. In the case of FMWCNTs-CNCMs, the highest compressive strength enhancement of 8.73 has been obtained for 0.0015% FMWCNTs-CNCMs after 90 days of curing. The highest compressive strength for HCNMs-CNCMs was observed at the 0.0015% dosage, resulting in a remarkable improvement compared to the control. The maximum enhancement in compressive strength by 21.32% has been witnessed on addition of 0.0015% HCNMs.
3. The enhanced strength properties of HCNMs incorporated CNCMs have been attributed to the superior dispersion of HCNMs in comparison to FMWCNTs and GO inside the cementitious matrix.

5.2.3 Conclusions derived from the analysis of Tensile Strength

1. The GO-CNCMs demonstrated their maximum tensile strength at a dosage of 0.0015%, resulting in a significant enhancement of 26.35% when compared to the control. Nevertheless, a further decline in strength was detected beyond the dosage of 0.0015%, which can be attributed to the diminished dispersion of nanomaterials. The FMWCNTs-CNCMs demonstrated a notable increase in tensile strength of 20.61% when subjected to a concentration of 0.0015% FMWCNTs-CNCMs, in comparison to the control sample.
2. On the other hand, HCNMs incorporated CNCMs demonstrated the highest increase in tensile strength at a relatively higher dosage of 0.0015%, resulting in a remarkable 35.27% improvement compared to the control mortar providing a possible pathway to pozzolana Portland cementitious mortar based in application of construction building materials.

5.2.4 Conclusions derived from the analysis of Microstructure

1. The incorporation of GO, FMWCNTs and HCNMs has been seen to enhance the microstructural characteristics of the CNCMs when compared to the control samples, given that CNMs/HCNMs have been included in an optimal dosage in the CNCMs. The examination of a control mortar sample has revealed the presence of

a microstructure characterized by loose packing cementitious composites. In this microstructure, the hydration products are distributed in a random manner at all stages of the curing process.

2. The utilization of GO, FMWCNTs, and HCNMs have been observed to result in the formation of dense and well-aligned hydration products in CNCMs. The utilization of GO has resulted in enhancements to the microstructural characteristics in following distinct manners: The alteration of crystal morphologies to various shapes, such as stacked, hexagonal, and polyhedral geometries, are observed. The enhancement of microstructural compactness attributed to the filling of pores and voids. The interfacial bonding between the cement and the interface site. Furthermore, the FMWCNTs attributed to key factors: The compactness of hydration products resulting from the filler effects of FMWCNTs. The crack-bridging effects of FMWCNTs across the hydration products. It's worth noting that for high dosages of FMWCNTs, specifically 0.003% in CNCMs, porous microstructural features were observed, leading to lower mechanical strength. The incorporation of HCNMs has enhanced the microstructure in significant ways: It combines the superior mechanical properties of FMWCNTs with the better dispersibility of GO, and the 3-D network leads to improved dispersion of HCNMs in the cement matrix compared to individual GO and FMWCNTs, resulting in better strengths. In the case of HCNMs-CNCMs, flower-shaped flaky hydration products were observed at early curing ages, which ultimately densify into firm polyhedral-shaped C-S-H bars. Additionally, the consumption rate of fly ash particles presents in by portlandite has found to be improved.

5.2.5 Conclusions derived from the analysis of Crystallization Behavior

1. The crystallization patterns observed in CNCMs revealed the formation of different cement hydrates, including ettringite (AFt) and calcium hydroxide (C-H). These crystalline phases are the result of the hydration of calcium aluminates (C_3A) and calcium silicates (C_3S and C_2S), respectively.
2. In the case of CNCMs, the introduction of GO, FMWCNTs, and HCNMs has accelerated the production rate of CSH, indicated the consumption of calcium silicates when compared to the control sample. The highest hydration rate of

cement phases was observed in HCNMs-CNCMs, as evidenced by the reduction in the crystallite size of C-H.

5.2.6 Durability Behaviour

5.2.6.1 Conclusions derived from the analysis of Electrical Resistivity behaviour

1. The addition of individual carbon nanomaterials (GO or FMWCNTs) as well as hybrid carbon nanomaterials (HCNMs) at various concentrations in cementitious nanocomposites results in an increase in electrical resistivity compared to control samples. This is attributed to the improved hydration degree and microstructural densification of the cementitious matrix containing CNMs/HCNMs, which hinders the movement of ions through capillary pores.
2. The addition of GO, FMWCNTs, and HCNMs at different concentrations to cementitious nanocomposites leads to an increase in electrical resistivity values when compared to the control samples. This shows that both GO, and FMWCNTs, have a non-conductive character due to perturbations in the sp^2 -electron network that are generated by functionalization. In addition, the dosage of CNMs/HCNMs remained well below the value that is considered to be the percolation threshold.
3. The electrical resistivity value for control sample was found to be 98.77 k-ohm-cm after 90 days of curing.
4. For FMWCNTs, the most significant improvement in electrical resistivity was observed in the case of 0.0015% FMWCNTs-CNCMs, with an electrical resistivity value of 104.67 k-ohm-cm.
5. GO-CNCMs and HCNMs-CNCMs exhibited their highest electrical resistivity values at dosages of 0.0015%, with resistivity values of 101.22 k-ohm-cm and 104.26 k-ohm-cm, respectively.
6. The electrical resistivity values of CNCMs have a tendency to be higher. There are two explanations for this: (a) The generation of extra C-S-H gel by pozzolanic reaction, thus refining the pores. (b) The reduction in the concentration of free alkali ions (i.e., Na^+ , Ca^{2+} , and K^+) in the cement matrix as a consequence of pozzolanic activity by pozzolanic materials. This reduction occurs as a direct result of the pozzolanic activity by pozzolanic materials present in the cement.
7. The higher electrical resistivity observed in CNCMs can be advantageous in applications where long-term structural durability is required. It restricts the

movement of charge carriers or ions within the cementitious matrix, contributing to enhanced performance and longevity.

5.2.6.2 Studies Conclusions derived from the analysis of Capillary Water Absorption

1. The incorporation of GO, FMWCNTs, and HCNMs at various concentrations into cementitious nanocomposites results in demoted water absorption values compared to the control samples.
2. The water absorption value for control sample was found to be 8.149mm and 7.177mm at the end of the saturation value, after 28 and 90, days of curing respectively.
3. For GO, the most significant decrement in water absorption was observed in the case of 0.0015% GO-CNCMs, with a water absorption value of 4.966mm and 1.527mm for 28 and 90 days respectively.
4. Regarding FMWCNTs, the most notable reduction in water absorption occurred in the case of 0.003% FMWCNTs-CNCMs, with water absorption values of 6.398mm and 1.489mm at 28 and 90 days, respectively.
5. In the context of HCNMs, the most significant decrease in water absorption was observed in the case of 0.0015% HCNMs-CNCMs, with water absorption values of 5.353mm and 5.306mm at 28 and 90 days, respectively.
6. GO-CNCMs demonstrated their most substantial reduction in water absorption at dosages of 0.0015%, with water absorption values of 4.966mm and 1.527mm at 28 and 90 days, respectively.

5.2.6.3 Studies Conclusions derived from the analysis compressive strength after acid and sulfate attack

1. The addition of individual carbon nanomaterials (such as GO and FMWCNTs) as well as hybrid carbon nanomaterials (GO and FMWCNTs) resulted in differing levels of improvement in the compressive strength after acid and sulfate attack of CNCMs. These improvements were noticeable at 28 and 90 days of curing.
2. For GO, the most notable improvement in compressive strength after acid attack, amounting to 38.67% and 36.21%, was achieved with a 0.0015% dosage of GO-CNCMs after curing for 28 days and 90 days, respectively.

3. In the case of FMWCNTs, the most significant improvement in compressive strength after acid attack, amounting to 43.63% and 47.59%, was achieved with a 0.006% FMWCNTs-CNCMs after curing for 28 days and 90 days, respectively.
4. In the case of HCNMs, the most significant enhancement in compressive strength after acid attack, amounting to 55.6% and 75.31%, was observed for 0.0015% HCNMs-CNCMs after curing for 28 days and 90 days, respectively.
5. The most significant enhancement in compressive strength following sulfate exposure was observed in the case of GO. Specifically, a dosage of 0.0015% of GO-CNCMs resulted in a noteworthy increase of 58% and 19.57% in compressive strength after a curing period of 28 days and 90 days, respectively.
6. In the context of FMWCNTs, a notable enhancement in compressive strength following sulfate attack was seen. Specifically, the addition of 0.0015% FMWCNTs-CNCMs resulted in a substantial increase of 3.05% and 14.98% after a curing period of 28 days and 90 days, respectively.
7. Following 28 and 90 days of curing, 0.003% HCNMs-CNCMs showed an improvement in compressive strength following acid assault, reaching to 15.93% and 15.20%, respectively.

5.3 CONCLUDING STATEMENT

The incorporation of HCNMs into CNCMs has resulted in enhanced physico-mechanical properties when compared to the individual carbon nanomaterials that were used to produce the nanocomposites. This demonstrates that synergy between GO and FMWCNTs as a reinforcing agent in the cementitious matrix is actually possible. The use of HCNMs-CNCMs with a concentration of 0.0015% produced the greatest increase in compressive strength, which was 21.32%. The 0.0015% HCNMs-CNCMs had the greatest increase in tensile strength, which was measured at 35.27%. This suggests that the utilization of GO and FMWCNTs in hybrid form has a significant potential for enhancing the quality of commercial Pozzolana Portland Cement, even at lowest dosages. These observations might be of use to the scientific community in paving the way for the use of Pozzolanic Portland cementitious material in environmentally friendly building materials.

The microstructural, crystalline, and durability analyses all provide support to the assertion that there was an increase in the material's mechanical strength. Because the insertion of carbon nanomaterials results in an increase in electrical resistivity and a reduction in water absorption, there is a good opportunity to use CNCMs in areas that require the durability of construction materials. The results of the current study are typical of the composition, source, quality, and size of raw materials and carbon nanomaterials, and are thus subject to vary. Nonetheless, the tendencies of the research results are well-defined and typical of the many attributes evaluated.

5.4 SCOPE FOR FUTURE RESEARCH

The primary objective of this study was to assess the impact of carbon nanomaterials, both in their pure form and as hybrids, on the physical and mechanical characteristics of cementitious nanocomposites. This assessment was carried out while considering the dosage of carbon nanomaterials and the curing duration. Additionally, the study conducted functionalization processes, transforming indigenously synthesized MWCNTs into FMWCNTs. Moreover, using Hummer's method to convert graphite powder into GO. Beyond the physico-mechanical strength, we delved into various other matrix properties, including microstructural behavior, crystalline patterns, and durability aspects. The following additional studies are recommended to enhance the information in this particular field of nanocomposites and its applications:

1. Further exploration is needed to understand how the presence of HCNMs affects the flexural strength and thermal conductivity of CNCMs, with the aim of developing more energy-efficient building materials.
2. The impact of carbon nanomaterials on the physico-mechanical and physico-chemical properties of the cementitious matrix can be examined in the presence of supplementary cementitious materials, such as bottom ash, silica fume, copper slag, and metakaolin, among others.
3. Sustainable and high-performance building materials can be developed by combining carbon nanomaterials with alternative binder systems like geopolymers or alkali-activated materials.
4. Research in these areas has the potential to contribute to the ongoing development and use of carbon-based cementitious materials in the construction sector, with a particular emphasis on sustainability, performance, and safety.

- Abedi, M., Fanguero, R., & Correia, A. G. (2020). An Effective Method for Hybrid CNT/GNP Dispersion and Its Effects on the Mechanical, Microstructural, Thermal, and Electrical Properties of Multifunctional Cementitious Composites. *Journal of Nanomaterials*, 2020. <https://doi.org/10.1155/2020/6749150>
- Abrão, P. C. R. A., Cardoso, F. A., & John, V. M. (2020). Efficiency of Portland-pozzolana cements: Water demand, chemical reactivity and environmental impact. *Construction and Building Materials*, 247. <https://doi.org/10.1016/j.conbuildmat.2020.118546>
- Ahmad, S., Baghabra Al-Amoudi, O. S., Khan, S. M. S., & Maslehuddin, M. (2022). Effect of silica fume inclusion on the strength, shrinkage and durability characteristics of natural pozzolan-based cement concrete. *Case Studies in Construction Materials*. <https://doi.org/10.1016/j.cscm.2022.e01255>
- Ahmaruzzaman, M. (2010). A review on the utilization of fly ash. In *Progress in Energy and Combustion Science*. <https://doi.org/10.1016/j.pecs.2009.11.003>
- Akkaya, Y., Ouyang, C., & Shah, S. P. (2007). Effect of supplementary cementitious materials on shrinkage and crack development in concrete. *Cement and Concrete Composites*, 29(2), 117–123. <https://doi.org/10.1016/j.cemconcomp.2006.10.003>
- Aldahdooh, M. A. A., Muhamad Bunnori, N., & Megat Johari, M. A. (2013). Development of green ultra-high performance fiber reinforced concrete containing ultrafine palm oil fuel ash. *Construction and Building Materials*, 48, 379–389. <https://doi.org/10.1016/j.conbuildmat.2013.07.007>
- Alharbi, Y., An, J., Cho, B. H., Khawaji, M., Chung, W., & Nam, B. H. (2018). Mechanical and sorptivity characteristics of edge-oxidized graphene oxide (EOGO)-cement composites: Dry-and wet-mix design methods. *Nanomaterials*, 8(9). <https://doi.org/10.3390/nano8090718>
- Ali, D., Sharma, U., Singh, R., & Singh, L. P. (2021). Impact of Silica Nanoparticles on the Durability of fly Ash Concrete. *Frontiers in Built Environment*, 7(May), 1–11. <https://doi.org/10.3389/fbuil.2021.665549>

Allahverdi, A., & Skvara, F. (2000). Acidic corrosion of hydrated cement based materials - Part 1. *Ceramics – Silikáty*, 3(44), 114–120.

Arrechea, S., Guerrero-Gutiérrez, E. M. A., Velásquez, L., Cardona, J., Posadas, R., Callejas, K., Torres, S., Díaz, R., Barrientos, C., & García, E. (2020). Effect of additions of multiwall carbon nanotubes (MWCNT, MWCNT-COOH and MWCNT-Thiazol) in mechanical compression properties of a cement-based material. *Materialia*, 11(May). <https://doi.org/10.1016/j.mtla.2020.100739>

Astm, C. (2012). Standard test methods for chemical resistance of mortars, grouts, and monolithic surfacings and polymer concretes. ASTM International.

ASTM C1585-13. (2013). Standard Test Method for Measurement of Rate of Absorption of Water by Hydraulic Cement Concretes. ASTM International, 41(147), 1–6.

Awoyera, P. O., Odutuga, O. L., Effiong, J. U., De Jesus Silvera Sarmiento, A., Mortazavi, S. J., & Hu, J. W. (2022). Development of Fibre-Reinforced Cementitious Mortar with Mineral Wool and Coconut Fibre. *Materials* (Basel, Switzerland), 15(13). <https://doi.org/10.3390/ma15134520>

Aziminezhad, M., Mahdikhani, M., & Memarpour, M. M. (2018). RSM-based modeling and optimization of self-consolidating mortar to predict acceptable ranges of rheological properties. *Construction and Building Materials*, 189, 1200–1213. <https://doi.org/10.1016/j.conbuildmat.2018.09.019>

Babak, F., Abolfazl, H., Alimorad, R., & Parviz, G. (2014). Preparation and mechanical properties of graphene oxide: Cement nanocomposites. *The Scientific World Journal*. <https://doi.org/10.1155/2014/276323>

Bache, H. H., Idorn, G. M., Nepper-Christensen, P., & Nielsen, J. (1966). Morphology of Calcium Hydroxide in Cement Paste. *Symposium on Structure of Portland Cement Paste and Concrete*, 90, 154–174. <http://onlinepubs.trb.org/Onlinepubs/sr/sr90/90-014.pdf>

Badhulika, S., Terse-Thakoor, T., Villarreal, C., & Mulchandani, A. (2015). Graphene hybrids: Synthesis strategies and applications in sensors and sensitized solar cells. In *Frontiers in Chemistry*. <https://doi.org/10.3389/fchem.2015.00038>

Bahurudeen, A., Marckson, A. V., Kishore, A., & Santhanam, M. (2014). Development of sugarcane bagasse ash based Portland pozzolana cement and evaluation of

compatibility with superplasticizers. *Construction and Building Materials*, 68, 465–475.
<https://doi.org/10.1016/j.conbuildmat.2014.07.013>

Banerjee, S., Naha, S., & Puri, I. K. (2008). Molecular simulation of the carbon nanotube growth mode during catalytic synthesis. *Applied Physics Letters*.
<https://doi.org/10.1063/1.2945798>

Banthia, N., Djeridane, S., & Pigeon, M. (1992). Electrical resistivity of carbon and steel micro-fiber reinforced cements. *Cement and Concrete Research*, 22(5), 804–814.

Barbudo, A., De Brito, J., Evangelista, L., Bravo, M., & Agrela, F. (2013). Influence of water-reducing admixtures on the mechanical performance of recycled concrete. *Journal of Cleaner Production*. <https://doi.org/10.1016/j.jclepro.2013.06.022>

Bastos, G., Patiño-Barbeito, F., Patiño-Cambeiro, F., & Armesto, J. (2016). Admixtures in cement-matrix composites for mechanical reinforcement, sustainability, and smart features. *Materials*, 9(12), 972.

Bazli, M., Li, Y.-L., Zhao, X.-L., Raman, R. K. S., Bai, Y., Al-Saadi, S., & Haque, A. (2020). Durability of seawater and sea sand concrete filled filament wound FRP tubes under seawater environments. *Composites Part B: Engineering*, 202, 108409.
<https://doi.org/https://doi.org/10.1016/j.compositesb.2020.108409>

Beaudoin, J., & Odler, I. (2019). Hydration, setting and hardening of Portland cement. *Lea's Chemistry of Cement and Concrete*, 5, 157–250.

Benmokrane, B., Chaallal, O., & Masmoudi, R. (1995). Glass fibre reinforced plastic (GFRP) rebars for concrete structures. *Construction and Building Materials*, 9(6), 353–364.

Berber, S., Kwon, Y. K., & Tománek, D. (2000). Unusually high thermal conductivity of carbon nanotubes. *Physical Review Letters*.
<https://doi.org/10.1103/PhysRevLett.84.4613>

Bhatrola, K., Maurya, S. K., Kaur, R., & Kothiyal, N. C. (2023). Materials Today : Proceedings Mechanical and electrical resistivity performance of Pozzolana Portland cement mortar admixed graphene oxide. *Materials Today: Proceedings*, xxxx.
<https://doi.org/10.1016/j.matpr.2022.11.414>

Bishop, M., Bott, S. G., & Barron, A. R. (2003). A new mechanism for cement hydration inhibition: Solid-state chemistry of calcium nitrilotris(methylene)triphosphonate. *Chemistry of Materials*, 15(16), 3074–3088. <https://doi.org/10.1021/cm0302431>

Björnström, J., Martinelli, A., Matic, A., Börjesson, L., & Panas, I. (2004). Accelerating effects of colloidal nano-silica for beneficial calcium-silicate-hydrate formation in cement. *Chemical Physics Letters*, 392(1–3), 242–248. <https://doi.org/10.1016/j.cplett.2004.05.071>

Borštnar, M., Lengauer, C. L., & Dolenec, S. (2021). Quantitative in situ x-ray diffraction analysis of early hydration of belite-calcium sulfoaluminate cement at various defined temperatures. *Minerals*, 11(3), 1–21. <https://doi.org/10.3390/min11030297>

Brodie, B. C. (1860). XXIII. - Researches on the atomic weight of graphite. *Quarterly Journal of the Chemical Society of London*. <https://doi.org/10.1039/QJ8601200261>

Buchsteiner, A., Lerf, A., & Pieper, J. (2006). Water dynamics in graphite oxide investigated with neutron scattering. *Journal of Physical Chemistry B*. <https://doi.org/10.1021/jp0641132>

Calloway, D. (1997). Beer-Lambert Law. *Journal of Chemical Education*. <https://doi.org/10.1021/ed074p744.3>

Campbell, F. C. (2010). Structural Composite Materials. In *Structural Composite Materials*. <https://doi.org/10.31399/asm.tb.scm.9781627083140>

Cao, C., Daly, M., Singh, C. V., Sun, Y., & Filleter, T. (2015). High strength measurement of monolayer graphene oxide. *Carbon*, 81(1), 497–504. <https://doi.org/10.1016/j.carbon.2014.09.082>

Cecchin, I., Reddy, K. R., Thomé, A., Tessaro, E. F., & Schnaid, F. (2017). Nanobioremediation: Integration of nanoparticles and bioremediation for sustainable remediation of chlorinated organic contaminants in soils. *International Biodeterioration & Biodegradation*, 119, 419–428. <https://doi.org/https://doi.org/10.1016/j.ibiod.2016.09.027>

Chaipanich, A., Nochaiya, T., Wongkeo, W., & Torkittikul, P. (2010). Compressive strength and microstructure of carbon nanotubes-fly ash cement composites. *Materials Science and Engineering A*. <https://doi.org/10.1016/j.msea.2009.09.039>

- Chaipanich, A., Rianyoi, R., & Nochaiya, T. (2017). The effect of carbon nanotubes and silica fume on compressive strength and flexural strength of cement mortars. *Materials Today: Proceedings*, 4(5), 6065–6071. <https://doi.org/10.1016/j.matpr.2017.06.095>
- Chakraborty, S., Kundu, S. P., Roy, A., Adhikari, B., & Majumder, S. B. (2013). Polymer modified jute fibre as reinforcing agent controlling the physical and mechanical characteristics of cement mortar. *Construction and Building Materials*, 49, 214–222. <https://doi.org/10.1016/j.conbuildmat.2013.08.025>
- Charlier, J. C., Blase, X., & Roche, S. (2007). Electronic and transport properties of nanotubes. *Reviews of Modern Physics*. <https://doi.org/10.1103/RevModPhys.79.677>
- Chen, H., Zheng, M., Sun, H., & Jia, Q. (2007). Characterization and properties of sepiolite/polyurethane nanocomposites. *Materials Science and Engineering A*. <https://doi.org/10.1016/j.msea.2006.10.008>
- Chen, J., Yao, B., Li, C., & Shi, G. (2013). An improved Hummers method for eco-friendly synthesis of graphene oxide. *Carbon*. <https://doi.org/10.1016/j.carbon.2013.07.055>
- Chen, Z., Xu, Y., Hua, J., Wang, X., Huang, L., & Zhou, X. (2020). Mechanical properties and shrinkage behavior of concrete-containing graphene-oxide nanosheets. *Materials*, 13(3), 1–15. <https://doi.org/10.3390/ma13030590>
- Cheng-yi, H., & Feldman, R. F. (1985). Hydration reactions in portland cement-silica fume blends. *Cement and Concrete Research*. [https://doi.org/10.1016/0008-8846\(85\)90056-0](https://doi.org/10.1016/0008-8846(85)90056-0)
- Cheng, Q., Debnath, S., Grogan, E., & Byrne, H. J. (2010). Ultrasound-Assisted swnts dispersion: Effects of sonication parameters and solvent properties. *Journal of Physical Chemistry C*. <https://doi.org/10.1021/jp101431h>
- Chintalapudi, K., & Pannem, R. M. R. (2020). An intense review on the performance of Graphene Oxide and reduced Graphene Oxide in an admixed cement system. *Construction and Building Materials*, 259, 120598. <https://doi.org/10.1016/j.conbuildmat.2020.120598>
- Chintalapudi, K., & Pannem, R. M. R. (2021a). Enhanced Strength, Microstructure, and Thermal properties of Portland Pozzolana Fly ash-based cement composites by

reinforcing Graphene Oxide nanosheets. *Journal of Building Engineering*, 42(February). <https://doi.org/10.1016/j.jobbe.2021.102521>

Choi, Y. C. (2022). Hydration and internal curing properties of plant-based natural fiber-reinforced cement composites. *Case Studies in Construction Materials*. <https://doi.org/10.1016/j.cscm.2022.e01690>

Choinska, M., Khelidj, A., Chatzigeorgiou, G., & Pijaudier-Cabot, G. (2007). Effects and interactions of temperature and stress-level related damage on permeability of concrete. *Cement and Concrete Research*, 37(1), 79–88. <https://doi.org/10.1016/j.cemconres.2006.09.015>

Chuah, S., Li, W., Chen, S. J., Sanjayan, J. G., & Duan, W. H. (2018). Investigation on dispersion of graphene oxide in cement composite using different surfactant treatments. *Construction and Building Materials*, 161, 519–527. <https://doi.org/10.1016/j.conbuildmat.2017.11.154>

Chuah, S., Pan, Z., Sanjayan, J. G., Wang, C. M., & Duan, W. H. (2014a). Nano reinforced cement and concrete composites and new perspective from graphene oxide. *Construction and Building Materials*, 73, 113–124.

Collins, F., Lambert, J., & Duan, W. H. (2012). The influences of admixtures on the dispersion, workability, and strength of carbon nanotube-OPC paste mixtures. *Cement and Concrete Composites*, 34(2), 201–207. <https://doi.org/10.1016/j.cemconcomp.2011.09.013>

Collins, P. G., & Avouris, P. (2000). Nanotubes for electronics. *Scientific American*. <https://doi.org/10.1038/scientificamerican1200-62>

Cui, H., Yan, X., Tang, L., & Xing, F. (2017). Possible pitfall in sample preparation for SEM analysis - A discussion of the paper “Fabrication of polycarboxylate/graphene oxide nanosheet composites by copolymerization for reinforcing and toughening cement composites” by Lv et al. *Cement and Concrete Composites*, 77, 81–85. <https://doi.org/10.1016/j.cemconcomp.2016.12.007>

Cui, K., Chang, J., Sabri, M. M. S., & Huang, J. (2022). Influence of Graphene Nanoplates on Dispersion, Hydration Behavior of Sulfoaluminate Cement Composites. *Materials*. <https://doi.org/10.3390/ma15155357>

Cui, X., Xu, S., Wang, X., & Chen, C. (2018). The nano-bio interaction and biomedical applications of carbon nanomaterials. In Carbon. <https://doi.org/10.1016/j.carbon.2018.07.069>

Damineli, B. L., Kemeid, F. M., Aguiar, P. S., & John, V. M. (2010). Measuring the eco-efficiency of cement use. *Cement and Concrete Composites*, 32(8), 555–562. <https://doi.org/10.1016/j.cemconcomp.2010.07.009>

Dash, P., Dash, T., Rout, T. K., Sahu, A. K., Biswal, S. K., & Mishra, B. K. (2016). Preparation of graphene oxide by dry planetary ball milling process from natural graphite. *RSC Advances*, 6(15), 12657–12668. <https://doi.org/10.1039/c5ra26491j>

Delgado, A. H., Paroli, R. M., & Beaudoin, J. J. (1996). Comparison of IR techniques for the characterization of construction cement minerals and hydrated products. *Applied Spectroscopy*, 50(8), 970–976. <https://doi.org/10.1366/0003702963905312>

Dheyaaldin, M. H., Mosaberpanah, M. A., & Alzebaree, R. (2022). Shrinkage behavior and mechanical properties of alkali activated mortar incorporating nanomaterials and polypropylene fiber. *Ceramics International*, 48(16), 23159–23171. <https://doi.org/10.1016/j.ceramint.2022.04.297>

Dikin, D. A., Stankovich, S., Zimney, E. J., Piner, R. D., Dommett, G. H. B., Evmenenko, G., Nguyen, S. T., & Ruoff, R. S. (2007). Preparation and characterization of graphene oxide paper. *Nature*. <https://doi.org/10.1038/nature06016>

Dong, P., Allahverdi, A., Andrei, C. M., & Bassim, N. D. (2022). The effects of nano-silica on early-age hydration reactions of nano Portland cement. *Cement and Concrete Composites*. <https://doi.org/10.1016/j.cemconcomp.2022.104698>

Du, M., Jing, H., Gao, Y., Su, H., & Fang, H. (2020). Carbon nanomaterials enhanced cement-based composites: Advances and challenges. *Nanotechnology Reviews*, 9(1), 115–135. <https://doi.org/10.1515/ntrev-2020-0011>

Du, S., Jiang, Y., Zhong, J., Ge, Y., & Shi, X. (2020). Surface abrasion resistance of high-volume fly ash concrete modified by graphene oxide: Macro- and micro-perspectives. *Construction and Building Materials*, 237, 117686. <https://doi.org/10.1016/j.conbuildmat.2019.117686>

Du, Y.-J., Wei, M.-L., Reddy, K. R., Liu, Z.-P., & Jin, F. (2014). Effect of acid rain pH on leaching behavior of cement stabilized lead-contaminated soil. *Journal of Hazardous Materials*, 271, 131–140. <https://doi.org/https://doi.org/10.1016/j.jhazmat.2014.02.002>

Du, Y., Yang, J., Skariah Thomas, B., Li, L., Li, H., Mohamed Shaban, W., & Tung Chong, W. (2020). Influence of hybrid graphene oxide/carbon nanotubes on the mechanical properties and microstructure of magnesium potassium phosphate cement paste. *Construction and Building Materials*, 260, 120449. <https://doi.org/10.1016/j.conbuildmat.2020.120449>

Eatemadi, A., Daraee, H., Karimkhanloo, H., Kouhi, M., Zarghami, N., Akbarzadeh, A., Abasi, M., Hanifehpour, Y., & Joo, S. W. (2014). Carbon nanotubes: Properties, synthesis, purification, and medical applications. *Nanoscale Research Letters*. <https://doi.org/10.1186/1556-276X-9-393>

Ehtesabi, H. (2020). Application of carbon nanomaterials in human virus detection. In *Journal of Science: Advanced Materials and Devices*. <https://doi.org/10.1016/j.jsamd.2020.09.005>

Farbod, M., Tadavani, S. K., & Kiasat, A. (2011). Surface oxidation and effect of electric field on dispersion and colloids stability of multiwalled carbon nanotubes. *Colloids and Surfaces A: Physicochemical and Engineering Aspects*. <https://doi.org/10.1016/j.colsurfa.2011.05.041>

Feng, P., Chang, H., Liu, X., Ye, S., Shu, X., & Ran, Q. (2020). The significance of dispersion of nano-SiO₂ on early age hydration of cement pastes. *Materials and Design*, 186, 108320. <https://doi.org/10.1016/j.matdes.2019.108320>

Fuji, M., Takai, C., Tarutani, Y., Takei, T., & Takahashi, M. (2007). Surface properties of nanosize hollow silica particles on the molecular level. *Advanced Powder Technology*, 18(1), 81–91. <https://doi.org/10.1163/156855207779768124>

G.S., G., & N., M. S. (2011). Effect of PFA on Strength and Water Absorption of Mortar. *Journal of Civil Engineering, Science and Technology*, 2(1), 7–11. <https://doi.org/10.33736/jcest.81.2011>

Gamal, H. A., El-Feky, M. S., Alharbi, Y. R., Abadel, A. A., & Kohail, M. (2021). Enhancement of the concrete durability with hybrid nano materials. *Sustainability (Switzerland)*, 13(3), 1–17. <https://doi.org/10.3390/su13031373>

Gao, Y., Jing, H. W., Chen, S. J., Du, M. R., Chen, W. Q., & Duan, W. H. (2019a). Influence of ultrasonication on the dispersion and enhancing effect of graphene oxide—

carbon nanotube hybrid nanoreinforcement in cementitious composite. *Composites Part B: Engineering*, 164, 45–53. <https://doi.org/10.1016/j.compositesb.2018.11.066>

Gartner, E. M. (1997). A proposed mechanism for the growth of C-S-H during the hydration of tricalcium silicate. *Cement and Concrete Research*. [https://doi.org/10.1016/S0008-8846\(97\)00049-5](https://doi.org/10.1016/S0008-8846(97)00049-5)

Gebrekrstos, A., Muzata, T. S., & Ray, S. S. (2022). Nanoparticle-Enhanced β -Phase Formation in Electroactive PVDF Composites: A Review of Systems for Applications in Energy Harvesting, EMI Shielding, and Membrane Technology. *ACS Applied Nano Materials*, 5(6), 7632–7651. <https://doi.org/10.1021/acsanm.2c02183>

Ghazizadeh, S., Duffour, P., Skipper, N. T., Billing, M., & Bai, Y. (2017). An investigation into the colloidal stability of graphene oxide nano-layers in alite paste. *Cement and Concrete Research*. <https://doi.org/10.1016/j.cemconres.2017.05.011>

Gholampour, A., Valizadeh Kiamahalleh, M., Tran, D. N. H., Ozbakkaloglu, T., & Losic, D. (2017). From Graphene Oxide to Reduced Graphene Oxide: Impact on the Physiochemical and Mechanical Properties of Graphene-Cement Composites. *ACS Applied Materials and Interfaces*. <https://doi.org/10.1021/acsami.7b16736>

Gong, K., Asce, S. M., Pan, Z., Korayem, A. H., Ph, D., Qiu, L., Li, D., Collins, F., Wang, C. M., Duan, W. H., & Asce, a M. (2014). Reinforcing Effects of Graphene Oxide on Portland Cement Paste. *Journal of Materials in Civil Engineering*.

Gong, K., Pan, Z., Korayem, A. H., Qiu, L., Li, D., Collins, F., Wang, C. M., & Duan, W. H. (2015). Reinforcing Effects of Graphene Oxide on Portland Cement Paste. *Journal of Materials in Civil Engineering*. [https://doi.org/10.1061/\(asce\)mt.1943-5533.0001125](https://doi.org/10.1061/(asce)mt.1943-5533.0001125)

Goswami, S., Maheshwari, M., & Nema, A. K. (2011). Mineral sequestration of CO₂ generated in landfills. *Proceedings of the 3rd International Conference on Environmental Management, Engineering, Planning, and Economics \& SECOTOX Conference*, June, 19–24.

Guo, T., Nikolaev, P., Rinzler, A. G., Tomanek, D., Colbert, D. T., & Smalley, R. E. (1995). Self-assembly of tubular fullerenes. *Journal of Physical Chemistry*. <https://doi.org/10.1021/j100027a002>

Guo, Z., Mao, J., Ouyang, Q., Zhu, Y., He, L., Lv, X., Liang, L., Ren, D., Chen, Y., & Zheng, J. (2010). Noncovalent functionalization of single-walled carbon nanotube by

porphyrin: Dispersion of carbon nanotubes in water and formation of self-assembly donor-acceptor nanoensemble. *Journal of Dispersion Science and Technology*. <https://doi.org/10.1080/01932690903107133>

Gupta, S., Mohapatra, B. N., & Bansal, M. (2020). A review on development of Portland limestone cement: A step towards low carbon economy for Indian cement industry. *Current Research in Green and Sustainable Chemistry*, 3(August), 100019. <https://doi.org/10.1016/j.crgsc.2020.100019>

Han, B., Zhang, K., Yu, X., Kwon, E., & Ou, J. (2012a). Electrical characteristics and pressure-sensitive response measurements of carboxyl MWNT/cement composites. *Cement and Concrete Composites*, 34(6), 794–800. <https://doi.org/10.1016/j.cemconcomp.2012.02.012>

Han, B., Zhang, K., Yu, X., Kwon, E., & Ou, J. (2012b). Fabrication of Piezoresistive CNT/CNF Cementitious Composites with Superplasticizer as Dispersant. *Journal of Materials in Civil Engineering*, 24(6), 658–665. [https://doi.org/10.1061/\(asce\)mt.1943-5533.0000435](https://doi.org/10.1061/(asce)mt.1943-5533.0000435)

Hariyadi, H., Fajrin, J., & Rahmatika, A. (2019). The Application of Response Surface Methods (RSM) to Study the Effect of Partial Portland Cement Replacement Using Silica Fume on the Properties of Mortar. *International Journal of Civil Engineering and Technology*, 10(4), 2356–2364. <http://www.iaeme.com/IJCIET/index.asp2356><http://www.iaeme.com/ijmet/issues.asp?JType=IJCIET&VType=10&IType=4><http://www.iaeme.com/IJCIET/index.asp2357><http://www.iaeme.com/IJCIET/issues.asp?JType=IJCIET&VType=10&IType=4>

Hassan, A., Elkady, H., & Shaaban, I. G. (2019). Effect of Adding Carbon Nanotubes on Corrosion Rates and Steel-Concrete Bond. *Scientific Reports*, 9(1), 1–12. <https://doi.org/10.1038/s41598-019-42761-2>

Hawreen, A., Bogas, J. A., & Dias, A. P. S. (2018). On the mechanical and shrinkage behavior of cement mortars reinforced with carbon nanotubes. *Construction and Building Materials*, 168, 459–470. <https://doi.org/10.1016/j.conbuildmat.2018.02.146>

He, T. B., Hu, R. W., He, X. L., & Li, P. Y. (2015). Progress in research on carbon nanotube reinforced metal matrix composites. *Cailiao Gongcheng/Journal of Materials Engineering*, 43(10), 91–101. <https://doi.org/10.11868/j.issn.1001-4381.2015.10.015>

- He, Z. Z., Zhu, Y. B., & Wu, H. A. (2022). A universal mechanical framework for noncovalent interface in laminated nanocomposites. *Journal of the Mechanics and Physics of Solids*. <https://doi.org/10.1016/j.jmps.2021.104560>
- Hewlett, P. C. (2003). Lea's Chemistry of Cement and Concrete. In Lea's Chemistry of Cement and Concrete. <https://doi.org/10.1016/B978-0-7506-6256-7.X5007-3>
- Hone, J., Llaguno, M. C., Nemes, N. M., Johnson, A. T., Fischer, J. E., Walters, D. A., Casavant, M. J., Schmidt, J., & Smalley, R. E. (2000). Electrical and thermal transport properties of magnetically aligned single wall carbon nanotube films. *Applied Physics Letters*. <https://doi.org/10.1063/1.127079>
- Hong, S., & Myung, S. (2007). Nanotube electronics: A flexible approach to mobility. In *Nature Nanotechnology*. <https://doi.org/10.1038/nnano.2007.89>
- Horszczaruk, E., Mijowska, E., Kalenczuk, R. J., Aleksandrak, M., & Mijowska, S. (2015). Nanocomposite of cement/graphene oxide - Impact on hydration kinetics and Young's modulus. *Construction and Building Materials*, 78, 234–242. <https://doi.org/10.1016/j.conbuildmat.2014.12.009>
- Hossain, M. U., Cai, R., Ng, S. T., Xuan, D., & Ye, H. (2021). Sustainable natural pozzolana concrete – A comparative study on its environmental performance against concretes with other industrial by-products. *Construction and Building Materials*, 270(xxxx), 121429. <https://doi.org/10.1016/j.conbuildmat.2020.121429>
- Hu, M., Guo, J., Fan, J., li, P., & Chen, D. (2019). Dispersion of triethanolamine-functionalized graphene oxide (TEA-GO) in pore solution and its influence on hydration, mechanical behavior of cement composite. *Construction and Building Materials*, 216, 128–136. <https://doi.org/10.1016/j.conbuildmat.2019.04.180>
- Huan, S., Liu, G., Cheng, W., Han, G., & Bai, L. (2018). Electrospun Poly(lactic acid)-Based Fibrous Nanocomposite Reinforced by Cellulose Nanocrystals: Impact of Fiber Uniaxial Alignment on Microstructure and Mechanical Properties. *Biomacromolecules*. <https://doi.org/10.1021/acs.biomac.8b00023>
- Huang, G., Pudasainee, D., Gupta, R., & Liu, W. V. (2019). Hydration reaction and strength development of calcium sulfoaluminate cement-based mortar cured at cold temperatures. *Construction and Building Materials*. <https://doi.org/10.1016/j.conbuildmat.2019.07.085>

Huh, S. H. (2011). Thermal reduction of graphene oxide. *Physics and Applications of Graphene-Experiments*, 19, 73–90.

Hummers, W. S., & Offeman, R. E. (1958). Preparation of Graphitic Oxide. *Journal of the American Chemical Society*, 80(6), 1339. <https://doi.org/10.1021/ja01539a017>

Hussin, M. W., Bhutta, M. A. R., Azreen, M., Ramadhansyah, P. J., & Mirza, J. (2015). Performance of blended ash geopolymer concrete at elevated temperatures. *Materials and Structures/Materiaux et Constructions*, 48(3), 709–720. <https://doi.org/10.1617/s11527-014-0251-5>

Iijima, S. (1991). Helical microtubules of graphitic carbon. *Nature*. <https://doi.org/10.1038/354056a0>

Indukuri, C. S. R., Nerella, R., & Madduru, S. R. C. (2019). Effect of graphene oxide on microstructure and strengthened properties of fly ash and silica fume based cement composites. *Construction and Building Materials*, 229, 116863. <https://doi.org/10.1016/j.conbuildmat.2019.116863>

International Energy Agency. (2021). Net Zero by 2050: A Roadmap for the Global Energy Sector. International Energy Agency, 224. <https://www.iea.org/reports/net-zero-by-2050>

Ishigami, N., Ago, H., Imamoto, K., Tsuji, M., Iakoubovskii, K., & Minami, N. (2008). Crystal plane dependent growth of aligned single-walled carbon nanotubes on sapphire. *Journal of the American Chemical Society*. <https://doi.org/10.1021/ja8024752>

Jadhav, R., & Debnath, N. C. (2011). Computation of X-ray powder diffractograms of cement components and its application to phase analysis and hydration performance of OPC cement. *Bulletin of Materials Science*. <https://doi.org/10.1007/s12034-011-0134-0>

Jain, P., Patidar, B., & Bhawsar, J. (2020). Potential of Nanoparticles as a Corrosion Inhibitor: A Review. In *Journal of Bio- and Tribo-Corrosion*. <https://doi.org/10.1007/s40735-020-00335-0>

Jalal, M., Fathi, M., & Farzad, M. (2013). Effects of fly ash and TiO₂ nanoparticles on rheological, mechanical, microstructural and thermal properties of high strength self compacting concrete. *Mechanics of Materials*, 61, 11–27. <https://doi.org/10.1016/j.mechmat.2013.01.010>

Jawed, I. (1983). HYDRATION OF PORTLAND CEMENT. *Cements Research Progress*. <https://doi.org/10.1201/9781482295016-9>

Jena, B. K., & Raj, C. R. (2007). Ultrasensitive nanostructured platform for the electrochemical sensing of hydrazine. *The Journal of Physical Chemistry C*, 111(17), 6228–6232.

Jena, B. K., & Raj, C. R. (2008a). Highly sensitive and selective electrochemical detection of sub-ppb level chromium (VI) using nano-sized gold particle. *Talanta*, 76(1), 161–165.

Jena, B. K., & Raj, C. R. (2008b). Optical sensing of biomedically important polyionic drugs using nano-sized gold particles. *Biosensors and Bioelectronics*, 23(8), 1285–1290.

Ji, T. (2005). Preliminary study on the water permeability and microstructure of concrete incorporating nano-SiO₂. *Cement and Concrete Research*, 35(10), 1943–1947. <https://doi.org/10.1016/j.cemconres.2005.07.004>

Ji, X., Xu, Y., Zhang, W., Cui, L., & Liu, J. (2016). Review of functionalization, structure and properties of graphene/polymer composite fibers. *Composites Part A: Applied Science and Manufacturing*, 87, 29–45. <https://doi.org/10.1016/j.compositesa.2016.04.011>

Jing, G. J., Ye, Z. M., Li, C., Cui, J., Wang, S. X., & Cheng, X. (2019). A ball milling strategy to disperse graphene oxide in cement composites. *Xinxing Tan Cailiao/New Carbon Materials*. [https://doi.org/10.1016/S1872-5805\(19\)60032-6](https://doi.org/10.1016/S1872-5805(19)60032-6)

Jing, G., Ye, Z., Wu, J., Wang, S., Cheng, X., Strokova, V., & Nelyubova, V. (2020). Introducing reduced graphene oxide to enhance the thermal properties of cement composites. *Cement and Concrete Composites*, 109(August 2019), 103559. <https://doi.org/10.1016/j.cemconcomp.2020.103559>

Jo, B. W., Sikandar, M. A., Chakraborty, S., & Baloch, Z. (2017). Investigation of the acid and sulfate resistance performances of hydrogen-rich water based mortars. *Construction and Building Materials*, 137, 1–11. <https://doi.org/10.1016/j.conbuildmat.2017.01.074>

Jung, I., Dikin, D., Park, S., Cai, W., Mielke, S. L., & Ruoff, R. S. (2008). Effect of water vapor on electrical properties of individual reduced graphene oxide sheets. *Journal of Physical Chemistry C*. <https://doi.org/10.1021/jp807525d>

Junk, A., & Riess, F. (2006). From an idea to a vision: There's plenty of room at the bottom. *American Journal of Physics*, 74(9), 825–830. <https://doi.org/10.1119/1.2213634>

Kanaujia, P., Banerjee, R., Mohammad, S., Husain, A., & Ahmed, S. (2021). The Effect of Sulfate Attack on Physical Properties of Concrete. 3878(2), 21–27. <https://doi.org/10.35940/ijrte.B6092.0710221>

Kaur, R., & Kothiyal, N. C. (2019a). Comparative effects of sterically stabilized functionalized carbon nanotubes and graphene oxide as reinforcing agent on physico-mechanical properties and electrical resistivity of cement nanocomposites. *Construction and Building Materials*, 202, 121–138. <https://doi.org/10.1016/j.conbuildmat.2018.12.220>

Kaur, R., & Kothiyal, N. C. (2020). Synergic influence of fly ash and graphene oxide-carbon nanotubes hybrid on mechanical , microstructural and porosity properties of cement mortars. *Journal of Adhesion Science and Technology*, 0(0), 1–29. <https://doi.org/10.1080/01694243.2020.1860548>

Kaur, R., Kothiyal, N. C., & Arora, H. (2020). Studies on combined effect of superplasticizer modified graphene oxide and carbon nanotubes on the physico-mechanical strength and electrical resistivity of fly ash blended cement mortar. *Journal of Building Engineering*, 30(November 2019), 101304. <https://doi.org/10.1016/j.job.2020.101304>

Kaur, R., Kothiyal, N. C., & Singh, J. (2020). Ultrasonic and superplasticizer assisted dispersion of hybrid carbon nanomaterials (FCNT and GO): its effect on early stage hydration and physico-mechanical strength of cement mortar. *Journal of Adhesion Science and Technology*, 34(2), 192–218. <https://doi.org/10.1080/01694243.2019.1664214>

Ke, G., & Zhang, J. (2020). Effects of retarding admixture, superplasticizer and supplementary cementitious material on the rheology and mechanical properties of high strength calcium sulfoaluminate cement paste. *Journal of Advanced Concrete Technology*. <https://doi.org/10.3151/jact.18.17>

Kharisov, B. I., Kharissova, O. V., & Méndez, U. O. (2014). Methods for Dispersion of Carbon Nanotubes in Water and Common Solvents. *MRS Online Proceedings Library*, 1700(1), 109–114. <https://doi.org/10.1557/opl.2014.605>

- Kim, H. K., Nam, I. W., & Lee, H. K. (2014). Enhanced effect of carbon nanotube on mechanical and electrical properties of cement composites by incorporation of silica fume. *Composite Structures*, 107, 60–69. <https://doi.org/10.1016/j.compstruct.2013.07.042>
- Kim, H. K., Park, I. S., & Lee, H. K. (2014). Improved piezoresistive sensitivity and stability of CNT/cement mortar composites with low water-binder ratio. *Composite Structures*, 116(1), 713–719. <https://doi.org/10.1016/j.compstruct.2014.06.007>
- Kioumars, M., Azarhomayun, F., Haji, M., & Shekarchi, M. (2020). Effect of shrinkage reducing admixture on drying shrinkage of concrete with different W/C ratios. *Materials*. <https://doi.org/10.3390/ma13245721>
- Kobayashi, K., & Kojima, Y. (2017). Effect of fine crack width and water cement ratio of SHCC on chloride ingress and rebar corrosion. *Cement and Concrete Composites*, 80, 235–244. <https://doi.org/10.1016/j.cemconcomp.2017.03.006>
- Kong, F. R., Pan, L. S., Wang, C. M., Zhang, D. La, & Xu, N. (2016). Effects of polycarboxylate superplasticizers with different molecular structure on the hydration behavior of cement paste. *Construction and Building Materials*, 105, 545–553. <https://doi.org/10.1016/j.conbuildmat.2015.12.178>
- Konsta-Gdoutos, M. S., Batis, G., Danoglidis, P. A., Zacharopoulou, A. K., Zacharopoulou, E. K., Falara, M. G., & Shah, S. P. (2017). Effect of CNT and CNF loading and count on the corrosion resistance, conductivity and mechanical properties of nanomodified OPC mortars. *Construction and Building Materials*, 147, 48–57. <https://doi.org/10.1016/j.conbuildmat.2017.04.112>
- Konsta-Gdoutos, M. S., Metaxa, Z. S., & Shah, S. P. (2010). Highly dispersed carbon nanotube reinforced cement based materials. *Cement and Concrete Research*, 40(7), 1052–1059. <https://doi.org/10.1016/j.cemconres.2010.02.015>
- Kothiyal, N. C., & Kaur, R. (2021). Synergistic Effect of Hybrid Carbon Nanomaterials as Reinforcing Phase on the Physico-Mechanical Properties and Pore Structure Refinement of Cementitious Nanocomposites. *Lecture Notes in Civil Engineering*, 90(16411103), 83–94. https://doi.org/10.1007/978-3-030-51354-2_8
- Kovtyukhova, N. I., Ollivier, P. J., Martin, B. R., Mallouk, T. E., Buzaneva, E. V., & Gorchinskiy, A. D. (1999). Layer-by-layer assembly of ultrathin composite films from

micron-sized graphite oxide sheets and polycations. *Chemistry of Materials*. <https://doi.org/10.1021/cm981085u>

Krishnan, A., Dujardin, E., Ebbesen, T. W., Yianilos, P. N., & Treacy, M. M. J. (1998). Young's modulus of single-walled nanotubes. *Phys. Rev. B*, 58(20), 14013–14019. <https://doi.org/10.1103/PhysRevB.58.14013>

Kruis, F. E., Fissan, H., & Peled, A. (1998). Synthesis of nanoparticles in the gas phase for electronic, optical and magnetic applications—a review. *Journal of Aerosol Science*, 29(5–6), 511–535.

Kudin, K. N., Ozbas, B., Schniepp, H. C., Prud'homme, R. K., Aksay, I. A., & Car, R. (2008). Raman spectra of graphite oxide and functionalized graphene sheets. *Nano Letters*. <https://doi.org/10.1021/nl071822y>

Kumar, G., & Badoni, P. (2018). *Arisaema tortuosum* Leaf Extract Mediated Synthesis of Silver Nanoparticles, Characterization and their Antibacterial Activity . *Asian Journal of Research in Chemistry*. <https://doi.org/10.5958/0974-4150.2018.00076.7>

Kurda, R., de Brito, J., & Silvestre, J. D. (2019). Water absorption and electrical resistivity of concrete with recycled concrete aggregates and fly ash. *Cement and Concrete Composites*. <https://doi.org/10.1016/j.cemconcomp.2018.10.004>

L P Singh S K Bhattacharyya, G. M., & Ahalawat, S. (2012). Reduction of calcium leaching in cement hydration process using nanomaterials. *Materials Technology*, 27(3), 233–238. <https://doi.org/10.1179/1753555712Y.0000000005>

Lambert, T. N., Chavez, C. A., Hernandez-Sanchez, B., Lu, P., Bell, N. S., Ambrosini, A., Friedman, T., Boyle, T. J., Wheeler, D. R., & Huber, D. L. (2009). Synthesis and characterization of titania-graphene nanocomposites. *Journal of Physical Chemistry C*. <https://doi.org/10.1021/jp905456f>

Lee, C., Wei, X., Kysar, J. W., & Hone, J. (2008). Measurement of the elastic properties and intrinsic strength of monolayer graphene. *Science*. <https://doi.org/10.1126/science.1157996>

Lerf, A., Buchsteiner, A., Pieper, J., Schöttl, S., Dekany, I., Szabo, T., & Boehm, H. P. (2006). Hydration behavior and dynamics of water molecules in graphite oxide. *Journal of Physics and Chemistry of Solids*. <https://doi.org/10.1016/j.jpcs.2006.01.031>

- Li, C. Y., Chen, S. J., Li, W. G., Li, X. Y., Ruan, D., & Duan, W. H. (2019). Dynamic increased reinforcing effect of graphene oxide on cementitious nanocomposite. *Construction and Building Materials*, 206, 694–702. <https://doi.org/10.1016/j.conbuildmat.2019.02.001>
- Li, D., Müller, M. B., Gilje, S., Kaner, R. B., & Wallace, G. G. (2008). Processable aqueous dispersions of graphene nanosheets. *Nature Nanotechnology*. <https://doi.org/10.1038/nnano.2007.451>
- Li, G. (2004). Properties of high-volume fly ash concrete incorporating nano-SiO₂. *Cement and Concrete Research*, 34(6), 1043–1049.
- Li, G. Y., Wang, P. M., & Zhao, X. (2005). Mechanical behavior and microstructure of cement composites incorporating surface-treated multi-walled carbon nanotubes. *Carbon*, 43(6), 1239–1245. <https://doi.org/10.1016/j.carbon.2004.12.017>
- Li, H., Zhang, M. hua, & Ou, J. ping. (2007). Flexural fatigue performance of concrete containing nano-particles for pavement. *International Journal of Fatigue*, 29(7), 1292–1301. <https://doi.org/10.1016/j.ijfatigue.2006.10.004>
- Li, Q., Liu, J., & Xu, S. (2015). Progress in Research on Carbon Nanotubes Reinforced Cementitious Composites. In *Advances in Materials Science and Engineering* (Vol. 2015). Hindawi Publishing Corporation. <https://doi.org/10.1155/2015/307435>
- Li, V. C., & Obla, K. H. (1994). Effect of fiber length variation on tensile properties of carbon-fiber cement composites. *Composites Engineering*, 4(9), 947–964.
- Li, W., Li, X., Chen, S. J., Liu, Y. M., Duan, W. H., & Shah, S. P. (2017). Effects of graphene oxide on early-age hydration and electrical resistivity of Portland cement paste. *Construction and Building Materials*, 136, 506–514. <https://doi.org/10.1016/j.conbuildmat.2017.01.066>
- Li, X., Korayem, A. H., Li, C., Liu, Y., He, H., Sanjayan, J. G., & Duan, W. H. (2016). Incorporation of graphene oxide and silica fume into cement paste: A study of dispersion and compressive strength. *Construction and Building Materials*, 123, 327–335.
- Li, X., Li, C., Liu, Y., Chen, S. J., Wang, C. M., Sanjayan, J. G., & Duan, W. H. (2018). Improvement of mechanical properties by incorporating graphene oxide into cement mortar. *Mechanics of Advanced Materials and Structures*, 25(15–16), 1313–1322. <https://doi.org/10.1080/15376494.2016.1218226>

- Li, X., Qin, D., Hu, Y., Ahmad, W., Ahmad, A., Aslam, F., & Joyklad, P. (2022). A systematic review of waste materials in cement-based composites for construction applications. In *Journal of Building Engineering* (Vol. 45, Issue July 2021, p. 103447). Elsevier Ltd. <https://doi.org/10.1016/j.jobe.2021.103447>
- Li, X., Wang, L., Liu, Y., Li, W., Dong, B., & Duan, W. H. (2018). Dispersion of graphene oxide agglomerates in cement paste and its effects on electrical resistivity and flexural strength. *Cement and Concrete Composites*, 92(June), 145–154. <https://doi.org/10.1016/j.cemconcomp.2018.06.008>
- Li, X., Wei, W., Qin, H., & Hang Hu, Y. (2015). Co-effects of graphene oxide sheets and single wall carbon nanotubes on mechanical properties of cement. *Journal of Physics and Chemistry of Solids*, 85, 39–43. <https://doi.org/https://doi.org/10.1016/j.jpcs.2015.04.018>
- Liao, W., Sun, X., Kumar, A., Sun, H., & Ma, H. (2019). Hydration of binary portland cement blends containing silica fume: A decoupling method to estimate degrees of hydration and pozzolanic reaction. *Frontiers in Materials*. <https://doi.org/10.3389/fmats.2019.00078>
- Lin, X., Pang, H., Wei, D., Lu, M., & Liao, B. (2021). Effect of superplasticizers with different anchor groups on the properties of cementitious systems. *Colloids and Surfaces A: Physicochemical and Engineering Aspects*. <https://doi.org/10.1016/j.colsurfa.2021.127207>
- Liu, C., Guo, Y., Wei, X., Wang, C., Qu, M., Schubert, D. W., & Zhang, C. (2019). An outstanding antichlorine and antibacterial membrane with quaternary ammonium salts of alkenes via in situ polymerization for textile wastewater treatment. *Chemical Engineering Journal*, 123306. <https://doi.org/10.1016/j.cej.2019.123306>
- Liu, D., Zhu, Z., Zhao, Y., Chen, Y., Tan, Y., & Zhang, Y. (2019). Science of the Total Environment Low pressure modified polyamide 6 membrane for effective fractionation of dyes and NaCl. *Science of the Total Environment*, 695, 133908. <https://doi.org/10.1016/j.scitotenv.2019.133908>
- Liu, J., Fu, J., Yang, Y., & Gu, C. (2019). Study on dispersion, mechanical and microstructure properties of cement paste incorporating graphene sheets. *Construction and Building Materials*, 199, 1–11. <https://doi.org/10.1016/j.conbuildmat.2018.12.006>

- Liu, X., Chen, L., Liu, A., & Wang, X. (2012). Effect of nano-CaCO₃ on properties of cement paste. *Energy Procedia*, 16, 991–996.
- Lothenbach, B., Scrivener, K., & Hooton, R. D. (2011). Supplementary cementitious materials. *Cement and Concrete Research*, 41(12), 1244–1256. <https://doi.org/https://doi.org/10.1016/j.cemconres.2010.12.001>
- Lu, D., & Zhong, J. (2022). Carbon-based nanomaterials engineered cement composites: a review. *Journal of Infrastructure Preservation and Resilience*, 3(1). <https://doi.org/10.1186/s43065-021-00045-y>
- Lu, K. L., Lago, R. M., Chen, Y. K., Green, M. L. H., Harris, P. J. F., & Tsang, S. C. (1996). Mechanical damage of carbon nanotubes by ultrasound. In *Carbon*. [https://doi.org/10.1016/0008-6223\(96\)89470-X](https://doi.org/10.1016/0008-6223(96)89470-X)
- Lu, L., Zhao, P., & Lu, Z. (2018). A short discussion on how to effectively use graphene oxide to reinforce cementitious composites. *Construction and Building Materials*, 189, 33–41. <https://doi.org/10.1016/j.conbuildmat.2018.08.170>
- Lu, X., & Chen, Z. (2005). Curved Pi-conjugation, aromaticity, and the related chemistry of small fullerenes (<C₆₀) and single-walled carbon nanotubes. In *Chemical Reviews*. <https://doi.org/10.1021/cr030093d>
- Lu, Z., Hanif, A., Ning, C., Shao, H., Yin, R., & Li, Z. (2017a). Steric stabilization of graphene oxide in alkaline cementitious solutions: Mechanical enhancement of cement composite. *Materials and Design*, 127, 154–161. <https://doi.org/10.1016/j.matdes.2017.04.083>
- Lu, Z., Hanif, A., Sun, G., Liang, R., Parthasarathy, P., & Li, Z. (2018). Highly dispersed graphene oxide electrodeposited carbon fiber reinforced cement-based materials with enhanced mechanical properties. *Cement and Concrete Composites*, 87, 220–228. <https://doi.org/10.1016/j.cemconcomp.2018.01.006>
- Lu, Z., Hou, D., Hanif, A., Hao, W., Sun, G., & Li, Z. (2018). Comparative evaluation on the dispersion and stability of graphene oxide in water and cement pore solution by incorporating silica fume. *Cement and Concrete Composites*, 94(July), 33–42. <https://doi.org/10.1016/j.cemconcomp.2018.08.011>
- Lu, Z., Hou, D., Ma, H., Fan, T., & Li, Z. (2016). Effects of graphene oxide on the properties and microstructures of the magnesium potassium phosphate cement paste.

Construction and Building Materials, 119, 107–112.
<https://doi.org/10.1016/j.conbuildmat.2016.05.060>

Lu, Z., Hou, D., Meng, L., Sun, G., Lu, C., & Li, Z. (2015). Mechanism of cement paste reinforced by graphene oxide/carbon nanotubes composites with enhanced mechanical properties. RSC Advances, 5(122), 100598–100605.
<https://doi.org/10.1039/c5ra18602a>

Lu, Z., Li, X., Hanif, A., Chen, B., Parthasarathy, P., Yu, J., & Li, Z. (2017). Early-age interaction mechanism between the graphene oxide and cement hydrates. Construction and Building Materials, 152, 232–239.
<https://doi.org/10.1016/j.conbuildmat.2017.06.176>

Lu, Z., Lu, C., Leung, C. K. Y., & Li, Z. (2019). Graphene oxide modified Strain Hardening Cementitious Composites with enhanced mechanical and thermal properties by incorporating ultra-fine phase change materials. Cement and Concrete Composites, 98(September 2018), 83–94. <https://doi.org/10.1016/j.cemconcomp.2019.02.010>

Lv, S. H., Deng, L. J., Yang, W. Q., Zhou, Q. F., & Cui, Y. Y. (2016). Fabrication of polycarboxylate/graphene oxide nanosheet composites by copolymerization for reinforcing and toughening cement composites. Cement and Concrete Composites, 66, 1–9. <https://doi.org/https://doi.org/10.1016/j.cemconcomp.2015.11.007>

Lv, S., Liu, J., Sun, T., Ma, Y., & Zhou, Q. (2014). Effect of GO nanosheets on shapes of cement hydration crystals and their formation process. Construction and Building Materials, 64, 231–239. <https://doi.org/10.1016/j.conbuildmat.2014.04.061>

Lv, S., Ma, Y., Qiu, C., Sun, T., Liu, J., & Zhou, Q. (2013a). Effect of graphene oxide nanosheets of microstructure and mechanical properties of cement composites. Construction and Building Materials, 49, 121–127.
<https://doi.org/10.1016/j.conbuildmat.2013.08.022>

Lv, S., Ma, Y., Qiu, C., & Zhou, Q. (2013). Regulation of GO on cement hydration crystals and its toughening effect. Magazine of Concrete Research, 65(20), 1246–1254.
<https://doi.org/10.1680/mac.13.00190>

Lv, S., Ting, S., Liu, J., & Zhou, Q. (2014). Use of graphene oxide nanosheets to regulate the microstructure of hardened cement paste to increase its strength and toughness. CrystEngComm, 16(36), 8508–8516. <https://doi.org/10.1039/c4ce00684d>

- Ma, P. C., Siddiqui, N. A., Marom, G., & Kim, J. K. (2010). Dispersion and functionalization of carbon nanotubes for polymer-based nanocomposites: A review. In *Composites Part A: Applied Science and Manufacturing*. <https://doi.org/10.1016/j.compositesa.2010.07.003>
- Ma, X., He, T., Xu, Y., Yang, R., & Sun, Y. (2022). Case Studies in Construction Materials Hydration reaction and compressive strength of small amount of silica fume on cement-fly ash matrix. *Case Studies in Construction Materials*, 16(March), e00989. <https://doi.org/10.1016/j.cscm.2022.e00989>
- MacLeod, A. J. N., Gates, W. P., & Collins, F. (2020). Durability characterisation of portland cement-carbon nanotube nanocomposites. *Materials*, 13(18). <https://doi.org/10.3390/ma13184097>
- Madloul, N. A., Saidur, R., Hossain, M. S., & Rahim, N. A. (2011). A critical review on energy use and savings in the cement industries. *Renewable and Sustainable Energy Reviews*, 15(4), 2042–2060. <https://doi.org/10.1016/j.rser.2011.01.005>
- Makar, J. (2011). The Effect of SWCNT and Other Nanomaterials on Cement Hydration and Reinforcement. In *Nanotechnology in Civil Infrastructure*. https://doi.org/10.1007/978-3-642-16657-0_4
- Malaki, M., Xu, W., Kasar, A. K., Menezes, P. L., Dieringa, H., Varma, R. S., & Gupta, M. (2019). Advanced metal matrix nanocomposites. *Metals*. <https://doi.org/10.3390/met9030330>
- Mani, V., Chen, S. M., & Lou, B. S. (2013). Three dimensional graphene oxide-carbon nanotubes and graphene-carbon nanotubes hybrids. *International Journal of Electrochemical Science*. [https://doi.org/10.1016/s1452-3981\(23\)13212-3](https://doi.org/10.1016/s1452-3981(23)13212-3)
- Mansouri Sarvandani, M., Mahdikhani, M., Aghabarati, H., & Haghparast Fatmehsari, M. (2021). Effect of functionalized multi-walled carbon nanotubes on mechanical properties and durability of cement mortars. *Journal of Building Engineering*, 41(February), 102407. <https://doi.org/10.1016/j.jobbe.2021.102407>
- Mathur, R. B., Chatterjee, S., & Singh, B. P. (2008). Growth of carbon nanotubes on carbon fibre substrates to produce hybrid/phenolic composites with improved mechanical properties. *Composites Science and Technology*, 68(7–8), 1608–1615. <https://doi.org/10.1016/j.compscitech.2008.02.020>

Matthews, F. L., & Rawlings, R. D. (n.d.). 2-Reinforcements and the reinforcement--matrix interface.

Maurya, S. K., Bhatrola, K., Kothiyal, N. C., & Choudhary, M. (2023). Materials Today: Proceedings Comparative effects of nano-silica and graphene oxide on Pozzolana Portland cement nanocomposites. *Materials Today: Proceedings*, xxxx. <https://doi.org/10.1016/j.matpr.2022.12.019>

Mendoza, O., Sierra, G., & Tobón, J. I. (2013). Influence of super plasticizer and $\text{Ca}(\text{OH})_2$ on the stability of functionalized multi-walled carbon nanotubes dispersions for cement composites applications. *Construction and Building Materials*, 47, 771–778. <https://doi.org/10.1016/j.conbuildmat.2013.05.100>

Mendoza Reales, O. A., & Dias Toledo Filho, R. (2017). A review on the chemical, mechanical and microstructural characterization of carbon nanotubes-cement based composites. In *Construction and Building Materials* (Vol. 154, pp. 697–710). Elsevier Ltd. <https://doi.org/10.1016/j.conbuildmat.2017.07.232>

Meng, S., Ouyang, X., Fu, J., Niu, Y., & Ma, Y. (2021). The role of graphene/graphene oxide in cement hydration. *Nanotechnology Reviews*. <https://doi.org/10.1515/ntrev-2021-0055>

Meng, W., & Khayat, K. H. (2016). Mechanical properties of ultra-high-performance concrete enhanced with graphite nanoplatelets and carbon nanofibers. *Composites Part B: Engineering*, 107, 113–122. <https://doi.org/10.1016/j.compositesb.2016.09.069>

Mera, G., Gallei, M., Bernard, S., & Ionescu, E. (2015). Ceramic nanocomposites from tailor-made preceramic polymers. In *Nanomaterials*. <https://doi.org/10.3390/nano5020468>

Mitchell, D. R. G., Hinczak, I., & Day, R. A. (1998). Interaction of silica fume with calcium hydroxide solutions and hydrated cement pastes. *Cement and Concrete Research*, 28(11), 1571–1584.

Mkhoyan, K. A., Contryman, A. W., Silcox, J., Stewart, D. A., Eda, G., Mattevi, C., Miller, S., & Chhowalla, M. (2009). Atomic and electronic structure of graphene-oxide. *Nano Letters*. <https://doi.org/10.1021/nl8034256>

Mohammed, A., Sanjayan, J. G., Duan, W. H., & Nazari, A. (2015). Incorporating graphene oxide in cement composites: A study of transport properties. *Construction and Building Materials*. <https://doi.org/10.1016/j.conbuildmat.2015.01.083>

Moore, K., & Wei, W. (2021). Applications of carbon nanomaterials in perovskite solar cells for solar energy conversion. *Nano Materials Science*. <https://doi.org/10.1016/j.nanoms.2021.03.005>

Moraes, R. A., Matos, C. F., Castro, E. G., Schreiner, W. H., Oliveira, M. M., & Zarbin, A. J. G. (2011). The effect of different chemical treatments on the structure and stability of aqueous dispersion of iron- and iron oxide-filled multi-walled carbon nanotubes. *Journal of the Brazilian Chemical Society*. <https://doi.org/10.1590/S0103-50532011001100024>

Mousavi, M. A., Sadeghi-Nik, A., Bahari, A., Jin, C., Ahmed, R., Ozbakkaloglu, T., & de Brito, J. (2021). Strength optimization of cementitious composites reinforced by carbon nanotubes and Titania nanoparticles. *Construction and Building Materials*, 303(July), 124510. <https://doi.org/10.1016/j.conbuildmat.2021.124510>

Mukhopadhyay, K., Dwivedi, C. D., & Mathur, G. N. (2002). Conversion of carbon nanotubes to carbon nanofibers by sonication. *Carbon*, 40(8), 1373–1376.

Muthu, M., & Santhanam, M. (2018). Effect of reduced graphene oxide, alumina and silica nanoparticles on the deterioration characteristics of Portland cement paste exposed to acidic environment. *Cement and Concrete Composites*, 91(April), 118–137. <https://doi.org/10.1016/j.cemconcomp.2018.05.005>

Najimi, M., Sobhani, J., Ahmadi, B., & Shekarchi, M. (2012). An experimental study on durability properties of concrete containing zeolite as a highly reactive natural pozzolan. *Construction and Building Materials*, 35, 1023–1033. <https://doi.org/10.1016/j.conbuildmat.2012.04.038>

Napierska, D., Thomassen, L. C. J., Lison, D., Martens, J. A., & Hoet, P. H. (2010). The nanosilica hazard: another variable entity. *Particle and Fibre Toxicology*, 7, 1–32.

Nazari, A., & Riahi, S. (2011a). Improvement compressive strength of concrete in different curing media by Al₂O₃ nanoparticles. *Materials Science and Engineering: A*, 528(3), 1183–1191.

Nazari, A., Riahi, S., Riahi, S., Shamekhi, S. F., & Khademno, A. (2010). Benefits of Fe₂O₃ nanoparticles in concrete mixing matrix. *Journal of American Science*, 6(4), 102–106.

Ngo, T.-D. . (2020). *Composite and Nanocomposite Materials-From Knowledge to Industrial Applications*.

Nochaiya, T., & Chaipanich, A. (2011). Behavior of multi-walled carbon nanotubes on the porosity and microstructure of cement-based materials. *Applied Surface Science*. <https://doi.org/10.1016/j.apsusc.2010.09.030>

Nonat, A., & Lecoq, X. (1998). The Structure, Stoichiometry and Properties of C-S-H Prepared by C3S Hydration Under Controlled Condition. In *Nuclear Magnetic Resonance Spectroscopy of Cement-Based Materials*. https://doi.org/10.1007/978-3-642-80432-8_14

Novoselov, K. S., Fal'ko, V. I., Colombo, L., Gellert, P. R., Schwab, M. G., & Kim, K. (2012). A roadmap for graphene. *Nature*, 490(7419), 192–200.

Onaizi, A. M., Huseien, G. F., Lim, N. H. A. S., Amran, M., & Samadi, M. (2021). Effect of nanomaterials inclusion on sustainability of cement-based concretes: A comprehensive review. *Construction and Building Materials*, 306(September), 124850. <https://doi.org/10.1016/j.conbuildmat.2021.124850>

Orasugh, J. T., Saasa, V., Ray, S. S., & Mwakikunga, B. (2023). Supersensitive metal free in-situ synthesized graphene oxide@cellulose nanocrystals acetone sensitive bioderived sensors. *International Journal of Biological Macromolecules*, 241(April), 124514. <https://doi.org/10.1016/j.ijbiomac.2023.124514>

Pal, P. (2019). Dynamic poisson's ratio and modulus of elasticity of pozzolana Portland cement concrete. *International Journal of Engineering and Technology Innovation*.

Pan, Y., Wu, T., Bao, H., & Li, L. (2011). Green fabrication of chitosan films reinforced with parallel aligned graphene oxide. *Carbohydrate Polymers*, 83(4), 1908–1915. <https://doi.org/10.1016/j.carbpol.2010.10.054>

Pandey, D., Reifengerger, R., & Piner, R. (2008). Scanning probe microscopy study of exfoliated oxidized graphene sheets. *Surface Science*. <https://doi.org/10.1016/j.susc.2008.02.025>

Panjehpour, M., Ali, A. A. A., & Demirboga, R. (2011). A review for characterization of silica fume and its effects on concrete properties. *International Journal of Sustainable Construction Engineering and Technology*, 2(2).

Park, S.-J., & Seo, M.-K. (2011). Interface Applications in Nanomaterials. In *Interface Science and Technology* (Vol. 18, pp. 333–429). Elsevier.

- Park, S., & Ruoff, R. S. (2009). Chemical methods for the production of graphenes. *Nature Nanotechnology*. <https://doi.org/10.1038/nnano.2009.58>
- Parveen, S., Rana, S., Fanguero, R., & Paiva, M. C. (2015). Microstructure and mechanical properties of carbon nanotube reinforced cementitious composites developed using a novel dispersion technique. *Cement and Concrete Research*, 73, 215–227. <https://doi.org/10.1016/j.cemconres.2015.03.006>
- Pathak, A. K., Borah, M., Gupta, A., Yokozeki, T., & Dhakate, S. R. (2016). Improved mechanical properties of carbon fiber/graphene oxide-epoxy hybrid composites. *Composites Science and Technology*, 135, 28–38. <https://doi.org/10.1016/j.compscitech.2016.09.007>
- Paul, S. C., Van Rooyen, A. S., van Zijl, G. P. A. G., & Petrik, L. F. (2018). Properties of cement-based composites using nanoparticles: A comprehensive review. *Construction and Building Materials*, 189, 1019–1034.
- Pelisser, F., Neto, A. B. da S. S., La Rovere, H. L., & de Andrade Pinto, R. C. (2010). Effect of the addition of synthetic fibers to concrete thin slabs on plastic shrinkage cracking. *Construction and Building Materials*, 24(11), 2171–2176.
- Peng, B., Locascio, M., Zapol, P., Li, S., Mielke, S. L., Schatz, G. C., & Espinosa, H. D. (2008). Measurements of near-ultimate strength for multiwalled carbon nanotubes and irradiation-induced crosslinking improvements. *Nature Nanotechnology*. <https://doi.org/10.1038/nnano.2008.211>
- Peng, X. Y., & Xia, M. G. (2013). Synthesis and microstructure study of polycarboxylated superplasticizer with different carboxylic group content. *Applied Mechanics and Materials*. <https://doi.org/10.4028/www.scientific.net/AMM.328.802>
- Peyvandi, A., Sbia, L. A., Soroushian, P., & Sobolev, K. (2013). Effect of the cementitious paste density on the performance efficiency of carbon nanofiber in concrete nanocomposite. *Construction and Building Materials*, 48, 265–269. <https://doi.org/10.1016/j.conbuildmat.2013.06.094>
- Pinto, S. R., Angulski da Luz, C., Munhoz, G. S., & Medeiros-Junior, R. A. (2020). Durability of phosphogypsum-based supersulfated cement mortar against external attack by sodium and magnesium sulfate. *Cement and Concrete Research*, 136(July), 106172. <https://doi.org/10.1016/j.cemconres.2020.106172>

Pitroda, J., Zala, L. B., & Umrigar, F. S. (2012). Experimental Investigations on Partial Replacement of Cement with Fly Ash in Design Mix Concrete. *International Journal of Advanced Engineering Technology E*, 3(4), 126–129.

Pop, E., Mann, D., Wang, Q., Goodson, K., & Dai, H. (2006). Thermal conductance of an individual single-wall carbon nanotube above room temperature. *Nano Letters*. <https://doi.org/10.1021/nl052145f>

Popov, M., Kyotani, M., Nemanich, R. J., & Koga, Y. (2002). Superhard phase composed of single-wall carbon nanotubes. *Physical Review B - Condensed Matter and Materials Physics*. <https://doi.org/10.1103/PhysRevB.65.033408>

Prabavathy, S., Jeyasubramanian, K., Prasanth, S., Hikku, G. S., & Robert, R. B. J. (2020). Enhancement in behavioral properties of cement mortar cubes admixed with reduced graphene oxide. *Journal of Building Engineering*, 28(July 2019), 101082. <https://doi.org/10.1016/j.jobbe.2019.101082>

Prasad, R., Gupta, S. K., Shabnam, N., Oliveira, C. Y. B., Nema, A. K., Ansari, F. A., & Bux, F. (2021). Role of microalgae in global CO₂ sequestration: Physiological mechanism, recent development, challenges, and future prospective. *Sustainability*, 13(23), 13061.

Praseeda, D., & Rao, K. S. (2022). Investigation of sulphate resistance of the nano reinforced blended concrete. *Cleaner Materials*, 3(October 2021), 100047. <https://doi.org/10.1016/j.clema.2022.100047>

Priyap, P. K., & Vanitha, S. (2021). Effect of nano silica on the properties of concrete and mortar - A state of art. *International Review of Applied Sciences and Engineering*, 13(1), 70–79. <https://doi.org/10.1556/1848.2021.00309>

Provis, J. L., Palomo, A., & Shi, C. (2015). Advances in understanding alkali-activated materials. *Cement and Concrete Research*, 78, 110–125.

Punurai, W., Kroehong, W., Saptamongkol, A., & Chindaprasirt, P. (2018). Mechanical properties , microstructure and drying shrinkage of hybrid fly ash-basalt fiber geopolymer paste. *Construction and Building Materials*, 186, 62–70. <https://doi.org/10.1016/j.conbuildmat.2018.07.115>

Purty, B., Choudhary, R. B., Biswas, A., & Udayabhanu, G. (2019). Chemically grown mesoporous f-CNT/ α -MnO₂ /PIn nanocomposites as electrode materials for

supercapacitor application. *Polymer Bulletin*, 76(4), 1619–1640. <https://doi.org/10.1007/s00289-018-2458-z>

Qi, X., Zhang, S., Wang, T., Guo, S., & Ren, R. (2021). Effect of high-dispersible graphene on the strength and durability of cement mortars. *Materials*, 14(4), 1–17. <https://doi.org/10.3390/ma14040915>

Qiu, L., Yang, X., Gou, X., Yang, W., Ma, Z. F., Wallace, G. G., & Li, D. (2010). Dispersing carbon nanotubes with graphene oxide in water and synergistic effects between graphene derivatives. *Chemistry - A European Journal*. <https://doi.org/10.1002/chem.201001771>

Qureshi, T. S., & Panesar, D. K. (2019). Impact of graphene oxide and highly reduced graphene oxide on cement based composites. *Construction and Building Materials*, 206, 71–83. <https://doi.org/10.1016/j.conbuildmat.2019.01.176>

Qureshi, T. S., & Panesar, D. K. (2020a). Nano reinforced cement paste composite with functionalized graphene and pristine graphene nanoplatelets. *Composites Part B: Engineering*, 197(April), 108063. <https://doi.org/10.1016/j.compositesb.2020.108063>

Qureshi, T. S., & Panesar, D. K. (2020b). Nano reinforced cement paste composite with functionalized graphene and pristine graphene nanoplatelets. *Composites Part B: Engineering*, 197, 108063. <https://doi.org/10.1016/j.compositesb.2020.108063>

Qureshi, T. S., Panesar, D. K., Sidhureddy, B., Chen, A., & Wood, P. C. (2019). Nano-cement composite with graphene oxide produced from epigenetic graphite deposit. *Composites Part B: Engineering*, 159(August 2018), 248–258. <https://doi.org/10.1016/j.compositesb.2018.09.095>

Raghavendra Prasad, H. D., & Sitaram, N. (2020). Performance of nano materials for the strength development in concrete cube used as Partial replacement for cement at different temperatures. *Materials Today: Proceedings*, 45, 7253–7258. <https://doi.org/10.1016/j.matpr.2021.03.415>

Rajkumar, R., Teja, A. S., & Sajeewan, R. (2016). Experimental study on the strength and durability of nano concrete. *International Journal of Applied Engineering Research*, 11(4), 2854 – 2858. <https://www.scopus.com/inward/record.uri?eid=2-s2.0-84961725581&partnerID=40&md5=c875cc2a543fbc089fd39176cdb2f4d9>

Rehman, S. K. U., Ibrahim, Z., Memon, S. A., Javed, M. F., & Khushnood, R. A. (2017). A sustainable graphene based cement composite. *Sustainability*, 9(7), 1229.

Ren, J., Zhang, L., Walkley, B., Black, J. R., & San Nicolas, R. (2022). Degradation resistance of different cementitious materials to phosphoric acid attack at early stage. *Cement and Concrete Research*, 151(September 2021), 106606. <https://doi.org/10.1016/j.cemconres.2021.106606>

Report, A. (2021). Activity report.

Richardson, I. G. (1999). Nature of C-S-H in hardened cements. *Cement and Concrete Research*. [https://doi.org/10.1016/S0008-8846\(99\)00168-4](https://doi.org/10.1016/S0008-8846(99)00168-4)

Ricohermoso, E., Rosenberg, F., Klug, F., Nicoloso, N., Schlaak, H. F., Riedel, R., & Ionescu, E. (2021). Piezoresistive carbon-containing ceramic nanocomposites – A review. In *Open Ceramics*. <https://doi.org/10.1016/j.oceram.2021.100057>

Saafi, M., Tang, L., Fung, J., Rahman, M., & Liggat, J. (2015). Enhanced properties of graphene/fly ash geopolymetric composite cement. *Cement and Concrete Research*, 67, 292–299. <https://doi.org/10.1016/j.cemconres.2014.08.011>

Safdari, M., & Al-Haik, M. S. (2018). A review on polymeric nanocomposites: effect of hybridization and synergy on electrical properties. *Carbon-Based Polymer Nanocomposites for Environmental and Energy Applications*, 113–146.

Saha, A. K. (2018). Effect of class F fly ash on the durability properties of concrete. *Sustainable Environment Research*. <https://doi.org/10.1016/j.serj.2017.09.001>

Samimi, K., & Zareechian, M. (2022). Chemical resistance of synthesized graphene-modified cement paste containing natural pozzolans to acid attack CL. *Journal of Building Engineering*, 60(August), 105174. <https://doi.org/10.1016/j.jobbe.2022.105174>

Sanchez, F., & Sobolev, K. (2010). Nanotechnology in concrete--a review. *Construction and Building Materials*, 24(11), 2060–2071.

Sang, L., Zhao, Y., & Burda, C. (2014). TiO₂ nanoparticles as functional building blocks. *Chemical Reviews*, 114(19), 9283–9318.

Sanjuán, M. Á., Argiz, C., Gálvez, J. C., & Moragues, A. (2015). Effect of silica fume fineness on the improvement of Portland cement strength performance. *Construction and Building Materials*, 96, 55–64.

Sathyan, D., & Anand, K. B. (2019). Influence of superplasticizer family on the durability characteristics of fly ash incorporated cement concrete. *Construction and Building Materials*, 204, 864–874. <https://doi.org/10.1016/j.conbuildmat.2019.01.171>

Sathyan, D., Anand, K. B., Prakash, A. J., & Premjith, B. (2018). Modeling the Fresh and Hardened Stage Properties of Self-Compacting Concrete using Random Kitchen Sink Algorithm. *International Journal of Concrete Structures and Materials*, 12(1). <https://doi.org/10.1186/s40069-018-0246-7>

Seretis, G. V., Polyzou, A. K., Manolakos, D. E., & Provatidis, C. G. (2019). Multi-parameter analysis of curing cycle for GNPs/glass fabric/epoxy laminated nanocomposites. *Frattura Ed Integrità Strutturale*. <https://doi.org/10.3221/IGF-ESIS.50.43>

Shah, S. P., Hou, P., & Konsta-Gdoutos, M. S. (2016). Nano-modification of cementitious material: Toward a stronger and durable concrete. *Journal of Sustainable Cement-Based Materials*, 5(1–2), 1–22.

Shaikh, F. U. A., & Supit, S. W. M. (2014). Mechanical and durability properties of high volume fly ash (HVFA) concrete containing calcium carbonate (CaCO₃) nanoparticles. *Construction and Building Materials*, 70, 309–321. <https://doi.org/10.1016/j.conbuildmat.2014.07.099>

Shamsaei, E., de Souza, F. B., Yao, X., Benhelal, E., Akbari, A., & Duan, W. (2018). Graphene-based nanosheets for stronger and more durable concrete: A review. *Construction and Building Materials*, 183, 642–660. <https://doi.org/10.1016/j.conbuildmat.2018.06.201>

Shang, Y., Zhang, D., Yang, C., Liu, Y., & Liu, Y. (2015). Effect of graphene oxide on the rheological properties of cement pastes. *Construction and Building Materials*, 96, 20–28. <https://doi.org/10.1016/j.conbuildmat.2015.07.181>

Sharma, S., & Arora, S. (2018). Economical graphene reinforced fly ash cement composite made with recycled aggregates for improved sulphate resistance and mechanical performance. *Construction and Building Materials*. <https://doi.org/10.1016/j.conbuildmat.2017.12.027>

Sharma, S., Dhakate, S. R., Majumdar, A., & Singh, B. P. (2019). Improved static and dynamic mechanical properties of multiscale bucky paper interleaved Kevlar fiber composites. *Carbon*, 152, 631–642. <https://doi.org/10.1016/j.carbon.2019.06.055>

Sharma, S., & Kothiyal, N. C. (2015). Influence of graphene oxide as dispersed phase in cement mortar matrix in defining the crystal patterns of cement hydrates and its effect

on mechanical, microstructural and crystallization properties. *RSC Advances*, 5(65), 52642–52657. <https://doi.org/10.1039/c5ra08078a>

Sharma, S., Pathak, A. K., Singh, V. N., Teotia, S., Dhakate, S. R., & Singh, B. P. (2018). Excellent mechanical properties of long multiwalled carbon nanotube bridged Kevlar fabric. *Carbon*, 137, 104–117.

Sharma, S., Susan, D., Kothiyal, N. C., & Kaur, R. (2018). Graphene oxide prepared from mechanically milled graphite: Effect on strength of novel fly-ash based cementitious matrix. *Construction and Building Materials*, 177, 10–22. <https://doi.org/10.1016/j.conbuildmat.2018.05.051>

Shen, W., Cao, L., Li, Q., Zhang, W., Wang, G., & Li, C. (2015). Quantifying CO₂ emissions from China's cement industry. *Renewable and Sustainable Energy Reviews*, 50, 1004–1012. <https://doi.org/10.1016/j.rser.2015.05.031>

Shrestha, S. L. (2018). Characterization of Some Cement Samples of Nepal Using FTIR Spectroscopy. *International Journal of Advanced Research in Chemical Science*, 5(7), 19–23. <https://doi.org/10.20431/2349-0403.0507004>

Silvestro, L., & Jean Paul Gleize, P. (2020). Effect of carbon nanotubes on compressive, flexural and tensile strengths of Portland cement-based materials: A systematic literature review. *Construction and Building Materials*, 264, 120237. <https://doi.org/10.1016/j.conbuildmat.2020.120237>

Sindu, B. S., & Sasmal, S. (2017). Properties of carbon nanotube reinforced cement composite synthesized using different types of surfactants. *Construction and Building Materials*, 155, 389–399. <https://doi.org/10.1016/j.conbuildmat.2017.08.059>

Singh, J., Kothiyal, N. C., & Pathania, D. (2011). Synthesis of highly dispersed single walled carbon nanotubes from furnace oil and light diesel oil by modified chemical vapour deposition method. *International Journal of Theoretical and Applied Science*, 3(2), 15–20.

Singh, L. P., Bhattacharyya, S. K., Shah, S. P., Mishra, G., Ahalawat, S., & Sharma, U. (2015). Studies on early stage hydration of tricalcium silicate incorporating silica nanoparticles: Part I. *Construction and Building Materials*. <https://doi.org/10.1016/j.conbuildmat.2014.08.046>

Singh Raman, R. K., & Tiwari, A. (2014). Graphene: The Thinnest Known Coating for Corrosion Protection. *JOM*, 66(4), 637–642. <https://doi.org/10.1007/s11837-014-0921-3>

Sinha, S., Barjami, S., Iannacchione, G., Schwab, A., & Muench, G. (2005). Off-axis thermal properties of carbon nanotube films. *Journal of Nanoparticle Research*. <https://doi.org/10.1007/s11051-005-8382-9>

Skibsted, J., & Snellings, R. (2019). Reactivity of supplementary cementitious materials (SCMs) in cement blends. In *Cement and Concrete Research*. <https://doi.org/10.1016/j.cemconres.2019.105799>

Snellings, R., Salze, A., & Scrivener, K. L. (2014). Use of X-ray diffraction to quantify amorphous supplementary cementitious materials in anhydrous and hydrated blended cements. *Cement and Concrete Research*. <https://doi.org/10.1016/j.cemconres.2014.06.011>

Sobolkina, A., Mechtcherine, V., Khavrus, V., Maier, D., Mende, M., Ritschel, M., & Leonhardt, A. (2012a). Dispersion of carbon nanotubes and its influence on the mechanical properties of the cement matrix. *Cement and Concrete Composites*, 34(10), 1104–1113. <https://doi.org/10.1016/j.cemconcomp.2012.07.008>

Sotiriadis, K., Mácová, P., Mazur, A. S., Viani, A., Tolstoy, P. M., & Tsivilis, S. (2020). Long-term thaumasite sulfate attack on Portland-limestone cement concrete: A multi-technique analytical approach for assessing phase assemblage. *Cement and Concrete Research*, 130(January), 105995. <https://doi.org/10.1016/j.cemconres.2020.105995>

Staudenmaier, L. (1898). Process for the preparation of graphitic acid. *Ber. Dtsch. Chem. Ges*, 31, 1481–1487.

Subrahmanyam, K. S., Vivekchand, S. R. C., Govindaraj, A., & Rao, C. N. R. (2008). A study of graphenes prepared by different methods: Characterization, properties and solubilization. *Journal of Materials Chemistry*. <https://doi.org/10.1039/b716536f>

Sujay, H. M., Nair, N. A., Sudarsana Rao, H., & Sairam, V. (2020). Experimental study on durability characteristics of composite fiber reinforced high-performance concrete incorporating nanosilica and ultra fine fly ash. *Construction and Building Materials*, 262, 120738. <https://doi.org/10.1016/j.conbuildmat.2020.120738>

Sun, Y., Li, A., Hu, Y., Wang, X., & Liu, M. (2022). Simultaneously enhanced strength-plasticity of graphene/metal nanocomposites via interfacial microstructure regulation. *International Journal of Plasticity*. <https://doi.org/10.1016/j.ijplas.2021.103143>

Suo, Y., Guo, R., Xia, H., Yang, Y., Yan, F., & Ma, Q. (2020). Study on modification mechanism of workability and mechanical properties for graphene oxide-reinforced cement composite. *Nanomaterials and Nanotechnology*, 10, 1–12. <https://doi.org/10.1177/1847980420912601>

Szeluga, U., Kumanek, B., & Trzebicka, B. (2015). Synergy in hybrid polymer/nanocarbon composites. A review. In *Composites Part A: Applied Science and Manufacturing*. <https://doi.org/10.1016/j.compositesa.2015.02.021>

Tabish, M., Zaheer, M. M., & Baqi, A. (2023). Effect of nano-silica on mechanical, microstructural and durability properties of cement-based materials: A review. *Journal of Building Engineering*, 65(December 2022), 105676. <https://doi.org/10.1016/j.job.2022.105676>

Takai, C., Fuji, M., & Takahashi, M. (2007). A novel surface designed technique to disperse silica nano particle into polymer. *Colloids and Surfaces A: Physicochemical and Engineering Aspects*, 292(1), 79–82. <https://doi.org/https://doi.org/10.1016/j.colsurfa.2006.06.007>

Takigawa, M., Nemoto, H., Hashimoto, S. ichiro, & Date, S. (2022). Effectiveness of Thermal Stimulation of Superplasticizers on Fresh Properties of Cement Mortar. *Iranian Journal of Science and Technology - Transactions of Civil Engineering*. <https://doi.org/10.1007/s40996-021-00777-7>

Tang, L., Li, X., Ji, R., Teng, K. S., Tai, G., Ye, J., Wei, C., & Lau, S. P. (2012). Bottom-up synthesis of large-scale graphene oxide nanosheets. *Journal of Materials Chemistry*. <https://doi.org/10.1039/c2jm15944a>

Tayeh, B. A., Al Saffar, D. M., Aadi, A. S., & Almeshal, I. (2020). Sulphate resistance of cement mortar contains glass powder. *Journal of King Saud University - Engineering Sciences*, 32(8), 495–500. <https://doi.org/10.1016/j.jksues.2019.07.002>

Thess, A., Lee, R., Nikolaev, P., Dai, H., Petit, P., Robert, J., Xu, C., Lee, Y. H., Kim, S. G., Rinzler, A. G., Colbert, D. T., Scuseria, G. E., Tománek, D., Fischer, J. E., & Smalley, R. E. (1996). Crystalline ropes of metallic carbon nanotubes. *Science*. <https://doi.org/10.1126/science.273.5274.483>

- Tian, L., Meziani, M. J., Lu, F., Kong, C. Y., Cao, L., Thorne, T. J., & Sun, Y. P. (2010). Graphene oxides for homogeneous dispersion of carbon nanotubes. *ACS Applied Materials and Interfaces*. <https://doi.org/10.1021/am100687n>
- Tîlmaciu, C. M., & Morris, M. C. (2015). Carbon nanotube biosensors. In *Frontiers in Chemistry*. <https://doi.org/10.3389/fchem.2015.00059>
- Tobón, J. I., Payá, J., & Restrepo, O. J. (2015). Study of durability of Portland cement mortars blended with silica nanoparticles. *Construction and Building Materials*, 80, 92–97. <https://doi.org/10.1016/j.conbuildmat.2014.12.074>
- Torabian Isfahani, F., Li, W., & Redaelli, E. (2016a). Dispersion of multi-walled carbon nanotubes and its effects on the properties of cement composites. *Cement and Concrete Composites*, 74, 154–163. <https://doi.org/10.1016/j.cemconcomp.2016.09.007>
- Tornabene, F., Baccocchi, M., Fantuzzi, N., & Reddy, J. N. (2019). Multiscale approach for three-phase CNT/polymer/fiber laminated nanocomposite structures. *Polymer Composites*. <https://doi.org/10.1002/pc.24520>
- Trens, P., Denoyel, R., & Guilloteau, E. (1996). Evolution of surface composition, porosity, and surface area of glass fibers in a moist atmosphere. *Langmuir*, 12(5), 1245–1250.
- Trout, E. A. R. (2019). The history of calcareous cements. In *Lea's Chemistry of Cement and Concrete* (5th ed.). Elsevier Ltd. <https://doi.org/10.1016/B978-0-08-100773-0.00001-0>
- Tulashie, S. K., Ebo, P., Ansah, J. K., & Mensah, D. (2021). Production of Portland pozzolana cement from rice husk ash. *Materialia*, 16(February), 101048. <https://doi.org/10.1016/j.mtla.2021.101048>
- Tunstall, L. E., Ley, M. T., & Scherer, G. W. (2021). Air entraining admixtures: Mechanisms, evaluations, and interactions. *Cement and Concrete Research*. <https://doi.org/10.1016/j.cemconres.2021.106557>
- Vafaei, M., Allahverdi, A., Dong, P., & Bassim, N. (2018). Acid attack on geopolymer cement mortar based on waste-glass powder and calcium aluminate cement at mild concentration. *Construction and Building Materials*, 193, 363–372. <https://doi.org/10.1016/j.conbuildmat.2018.10.203>

Verma, M. A., & Srivastava, M. D. (2017). A Review on Partial Replacement of Cement by Flyash and Effect of Steel Fibers. *IOSR Journal of Mechanical and Civil Engineering*, 14(03), 104–107. <https://doi.org/10.9790/1684-140301104107>

Verma, P., Chowdhury, R., & Chakrabarti, A. (2023). Effect of adding highly reduced graphene oxide (rGO) nanosheets based nanomaterial on cement composites. *Materials Today: Proceedings*, xxxx, 3–9. <https://doi.org/10.1016/j.matpr.2023.03.616>

Visakh, P. M., Markovic, G., & Pasquini, D. (2016). Recent Developments in Polymer Macro, Micro and Nano Blends: Preparation and Characterisation. In *Recent Developments in Polymer Macro, Micro and Nano Blends: Preparation and Characterisation*.

Walters, Da., Ericson, L. M., Casavant, M. J., Liu, J., Colbert, D. T., Smith, K. A., & Smalley, R. E. (1999). Elastic strain of freely suspended single-wall carbon nanotube ropes. *Applied Physics Letters*, 74(25), 3803–3805.

Wang, B., Han, Y., & Liu, S. (2013). Effect of highly dispersed carbon nanotubes on the flexural toughness of cement-based composites. *Construction and Building Materials*, 46, 8–12. <https://doi.org/10.1016/j.conbuildmat.2013.04.014>

Wang, L., Zheng, D., Zhang, S., Cui, H., & Li, D. (2016). Effect of nano-SiO₂ on the hydration and microstructure of Portland cement. *Nanomaterials*, 6(12). <https://doi.org/10.3390/nano6120241>

Wang, Q., Li, S., Pan, S., Cui, X., Corr, D. J., & Shah, S. P. (2019). Effect of graphene oxide on the hydration and microstructure of fly ash-cement system. *Construction and Building Materials*, 198, 106–119. <https://doi.org/10.1016/j.conbuildmat.2018.11.199>

Wang, Q., Wang, J., Lu, C. X., Liu, B. W., Zhang, K., & Li, C. Z. (2015). Influence of graphene oxide additions on the microstructure and mechanical strength of cement. *Xinxing Tan Cailiao/New Carbon Materials*, 30(4), 349–356. [https://doi.org/10.1016/s1872-5805\(15\)60194-9](https://doi.org/10.1016/s1872-5805(15)60194-9)

Wang, Y., Li, V. C., & Backer, S. (1990). Tensile properties of synthetic fiber reinforced mortar. *Cement and Concrete Composites*, 12(1), 29–40.

Wang, Z., Wu, Q., Zhang, F. Y., & Cui, Y. Y. (2007). Synthesis of multi-walled carbon nanotube bundles with uniform diameter. *Materials Letters*. <https://doi.org/10.1016/j.matlet.2006.07.111>

Wegner, S., & Janiak, C. (2017). Metal Nanoparticles in Ionic Liquids. In *Topics in Current Chemistry* (Vol. 375, Issue 4). Springer International Publishing. <https://doi.org/10.1007/s41061-017-0148-1>

Wetwet, M. M., Ramadan, M., & Hazem, M. M. (2023). Multifunctional cementitious blends containing zirconia nanoparticles: Mechanical characteristics , gamma attenuation behavior , and self-cleaning performance. *Journal of Building Engineering*, 65(August 2022), 105736. <https://doi.org/10.1016/j.jobbe.2022.105736>

Wu, H. (2021). Toughening and strengthening mechanisms in ceramic nanocomposites. In *Residual Stresses in Composite Materials*. <https://doi.org/10.1016/B978-0-12-818817-0.00012-3>

Xiao, C., Li, C., Hu, J., & Zhu, L. (2022). The Application of Carbon Nanomaterials in Sensing, Imaging, Drug Delivery and Therapy for Gynecologic Cancers: An Overview. In *Molecules*. <https://doi.org/10.3390/molecules27144465>

Xing, T., Li, L. H., Hou, L., Hu, X., Zhou, S., Peter, R., Petravic, M., & Chen, Y. (2013). Disorder in ball-milled graphite revealed by Raman spectroscopy. *Carbon*. <https://doi.org/10.1016/j.carbon.2013.02.029>

Xiong, H., Yuan, K., Xu, J., & Wen, M. (2021). Pore structure, adsorption, and water absorption of expanded perlite mortar in external thermal insulation composite system during aging. *Cement and Concrete Composites*, 116, 103900. <https://doi.org/10.1016/j.cemconcomp.2020.103900>

Xu, G., Du, S., He, J., & Shi, X. (2019). The role of admixed graphene oxide in a cement hydration system. *Carbon*, 148, 141–150. <https://doi.org/10.1016/j.carbon.2019.03.072>

Xu, G., Zhong, J., & Shi, X. (2018). Influence of graphene oxide in a chemically activated fly ash. *Fuel*, 226(April), 644–657. <https://doi.org/10.1016/j.fuel.2018.04.033>

Yaghobian, M., & Whittleston, G. (2022b). A critical review of carbon nanomaterials applied in cementitious composites – A focus on mechanical properties and dispersion techniques. *Alexandria Engineering Journal*, 61(5), 3417–3433. <https://doi.org/10.1016/j.aej.2021.08.053>

Yamada, K., Takahashi, T., Hanehara, S., & Matsuhisa, M. (2000). Effects of the chemical structure on the properties of polycarboxylate-type superplasticizer. *Cement and Concrete Research*. [https://doi.org/10.1016/S0008-8846\(99\)00230-6](https://doi.org/10.1016/S0008-8846(99)00230-6)

- Yan, X., Zheng, D., Yang, H., Cui, H., Monasterio, M., & Lo, Y. (2020). Study of optimizing graphene oxide dispersion and properties of the resulting cement mortars. *Construction and Building Materials*, 257, 119477. <https://doi.org/10.1016/j.conbuildmat.2020.119477>
- Yang, K., Wan, J., Zhang, S., Tian, B., Zhang, Y., & Liu, Z. (2012). The influence of surface chemistry and size of nanoscale graphene oxide on photothermal therapy of cancer using ultra-low laser power. *Biomaterials*, 33(7), 2206–2214.
- Yao, W., Li, J., & Wu, K. (2003). Mechanical properties of hybrid fiber-reinforced concrete at low fiber volume fraction. *Cement and Concrete Research*, 33(1), 27–30.
- Ylmén, R., & Jäglid, U. (2013). Carbonation of Portland Cement Studied by Diffuse Reflection Fourier Transform Infrared Spectroscopy. *International Journal of Concrete Structures and Materials*, 7(2), 119–125. <https://doi.org/10.1007/s40069-013-0039-y>
- Yoda, Y., Aikawa, Y., & Sakai, E. (2017). Analysis of the hydration reaction of the Portland cement composition based on the hydration equation. *Journal of the Ceramic Society of Japan*. <https://doi.org/10.2109/jcersj2.16290>
- Yu, M.-F., Lourie, O., Dyer, M. J., Moloni, K., Kelly, T. F., & Ruoff, R. S. (2000). Strength and breaking mechanism of multiwalled carbon nanotubes under tensile load. *Science*, 287(5453), 637–640.
- Zare, Y., Rhee, K. Y., & Park, S. J. (2017). Predictions of micromechanics models for interfacial/interphase parameters in polymer/metal nanocomposites. *International Journal of Adhesion and Adhesives*. <https://doi.org/10.1016/j.ijadhadh.2017.09.015>
- Zare, Y., & Shabani, I. (2016). Polymer/metal nanocomposites for biomedical applications. In *Materials Science and Engineering C*. <https://doi.org/10.1016/j.msec.2015.11.023>
- Zhan, P. min, & He, Z. hai. (2019). Application of shrinkage reducing admixture in concrete: A review. In *Construction and Building Materials*. <https://doi.org/10.1016/j.conbuildmat.2018.12.209>
- Zhang, A., Yang, W., Ge, Y., Du, Y., & Liu, P. (2021). Effects of nano-SiO₂ and nano-Al₂O₃ on mechanical and durability properties of cement-based materials: A comparative study. *Journal of Building Engineering*, 34(May 2020), 101936. <https://doi.org/10.1016/j.jobbe.2020.101936>

- Zhang, C., Ren, L., Wang, X., & Liu, T. (2010). Graphene oxide-assisted dispersion of pristine multiwalled carbon nanotubes in aqueous media. *Journal of Physical Chemistry C*, 114(26), 11435–11440. <https://doi.org/10.1021/jp103745g>
- Zhang, C., Yang, F., Wang, W., & Chen, B. (2008). Preparation and characterization of hydrophilic modification of polypropylene non-woven fabric by dip-coating PVA (polyvinyl alcohol). *61*, 276–286. <https://doi.org/10.1016/j.seppur.2007.10.019>
- Zhang, M., Bai, L., Shang, W., Xie, W., Ma, H., Fu, Y., Fang, D., Sun, H., Fan, L., Han, M., Liu, C., & Yang, S. (2012). Facile synthesis of water-soluble, highly fluorescent graphene quantum dots as a robust biological label for stem cells. *Journal of Materials Chemistry*. <https://doi.org/10.1039/c2jm16835a>
- Zhao, G., Li, J., Shi, M., Fan, H., Cui, J., & Xie, F. (2020). Degradation mechanisms of cast-in-situ concrete subjected to internal-external combined sulfate attack. *Construction and Building Materials*. <https://doi.org/10.1016/j.conbuildmat.2020.118683>
- Zhao, L., Guo, X., Ge, C., Li, Q., Guo, L., Shu, X., & Liu, J. (2017a). Mechanical behavior and toughening mechanism of polycarboxylate superplasticizer modified graphene oxide reinforced cement composites. *Composites Part B: Engineering*, 113, 308–316. <https://doi.org/10.1016/j.compositesb.2017.01.056>
- Zhao, L., Guo, X., Liu, Y., Ge, C., Chen, Z., Guo, L., Shu, X., & Liu, J. (2018a). Investigation of dispersion behavior of GO modified by different water reducing agents in cement pore solution. *Carbon*, 127, 255–269. <https://doi.org/https://doi.org/10.1016/j.carbon.2017.11.016>
- Zhao, L., Guo, X., Liu, Y., Ge, C., Guo, L., Shu, X., & Liu, J. (2017). Synergistic effects of silica nanoparticles/polycarboxylate superplasticizer modified graphene oxide on mechanical behavior and hydration process of cement composites. *RSC Advances*, 7(27), 16688–16702. <https://doi.org/10.1039/c7ra01716b>
- Zhao, L., Guo, X., Liu, Y., Zhao, Y., Chen, Z., Zhang, Y., Guo, L., Shu, X., & Liu, J. (2018). Hydration kinetics, pore structure, 3D network calcium silicate hydrate, and mechanical behavior of graphene oxide reinforced cement composites. *Construction and Building Materials*, 190, 150–163. <https://doi.org/10.1016/j.conbuildmat.2018.09.105>

Zhao, L., Guo, X., Song, L., Song, Y., Dai, G., & Liu, J. (2020). An intensive review on the role of graphene oxide in cement-based materials. *Construction and Building Materials*, 241, 117939. <https://doi.org/10.1016/j.conbuildmat.2019.117939>

Zhao, L., Zhu, S., Wu, H., Zhang, X., Tao, Q., Song, L., Song, Y., & Guo, X. (2020). Deep research about the mechanisms of graphene oxide (GO) aggregation in alkaline cement pore solution. *Construction and Building Materials*, 247, 118446. <https://doi.org/10.1016/j.conbuildmat.2020.118446>

Zhao, N., & Zhang, Y. (2009). The relation between organized structure and maintaining cost in WSN. *Proceedings - 5th International Conference on Wireless Communications, Networking and Mobile Computing, WiCOM 2009*. <https://doi.org/10.1109/WICOM.2009.5303746>

Zhou, C., Li, F., Hu, J., Ren, M., Wei, J., & Yu, Q. (2017a). Enhanced mechanical properties of cement paste by hybrid graphene oxide/carbon nanotubes. *Construction and Building Materials*, 134, 336–345. <https://doi.org/10.1016/j.conbuildmat.2016.12.147>

Zhu, S., Zhang, J., Qiao, C., Tang, S., Li, Y., Yuan, W., Li, B., Tian, L., Liu, F., Hu, R., Gao, H., Wei, H., Zhang, H., Sun, H., & Yang, B. (2011). Strongly green-photoluminescent graphene quantum dots for bioimaging applications. *Chemical Communications*. <https://doi.org/10.1039/c1cc11122a>

Zhu, Z., Xu, W., Chen, H., & Tan, Z. (2020). Evolution of microstructures of cement paste via continuous-based hydration model of non-spherical cement particles. *Composites Part B: Engineering*, 185(November 2019), 107795. <https://doi.org/10.1016/j.compositesb.2020.107795>

Živica, V. (2004). Acidic attack of cement based materials - A review Part 3: Research and test methods. *Construction and Building Materials*, 18(9), 683–688. <https://doi.org/10.1016/j.conbuildmat.2004.04.030>

PUBLICATIONS IN INTERNATIONAL JOURNAL

1. **Kanchna Bhatrola**, and N. C. Kothiyal, (2023), “Influence of (1D/2D) hybrid nanomaterials on the mechanical and durability properties of pozzolana portland cementitious mortar”, **Journal of Adhesion Science and Technology**, 0(0), pp. 1–25. Available at: <https://doi.org/10.1080/01694243.2023.2226287>.
2. **Kanchna Bhatrola**, and N. C. Kothiyal, (2023) “Comparative study of physico-mechanical performance of PPC mortar incorporated 1D/2D functionalized nanomaterials”, **International Journal of Applied Ceramic Technology**, Vol. 20, pp. 2478-2498. Available at: <https://doi.org/10.1111/ijac.14372>.
3. **Kanchna Bhatrola**, N. C. Kothiyal, and Sameer Kumar Maurya, (2023) “Durability & mechanical properties of functionalized multiwalled carbon nanotube incorporated pozzolana portland cement composite”, **Materials Today: Proceedings** [Preprint]. Available at: <https://doi.org/https://doi.org/10.1016/j.matpr.2023.07.178>.
4. **Kanchna Bhatrola**, Sameer Kumar Maurya, Ramanjit Kaur, and N. C. Kothiyal, (2022) "Mechanical and electrical resistivity performance of Pozzolana Portland cement mortar admixed graphene oxide" **Materials Today: Proceedings**, Vol. 78, pp. 830-838. Available at: <https://doi.org/10.1016/j.matpr.2022.11.414>.
5. Sameer Kumar Maurya, **Kanchna Bhatrola**, and N. C. Kothiyal, (2023) “Sustainable development of mortar with low carbon admixed High Volume Fly Ash”, **Materials Today: Proceedings** [Preprint]. Available at: <https://doi.org/https://doi.org/10.1016/j.matpr.2023.08.067>
6. Sameer Kumar Maurya, **Kanchna Bhatrola**, N. C. Kothiyal, and Maina Choudhary, (2022) “Comparative effects of nano-silica and graphene oxide on Pozzolana Portland cement nanocomposites” **Materials Today: Proceedings**, Vol. 78, pp. 864-870. <https://doi.org/10.1016/j.matpr.2022.12.019>
7. Ramanjit Kaur, **Kanchna Bhatrola**, Sameer Kumar Maurya, Ajay Kumar, Jaswinder Kaur, Sweeti Suhag, N. C. Kothiyal, (2023) “Durability of Cementitious Mortar: Incorporation of Highly Dispersed Superplasticizer Modified Graphene Oxide in Fly Ash Blended Mortar” **Journal of Building Engineering**, 107888. <https://doi.org/10.1016/j.jobbe.2023.107888>.

8. **Kanchna Bhatrola**, Sameer Kumar Maurya, and N C Kothiyal, (2023) “An updated review on scientometric analysis & physico-mechanical performance of nanomaterials in cementitious composites” **Structures**, <https://doi.org/10.1016/j.istruc.2023.105421>.
9. **Kanchna Bhatrola**, Sameer Kumar Maurya, and N C Kothiyal, (2024) “Research on the influence of dispersed carbon nanomaterials with different water reducing agent in cementitious mortar”. **Fullerenes, Nanotubes and Carbon Nanostructures**, 1-16. <https://doi.org/10.1080/1536383X.2024.2306806>.
10. **Kanchna Bhatrola**, and N C Kothiyal, (2024) “Nanomaterial-infused pozzolana portland cement composite: Exploring mechanical strength, durability, and microstructure properties. **Fullerenes, Nanotubes and Carbon Nanostructures**”, 1-18. <https://doi.org/10.1080/1536383X.2024.2306810>.
11. **Kanchna Bhatrola**, and N C Kothiyal, “Optimizing Dosage of Functionalized Carbon Nanomaterials in Mortar Using Response Surface Methodology” submitted to **Materials Research Bulletin (Communicated)**.

BOOK CHAPTERS

sKanchna Bhatrola, Sameer Kumar Maurya, N. C. Kothiyal, and Vaneet Kumar (2022), “Polymer Membrane in Textile Wastewater” In: **Polymer Technology in Dye-containing Wastewater**, Vol. 2, pp. 53-84. Springer, Singapore, [DOI: 10.1007/978-981-19-0886-6_3](https://doi.org/10.1007/978-981-19-0886-6_3).

1. **Kanchna Bhatrola**, Sameer Kumar Maurya, N. C. Kothiyal, and Bharti Budhalakoti (2022), “An Investigation on Mechanical Characteristics of Carbon Nanomaterials Used in Cementitious Composites”, In: **Handbook of Green and Sustainable Nanotechnology**, pp. 1-22. Springer, Cham. https://doi.org/10.1007/978-3-030-69023-6_93-1
2. Sameer Kumar Maurya, Bharti Budhalakoti, **Kanchna Bhatrola**, and N. C. Kothiyal, and Vaneet Kumar (2023) "Nano-engineered Material and Remediation Strategy" In: **Nano-engineered Materials for Textile Waste Remediation**, pp. 179-199. Springer, Singapore, [DOI: 10.1007/978-981-19-7978-1_9](https://doi.org/10.1007/978-981-19-7978-1_9)
3. Bharti Budhalakoti, Sameer Kumar Maurya, **Kanchna Bhatrola**, N C Kothiyal, and Vaneet Kumar (2023), “Potential of Atmospheric Water Harvesting In Arid Regions: Case Studies” In: **Atmospheric Water Harvesting Development and Challenges. Water Science and Technology Library**, vol. 122, pp.115-133. Springer, Cham. https://doi.org/10.1007/978-3-031-21746-3_6

4. Sakshi Bawa, N.C. Kothiyal, Sameer Kumar Maurya, **Kanchna Bhatrola**, Bharti Budhalakoti, (2024) “Polymeric-Aluminosilicate Mixed Membranes and Their Properties” In **Reference Module in Materials Science and Materials Engineering**, Elsevier, <https://doi.org/10.1016/B978-0-323-95486-0.00017-X>.
5. Bharti Budhalakoti, N. C. Kothiyal, Sameer Kumar Maurya, **Kanchna Bhatrola**, and Sakshi Bawa (2024) “Application of Dendritic Polymers for Remediation of Water Pollution” In **Reference Module in Materials Science and Materials Engineering**, Elsevier, <https://doi.org/10.1016/B978-0-323-95486-0.00016-8>.

PUBLICATIONS IN INTERNATIONAL CONFERENCES

1. **Kanchna Bhatrola**, N C Kothiyal, and Sameer Kumar Maurya (2021), “Synthesis of Graphene Oxide Via Microwave Assisted Eco-Friendly Method Versus Modified Hummer Method”, **International Journal of Advanced Research in Science, Communication and Technology**, vol. 12, pp. 2581-9429(4).

POSTER/ORAL PRENTATIONS IN INTERNATIONAL CONFERENCES

1. **Kanchna Bhatrola**, and N C Kothiyal, presented **Poster** entitled “Mechanical & Durability Properties of Cement Composites Upon the Addition of Carbon Nanomaterials” in **International Conference on “Chemical Constellation Cheminar -2019 (C³)”** held at Dr B R Ambedkar National Institute of Technology Jalandhar-144011 Punjab (India) from October 12-13, 2019.
2. **Kanchna Bhatrola**, and N C Kothiyal, presented **Poster** entitled “Dispersion study of graphene oxide in various Polycarboxylate based superplasticizer” in the **International Conference on “Molecules to Materials (MTM – 2020)”** held at Sardar Vallabhbhai National Institute of Technology (SVNIT), Gujarat, India from December 17-18, 2020.
3. **Kanchna Bhatrola**, and N C Kothiyal, presented **Oral** entitled “Superplasticizer Aided Dispersion Study of Carbon Nanomaterials in Aqueous Medium” in the **International Conference on “Emerging Trends in Chemical and Applied Sciences for Sustainable Future”** held at Hansraj College, University of Delhi, on October 30th, 2021.
4. **Kanchna Bhatrola**, and N C Kothiyal, presented **Poster** entitled “Superplasticizer Aided Dispersion Study of Carbon Nanomaterials in Aqueous Medium” in the **International E-Conference on “Sustainable and Futuristic Materials (SFM-2021)”** held at International Research Centre and Department of Chemistry, Kalasalingam Academy of Research and Education, Krishnankoil from November

29-30, 2021.

5. **Kanchna Bhatrola**, and N C Kothiyal, presented **Oral** entitled “Mechanical and Electrical Resistivity Performance of Pozzolana Portland Cement Mortar Admixed Stabilized Graphene Oxide” in the **International Conference on “Advanced Functional Materials-Future Perspectives (AFMFP-2022)”** held at Dr B R Ambedkar National Institute of Technology Jalandhar-144011 Punjab (India) from August 06-08, 2022.

PARTICIPATION IN INTERNATIONAL CONFERENCES

1. **An International Conference on “Chemical Constellation Ceminar (C³ -2019)”** organized by Department of Chemistry, Dr B R Ambedkar National Institute of Technology Jalandhar-144011 Punjab (India) from October 06-08, 2022.
2. **An International Conference on “Advanced Functional Materials-Future Perspectives (AFMFP-2022)”** organized by Department of Chemistry, Dr B R Ambedkar National Institute of Technology Jalandhar-144011 Punjab (India) from August 06-08, 2022.
3. **A Session Coordinator: Organizing Committee Member in:** International Conference on Advanced Function Materials: Future Perspectives (AFMFP-2022). organized by Department of Chemistry, Dr B R Ambedkar National Institute of Technology Jalandhar-144011 Punjab (India) from August 06-08, 2022.

SHORT TERM COURSES, WORKSHOPS, AND WEBINARS ATTENDED

1. Attended a Short Term Course on **“Material Processing and Characterization (MPC 2019)”** organized by the CSIR- National Physical Laboratory, New Delhi from August 26-30, 2019
2. Attended a One Week Short Term Course on **“Effective Research Proposal and Paper Writing”** being organized by Dr B R Ambedkar National Institute of Technology Jalandhar-144011 Punjab (India) from December, 20-24, 2019.
3. Attended a National Workshop on **“Innovation and Intellectual Property Rights Filing”** organized by the Innovation Club (Institute Innovation Council), Dr B R Ambedkar National Institute of Technology Jalandhar-144011 Punjab (India) held on July 01, 2020.
4. Attended an International Webinar on **“Advance in Chemical Science and Engineering”** organized by the Govt. Bilasa Girls P. G. Autonomous College Bilaspur, Chhattisgarh held on July, 18, 2020.

Introduction & Literature survey

Abhishek Kanchha Bhatnagar

ORIGINALITY REPORT

14%	9%	8%	10%
SIMILARITY INDEX	INTERNET SOURCES	PUBLICATIONS	STUDENT PAPERS

PRIMARY SOURCES

- 1** www.inderscience.com 1%
Internet Source
- 2** Submitted to National Institute of Technology, Rourkela 1%
Student Paper
- 3** Submitted to Middle East Technical University 1%
Student Paper
- 4** Ramanjit Kaur, N.C. Kothiyal. "Comparative effects of sterically stabilized functionalized carbon nanotubes and graphene oxide as reinforcing agent on physico-mechanical properties and electrical resistivity of cement nanocomposites", Construction and Building Materials, 2019 1%
Publication
- 5** mafiadoc.com 1%
Internet Source
- 6** etd.uwc.ac.za 1%
Internet Source
- 7** Submitted to Manipal University

Experimental and results

*Bhush
Kanchana Bhatnagar*

ORIGINALITY REPORT

10%

SIMILARITY INDEX

7%

INTERNET SOURCES

6%

PUBLICATIONS

2%

STUDENT PAPERS

PRIMARY SOURCES

1

Submitted to Birla Institute of Technology and Science Pilani

Student Paper

<1%

2

Liping Bi, Guangcheng Long, Cong Ma, Youjun Xie. "Mechanical properties and water absorption of steam-cured mortar containing phase change composites", Construction and Building Materials, 2020

Publication

<1%

3

discovery.dundee.ac.uk

Internet Source

<1%

4

mdpi-res.com

Internet Source

<1%

5

spiral.imperial.ac.uk

Internet Source

<1%

6

ir.lib.uwo.ca

Internet Source

<1%

7

Elena Cerro-Prada, Rosalía Pacheco-Torres, Fernando Varela. "Effect of Multi-Walled Carbon Nanotubes on Strength and Electrical

<1%